



BRNO UNIVERSITY OF TECHNOLOGY

VYSOKÉ UČENÍ TECHNICKÉ V BRNĚ

FACULTY OF MECHANICAL ENGINEERING

FAKULTA STROJNÍHO INŽENÝRSTVÍ

INSTITUTE OF MACHINE AND INDUSTRIAL DESIGN

ÚSTAV KONSTRUOVÁNÍ

**STATIC AND TRANSIENT BEHAVIOUR OF
MAGNETORHEOLOGICAL FLUID AND DEVICES**

STATICKÉ A PŘECHODOVÉ CHOVÁNÍ MAGNETOREOLOGICKÉ KAPALINY A ZAŘÍZENÍ

HABILITATION THESIS

HABILITAČNÍ PRÁCE

AUTHOR

AUTOR

Ing. Michal KUBÍK, Ph.D.

BRNO 2022

„My vědci máme obrovské štěstí. Můžeme dělat to, co opravdu chceme, děláme svůj koníček. To není jako, že přijdete do práce, něco tam uděláte, pak v pět zazvoní zvonek a jdete pryč si dělat něco svého. Já myslím, že spousta z nás by se nejradši hned pustila do dalšího experimentu. A proto se považuju za hobbyholika, to je přesnější popis.“

Charles Rice
Nositel Nobelovy ceny

So we're actually very fortunate as scientists that is that we're sort of allowed to pursue our passion or hobby. It's not like coming to work to do a job and then the bell rings at five o'clock and you go off and do something else. I think a lot of us just would rather be starting the next experiment. That's why I guess sort of a hobbyholic.¹

Charles Rice
Nobel Prize laureate

¹ Original version of interview from 15.5.2021 in Hyde Park Civilization TV show

ACKNOWLEDGMENT

I wish to thank assoc. prof. Ivan Mazůrek and dr. Zbyněk Strecker for their ongoing support and encouragement to the research throughout my whole career. I know, sometimes it wasn't easy.

Furthermore, I would like to thank assoc. prof. Janusz Goldasz from the Cracow University of Technology who invaluabley influenced my research career.

Last but not least, I would like to thank my wife Dáša, daughters (Terezka a Katka), my parents, and whole my family for their support and patience.

Static and transient behaviour of magnetorheological fluid and devices

ABSTRACT

Magnetorheological fluid is one of the smart materials that change its rheological behaviour in the presence of a magnetic field. This fluid has found application in electronically controlled dampers and is widely used in automotive with semi-active control. This thesis focuses on the issues of rheology, tribology, and transient behaviour of the MR fluid itself, as well as on MR devices and their transient behaviour. Each chapter provides an overview of the current state of the art, followed by a description of the author's contribution to this research area. A total of 7 papers were published in scientific journals with high impact factors.

KEYWORDS: magnetorheological fluid; rheology; tribology; transient response; response time; MR damper; eddy currents

Statické a dynamické chování magnetoreologické kapaliny a zařízení

ABSTRAKT

Magnetoreologická kapalina je jeden ze smart materiálů, který mění své reologické vlastnosti v přítomnosti magnetického pole. Tato kapalina našla uplatnění v elektronicky říditelných tlumičích a je široce používána v automotive spolu se semiaktivním řízením. Tato práce se zaměřuje na problematiku reologie, tribologie a přechodového chování samotné MR kapaliny a také na MR zařízení a jejich přechodového chování. Jednotlivé kapitoly poskytují vhled do problematiky, následovaný popisem vlastního přínosu autora do dané oblasti. Celkem bylo publikováno 7 prací ve vědeckých časopisech s vysokým impaktním číslem.

KLÍČOVÁ SLOVA: magnetoreologická kapaliny; reologie; tribologie; přechodové chování; časová odezva; MR tlumič; vířivé proudy

CONTENTS

1. INTRODUCTION	11
2. MAGNETORHEOLOGICAL FLUID	13
2.1 Rheology of magnetorheological fluid	14
2.2 Tribology of magnetorheological fluid	16
2.3 Transient response of magnetorheological fluid	17
2.3.1 Particle structure development response time	18
2.3.2 Rheological response time	18
2.3.3 Hydrodynamic response time	19
2.4 Knowledge gaps	20
2.5 Author' s contribution to the field	20
2.5.1 Hydrodynamic response time of magnetorheological fluid in valve mode: model and experimental verification [79]	21
2.5.2 Transient Response of Magnetorheological Fluid on Rapid Change of Magnetic Field in Shear Mode [80]	22
2.5.3 Stribeck Curve of Magnetorheological Fluid within Pin-on-Disc Configuration: An Experimental Investigation [81]	23
3. MAGNETORHEOLOGICAL FLUID DEVICES	59
3.1 Magnetorheological devices	59
3.1.1 Magnetorheological dampers	60
3.1.2 Magnetorheological fluid seal	62
3.2 Transient response of magnetorheological damper	62
3.2.1 The inductance of an electromagnetic coil	63
3.3 Knowledge gaps	65
3.4 Author's contribution to the field	66
3.4.1 Insight into the response time of fail-safe magnetorheological damper [135]	67
3.4.2 Structured magnetic circuit for magnetorheological damper made by selective laser melting technology [136].	68
3.4.3 Multiphysics Model of an MR Damper including Magnetic Hysteresis [137]	69
3.4.4 A magnetorheological fluid shaft seal with low friction torque [138]	70
4. CONCLUSIONS AND IMPLICATIONS FOR FURTHER RESEARCH	127
5. REFERENCES	129
LIST OF FIGURES	137
LIST OF ABBREVIATIONS	139

INTRODUCTION

Transporting people or cargo is an integral part of today's society. We live in an age when technologies and transport are evolving significantly. Ongoing development in transportation aims to increase safety, speed, reduce operating or production costs, environmental impact, or noise emissions. However, the most important is traffic safety. The number of seriously injured and dead persons in road accidents has been declining for a long time[1]. The main reason is that transportation safety is constantly increasing due to developments in electronics, driving assistants, intelligent transport communications, and also the materials themselves.

The so-called Smart Materials are increasingly used in transportation. Smart material is a material that one or more properties can be significantly changed by external stimuli, such as mechanical stress, temperature, light, electric or magnetic field, etc. These materials are used in smart sensors (vehicle condition monitoring, monitoring of concrete structures, roadways, and bridges for internal flaws cracks, corrosion, and movement), smart glass windows (reflectivity of infrared light could be changed automatically to maintain internal temperatures), smart coatings (improved reflectivity), actuators (smart suspensions systems), etc.

One of the commonly used smart material in transport is the so-called magnetorheological (MR) fluid. It is a magnetically sensitive fluid which can change its apparent viscosity by applying an external magnetic field. Approximately 80 years ago, Jacob Rabinow [2] discovered the MR fluid at the US National Bureau of Standards. However, significant research started roughly 35 years ago. Since then, MR fluid has undergone tremendous development. This fluid has been used in dampers, clutches, brakes, or engine mounts. However, the most important application is an electronically controlled suspension damper in automotive. MR dampers with semi-active control have been used since 1998 for damping seats in heavy-duty vehicles to improve rider comfort and safety [3]. MR dampers have also been used commercially since 2002 in the vehicle suspension system (GM's Cadillac Seville STS)[3]. This technology is currently used by companies Ford, Ferrari, Audi, Chevrolet, Lamborghini, Range Rover, Porsche, etc. This system improves driving handling, comfort, and safety (reduction of braking distance)[4]. In 2007, more than 100 000 MR devices were used in the automotive industry [3]. The first application of this technology also appears in railways. The research team at the Brno University of Technology tested yaw MR damper on a real track [5], see Figure 1.

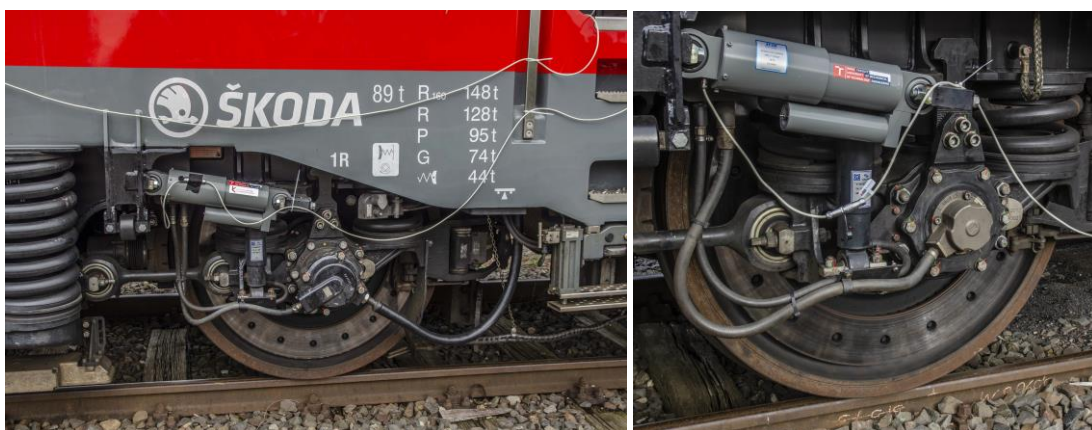


Figure 1 Mounted MR damper on railway vehicle during testing on real track [5]

As mentioned, this technology is currently widely used in automotive. However, intensive fundamental research is still underway in the area of MR fluid itself and the development of new and progressive MR devices. This intensive research can be documented by more than 400 scientific publications in the WOS database in 2021. The recent trend is the use of MR dampers with fast semi-active control, where the transient behaviour of the MR damper is very important (short response time). This can be documented by the two most cited papers in this research area in 2021², which focus on semi-active control. The papers show that fast semi-active control significantly improves the behaviour of the vehicle, especially in terms of safety. Currently, the development of new generations of MR fluids that have better rheological, tribological, transient behaviour, or sedimentation stability is performed.

The main aim of the thesis is to provide an insight into the current state of the art in the static and transient behaviour of magnetorheological fluids and devices to demonstrate the author's contribution to this research field. Chapter 2 deals with the rheological, tribological, and transient behaviour of the magnetorheological fluid itself. Chapter 3 focused on the magnetorheological devices and their transient behaviour. It should be noted that the presented state of the art in magnetorheological technology is not complete and provide just basic insight into this research field. At the end of each chapter, the research gap is listed to clearly show the author's contribution and the novelty of each presented study. In total, the thesis is built on 7 journal papers (four times first author, twice second author, and once corresponding author). Chapter 2 includes 3 papers, and chapter 3 includes 4 papers. Focusing on the papers with IF, five documents were published in journals in the first quartile (Q1), one paper in the second quartile (Q2), and one paper in the third quartile (Q3). More detailed information about author papers, citations, etc., can be found in the document “Autoevaluation criteria of the applicant for habilitation”.

² Magnetorheological keyword used in the WOS database.

MAGNETORHEOLOGICAL FLUID

The word "smart" has become one of the keywords connected with modern scientific and technological progress. In everyday life, we encounter “smart” phones, appliances, and materials. Smart material is a material that one or more properties can be significantly changed by external stimuli, such as mechanical stress, temperature, light, electric or magnetic field, etc. One of those materials is magnetorheological (MR) fluid which is a magnetic field responsive material. MR fluid exhibits a reversible and very fast transition from a liquid to a nearly solid state under the application of external magnetic fields.

MR fluid is a suspension of fine, non-colloidal, low-coercivity, high-magnetisable particles in a carrier fluid [6]. Particles are usually made of carbonyl iron [7], iron/cobalt alloy [8], iron oxides (Fe_2O_3 , Fe_3O_4) [9, 10], nickel, cobalt, silicon steel, and their alloys. These materials usually exhibit magnetic saturation up to 2.1 T ($\mu_0 M_s = 2.1$ T). The most used is carbonyl iron powder (CIP) which is obtained by the thermal decomposition method [11]. However, the CIP manufacturing process is very expensive compared to other methods of producing iron particles. This is the most expensive item of the total price of MR fluid (1 kg of CI powder = app. 300 USD). The vast majority of commercially available MR fluids are CIP-based. The solid phase by the volume is in the range of 20 % to 48 %. In the automotive industry, the typical particle content by volume is 26 % [6]. The particle size is in the range of 1 to 100 μm , preferably in the range of 1 to 10 μm . The ferromagnetic particles have a spherical shape due to durability and tribological properties. Occasionally, flakes [12] or plates shape [13] of particles appear.

The continuous phase of MR fluids are typically silicon oils [14, 15], mineral oils [16], synthetic hydrocarbon oils (PAO)[17], water [18], glycols [19], or ferrofluids [20]. The carrier fluid should be chemically compatible with particles, exhibit low thermal expansion, excellent lubricity, low viscosity in the high-temperature range, and be economical. The preferred carrier fluid is polyalphaolefin (PAO). This oil exhibits a great operating temperature range, lubrication properties, and chemical stability. The typical dynamic viscosity of carrier fluid is between 0.01 to 0.1 Pa.s at ambient temperature. The commercial MR fluid manufacturers use a hydrocarbon-based carrier fluid (Lord corporation [21] or FemFluid corporation).

The MR fluid exhibits a rapid change of apparent viscosity in several orders of magnitude under the application of an external magnetic field [11]. When the MR fluid is energized by the magnetic field, the ferromagnetic particles are magnetized and form chain-like structures in the direction of the magnetic field, see Figure 2. The fluid then exhibits a significant increase of the yield stress in tens of kPa.

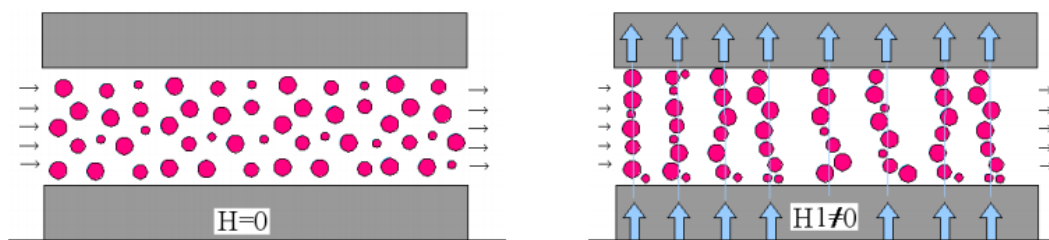


Figure 2 Magnetorheological effect; left: without the magnetic field, right: with the application of magnetic field (blue arrow)[22]

Oclan and McKinley [23] from MIT visualized microstructural development in the pressure-driven flow of magnetorheological fluid in valve mode. Figure 3 shows how MR fluid particles chains (clusters) look during a flow in the case of (a) MR fluid flow without a magnetic field, (b) after applying a magnetic field, (c) after turning off the magnetic field, and (d) after applying demagnetization magnetic field. In my opinion, this research/ figure gives a good insight into the behaviour of particle chains during the fluid flow. However, the visualization of particle chain behaviour has been addressed by many other research teams [24, 25]. A large research area is also micromechanical modeling of chain (microstructure) behaviour and its impact on rheological properties [26–28]. However, this issue is not described in this thesis.

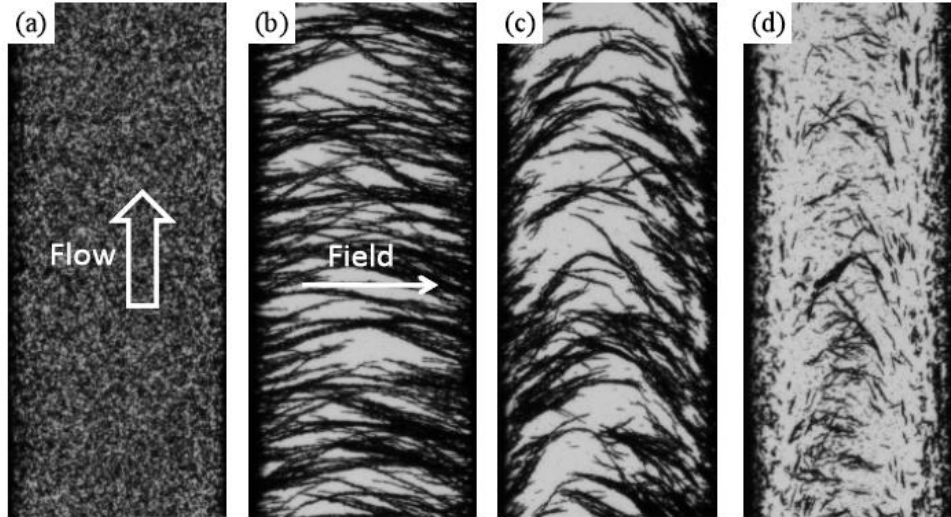


Figure 3 The particle chains behaviour of MR fluid during flow in the case: (a) without magnetic field, (b) with the magnetic field, (c) after turning off the magnetic field, and (d) after applying demagnetization magnetic field [23]

In the next parts of the thesis, the current state of the art in the field of rheological, tribological properties, and transient behaviour of MR fluid is described. The chapter on the rheology of MR fluid is important because it provides basic information, which is essential for the section on transient behaviour. These next chapters aim to meet the reader with basic information about the selected research area with regard to defining the author's contribution to this research area. However, sedimentation stability [29, 30], fluid durability [31], etc., are also important areas but in the thesis are not discussed.

2.1 Rheology of magnetorheological fluid

The rheological behaviour of MR fluid is affected by several factors such as particle concentration, particle size [32], particle shape [33–35], particle distribution [36], properties of carrier fluid, temperature [37], magnetic field, or additives. The rheological behaviour of MR fluid can be divided into off-state and on-state (energized) behaviour. In an on-state regime, the magnetic field is applied.

In the off-state, MR fluid appears similar to liquid paints and exhibits a comparable value of apparent viscosity ($0.1 - 1 \text{ Pa}\cdot\text{s}^{-1}$, at low shear rates). The off-state behaviour depends on particle volume concentration, particle size [32], additives [38], and carrier fluid properties [39]. In general, viscosity increases with particle concentration. In 1940, the equation (Einstein equation) describing the viscosity of a suspension of solid spheres η_{MRF} as a function of the viscosity of the carrier liquid η_0 , and the volume concentration of the particles ϕ_v was published [40], see below.

$$\eta_{MRF} = \eta_0(1 + 2.5\phi_v) \quad (1)$$

The other more advanced models were also published as the Batchelor equation [41], Krieger-Dougherty equation [41], Mooney [42], etc. MR fluid in off-state exhibits Non-Newtonian behaviour because it usually has a small yield stress in units or tens of Pascals. However, for MR device modeling, the Newtonian behaviour of MR fluid is usually assumed [43].

The rheology of MR fluid in on-state is characterized by pre-yield and post-yield regimes [44, 45]. In the pre-yield regime, the MR fluid usually exhibits viscoelastic behaviour. The complex modulus G is a magnetic field and particle concentration-dependent [46]. The shear stress τ in the fluid can be described by the equation below:

$$\tau = G\gamma, \quad \tau < \tau_0(H) \text{ and } \dot{\gamma} = 0 \quad (2)$$

where γ is shear strain, $\dot{\gamma}$ is shear strain rate and $\tau_0(H)$ is dynamic yield stress. The shear strain is usually in the order of 10^{-3} [43]. However, several models have been presented to characterize the pre-yield behavior of MR fluids. These models are composed of elastic springs and viscous dashpot elements [47].

The post-yield regime of MR fluids has been experimentally determined and described by models in a number of publications. Thus behavior is often represented as a Bingham plastic having variable yield stress [48] by the equation:

$$\tau = \tau_0(H) + \eta\dot{\gamma}, \quad \tau > \tau_0(H) \quad (3)$$

Where η is dynamic fluid viscosity. However, the Bingham model is insufficient to characterize the MR fluid at high shear rates [6]. Shear-thinning ($m < 1$) or shear-thickening ($m > 1$) effect dominates at high shear rates. The Herschel-Bulkley model can describe this behaviour:

$$\tau = \tau_0(H) + \eta\dot{\gamma}^{\frac{1}{m}}, \quad \tau > \tau_0(H) \quad (4)$$

Where m is the consistency index. For example, MR fluid MRC-C1L made by CK materials lab company exhibits shear thinning behaviour. In both models, the most relevant rheological property of an MR fluid is the dynamic yield stress $\tau_0(H)$. It should be noted that this value is usually determined by the fitting method. The paper of de Vicente et al. [11] or Seo et al. [49] pointed out that yield stresses are three types: the elastic limit, the static τ_{sy} , and the dynamic τ_{dy} , see Figure 4. The static (or frictional) yield stress is the minimum stress which creates the fluid to flow. The static yield stress is typically experimentally determined by using creep tests. The dynamic yield stress corresponds to the stress needed to continuously break the particle chains, which reform in the presence of the magnetic forces.

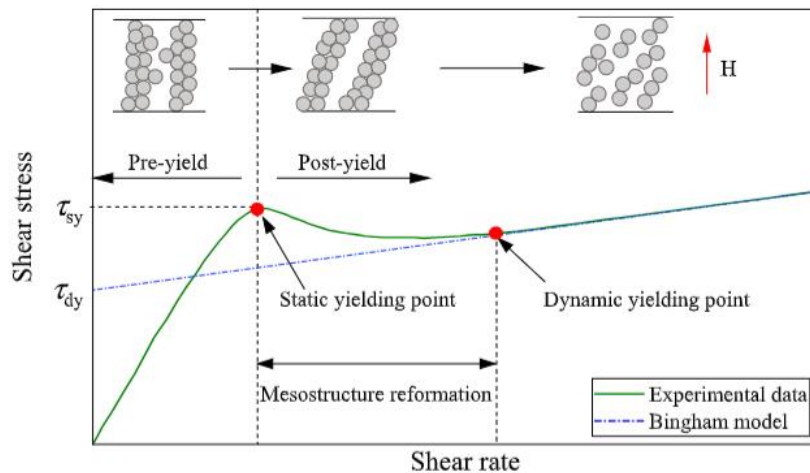


Figure 4 Typical yield stresses [50]

The dynamic yield stress of MR fluid depends on particle size [51], particle volume fraction [52], particle material [53], particle distribution [36], type of carrier fluid [43], magnetic field [36, 54], additives [55], etc. However, the dynamic yield stress is insensitive to operating temperature. The yield stress of MR fluid can also be modelled. In the literature, these models can be classified into two groups [11]: Macroscopic and Microscopic models. Macroscopic models take into account the magnetic energy minimization principle and assume a homogenous structure [11]. The microscopic model works with interparticle interactions. For example, papers dealing with the modelling of the yield stress of MR fluid are [10, 11, 28]. The measurement or modelling of rheological behaviour of MR fluid is a quite complex and huge research area. In this section, just a basic insight into this area was provided.

2.2 Tribology of magnetorheological fluid

The tribological properties of MR fluid can be strongly moderated by their composition. The special group of MR fluid is a so-called Magnetorheological polishing fluid [56], where a significant part of the fluid consists of abrasive particles such as alumina, silicon carbide, or diamond particles. This fluid is used as a magnetic field-assisted finishing method (Magnetorheological Polishing method). This method is used for manufacturing the lowest surface roughness values for optics of the highest quality. However, in the other applications of MR fluids is a fundamental improvement in the tribological properties as a decrease of friction coefficient and wear.

The surfaces of MR devices (MR dampers, clutches, brakes, etc.) are in contact with the MR fluid, and it works with relative motion. The wear of MR devices is much faster than hydraulic oil devices because of the abrasive nature of the iron particles. The particle material, hardness, size [57], shape [58], carrier fluid [59], magnetic field [60], and additives [59, 61] significantly affect the tribological properties. The additives in the form of anti-wear agents such as zinc dialkyl dithiophosphate (ZDDP) and anti-friction agents such as molybdenum-dithiocarbamate (Mo-DTC) or organomolybdenums (MOLY) are used [59, 61]. Those additives are also generally used for hydraulic oils. The nano-sized particles are also used when friction and wear need to be reduced. The low concentration of colloiddally stable nanoparticles (app.1 wt %) is sufficient to improve tribological properties (reducing wear and friction). If the concentration of nanoparticles exceeds a limit, the effect is insignificant. However, the exact composition of commercially available MR fluids is the know-how of the manufacturers. Hu et al. [60] experimentally determined that in the presence of a magnetic field, the friction coefficient is four times higher than without a magnetic field, see Figure 5 left. Similar results were published by Zhang et al. [62]. However, the increase in friction coefficient was not so significant because of the low level of magnetic field (app. 10 times lower than Hu et al. [60]).

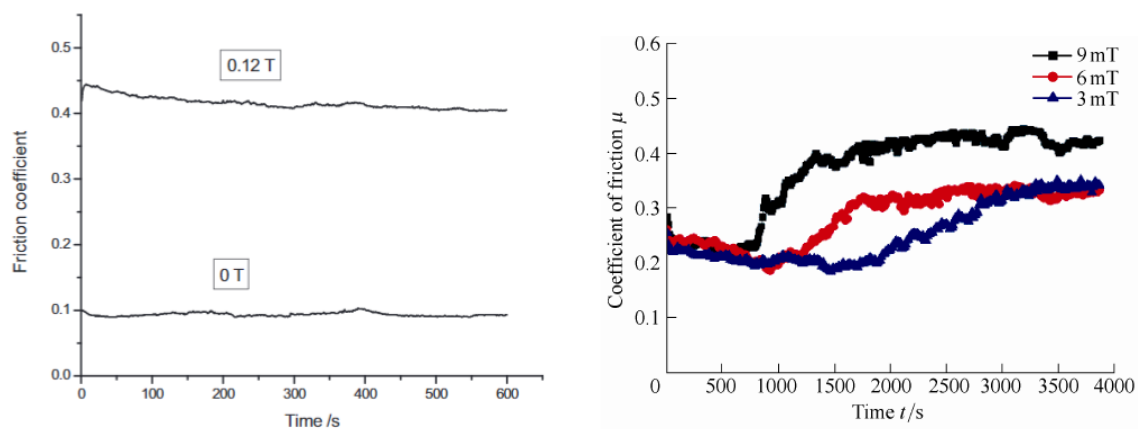


Figure 5 Effect of magnetic field on friction coefficient Hu et al. experiments (left) [60], Zhang experiments(right) [62]

Particles higher than 100 μm usually increase friction and accelerate wear. Gahr et al. [57] describe the effect of particle diameter on wear rate. The wear rate is linearly dependent on particle size. The higher the particle size is, the higher the wear rate is. It is necessary to note that this research was not performed with CI particles. Wang et al. [58] tested the effect of particle size on frictional coefficient and wear on o-ring flooded MR fluid. The higher the particle size is, the higher the frictional coefficient and wear are, see Figure 6. The friction coefficient slightly increases with increased particle concentration at low particle concentration (roughly 20 g/L)[63]. Walker et al. [64] studied the effect of particle shape of white iron slurry on wear. The wear rate decrease exponentially with increasing circularity factor CF (perfect circle CF = 1). However, these experiments were performed on high-size particles (roughly 300 μm) made of a different material than CI. Several authors measured the friction coefficient for commercially available MR fluids and also for homemade MR fluids. Wong et al. [63] measured COF using configuration block-on-ring, where the block is in contact with the cylindrical ring surface. The contact was lubricated by Lord MRF-132DG. The measured COF was in the range of 0.085 to 0.096. Shahrivar et al. [65] compared the friction coefficient of MR fluid and FF fluid as a function of sliding speed. Zhang et al. [66] measured COF for different particle volume content in commercial MR fluid from Lord Corp. The COF was almost identical (ca 0.35) for 22, 32, and 40 vol.% of CI particles. Jolly et al. [67] measured the coefficients of friction for MR fluid lubricated iron-on-iron and nylon-on-iron conformal interfaces. The COF was almost identical for both contact pairs. Jolly et al. [67] compared the four types of MR fluid from Lord corporation with dry friction (0.18), and the measured COF was in the range of 0.04 to 0.07 for all samples.

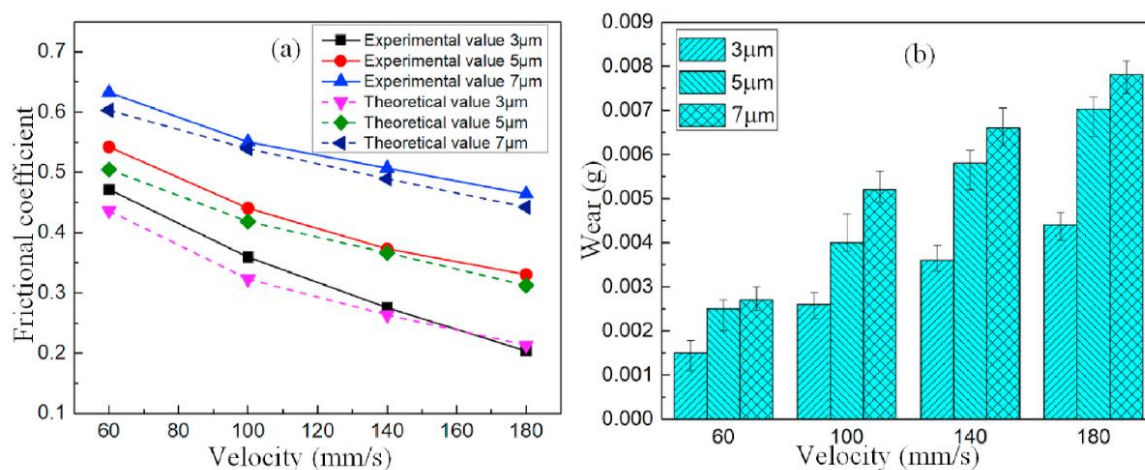


Figure 6 The effect of particle size on friction coefficient and wear for O-ring seal flooded in MR fluid [58]

2.3 Transient response of magnetorheological fluid

The MR fluid exhibits a time delay between the course of the magnetic field and dissipation energy (shear stress, force, torque, etc.). This time delay is associated with several factors such as particle microstructure development, deformation of particle chains (clusters) or hydrodynamic phenomena during the flow, which are differently important depending on loading mode and shear rates. The simplest dynamic system, which can serve as an approximation of the dynamic behaviour of MR fluid, is a first-order system. The response of such a system to a step control signal (magnetic field) is shown in Figure 7. The response is expressed by the time constant τ_{63} (primary response time), which determines the time when 63.2 % of the maximal controlled value is achieved. Despite this, several papers also use the response time (rise time) τ_{90} as the time when 90 % of the maximal controlled value is achieved [68–70]. The criterion of 90 % is frequently used for the description of the dynamic behaviour in industrial applications.

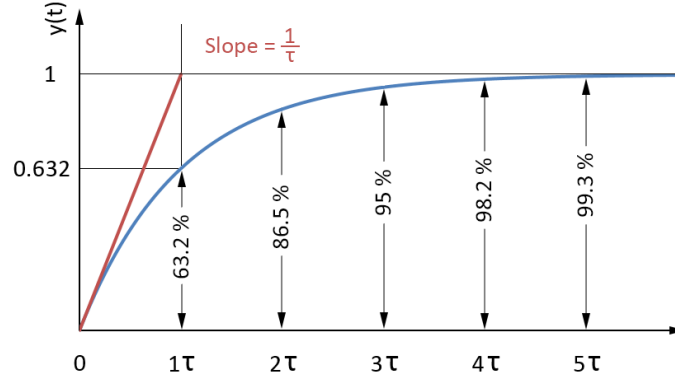


Figure 7 First-order system

The information for evaluation of the response time of MR fluid is always connected with the monitored phenomenon (physics) or the method of its measurement. It can be monitored shear stress [71], pressure drop [72], or magnetic permeability [73] of MR fluid. The MR fluid response time is composed of other partial time responses, which are differently important depending on the operating conditions and the method of MR fluid loading. The response time of MR fluid can be divided into (i) particle structure development response time, (ii) rheological response time, and (iii) hydrodynamic response time. It is necessary to note that this division is not stable and was introduced by the author of the thesis.

2.3.1 Particle structure development response time

This response time is related to the *chaining of particles* (particle microstructure development) in the direction of the magnetic field *without flow conditions* of MR fluid. Jolly et al. [73] proposed a method by which particle chaining time can be deduced from the transient change in the relative magnetic permeability of the MR fluid. Two-time responses were observed. The first attributes the connection with the transfer of particles into diverse chains (pair formation). The second (an order of magnitude slower) connection with the migration of these initial chains into longer and stronger structures. The response time was between 5 and 10 ms. The response time increases with increasing carrier fluid viscosity and decreases with increasing magnetic flux density [73]. A similar measurement method was also published by Horváth et al. [74].

2.3.2 Rheological response time

The rheological response time is connected with the *development of shear stresses* in MR fluid *during deformation/ flow* (shear rate) on step change of magnetic field. This response time also includes the response time of particle structure development (previous section). The mechanism in shear mode is relatively simple. The deformation of the particle chains (clusters) creates an increase in shear stress τ due to restoring force. The rheological response time is the time needed to increase 63.2 % or 90 % [70] of the final value of MR fluid shear stress. Sherman [70] noted that the MR fluids have no response time but instead a response shear γ_r . Therefore, this behaviour is connected with the pre-yield regime of MR fluid. The rheological response time τ_r can be determined by the equation:

$$\tau_r = \frac{\gamma_r}{\dot{\gamma}} \quad (5)$$

where γ_r is shear response and $\dot{\gamma}$ is shear strain rate. The information or papers in this research field is rare. Sherman et al. [70] created a chain model of MR fluid. This model is based on one million particles. One result of this paper is shear stress time history on step change of magnetic field, see Figure 8 left. The rheological response time $\tau_{r,90}$ was determined as roughly 0.4 ms. The MR fluid has a volume particle fraction of 25 % and was under the shear rate of 500 s^{-1} . Koyanagi et al. [75] developed a method for

the measurement response time of electrorheological (ER) fluid. ER fluids exhibit similar rheological behaviour as MR fluids. This team [75] experimentally determined the response time as 0.95 ms. Laun and Gabriel [71] determined the response time of MR fluid of 2.8 ms at a shear rate of 100 s^{-1} and magnetic flux density of 2.08 T. Sherman [70] also evaluated from the chain model results that the shear response of MR fluid is dependent on Mason number and also particle concentration. In the current state of the art can be found more papers dealing with the response time of MR fluid [76, 77]. In these cases, the authors measured the time constant of measuring devices instead of the time constant of MR fluid. A similar statement was made by Sherman [70].

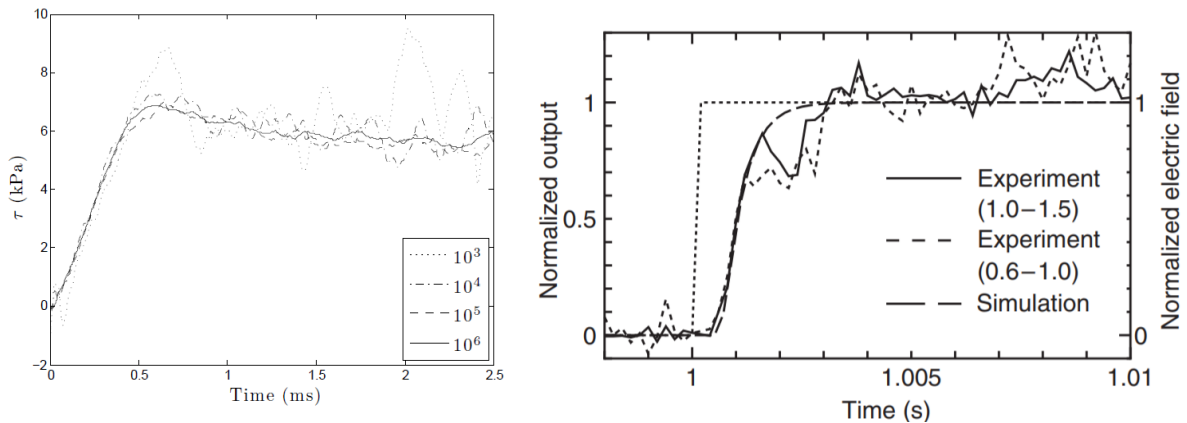


Figure 8 The time dependency of shear stress on step change of control signal from Sherman model (left) [70] and Koyanagi experiments (right) [75]

2.3.3 Hydrodynamic response time

The research studies of Sherman [70] or Goldasz et al. [6] show that pressure drop across the flow channel created by MR fluid yield stress decreases with the increasing gap velocity. This statement is based on CFD (computational fluid dynamics) simulations. This phenomenon is related to transient rheology connected with the *development of velocity profile in the gap* and is often referred to as the hydrodynamic fluid response time, see Figure 9. This response time is connected with high shear rates and valve mode. Goncalves [72] experimentally determined that the hydrodynamic response time (63.2 %) is 0.73 ms for magnetic field 100 kA/m and 0.53 ms for magnetic field 200 kA/m. The MRF-132LD was used in this study. Gavin et al. [78], in the study on ER dampers, modelled the transition from a fully developed Bingham profile to a Newtonian flow.

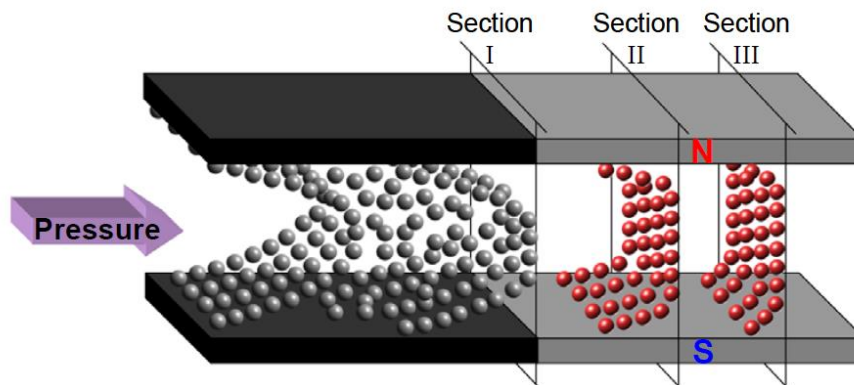


Figure 9 Velocity profile development of MR fluid under magnetic field [72]

The yield stress of ER fluid was assumed to drop to zero quicker than the dissipation energy due to the development of the velocity profile. The characteristic time scale is connected with an MR fluid density, the geometry of the gap, and the fluid's viscosity.

2.4 Knowledge gaps

In the current state of the art in the field of (i) tribological properties and (ii) transient response of MR fluid can be found several knowledge gaps.

(i) Transient response: hydrodynamic response time

Studies on the transient behaviour of MR fluid at shear rates encountered in MR dampers are relatively rare, especially with experimental data. The Goncalves [72] stated that the hydrodynamic response time decreases as the magnetic field increases. However, the trends are unknown. *The temperature effect (viscosity) on this behaviour was not studied.* Therefore, our study [79] deals with this knowledge gap.

(ii) Transient response: rheological response time

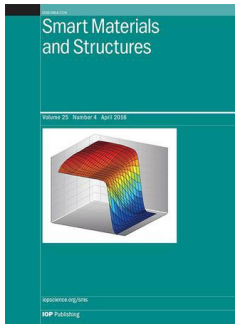
In general, the information about the transient response of MR fluid is limited. This issue is becoming more critical due to the development of MR devices with excellent transient behaviour, where the limiting part is the MR fluid itself. The rheological response time of MR or ER fluid was experimentally determined in two studies [75], [71]. Both studies presented response times for one experimental condition and one selected MR fluid. *The effect of shear rate or MR fluid composition on rheological response time is unknown.* Therefore, our study [80] deals with this knowledge gap.

(iii) Tribological properties

Many papers deal with the measurement of the friction coefficient of MR fluids [58, 61, 62]. However, most of these studies were limited to a narrow range of loads or speeds (low range of Hersey numbers). Only Shahrivar et al. [65] measured friction coefficient in the higher range of sliding speeds. Therefore, *the information on the course of the friction coefficient in a wide range of Hersey numbers (Stribeck curve) is limited.* The effect of particle concentration on each lubrication regime is also limited. Therefore, our study [81] deals with this knowledge gap.

2.5 Author's contribution to the field

Based on the above references, the information about the tribological properties and transient behaviour of MR fluid is still limited. Therefore, the author of the thesis published three papers focused on those research fields. The *first study (i)* deals with determining the hydrodynamic response time of MR fluid. The new experimental approach and unique rheometer design were published. The effect of the magnetic field, viscosity (temperature), and gap size were determined. The *second study (ii)* contains the measurement of transient response (rheological response time) of MR fluid on the rapid change of magnetic field in shear mode. The effect of carrier fluid viscosity, fluid magnetization, or the shear rate was determined and discussed. The *third study (iii)* deals with measuring friction coefficient in the high range of Hersey number. The effects of particle concentration and temperature were presented. All the papers were published in peer-reviewed WOS journals with IF. The list of the included papers is as follows:



[79] KUBÍK, M., K ŠEBESTA, Z STRECKER, F JENIŠ, J GOLDASZ and I MAZŮREK. Hydrodynamic response time of magnetorheological fluid in valve mode: model and experimental verification. *Smart Materials and Structures*. **2021**, 30(12)

Author's contribution (BUT) = 60 %
 Journal impact factor (IF₂₀₂₀) = 3.585
 JIF Quartile = Q1
 Citations (WOS) = 1 (excl. self-citations)



[80] KUBÍK, M., J VÁLEK, J ŽÁČEK, F JENIŠ, D BORIN, Z STRECKER, I MAZŮREK. Transient Response of Magnetorheological Fluid on Rapid Change of Magnetic Field in Shear Mode. *Scientific reports*, **2022**, accepted

Author's contribution (BUT) = 70 %
 Journal impact factor (IF₂₀₂₀) = 4.38
 JIF Quartile = Q1
 Citations (WOS) = 0



[81] ROUPEC, J, F JENIŠ, Z STRECKER, M KUBÍK and O MACHÁČEK. Stribeck Curve of Magnetorheological Fluid within Pin-on-Disc Configuration: An Experimental Investigation. *Materials*. **2020**, 13(20)
 (Author thesis: corresponding author)

Author's contribution = 20 %
 Journal impact factor (IF₂₀₂₀) = 3.623
 JIF Quartile = Q2
 Citations (WOS) = 3 (excl. self-citations)

2.5.1 Hydrodynamic response time of magnetorheological fluid in valve mode: model and experimental verification [79]

The first paper demonstrates the author's contribution to the field of the transient response of magnetorheological fluid. The main aim of this paper was to determine the hydrodynamic response time of MR fluid operating in valve mode and the result compared with analytical formula and CFD simulations. The new and unique slit-flow rheometer design and method evaluation of MR fluid response time (time constant) was published, see Figure 10. This method is based on how much time the ferromagnetic particles of MR fluid spend in the presence of the magnetic field. The magnetic model and CFD model were also described in this paper.

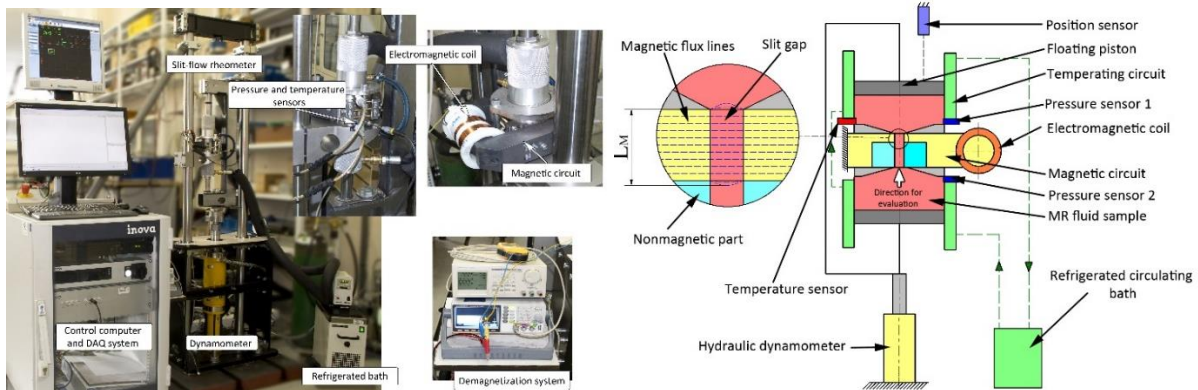


Figure 10 Layouts of the test rig [79]

The experimentally determined hydrodynamic response time τ_{90} of MR fluid varies from 0.4 ms to 1 ms for the selected gap size ($g = 0.65$ mm) and the selected ranges of magnetic field ($H = 11.2$ kA/m to 55 kA/m). The higher the magnetic field, the lower the hydrodynamic response time is. This dependence is nonlinear; see Figure 11 left. The analytical model shows the same trends as the CFD model and the experiment. The effect of temperature (MR fluid viscosity) and gap size was also presented. The hydrodynamic response time τ_{90} of MR fluid increases as the MR fluid temperatures increase (decrease viscosity). As the gap size increases, the hydrodynamic response time τ_{90} of MR fluid also increases significantly. The new analytical model was proposed according to experimental data and CFD simulation, see Figure 11, right.

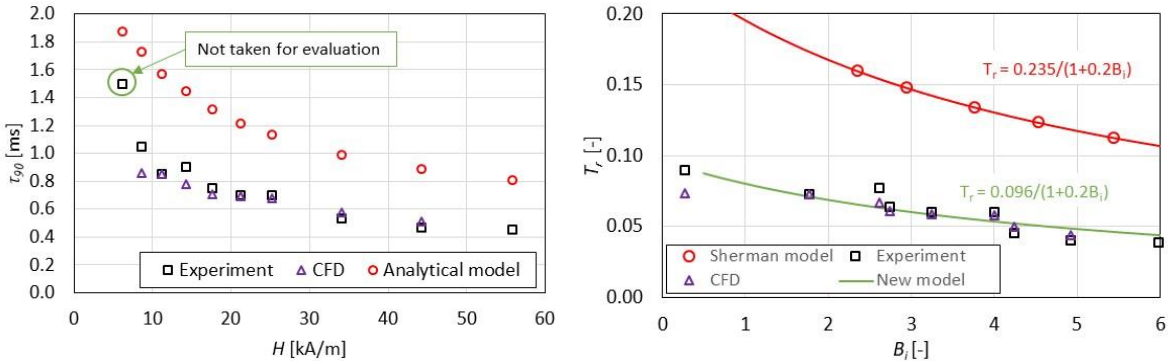


Figure 11 The results of the experiments [79]

2.5.2 Transient Response of Magnetorheological Fluid on Rapid Change of Magnetic Field in Shear Mode [80]

The second paper deals with the rheological response time of magnetorheological fluid in shear mode on the rapid change of magnetic field. The rheological response time is connected with the structuring particle's time and the development of shear stress in MR fluid during the deformation. The main aim of this paper was to experimentally determine the rheological response time of MR fluid and determine the effect of shear rate, magnetic field level, and carrier fluid viscosity. The unique design of the rheometer, which allows rapid change of magnetic field, was presented, see Figure 12. The new approach for evaluating MR fluid rheological response time was also presented.

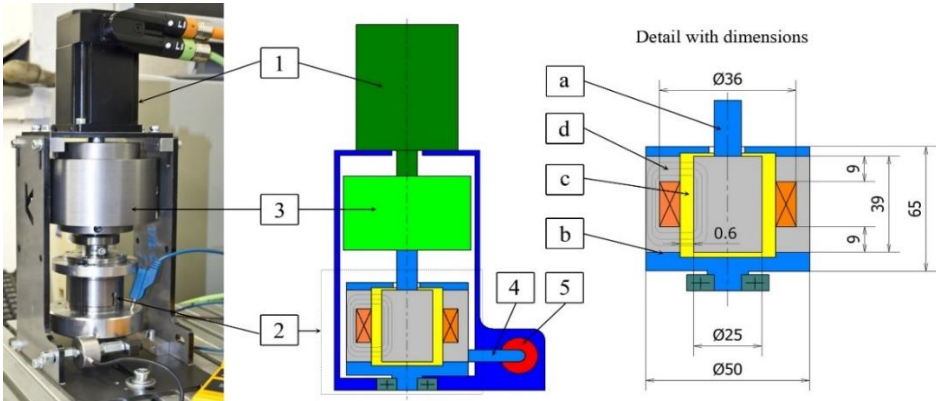


Figure 12 Experimental test rig [80]

The experimentally determined response time (90 %) of the magnetic field was 0.335 ms. The rheological response time of MRF 132-DG and MRC-C1L was in the range of 0.8 to 1.4 ms depending on the shear rate. The rheological response time of MR fluid MRHCCS4-A and MRHCCS4-B ranges from 5.5 ms to 1.9 ms for shear rate $\dot{\gamma}$ from 11 s^{-1} to 218 s^{-1} . The value of the shear rate significantly

influences the rheological response time at low shear rates. The higher the shear rate, the shorter the response time. The fluid magnetization M also significantly affected the rheological response time. The higher the magnetization M of the MR fluid, the lower the rheological response time. The MR fluid with a higher carrier fluid viscosity η shows a significantly higher response time. However, all measured data was generalized by Non-dimensional response time T^* and Mason number M_n . The one master curve was determined from measured data, see Figure 13. This is an important conclusion because the master curve allows the determination of rheological time response for a given MR fluid and given load (shear rates).

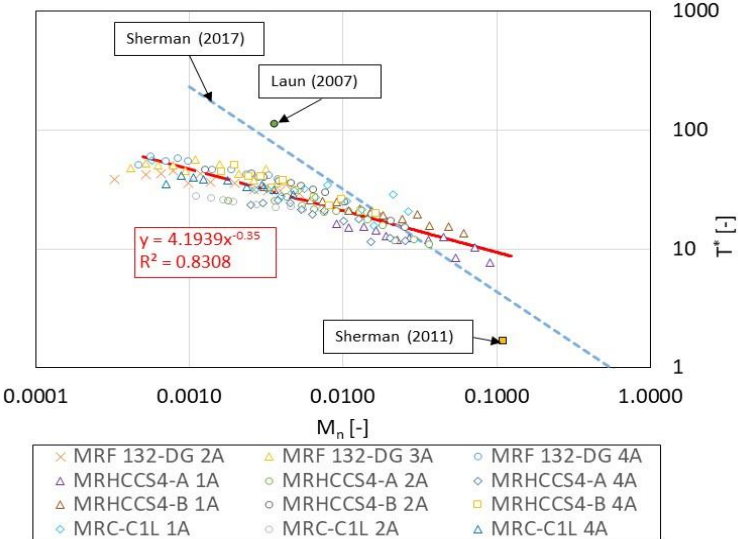


Figure 13 Generalization of measured data [80]

2.5.3 Stribeck Curve of Magnetorheological Fluid within Pin-on-Disc Configuration: An Experimental Investigation [81]

The last paper demonstrates the author’s contribution to the field of tribology of MR fluid. The main aim of the paper was to determine the COF of MR fluids in a large range of Hersey numbers. The effect of particle concentration and temperature was presented. In this study, a rotating friction tester was used to carry out all experiments. Tests were performed on the tribometer Bruker ZP-UMT TriboLab with a pin-on-disc configuration. Commercial MR fluids supplied by the LORD company (MRF-122EG, MRF-132DG, and MRF-140CG) were chosen as the MR fluid samples. These samples have different particle concentrations. The measurement was carried out for temperatures of 40 °C and 80 °C using a temperature chamber by Bruker. The COF of MR fluid was also compared with the COF of carrier fluid (PAO).

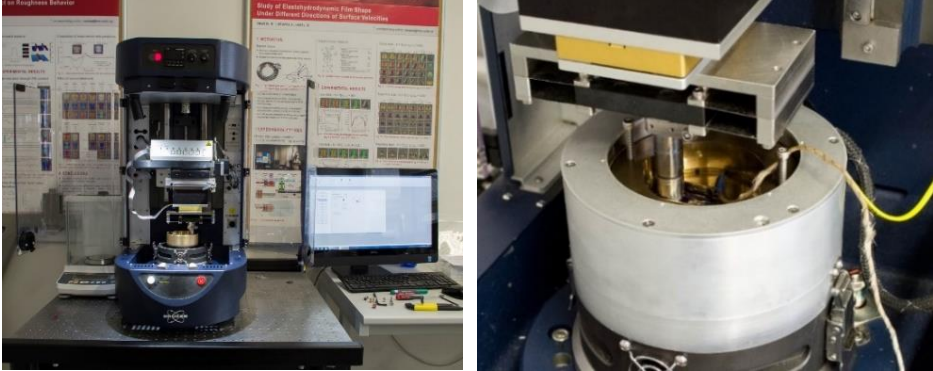


Figure 14 Layouts of the test rig [81]

It can be seen that the boundary, mixed, elastohydrodynamic (EHD), and hydrodynamic regimes of lubrication were measured. However, the EHD regime (the area with the lowest COF) at MR fluid came on at significantly higher COF than PAO. It was surprising that the COF in the boundary lubrication regime is almost identical for all MR fluids, despite the presence of iron particles in MR fluid. No significant temperature effect on COF was observed for MR fluid samples.

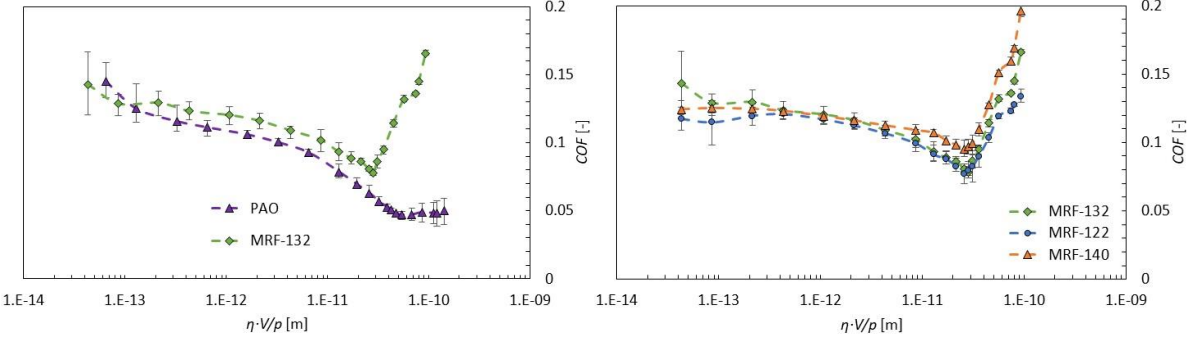


Figure 15 The results of the experiments [81]

Hydrodynamic response time of magnetorheological fluid in valve mode: model and experimental verification

M Kubík^{1,*} , K Šebesta¹, Z Strecker¹ , F Jeniš¹ , J Goldasz^{2,3} and I Mazurek¹

¹ Institute of Machine and Industrial Design, Faculty of Mechanical Engineering, Brno University of Technology, Brno, Czech Republic

² Faculty of Electrical and Computer Engineering, Cracow University of Technology, Kraków, Poland

³ Technical Center Kraków, BWI Group, Kraków, Poland

E-mail: michal.kubik@vutbr.cz

Received 10 September 2021, revised 18 October 2021

Accepted for publication 28 October 2021

Published 11 November 2021



CrossMark

Abstract

The transient behaviour of magnetorheological (MR) actuators affects their performance in progressive semiactive control suspension systems. The two sources of the time delay between the control signal and damping force are (a) dynamics of MR damper hardware and (b) the MR fluid dynamics. The significant part of the MR fluid response time is the so-called hydrodynamic response time which is connected with the transient flow. Due to the above, the main aim of this paper is to experimentally determine the hydrodynamic response time of MR fluid and present systematic means for characterizing it via computational fluid dynamics (CFD) or analytical tools. The unique measurement method using an in-house patented slit flow rheometer is presented. The essence of the method relies on determining the pressure drop variation with the time spent by the fluid in the MR gap. The experimentally determined hydrodynamic response time of MR fluid ranges from 0.4 to 1 ms for a selected gap size and a range of magnetic field stimuli. The results show that the higher the magnetic field, the lower the hydrodynamic response time is. Both CFD and analytical models exhibit similar trends as the experimental data. Moreover, the impact of temperature and gap size was determined. Here, the higher the gap size and temperature of MR fluid, the longer the response time is.

Keywords: transient rheology, unsteady flow, hydrodynamic response time, response time, MR fluid, MR damper, magnetorheological fluid

(Some figures may appear in colour only in the online journal)

1. Introduction

Magnetorheological (MR) fluid is a smart material that exhibits a reversible and fast transition from a liquid state to a pseudo-solid (an increase of yield stress) under the application of an external magnetic field. This phenomenon is called an MR effect. By principle, MR fluid is a two-phase fluid consisting of micron-sized highly magnetizable particles in a

non-magnetizable carrier fluid. When the MR fluid is energized by the magnetic field, the ferromagnetic particles are magnetized and form chain-like structures in the direction of the magnetic field. The fluid then exhibits a significant increase of the yield stress. The ferromagnetic particle size [1], its distribution [2], concentration, material, and the level of the magnetic field have a dominant effect on the value of MR fluid's yield stress. The carrier fluid is usually silicon oil, mineral oil, or synthetic oil [3]. Furthermore, additives are added to improve sedimentation stability [4–6], rheological or tribological [7] properties of MR fluid. These properties allow the use

* Author to whom any correspondence should be addressed.

of MR fluid in electro-mechanical systems such as dampers [8–11], clutches [12, 13], or seals [14–16]. MR dampers are currently used in the automotive/railway/aviation industries and the like. The transient (dynamic) behavior of the MR damper is a fundamental property affecting the performance of this technology in modern semi-actively controlled suspension systems [17]. The two sources of the time delay between the control signal and damping force are as follows (a) dynamics of MR damper hardware and (b) the MR fluid dynamics.

1.1. Response time of MR damper hardware

The significance of the response time (transient behaviour) of MR damper hardware was listed in several publications and the main sources of the delay were identified as (a) eddy currents in the coil core [18, 19], (b) inductance of the MR damper coil [11], or (c) compressibility of the hydraulic system of the MR damper [20]. When the magnetic field changes rapidly in the magnetic circuit of the damper, eddy currents are generated, which produce a magnetic field in the opposite direction than the induced magnetic field by the magnetizing current. The eddy currents can be reduced by either a selection of material properties (SMC—soft magnetic composite, ferrite, etc) [11] or the so-called shape approach [21]. The shape approach is based on the use of a magnetic circuit with thin sheets or with suitably located grooves. This approach is currently under development. The slow increase and decrease of electric current relative to the control voltage signal due to the inductance of the coil can be solved by the current controller with the over-voltage method [21]. The compressibility of the MR fluid also affects the transient behaviour of the MR damper especially at low piston velocities [20]. The subject of MR damper hardware dynamics has been relatively intensively described. The recently developed MR dampers achieve the response time of 1.2 ms which is probably within the time scale of the MR fluid response time itself.

1.2. Response time of MR fluid itself

Studies on the transient/dynamic behavior of MR fluids or ferrofluids are relatively rare. The best-known study which highlights the significance of MR fluid response time is the research of Goncalves *et al* [22]. This team published the results of their measurements of MR fluid response time using a slit-flow rheometer in valve mode. The author introduced the concept of fluid dwell time. This is the time that ferromagnetic particles of MR fluid spend in the presence of a magnetic field. The authors observed a decrease in MR fluid yield stress with the decreasing dwell time. By definition, the dwell time of 63.2% of the expected (steady-state) value of yield stress is equal to the response time. The authors assumed that this yield stress degradation is connected with the particle pair-formation time in fluid [22].

Carvalho and Gontijo [23] modeled the physical timescales responsible for ferrofluid dynamics. They identified three main sources: (a) Brownian relaxation time of particles, (b) magnetic timescales associated with the applied magnetic field, and (c) hydrodynamic timescale associated with the flow's

characteristics and geometry of the gap. The hydrodynamic timescale is significantly greater than the Brownian relaxation timescale and also than the magnetic time scale at low Péclet numbers.

Modeling of particle chain formations and their dynamics were dealt with by relatively many authors [24–26] and quite often resulting in spectacular visualizations of particle chaining structures (microstructure development) in time and relating it to flow characteristics of the fluid.

Jolly *et al* [27] developed a new method for indirect measurement of microstructure development in MR fluid. The method relies on measurements of magnetic induction change (change of MR fluid relative permeability) due to microstructure development. The characteristic time for particle structure development is proportional to the carrier fluid viscosity due to particle movement. The lower the viscosity, the lower the characteristic time is. The characteristic time is also dependent on particle concentration and magnetic induction magnitude. It should be noted that the measurement was done at a zero shear rate. A similar method was also published by Horváth *et al* [28].

Gavin *et al* [29] in their study on ER dampers modeled the transition from a fully developed Bingham profile to a Newtonian flow. The yield stress of ER fluid was assumed to drop to zero quicker than the dissipation energy due to the development of the velocity profile. The characteristic time scale is connected with a MR fluid density, the geometry of the gap, and the fluid's viscosity.

The research studies of Sherman [30] or Goldasz *et al* [31] show that pressure drop across the flow channel decreases with the increasing gap velocity. In Goncalves *et al* [22] experiments, this is related to transient rheology connected with the development of velocity profile in the gap. This statement is based on computational fluid dynamics (CFD) simulations. Laun *et al* [32] also stated that Goncalves results are connected with a hydraulic time constant of devices. This phenomenon is often referred to as the hydrodynamic fluid response time.

Sherman [30] published a model for the hydrodynamic response of MR fluids. This model is based on an analytical solution of the start-up flow of Bingham plastic fluid between parallel plates [33]. The author construct fit of data Darpa *et al* [33] in term of dimensionless response time T_r and Bingham number B_i as follows [30]:

$$T_r = \frac{0.235}{1 + 0.2B_i}.$$

The Bingham number B_i is defined as ration of yield stress forces to viscous stress forces as follows [34]:

$$B_i = \frac{\tau_y}{\eta\dot{\gamma}}$$

where τ_y is MR fluid yield stress, η is off-state viscosity, $\dot{\gamma}$ is characteristics shear rate of system. For a Newtonian fluid, the dimensionless response time can be calculated as follows [30]:

$$T_r = \frac{t_r\eta}{\rho h^2}$$

where t_r is response time, ρ is the density of the fluid, h is gap size. It is important to note that t_r is the time needed for the fluid to reach 90% of the final steady-state velocity. This formula applies to pressure-driven channel flows.

1.3. Problem formulation

Studies on the transient behaviour of MR fluid at shear rates encountered in MR actuators are relatively rare, especially with experimental data. Most authors only modeled this phenomenon [29–31, 33]. Sherman [30] stated that the validation of the models requires high-quality experimental data. The main requirements on the rheometer are temperature control and exclusion of entrance effects. The Goncalves [22] stated that the response time decreases as the magnetic field increases. However, the trends are unknowns. The temperature effect was not studied.

Given the above, the main aim of this paper is to experimentally determine the hydrodynamic response time of MR fluid operating in valve mode (at high shear rates). The developed rheometer respects the requirements above and a unique measurement method is presented. The measured data will be compared against the Sherman model and CFD results to verify the hydrodynamic response time hypothesis in valve mode. The effect of the magnetic field, temperature, and gap size on response time are presented.

2. Materials and methods

2.1. The main idea of the measurement method

This method is based on the measurement of pressure drop across the MR valve caused by an external magnetic field acting on the MR fluid Δp_τ in relation to the dwell time t_{dwell} . In our opinion, this method significantly extends the paper of Goncalves *et al* [22]. The challenge was to separate the effects of viscosity, temperature and entry/exit losses on pressure drop from the measured data.

Therefore, the measurement procedure consists of two parts. The first measurement part was carried out at zero magnetic fields ($H = 0 \text{ kA m}^{-1}$) and Newtonian behavior of the MR fluid is considered in areas I to III, see figure 1. As such, the pressure drop Δp_{off} ($H = 0 \text{ kA m}^{-1}$) across the region I–III can be calculated as follows:

$$p_I - p_{III} = \Delta p_{\text{off}} = \Delta p_\eta + \Delta p_\chi \quad (1)$$

where Δp_η is the viscous pressure drop and Δp_χ is the pressure drop due to entrance and exit losses to the gap. In the second series of the measurements, the test MR valve (gap) was split into two areas: (I–II) non-energized and (II–III) energized, see figure 1. It is assumed that the velocity profile at the interface (II) is fully developed (Newtonian). The second measurement of the pressure loss Δp_{on} is already in the presence of a magnetic field ($H \neq 0 \text{ kA m}^{-1}$) across the length L_M . The pressure drop Δp_{on} is then:

$$p_I - p_{III} = \Delta p_{\text{on}} = \Delta p_\eta + \Delta p_\chi + \Delta p_\tau = \Delta p_{\text{off}} + \Delta p_\tau \quad (2)$$

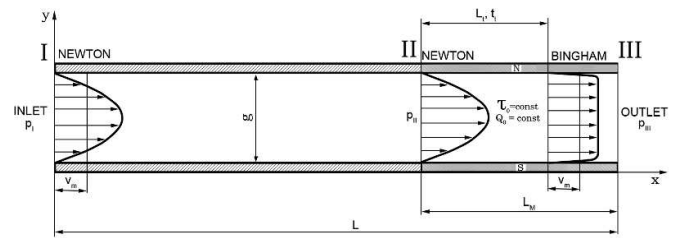


Figure 1. Flow channel.

where Δp_τ is pressure drop due to the yield stress of MR fluid on the length L_M . From the measured pressure drops Δp_{off} and Δp_{on} , the pressure drop due to the MR fluid yield stress Δp_τ is determined as follows:

$$\Delta p_\tau = \Delta p_{\text{on}} - \Delta p_{\text{off}}. \quad (3)$$

However, it is to be expected that the temperature will vary between the consecutive measurement series blocks. Therefore, it was necessary to use an external cooling circuit to stabilize the MR fluid sample temperature. The dwell time t_{dwell} was defined as the time that the MR fluid spends in the presence of the magnetic field. The dwell time t_{dwell} was calculated using the mean flow velocity in the gap v_m and the length L_M as follows:

$$t_{\text{dwell}} = \frac{v_m}{L_M}. \quad (4)$$

It is assumed that the MR fluid needs the time t_t or length L_t to transform the Newtonian velocity profile to a plug velocity profile (Bingham plastic) to exhibit the dissipation energy due to MR fluid yield stress. The time t_t or length L_t is probably the result of MR fluid deceleration/acceleration in the gap. In the case of $L_t \gg L_M$ and given the mean velocity in the gap v_m , the velocity profile is not developed from Newtonian profile to that of Bingham, and dissipation energy due to MR yield stress is not observed $\Delta p_\tau = 0$ although the yield stress is not zero ($H \neq 0 \text{ kA m}^{-1}$). Otherwise ($L_t \ll L_M$) the velocity profile is quickly developed and there is no significant effect of MR fluid deceleration/acceleration.

2.2. Experimental test rig

The functional layout of the apparatus is shown in figure 2. The experimental rig (slit-flow rheometer) is energized by the Inova hydraulic dynamometer AH 40–150 which imposes the motion of the floating piston ($d_p = 32 \text{ mm}$). The motion of the floating piston forces the test MR fluid to flow through the slit gap of the rheometer (MR valve). The slit gap (gap size $g = 0.65 \text{ mm}$, width $w_g = 32 \text{ mm}$ and length $L = 50 \text{ mm}$) is made of two grinded blocks. Each block consists of a component made of non-magnetic stainless steel (light blue) and a component made of pure iron (yellow). Therefore, the magnetic flux can flow just through the yellow part as can be seen in detail in figure 2. The geometry of the inlets to the gap was optimized with CFD simulations to minimize pressure drop at entry/exit Δp_χ (light grey).

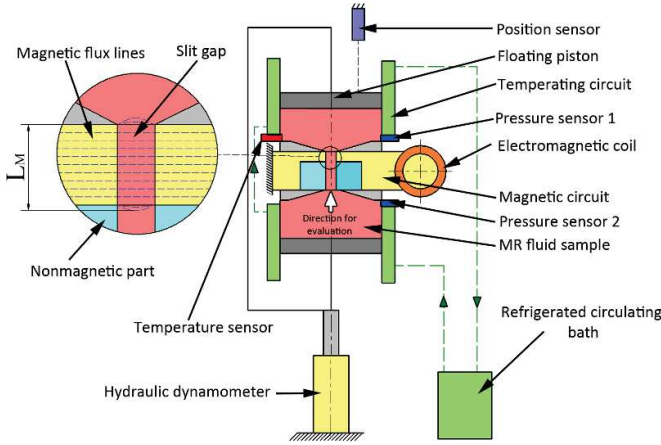


Figure 2. Functional layout of the rheometer.

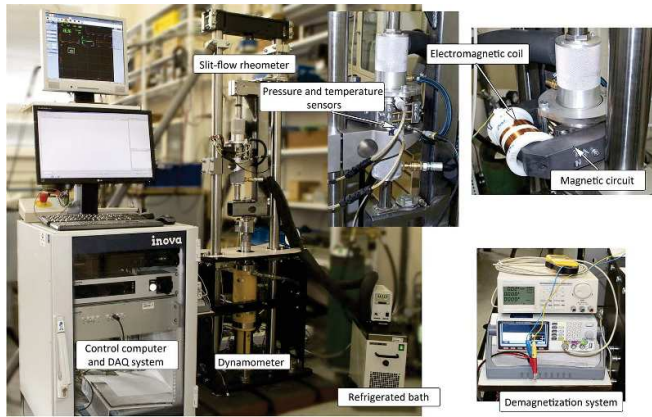


Figure 3. Rheometer configuration.

In order to stabilize the MR fluid sample temperature in the rheometer, a tempering circuit was used as shown in figure 2. This circuit was powered by a refrigerated circulating bath Haake K10 DC50, see figure 3. The demagnetization of the magnetic circuit was by a sinusoidal electric current signal with decreasing amplitude. The pressure drop across the slit gap was monitored with two pressure sensors HBM P8AP. The MR fluid temperature was acquired by a resistance temperature sensor PT100 which was located near the entrance to the slit gap. The motion of the floating piston was measured using the LVDT transducer/position sensor accommodated in a hydraulic dynamometer. These signals were recorded and conditioned at the sampling frequency of 2 kHz using the analyzer Dewe-800.

2.3. Measurement methodology and evaluation

The measurement procedure was as follows: (a) eight sinusoidal cycles at the given frequency f ; (b) pause to switch power supply current on and temperature stabilization; (c) eight sinusoidal cycles at the frequency f and electric current I ; (d) demagnetization of the magnetic circuit. Measurements were performed for various frequencies at the stroke amplitude

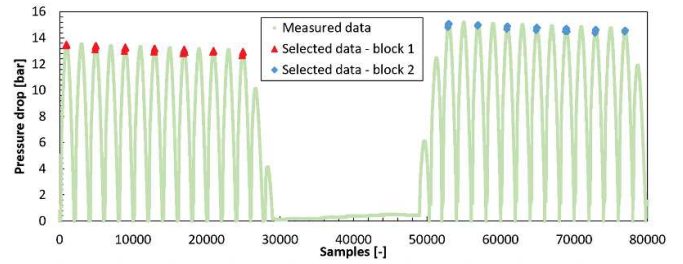


Figure 4. Pressure drop evaluation procedure example: 0.4 A, 0.5 Hz.

of 48 mm. The piston velocity v_p was determined by derivating the piston position. In order to estimate the pressure drop, the data points were selected which fell within the 2 mm margin from the midstroke position and at min. 99% of the maximum piston velocity. Furthermore, only one direction of flow through the gap was selected for the following evaluation fact that the MR fluid has a fully developed velocity profile on the entrance the field energized region of the flow channel, see figure 2. Exemplary results with the highlighted data points for the evaluation procedure can be seen in figure 4.

Next, in order to determine the yield stress from the measurement is presented equation below:

$$\tau_0 = \frac{\Delta p_\tau g}{2L_M}. \quad (5)$$

The results from the measurement of Δp_τ were normalized $\psi_{\Delta p_\tau}$ and compared using the following equation:

$$\psi_{\Delta p_\tau}(i) = \frac{\Delta p_\tau(i)}{\max[\Delta p_\tau(i)]} \quad (6)$$

where i is the measurement number and $\max(\Delta p_\tau)$ is the maximum value of Δp_τ that corresponds to the steady-state. The normalized data $\psi_{\Delta p_\tau}$ were then least-squares fitted in Matlab using the following function:

$$\psi = \left[1 - c_1 e^{c_2(t_{\text{dwell}} - c_4)} \right] \tanh[c_3(t_{\text{dwell}} - c_4)] \quad (7)$$

where c_1 , c_2 , c_3 , and c_4 are constants that were obtained by the curve fitting. This equation is necessary for precise calculation of the hydrodynamic response time τ_{90} of the MR fluid from measured data.

2.4. Test sample

MR fluid MRF-132DG from Lord Corporation was used for testing. This is hydrocarbon-based MR fluid using for general energy-dissipating applications as dampers or brakes. The volume concentration of ferromagnetic particles in the tested sample was experimentally determined to be 32.6% and the sample density was 3106 kg m^{-3} . These data were determined by volume and weight measurement. The particles are spherical and average size (diameter) is $2.1 \mu\text{m}$. The particle distribution is according Q3 [35]. The particle material is carbonyl iron.

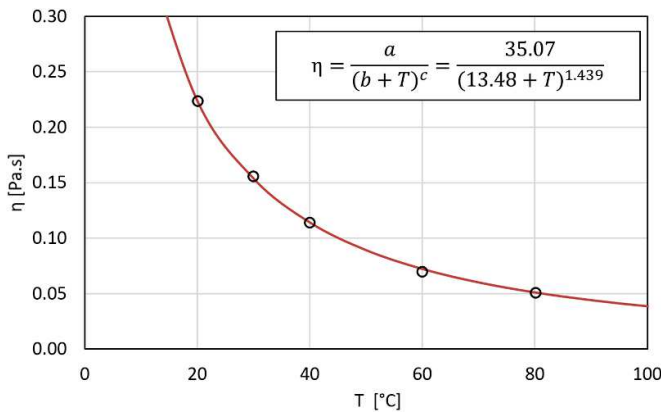


Figure 5. MR fluid sample viscosity data (black circle: measurement; red curve: Slotte model fit).

The viscosity of MR fluid was measured using the rotational rheometer Haake RotoVisco 1, the sensor system ISO 3219 Z20 DIN. The viscosity of MR fluid was measured at the constant shear rate 800 s^{-1} during 30 s at a selected temperature. This data is input to the CFD simulations and next evaluation. The measured data were curve fitted using the Slotte model, see figure 5.

2.5. Magnetic model

The magnetic model was created in Ansys Electronics Desktop 19.2. The geometry of the magnetic circuit was simplified and the symmetry boundary condition was used, see figure 6. The boundary condition Insulating was applied on the electromagnetic coil geometry. The excitation of the coil was by coil terminal. The magnetization curve of the magnetic circuit material (pure iron, trademark name Behanit) was determined using the measurement system Remagraph C-500. The magnetization curve of the MR fluid sample was extracted from the datasheet of the MR fluid supplier. The relative permeability of other materials was considered to be equal to 1. This magnetic model was necessary for the calculation of (a) the length L_M and (b) the magnetic field intensity H in the gap with MR fluid. The length L_M will be determined based on the drop of magnetic flux density to 10% of the maximum value.

2.6. CFD model

Ansys CFX 14.2 was used for transient simulations. The geometry of the flow domain was simplified to the 3D parallel plate configuration, see figure 7. The inlet boundary condition was set at the entrance and the output at the exit assuming the relative pressure of 1 bar. The prescribed velocity at the inlet varied sinusoidally. Moreover, no-slip wall boundary conditions were set in the remaining portions of the model. As the Reynolds number was below 500 at the highest frequency, the laminar flow model could be assumed for the analysis. The residual target was set to 5×10^{-5} . The time step was variable and each calculation was completed within 120 simulation steps.

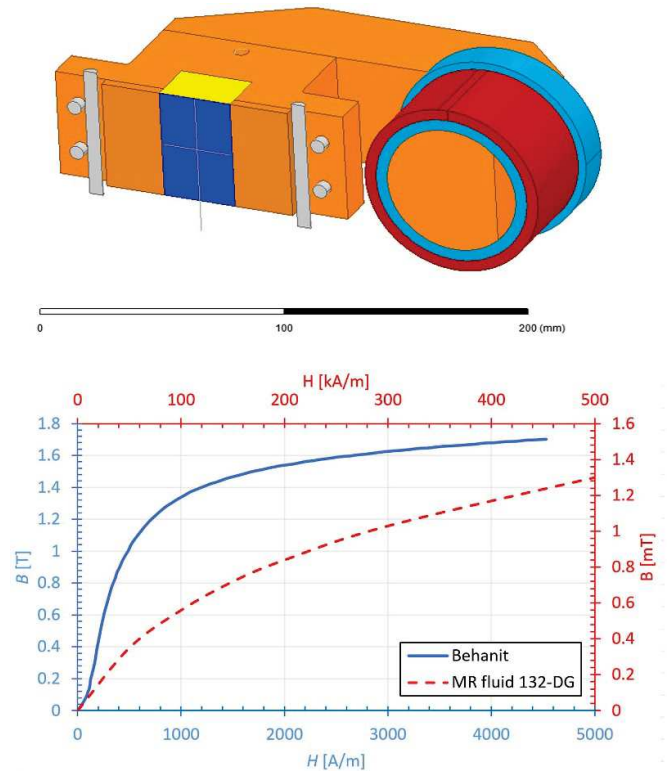


Figure 6. Simplified geometry of the magnetic circuit (orange: Behanit, blue: MR fluid/air, yellow: stainless steel, grey: brass, light blue: polyamide, red: copper)—above; magnetization curves of Behanit and MRF—down.

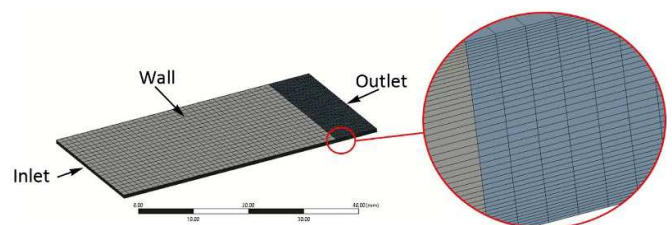


Figure 7. Flow domain and mesh.

The flow domain was divided into two sections corresponding to the illustration in figure 2. In both sections, 50 elements with the bias factor set to 3 were used across the flow gap. The MR fluid is assumed to be continuous fluid and its behavior under the magnetic field is described by the bi-viscous constitutive model, see figure 8. This MR fluid model was applied to the selected flow domain geometry using the CEL function. The bi-viscous model rather than the Bingham model was selected to avoid the singularity present in the latter at zero shear rate.

The limit of shear rate was set $\dot{\gamma}_{lim} = 0.01 \text{ s}^{-1}$. The bi-viscous model was set as follows:

$$\begin{aligned} \eta_{app} &= \frac{\tau_0}{\dot{\gamma}} + \eta_0 \dot{\gamma} > \dot{\gamma}_{lim} \\ \eta_{app} &= \frac{\tau_0}{\dot{\gamma}} \dot{\gamma} \leq \dot{\gamma}_{lim} \end{aligned} \quad (8)$$

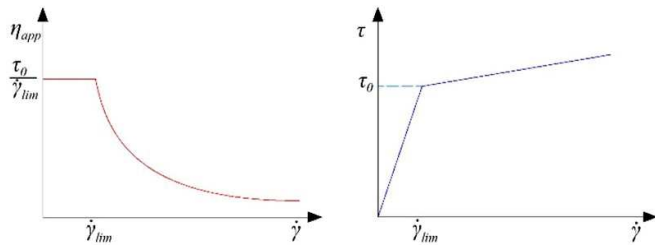


Figure 8. Bi-viscous model of MR fluid flow used in the simulation.

where η_{app} is apparent viscosity of MR fluid, η_0 is viscosity and $\dot{\gamma}$ is shear rate. This is a common approach often used in handling ER/MR fluid flows, e.g. Bullough *et al* [36].

3. Results and discussion

3.1. Calculation of the length L_M

The length of an active zone L_M is an important input for the dwell time calculation. The length L_M was determined from the magnetic model as the distance at which the magnetic flux density drops to 10% of the maximum value in the gap.

The results for the different electric currents are presented in figure 9 above. This data was normalized due to the different maximum values of magnetic flux density, see figure 9 down. The length L_M was determined to be equal to $L_M = 8.8$ mm. The length of the pole piece is 8 mm. The evaluated value is higher due to magnetic leakage. It is necessary to note that given the different magnetic properties of MR fluid (different particle concentration, particle size, etc) the length L_M will vary. The better the relative permeability of MR fluid, the lower the length L_M is. The other result of the magnetic model is the magnetic field intensity H in the MR fluid sample in the middle of pole pieces dependent on the electric current I of the coil, see figure 10. This information is important for generalizing the measured data.

3.2. Measured pressure drop and CFD model verification

Figure 11 shows the pressure drop Δp measurement on- as well off-state conditions, respectively for given electric current (only selected data are presented). The hydrodynamic response time was evaluated from this data. The MR fluid yield stress was evaluated at a low fluid velocity in the gap (4.6 m s^{-1}) to eliminate the transient effect on the data. Based on equation (5), the yield stress τ_0 was determined as a function of the magnetic field intensity H , see figure 12 above.

These data were compared against the MR fluid datasheet. At the higher magnetic field intensities H , the measured yield stress exhibits higher values than those advertised by the manufacturer. The maximum difference was 11% (at the magnetic field intensity of 56 kA m^{-1}) which is acceptable. The yield stress data were input to the CFD simulation. The comparison of pressure drop caused by the MR fluid yield stress Δp_τ from measurement and CFD simulation results can be seen in figure 12 down.

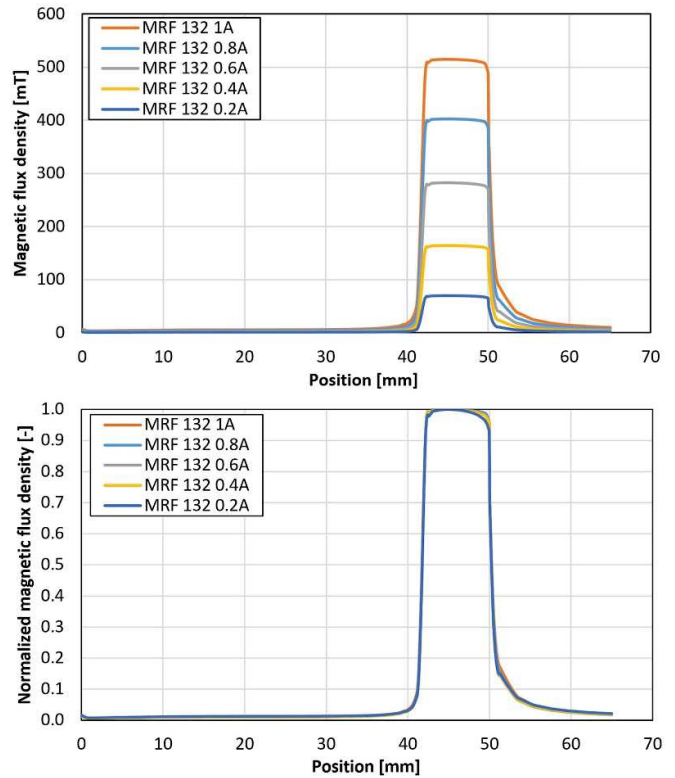


Figure 9. Magnetic flux density over the length of the gap in the direction of flow at various electric currents in the coil—above; normalized results of magnetic flux density—down.

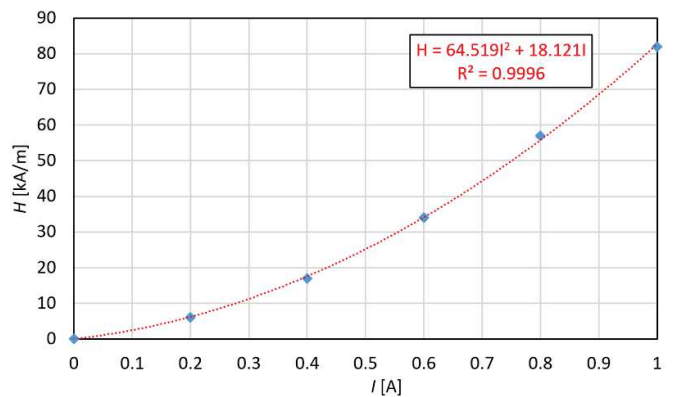


Figure 10. Magnetic field intensity H vs coil current I .

3.3. Dwell time effect on pressure drop

The normalized measured pressure drop data to the MR fluid yield stress $\psi_{\Delta p_\tau}$ (black circle) and CFD simulation (red square) dependency on dwell time t_{dwell} at various magnetic fields H are presented, see figure 13. The experimental data were curve-fitted using equation (5), see equation (7) the blue line in figure 13. The hydrodynamic response time τ_{90} was determined from this equation.

Very good agreement between experimental data and the numerical results was achieved. The most significant difference can be seen just at the low magnetic field intensity H ($I = 0.25 \text{ A}$). Most likely, the discrepancy was due to the

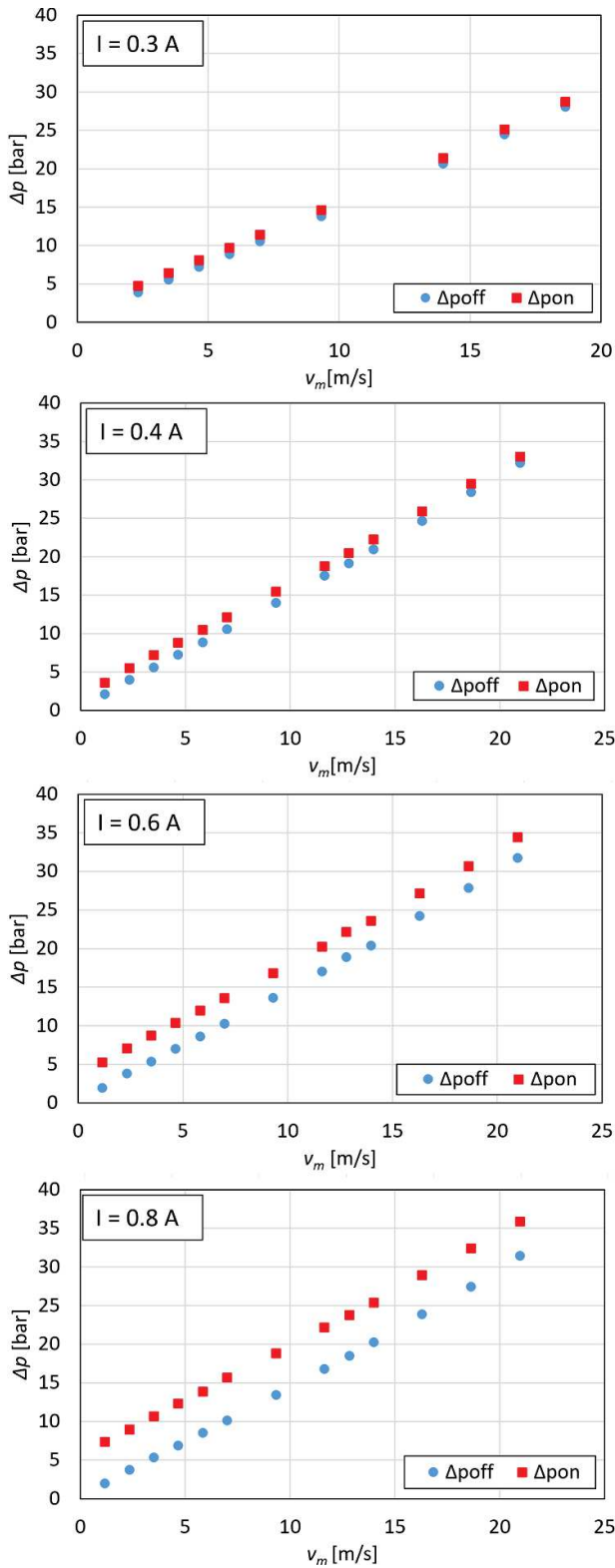


Figure 11. Selected raw experimental data: pressure drop vs velocity.

fluid heating contribution during the experiment. Another possible source of discrepancy is the accuracy of pressure sensors because in this case the pressure drop Δp_τ reached values were on the order of tenths of the bar. This result of the

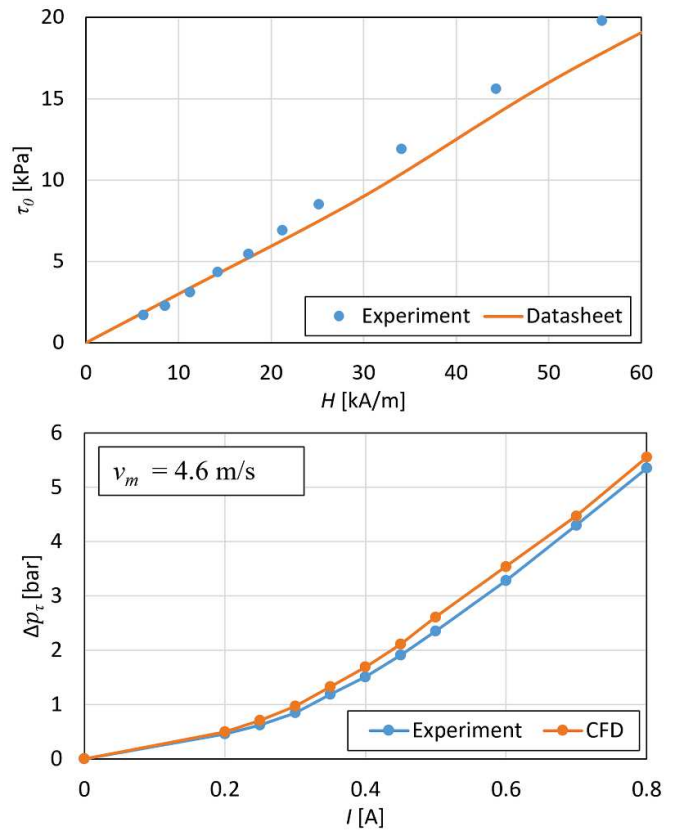


Figure 12. MR fluid yield stress: measurement vs datasheet—above; pressure drop due to the yield stress of MR fluid: measurement vs CFD—down.

hydrodynamic response time for the electric current 0.25 A should be taken carefully. The CFD results are probably more accurate at this electric current. The average temperature during the experiment was in the range from 40.03 °C to 40.15 °C which is acceptable.

3.4. Effect of magnetic field on hydrodynamic response time

The response time was determined as the time at which the pressure drop achieves 90% of the final value. The dependence of the hydrodynamic response time τ_{90} on the magnitude of the magnetic field intensity H in the gap is presented in figure 14. The CFD model shows good agreement with the experimental data at the field intensity H higher than 10 kA m⁻¹. It can be concluded that the higher the magnetic field intensity H , the shorter the response time τ_{90} is. The same trend confirms the Goncalves experiments. The study of Bullough *et al* [36] also shows the same trends. For our configuration ($g = 0.65$ mm, temperature 40 °C and MRF 132-DG) the response time τ_{90} ranges from 0.4 to 1 ms depending on the magnitude of the magnetic field H . Moreover, the experimental data and the CFD results were compared with the Sherman’s analytical model. The comparison was made at the corresponding shear rates and the same yield stresses, viscosity, gap size, and MR fluid density as was in the experiments.

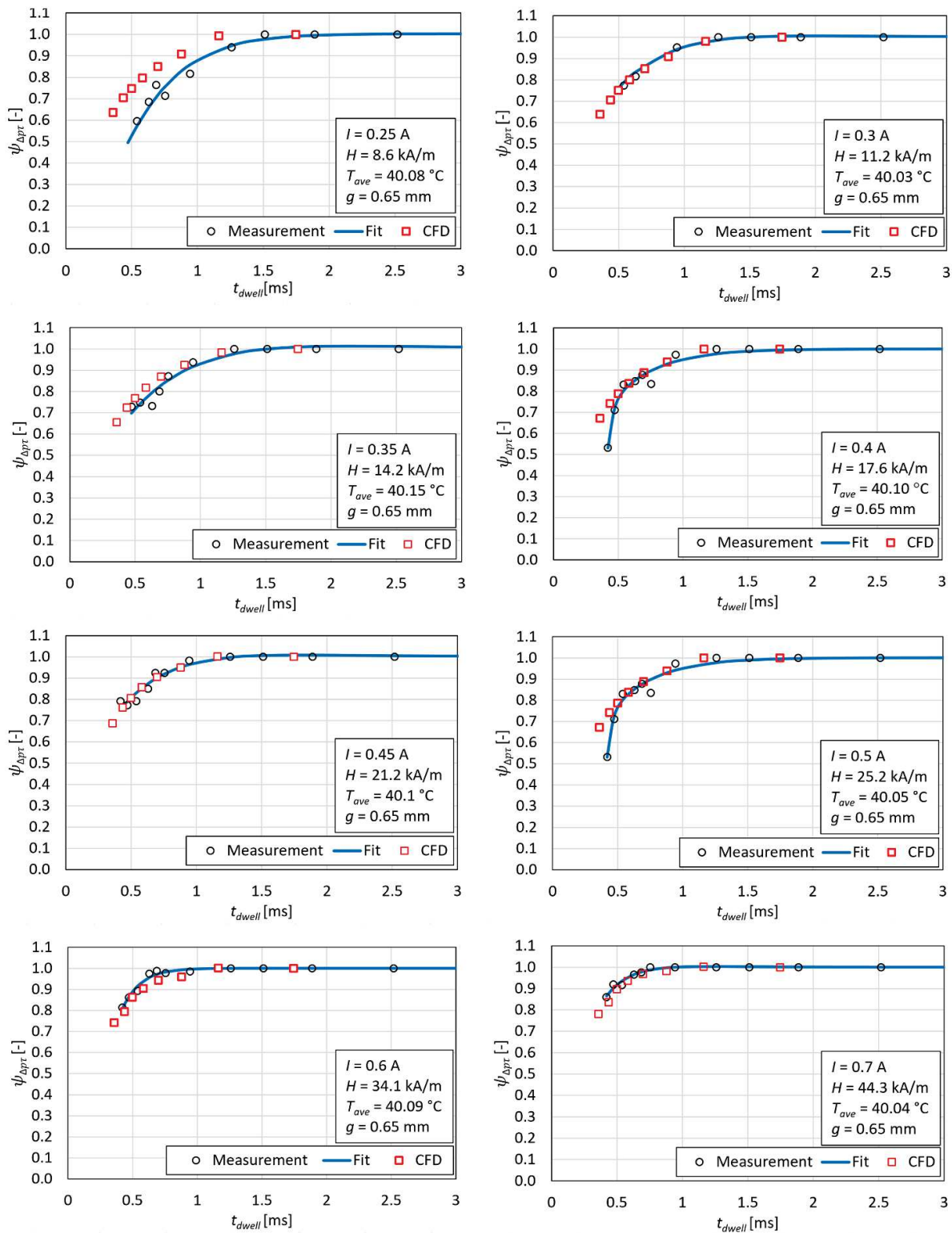


Figure 13. Normalized pressure drop vs dwell time and coil current.

The analytical model shows the same trends as the CFD model and the experiment, see figure 14. However, the absolute value of the response time τ_{90} is higher and varies from 0.8 to 1.6 ms. This difference is understandable because the analytical model was obtained by fitting the Darpa data. Darpa

et al [33] used different excitation inputs. They used a constant pressure gradient and monitored the flow rate.

In our case, we applied a constant flow rate and monitored the pressure gradient. Note that Sherman considered a planar 2D flow model with no contribution of the channel's side-

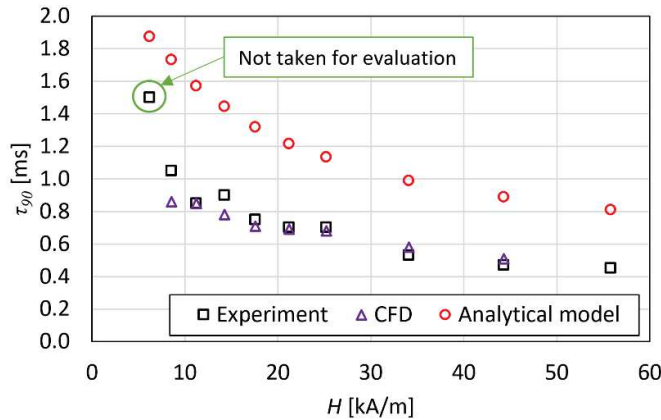


Figure 14. Effect of magnetic field H on hydrodynamic response time τ_{90} for the gap size 0.65 mm and the temperature 40 °C.

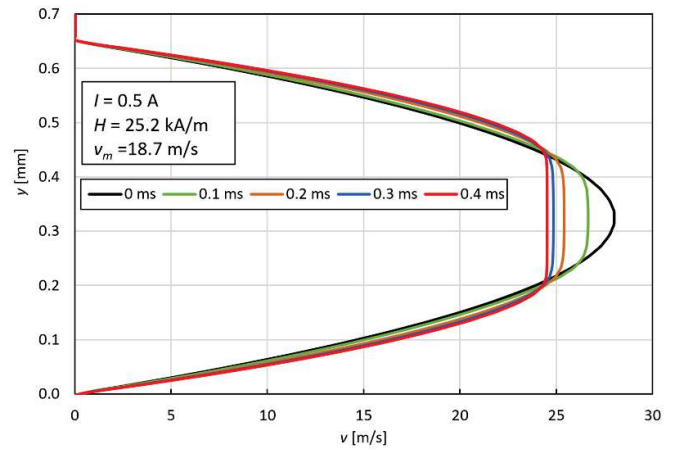


Figure 16. Velocity profile development in time.

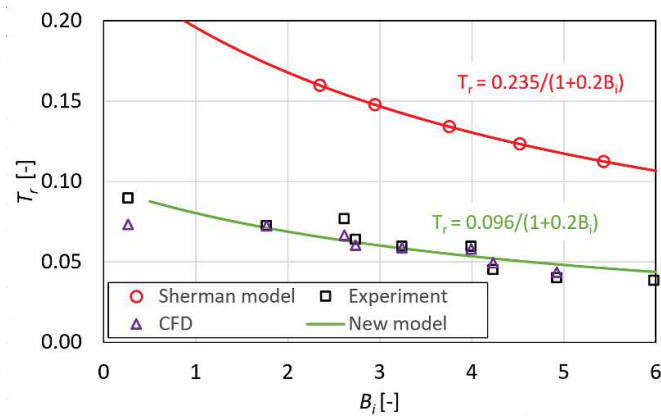


Figure 15. Dimensionless response time vs Bingham number.

walls which is likely to explain the differences. However, the analytical model of Sherman [30] respects the trends and is therefore conservative and easy to use for the design of MR devices. The measured data and results from the CFD simulation were recalculated to the dimensionless response time T_r with respect to the Bingham number B_i , see figure 15. Next, using the CFD simulations and experimental data, a dimensionless response time T_r curve fit was constructed, see figure 15 (green line). However, the validity of this model is only for the tested configuration and the transient flow from a fully developed Newtonian profile to a Bingham type plug flow. Figure 16 shows some insight into the velocity profile development in time for the selected yield stress.

The fully developed velocity profile and plug thickness can be also calculated analytically. In figure 16 case, the analytically determined plug thickness achieved a value of 0.26 mm which corresponds with results from CFD simulation, see figure 16 red.

3.5. Temperature effect on hydrodynamic response time

Three temperatures (40 °C, 50 °C, and 60 °C) and two coil current levels were selected to demonstrate the temperature effect on the hydrodynamic response time τ_{90} , see figure 17.

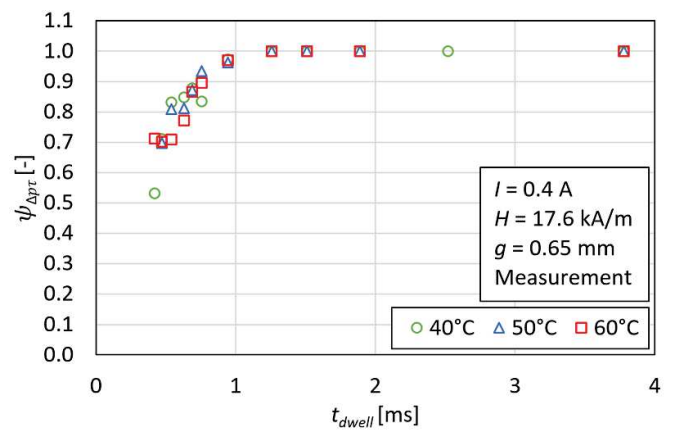
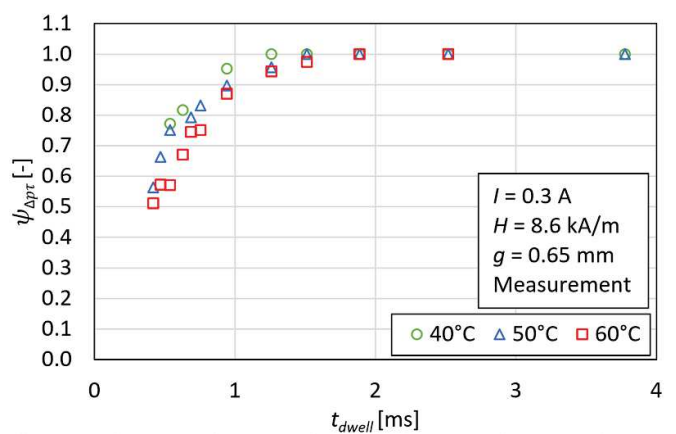


Figure 17. Impact of temperature on the normalized pressure drop (measurement).

The hydrodynamic response time increases as the MR fluid temperature increases as shown in figure 18.

However, the rate of the response time change is also dependent on the level of magnetic field intensity H (yield stress). The higher the yield stress, the lower rise of the hydrodynamic response time τ_{90} is. The data presented in figure 18 were determined by the new model and MRF 132-DG fluid viscosity data. The increase in response time is due to the decreased viscosity of the MR fluid and changes in the Bingham

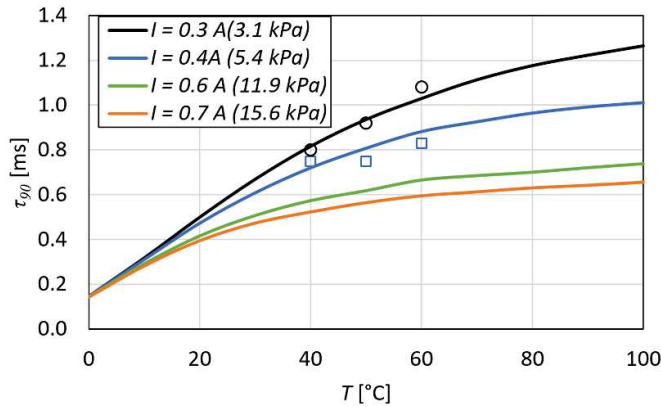


Figure 18. Impact of the temperature and yield stress on hydrodynamic response time.

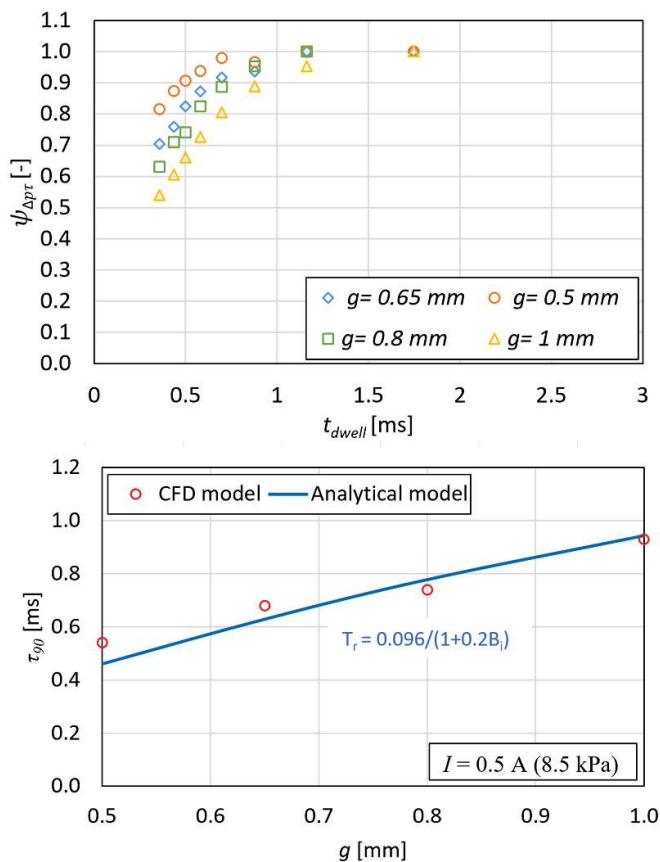


Figure 19. Impact of gap size on the hydrodynamic response time; MRF 132-DG, 40 °C.

number B_i . Bullough *et al* [36] showed that the viscosity of the fluid has a significant effect on the response time and thus the measured data corresponds with their results. Thus, it can be stated that the dependence of the hydrodynamic response time τ_{90} on temperature is strongly nonlinear and as the temperature increases (viscosity decreases) the response time τ_{90} increases significantly.

The low viscosity of MR fluids is advantageous in achieving the dynamic force range of the MR damper. However, as it can be seen from figure 18, it prolongs the hydrodynamic

response time. The design of the MR damper will therefore be a trade-off between the transient behavior and the dynamic force range.

3.6. Effect of gap size

Using the verified CFD model, the effect of gap size on the hydrodynamic response time τ_{90} was tested, see figure 19. As the gap size increases, the hydrodynamic response time also increases significantly. Within the examined gap size range from 0.5 to 1 mm, the effect of gap size on the response time is most linear. Increasing the gap increases the dynamic force range of the MR damper. However, its dynamic behavior deteriorates.

The same trends were described by Gavin *et al* [29] when studying the transition from a fully developed Bingham flow to a Newtonian one. Bullough *et al* [36] claimed that the gap size has a dominant effect on the hydraulic time constant.

3.7. Discussion on the impact of the results on the design of MR actuators

It is apparent that these results have a direct impact on the design of MR actuators, e.g. MR high-speed energy absorbers and MR dampers with fast semiactive control of damping force at high shear rates.

3.7.1. MR high-speed energy absorbers. These actuators suffer from the yield force fall-off in on-state at high piston velocities, which significantly reduces the dynamic force range of the damper at these velocities [12, 37]. This decrease is due to the heating of the fluid and the presented hydrodynamic response time contribution. Based on the presented data, the minimum length L_{\min} of the magnetic pole of the damper to eliminate the effect of transient flow on the pressure drop can be determined. The minimum length L_{\min} of the magnetic pole in the damper can be determined as follows:

$$L_{\min} = v_m \tau_{90}. \quad (9)$$

This problem is likely to be more significant for large dampers (with high damping force) due to the size of the gap.

3.7.2. Fast semi-active MR dampers. It can be expected that if the magnetic field changes rapidly (step change) then the yield stress of MR fluid also changing rapidly at high shear rates [30]. This rapid change of MR fluid yield stress leads to a change in the velocity profile from a Newton profile to the Bingham plug flow followed by dissipation of energy. This probably results in a time delay between the controlled magnetic field (control signal) and the dissipation energy (damping force). In our presented case, we had a different excitation of the fluid. We used a constant MR fluid yield stress and we determined the resulting pressure drop. It is uncertain whether the mechanism will be the same for the force rise to fast applied magnetic field variants. The authors of the paper assume that this model can be used to predict the

behaviour of fast changes of magnetic field (yield stress) with some error. A simple analysis is presented below. The hydrodynamic response time of the fast MR damper can be calculated using the presented method as $\tau_{90} = 0.39$ ms ($v_{\text{gap}} = 6$ m s⁻¹, yield stress of 10 kPa, plastic viscosity 0.11 Pa.s (40 °C), MRF 132, and geometry) [11]. This is within the time scale of the data presented by Strecker *et al* [11], where the damper force response time was measured as 1.3 ms. The force response time of the MR damper is also affected by the hydraulic system compliance and the response time of the electric current (coil inductance) in the coil (0.5 ms). Determining the MR fluid transient behaviour subjected to magnetic field step inputs will be subject to further research.

4. Conclusion

The paper deals with the measurement of the hydrodynamic response time of MR fluid operating in valve mode. The measurement method and the unique design of the slit flow rheometer is presented. The measured data were compared against the CFD results and the analytical model. The effect of a magnetic field, temperature (plastic viscosity), and gap size on the hydrodynamic response time were determined. The key findings of this study can be summarized as follows:

- The experimentally determined hydrodynamic response time τ_{90} of MR fluid varies from 0.4 to 1 ms for the selected gap size ($g = 0.65$ mm) and the selected ranges of magnetic field ($H = 11.2$ – 55 kA m⁻¹). The higher the magnetic field, the lower the hydrodynamic response time is. This dependence is nonlinear, see figure 14.
- The CFD model agrees with the experimental data. The analytical model presented by Sherman *et al* [29] shows the same trends as the CFD model and the experiment, see figure 14. However, the absolute value of the response time τ_{90} is higher. The differences can be explained due to different fluid excitation. However, the analytical model respects the trends and is, therefore, conservative and easy to use for the design of MR actuators.
- The hydrodynamic response time τ_{90} of MR fluid increases as the MR fluid temperatures increases (decrease viscosity). The higher the yield stress of MR fluid, the lower the temperature effect on the hydrodynamic response time τ_{90} is.
- As the gap size increases, the hydrodynamic response time τ_{90} of MR fluid also increases significantly. The gap size has also the dominant effect on the dynamic force range of the damper. The higher the gap size, the higher the dynamic force range is. The design of MR dampers is a trade-off between the dynamic force range and the dynamic behaviour (response time).




Data availability statement

The data that support the findings of this study are available upon reasonable request from the authors.

Acknowledgments

This paper and experiments have been made possible thanks to the Czech Science Foundation (GAČR) within the scope of the Project No. 20-23261Y.

ORCID iDs

M Kubík  <https://orcid.org/0000-0003-0105-2921>
 Z Strecker  <https://orcid.org/0000-0002-1598-487X>
 F Jeniš  <https://orcid.org/0000-0002-1753-1508>

References

- [1] Zhang Q, Liu X, Ren Y, Wang L and Hu Y 2016 Effect of particle size on the wear property of magnetorheological fluid *Adv. Mater. Sci. Eng.* **2016** 1–7
- [2] Chiriac H and Stoian G 2010 Influence of particle size distributions on magnetorheological fluid performances *J. Phys. Conf. Ser.* **200** 072095
- [3] Zhang Y, Jiang J, Ouyang C, Meng Y, Jia W, Ma L and Tian Y 2021 Effect of base oil lubrication properties on magnetorheological fluids *Smart Mater. Struct.* **30** 095011
- [4] Plachy T, Cvek M, Munster L, Hanulíková B, Suly P, Vesel A and Cheng Q 2021 Enhanced magnetorheological effect of suspensions based on carbonyl iron particles coated with poly(amidoamine) dendrons *Rheol. Acta* **60** 263–76
- [5] Cheng H, Wang M, Liu C and Wereley N M 2018 Improving sedimentation stability of magnetorheological fluids using an organic molecular particle coating *Smart Mater. Struct.* **27** 075030
- [6] Roupec J, Michal L, Strecker Z, Kubík M, Macháček O and Choi H J 2021 Influence of clay-based additive on sedimentation stability of magnetorheological fluid *Smart Mater. Struct.* **30** 027001
- [7] Lee C H, Lee D W, Choi J Y, Choi S B, Cho W O and Yun H C 2011 Tribological characteristics modification of magnetorheological fluid *J. Tribol.* **133** 6
- [8] Xi J, Dong X, Li W, Wang T, Song X and Zhang Z 2021 A novel passive adaptive magnetorheological energy absorber *Smart Mater. Struct.* **30** 014001
- [9] Jeniš F, Kubík M, Macháček O, Šebesta K and Strecker Z 2021 Insight into the response time of fail-safe magnetorheological damper *Smart Mater. Struct.* **30** 017004
- [10] Goldasz J 2019 Magnetostatic study of a dual-gap MR valve *Proc. 2019 20th Int. Conf. Res. Educ. Mechatronics, REM 2019* vol **5** pp 1–5
- [11] Strecker Z, Kubík M, Vitek P, Roupec J, Paloušek D and Šreibr V 2019 Structured magnetic circuit for magnetorheological damper made by selective laser melting technology *Smart Mater. Struct.* **28** 055016
- [12] Mao M, Hu W, Choi Y-T, Wereley N M, Browne A L, Ulicny J and Johnson N 2013 Nonlinear modeling of magnetorheological energy absorbers under impact conditions *Smart Mater. Struct.* **22** 115015
- [13] Zhang H, Du H, Sun S, Zhao J, Ning D, Li W and Wang Y 2021 A novel magneto-rheological fluid dual-clutch design for two-speed transmission of electric vehicles *Smart Mater. Struct.* **30** 075035
- [14] Zhou H, Zhao W, Zhang H, Wang Y, Wu X and Sun Z 2020 Magnetorheological seal: a review *Int. J. Appl. Electromagn. Mech.* **62** 763–86
- [15] Kubík M, Pavlíček D, Macháček O, Strecker Z and Roupec J 2019 A magnetorheological fluid shaft seal with low friction torque *Smart Mater. Struct.* **28** 12

- [16] Zheng J-N, Li Y-Z, Chen C and Chen S-M 2020 The sealing properties of magnetorheological fluids under quasi-static tensile *Smart Mater. Struct.* **29** 13
- [17] Strecker Z, Roupec J, Mazůrek I, Macháček O and Kubík M 2018 Influence of response time of magnetorheological valve in Skyhook controlled three-parameter damping system *Adv. Mech. Eng.* **10** 8
- [18] Mass J and Guth D 2011 Experimental investigation of the transient behaviour of MR fluids *ASME 2011 Conf. smart Mater. Adapt. Struct. Intel. Syst* (<https://doi.org/10.1115/SMASIS2011-5240>)
- [19] Yoon D S, Park Y J and Choi S B 2019 An eddy current effect on the response time of a magnetorheological damper: analysis and experimental validation *Mech. Syst. Signal Process.* **127** 23
- [20] Kubík M and Goldasz J 2019 Multiphysics model of an MR damper including magnetic hysteresis *Shock Vib.* **2019** 20
- [21] Strecker Z, Jeniš F, Kubík M, Macháček O and Choi S-B 2021 Novel approaches to the design of an ultra-fast magnetorheological valve for semi-active control *Materials* **14** 20
- [22] Goncalves F D, Ahmadian M and Carlson J D 2005 Investigating the magnetorheological effect at high flow velocities *Smart Mater. Struct.* **15** 75–85
- [23] De Carvalho D D and Gontijo R G 2020 Magnetization diffusion in duct flow: the magnetic entrance length and the interplay between hydrodynamic and magnetic timescales *Phys. Fluids* **32** 072007
- [24] Ido Y, Inagaki T and Yamaguchi T 2010 Numerical simulation of microstructure formation of suspended particles in magnetorheological fluids *J. Phys. Condens. Matter* **22** 324103
- [25] Han K, Feng Y T and Owen D R J 2010 Three-dimensional modelling and simulation of magnetorheological fluids *Int. J. Numer. Methods Eng.* **84** 1273–302
- [26] Hashemi M R, Manzari M T and Fatehi R 2017 Non-linear stress response of non-gap-spanning magnetic chains suspended in a newtonian fluid under oscillatory shear test: a direct numerical simulation *Phys. Fluids* **29** 107106
- [27] Jolly M R, Bender J W and Mathers R T 1999 Indirect measurements of microstructure development in magnetorheological fluids *Int. J. Mod. Phys. B* **13** 2036–43
- [28] Horváth B, Decsi P and Szalai I 2021 Measurement of the response time of magnetorheological fluids and ferrofluids based on the magnetic susceptibility response *J. Intell. Mater. Syst. Struct.* **32** 1045389X21110386
- [29] Gavin H P, Hanson R D and Filisko F E 1996 Electrorheological dampers, part I: analysis and design *J. Appl. Mech.* **63** 669–75
- [30] Sherman S G 2017 Magnetorheological Fluid Dynamics for High Speed Energy Absorbers *Disertation* University of Maryland
- [31] Gołdasz J and Sapiński B 2015 *Insight into Magnetorheological Shock Absorbers* (Switzerland: Springer) 224
- [32] Laun H M and Gabriel C 2007 Measurement modes of the response time of a magneto-rheological fluid (MRF) for changing magnetic flux density *Rheol. Acta* **46** 665–76
- [33] Dapri I and Scarpi G 2005 Start-up flow of a Bingham fluid in a pipe *Meccanica* **40** 49–63
- [34] Sherman S G, Becnel A C and Wereley N M 2015 Relating Mason number to Bingham number in magnetorheological fluids *J. Magn. Magn. Mater.* **380** 98–104
- [35] Roupec J, Jeniš F, Strecker Z, Kubík M and Macháček O 2020 Stribeck curve of magnetorheological fluid within pin-on-disc configuration: an experimental investigation *Materials* **13** 4670
- [36] Bullough W A, Ellam D J and Atkin R J 2005 Pre-prototype design of ER/MR devices using computational fluid dynamics: unsteady flow *Int. J. Mod. Phys. B* **19** 1605–11
- [37] Mao M, Hu W, Choi Y T, Wereley N, Browne A L and Ulicny J 2014 Experimental validation of a magnetorheological energy absorber design analysis *J. Intell. Mater. Syst. Struct.* **25** 352–63

Article

Stribeck Curve of Magnetorheological Fluid within Pin-on-Disc Configuration: An Experimental Investigation

Jakub Roupec, Filip Jeniš, Zbyněk Strecker, Michal Kubík * and Ondřej Macháček

Faculty of Mechanical Engineering, Brno University of Technology, Technická 2, 616 69 Brno, Czech Republic; roupec.j@fme.vutbr.cz (J.R.); filip.Jenis@vutbr.cz (F.J.); strecker@fme.vutbr.cz (Z.S.); ondrej.Machacek@vutbr.cz (O.M.)

* Correspondence: michal.kubik@vutbr.cz

Received: 1 September 2020; Accepted: 16 October 2020; Published: 20 October 2020



Abstract: The paper focuses on the coefficient of friction (COF) of a magnetorheological fluid (MRF) in the wide range of working conditions across all the lubrication regimes—boundary, mixed, elastohydrodynamic (EHD), and hydrodynamic (HD) lubrication, specifically focused on the common working area of MR damper. The coefficient of friction was measured for MR fluids from Lord company with concentrations of 22, 32, and 40 vol. % of iron particles at temperatures 40 and 80 °C. The results were compared with a reference fluid, a synthetic liquid hydrocarbon PAO4 used as a carrier fluid of MRF. The results show that at boundary regime and temperature 40 °C all the fluids exhibit similar COF of 0.11–0.13. Differences can be found in the EHD regime, where the MR fluid COF is significantly higher (0.08) in comparison with PAO4 (0.04). The COF of MR fluid in the HD regime rose very steeply in comparison with PAO4. The effect of particle concentration is significant in the HD regime.

Keywords: friction; Stribeck curve; magnetorheological fluid; pin on disc; MR damper; tribological performance

1. Introduction

Magnetorheological (MR) fluid belongs into the group of smart materials enabling a change in an apparent viscosity in over a great range, and this switching between two states can be reached within 1 ms [1]. The fluid is the suspension of micron-sized particles, which are usually made of pure iron because of their favorable magnetic properties. These particles have a globular shape, and they are suspended in the carrier fluid, for instance, water, silicone oil, or, in most cases, a synthetic hydrocarbon, say, polyalphaolefin (PAO). When the magnetic field is applied, the ferromagnetic particles are concatenated into chain formation along the magnetic flux lines. The cohesion of chain formations causes an increase in the apparent viscosity of MR fluid [2]. This property is most often exploited by MR dampers [3–5], brakes/clutches [6–8], seals [9,10], or flexible structures [11,12]. The applicability of these MR devices in smart mechanical systems has several limitations. The main issues are as follows: (i) the sedimentation stability [13,14]; (ii) an increase of MR fluid consistency during the MR fluid loading called an in-use-thickening [15,16]; (iii) and the abrasiveness and poor lubricating properties of the MR fluid [17]. Currently, the first two issues are being sufficiently solved by using suitable additives to prevent the sedimentation and oxidation of iron particles.

The MR device lifetime is limited by two major sources of wear: (i) fluid flow wear and (ii) wear inside the tribological contact pairs by iron particles or additives. Wear due to fluid flow in the damper has been described in, e.g., [18]. Wear causes a decrease in the required force or torque due to an

increase in the gap size. However, this problem can be solved by a suitable damper control strategy. The wear or higher friction losses of tribological contact pairs is a significant problem for MR device lifetime and performance. In the case of the MR damper, several tribological contact pairs can be found: sealing and guiding of (i) the floating piston, (ii) the piston, and (iii) the piston rod. Wear of these parts can cause worse functionality exhibited as a higher friction force and MR fluid leakage from the device or into the gas chamber in the damper. Therefore, the basic knowledge of wear and lubricating behavior of MR fluid in different tribological contact pairs can significantly help in practice. Jolly [19] measured the coefficients of friction for MR fluid lubricated iron-on-iron conformal interfaces. He compared the four types of MR fluid from Lord with dry friction (0.18), and the measured coefficient of friction (COF) was an interval from 0.04 to 0.07 for all samples. Song [20] tested material pairs of steel-on-steel and aluminum-on-aluminum. The normal force was applied at three levels and at three levels of speed rotation. The COF was lower for the highest speed and the highest load. The lowest COF was measured for the steel-on-steel configuration and the highest COF for the aluminum material pair. Shahrivar [21] measured Stribeck curves of ferrofluids and MR fluid MRF-132DG from LORD. He used configuration ball-on-three plates from stainless steel AIS 316. The COF was increased from 0.13 to 0.19. Rosa [22] measured the Stribeck curve and tested the influence of particle size. The volume concentration of the particle was very low, and it was set properly to 1 vol. %. The results indicate that the COF is much lower for MR fluid with 0.4 μm particles than at MR fluid with 1.3 and 2 μm , which have almost identical COF. Zhang [23] measured COF for different particle volume content in commercial MR fluid from Lord company. The COF were almost identical (ca. 0.35) for 22, 32, and 40 vol.% of CI particles. Leung [24] used, for wear and COF measurement, block-on-ring geometry equipped with a stirring mechanism. He used a commercial MR fluid MRF-132DG from LORD as a source of CI particles and substituted the original carrier fluid with similar viscosity as an original carrier fluid and with four times higher viscosity. The measured COF of suspensions with higher viscosity of carrier fluid was ca. 0.065 and it was almost identical for high concentration of CI particles. For lower concentration it was significantly lower. The suspension with low viscosity of carrier fluid had identical COF for all concentrations (ca. 0.08). It seems that the carrier fluid with higher viscosity can form sufficient lubricating film, which can ensure the separation of both surfaces in contact into such a level that the particles can move in the contact more freely.

The intention of detailed state-of-art synthesis was the comparison of the results from various studies. Only tests with MRF-132DG from Lord company or fluids with similar composition, performed in modes pin-on-disc, block-on-ring or block-on-ball on three plates were evaluated. From these data, the viscosity of carrier fluids, the contact pressure, and the sliding speed of surfaces in contact from several papers can be calculated or estimated. In some cases, the sliding speed was just estimated from RPM. The viscosity for a certain temperature during measurement was also estimated. The contact pressure was calculated as the ratio of the normal force to the contact area calculated from the used geometry according to Hertz. The estimated (red) and calculated (blue) values are presented in Table 1. In an MR damper, two important steel–steel tribological contacts are operating in the MR fluid, namely, the piston rod guide and piston guide (no effect of a magnetic field). Considering a piston velocity in the range of 0.05 to 2 m/s, a lateral force in the range of 50 to 1000 N, a piston diameter of 32 mm, and a piston rod diameter of 12 mm, the range of a Hersey number between 1.E-11 and 1.E-09 for the piston rod guide and piston guide was determined. It can be seen that there are relatively few studies in the usual working condition of an MR damper.

The main goal of the paper is to determine the COF of MR fluids in a large range of a Hersey numbers and to focus mainly on the working conditions in the MR damper, which is essential for practical applications. The secondary aims are to describe the effects of particles on COF in the largest possible range of Hersey number, the effect of particle concentration, and the effect of temperature.

Table 1. Comparison of results from published studies (red: estimation value, blue: calculation) [20,21,23,25–29].

Author	Geometry	Relative Speed [mm/s]	Normal Force [N]	Contact Pair	Viscosity [mPa.s]	COF [-]	Contact Pressure [GPa]
Sohn	Block on ring	950	40	S45C/S45C	14.2	0.8	1.433
Song	pin on disc	780	50	brass/brass	14.2	0.13	0.012
Song	pin on disc	780	20	steel/steel	13.6	0.12	1.367
		780	50	steel/steel	13.6	0.11	1.855
		780	100	steel/steel	13.6	0.1	2.337
		780	20	brass/brass	13.6	0.16	0.862
		780	100	brass/brass	13.6	0.1	1.474
		780	20	alu/alu	13.6	0.12	0.673
		780	50	alu/alu	13.6	0.15	0.913
		780	100	alu/alu	13.6	0.11	1.150
		330	50	steel/steel	13.6	0.12	1.855
		1120	50	steel/steel	13.6	0.11	1.855
		330	50	brass/brass	13.6	0.12	1.170
		1120	50	brass/brass	13.6	0.11	1.170
		330	50	alu/alu	13.6	0.14	0.913
1120	50	alu/alu	13.6	0.13	0.913		
Wong	block on ring	1623	292	steel/steel	15.1	0.06	2.658
		1623	292	steel/steel	15.1	0.08	26.585
Zhang	pin on disk	31.25	1	alu/alu	13.6	0.5	0.156
		31.25	5	alu/alu	13.6	0.25	0.267
		62.5	1	alu/alu	13.6	0.5	0.156
		62.5	5	alu/alu	13.6	0.25	0.267
Zhang	pin on disk	31.25	10	steel/steel	15.1	0.3	0.683
		31.25	10	alu/alu	15.1	0.3	0.336
		31.25	10	brass/brass	15.1	0.25	0.336
Lee	pin on disc	390	50	steel/steel	15.1	0.16	1.855
		390	100	steel/steel	15.1	0.2	2.337
		560	50	steel/steel	15.1	0.13	1.855
Shahrivar	ball-on-three plates	0.06	10	steel/steel	13.6	0.15	0.224
		0.1	10	steel/steel	13.6	0.14	0.224
		1	10	steel/steel	13.6	0.145	0.224
		10	10	steel/steel	13.6	0.15	0.224
		100	11	steel/steel	13.6	0.17	0.224
		1000	12	steel/steel	13.6	0.19	0.269

2. Materials and Methods

2.1. Measurement Method of COF

In this study, a rotating friction tester was used to carry out all experiments. Tests were performed on the tribometer Bruker ZP-UMT TriboLab (ZP-44957) (Figure 1a) with a pin-on-disc configuration (Figure 1b). This tester uses a rotary module to drive the disc sample fixed at the lower part. The pin was used during the measurement stationary with the possibility to set the radial and vertical position to the disc. The pin was fixed by an upper holder to the normal and radial force sensor. The measured MR fluid or oil was applied to the plate surface with a volume of 12 mL, which ensured the fully flooded contact. Experimental data, such as the friction force (F), temperature, and normal force (N) are measured using sensors. The COF is calculated using the following equation:

$$\text{COF} = \frac{F}{P} \quad (1)$$

where COF is the kinetic coefficient of friction, F is the nominal measured friction force during sliding, and P is the applied load (normal force). The normal force is ensured by an upper linear drive and the permanent pressure of the pin to the disc is ensured by the springy metal strips Figure 1b. A hardened

ball bearing with a diameter of 6.35 mm was used as a pin and a hardened tool steel as a disc. The disc had to be gently ground and polished up to less than R_a 0.025 μm to avoid the seizure at higher speed (Figure 2a). Generally, higher disc roughness resulted in seizure, especially at higher sliding speeds. However even polishing the disc did not fully prevent the contact from seizure (Figure 2b) because of the flexible mount of the pin, which started to vibrate at high turning speeds. For this reason, the maximal rotary speed had to be set on ca. 2400 rev/min. The corresponding sliding speed was insufficient to achieve the required values of the Hersey number. Therefore, to measure the Stribeck curve with this regime of lubrication, a normal force cannot stay constant for all measuring steps, and it had to be gradually reduced when the maximum permitted rotary speed was reached.

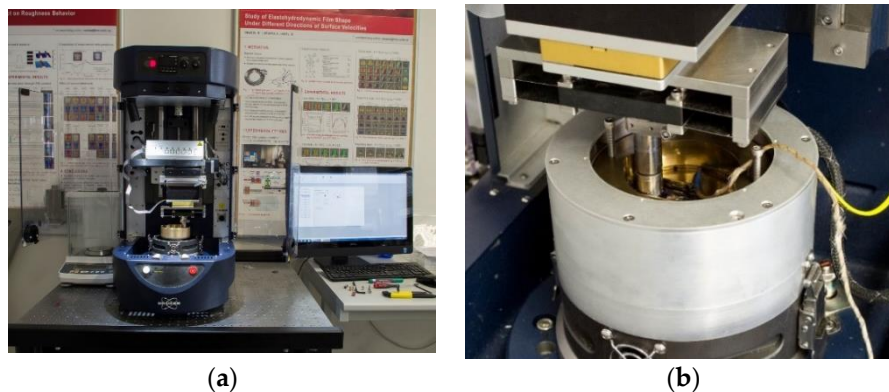


Figure 1. (a) Tribometer UMT Bruker; (b) pin-on-disc configuration with the heating module.

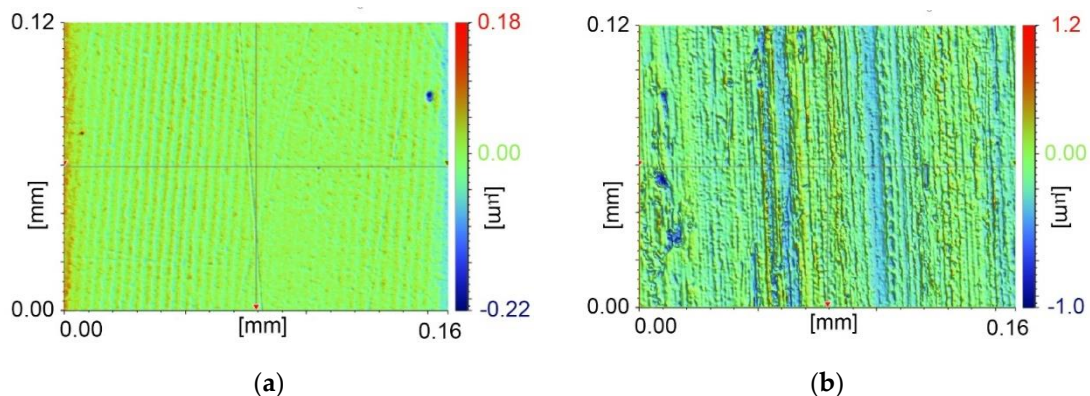


Figure 2. (a) Polished disc— R_a 0.014 μm ; (b) track roughness after test— R_a 0.110 μm .

Thus, the normal force was gradually decreased from 20 to 1 N. The revolution of the rotary test module was set according to the required sliding speed and actual radius of the pin on the disc sample. The sliding speed was changed from 5 to 4000 mm/s in 20 steps, which approximately corresponds to 2400 rpm for maximal sliding speed; see Table 2. The initialization procedure was performed for 120 s at sliding speed 125 mm/s and 60 s at sliding speed 1500 mm/s to neglect the effect of worn surfaces on measuring COF.

During the procedure of the measurement of one Stribeck curve, the hardened ball as a pin was twice changed to avoid contact seizure because of the escalated pin wear at a high rotational speed. The repeating of measurements was carried out for obtaining three Stribeck curves for one sample because of the higher statistical significance of data. An error bar was created from these data. The new radius, new pin, and new tested fluid were used for each repeating.

Table 2. Conditions for Stribeck curve measurement.

Step	F _z (N)	v (mm/s)	Step	F _z (N)	v (mm/s)
1	20	5	11	20	2500
2	20	10	12	20	3000
3	20	25	13	20	3300
4	20	50	14	15	3300
5	20	125	15	10	3300
6	20	250	16	5	3300
7	20	500	17	2.5	3300
8	20	1000	18	2	4000
9	20	1500	19	1.6	4000
10	20	2000	20	1	4000

The measurement was carried out for temperatures of 40 and 80 °C using a temperature chamber by Bruker. The delivered software with a tribometer cannot compile a Stribeck curve including the sliding speed, contact pressure, and dynamic viscosity on the x-axis. This software works only with revolutions of rotary drive, which is misleading when using a different radius of the pin. Therefore, the new script in Matlab for data evaluation was created. The one measurement (one repeating) of the Stribeck curve consists of 20 steps, as mentioned above when each step corresponds to one point on the Stribeck curve. For each step, the 16 changes in sense of the rotation were set for better flooding of the contact. Sometimes, the measured data included several types of instabilities that were solved by this script. Viscosity is an important input for calculation of Hersey number. The suspension viscosity (MR fluid) is dependent on the volume fraction of particles and carrier fluid viscosity. However, the amount of particles in contact is not known because some particles are probably excluded from the contact zone [30]. Therefore, the authors decided to use for calculation of Hersey number carrier fluid viscosity of MRF. The script calculates a relation among relative sliding speed of surfaces in contact v , contact pressure p_z , and dynamic viscosity of carrier fluid η and draws it on the x-axis (Hersey number). This relation is given by (2):

$$\text{axis value} = \frac{\eta \cdot v}{p_z} \quad (2)$$

2.2. Testing Samples

Commercial MR fluids supplied by the LORD company (MRF-122EG, MRF-132DG, and MRF-140CG) were chosen as the MR fluid samples. The properties from LORD Technical Datasheets are stated in Table 3.

Table 3. Properties of MR fluid samples and PAO.

Parameter	MRF-122EG	MRF-132DG	MRF-140CG	PAO4
Viscosity at 40 °C (Pa.s)	0.042 ± 0.02	0.112 ± 0.02	0.28 ± 0.07	0.014
Density (g/cm ³)	2.28–2.48	2.95–3.15	3.54–3.74	0.82
Solids content of weight (%)	72	80.98	85.44	0
Solids content of volume (%)	22	32	40	0

The Lord MR fluids were compared with base oil from the group of synthetic liquid hydrocarbons (poly-alpha-olefin). The tested MR fluids differed in iron particle concentration from 22 to 40 vol. %. The commonly accepted rheological model of MR fluid is the Bingham model:

$$\tau = \eta_0 \dot{\gamma} + \tau_0(H) \text{sign}(\dot{\gamma}) \text{ at } |\tau| \geq |\tau_0(H)|, \dot{\gamma} = 0 \text{ at } |\tau| \leq |\tau_0(H)|, \quad (3)$$

where τ is shear stress, η_0 is plastic viscosity, τ_0 is yield stress, H is magnetic flux intensity in MR fluid, and $\dot{\gamma}$ is shear strain rate. In the case of experiments, magnetic flux intensity is zero ($H = 0$ A/m). MR fluid in the non-activated state ($H = 0$ A/m) exhibits yield stress in tens of Pa. However, the MR fluid supplier usually states the Newtonian behavior of MR fluid and provides the value of viscosity at high shear rates. The particle size and distribution were measured by a scanning electron microscope FEG SEM ZEISS Ultra Plus and analyzed by script using tools for picture analysis in Matlab (R2018b). The particles were spherical and the average size (diameter approximately $2.1 \mu\text{m}$) and distribution according to Q3 were identical for all MR fluids (Figure 3).

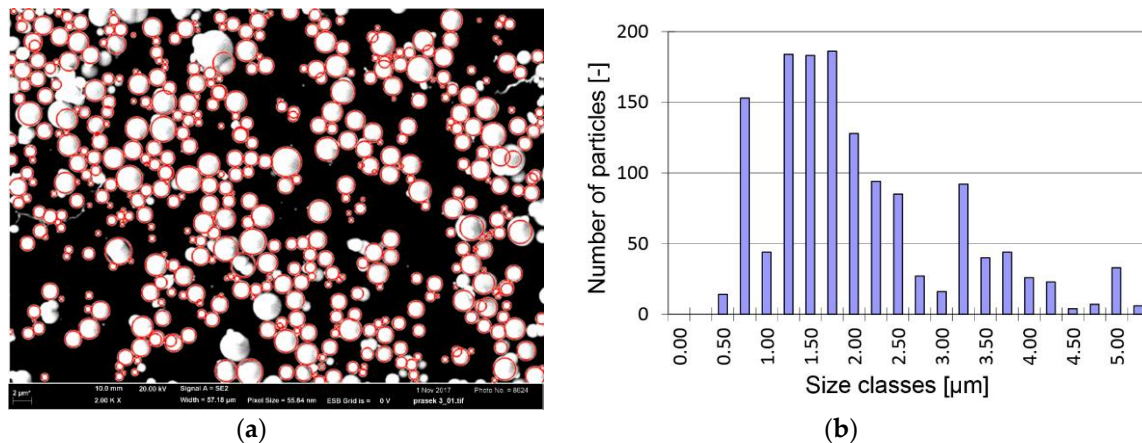


Figure 3. MRF-122EG (a) SEM picture of centrifuging particles; (b) histogram for 1399 detected particles.

3. Results and Discussion

3.1. COF Comparison of Oils and MR Fluid

Figure 4 compares the Stribeck curves of measured PAO and MRF-132DG for a temperature of 40°C . The results in Figure 4 indicate very high repeatability of the measurement; see error bars. Only at the boundary lubrication regime was the variance of values slightly higher. However, that can be understandable because in this area the solid surfaces come into contact and this event has a stochastic character. It can be seen that the boundary, mixed, elastohydrodynamic (EHD), and hydrodynamic regimes of lubrication were measured; see Figure 4. However, the EHD regime (the area with the lowest COF) at MR fluid came on at significantly higher COF than PAO, and then it rapidly rose. The EHD is defined as an area where the lubrication film has the same order of magnitude as the surface roughness. In this area, the iron particles of MR fluid probably work as a mediator at the interaction of both solid surfaces. The rapid increase of COF at the hydrodynamic regime at MR fluids can be explained by the presence of iron particles, which can form a higher lubricating wedge under the pin. The non-Newtonian rheological behavior of MR fluid may also affect the rapid increase of COF. The results indicate that the area with high relative sliding speed cannot be recommended as an operating point for MR fluid, which is the main contrast to common oils. Generally, for common oils, the hydrodynamic lubrication regime is desirable as an operating area. The hydrodynamic regime is defined as a regime fully separated from contacting surfaces by lubrication film and therefore the wear and COF are the lowest in this area. The measurements showed that the HD regime is also recommended for MR devices, but only in the narrow band up to sliding speed corresponding to COF of ca. 0.14. The measured value of COF in a mixed regime corresponds to the data published by Sohn [25] (COF 0.1–0.12) which was tested in the same configuration.

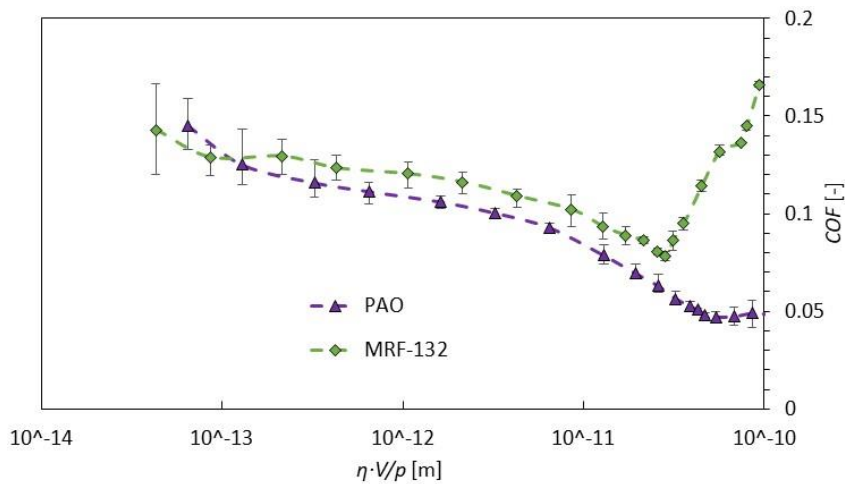


Figure 4. Stribeck curves comparison of PAO 4 and magnetorheological fluid MRF-132DG at 40 °C.

3.2. Particle Concentration Effect

It is surprising that the COF in the boundary lubrication regime is almost identical for all fluids, despite the presence of iron particles in MR fluid. Probably, only the viscosity of the carrier fluid and the friction surfaces affect the COF. It can be also deduced that the concentration of iron particles was already high enough for the fluid MRF-122EG (22 vol. %) to fully fill the lubrication gap between surfaces. Many studies suggest that the concentration above 10 vol. % of iron particles does not influence COF and wear [20]. In the hydrodynamic regime, the situation is different. The effect of particle concentration on COF is observable; see Figure 5. The higher the particle concentration, the higher the COF. The viscosity of the suspension (MR fluid) probably has a significant effect in the HD regime. Similar conclusions are presented in the paper [27].

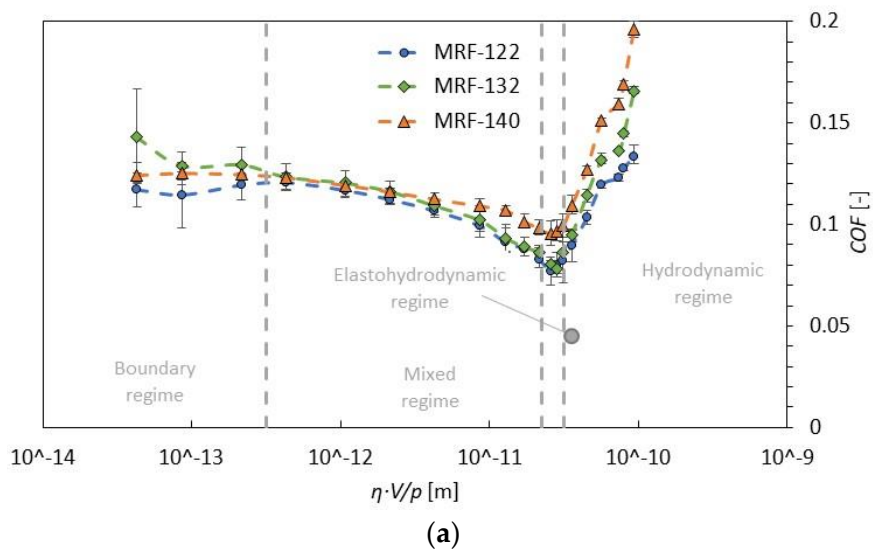


Figure 5. Cont.

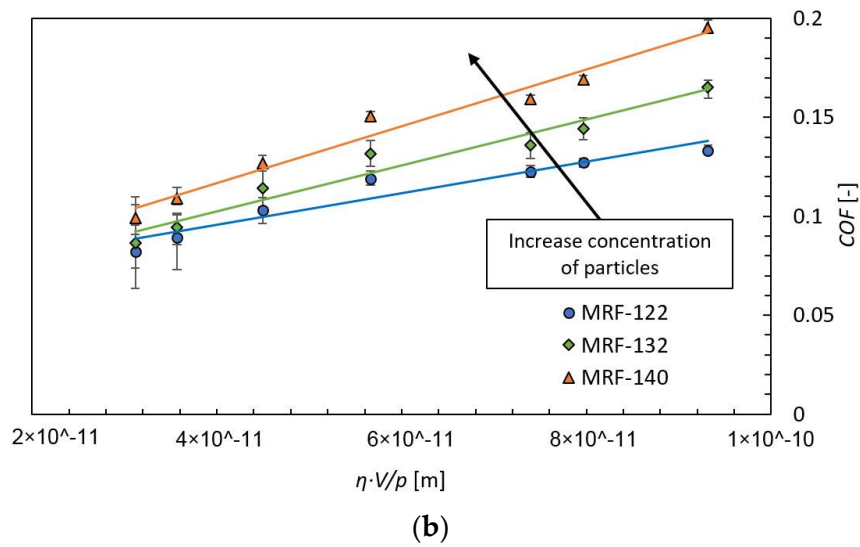


Figure 5. Stribeck curves of (a) MR fluids MRF-122EG, MRF-132DG, and MRF-140CG at 40 °C; (b) detail on HD regime.

3.3. Temperature Effect

Figure 6 shows the comparison between 40 and 80 °C, which can be considered as an operating point for linear actuators such as dampers. The viscosity was kept the same for both temperatures (0.01 Pa.s). No significant temperature effect was observed for MR fluids 122 and 140. For MR fluid 132, there is a slight difference in the minimum COF value. However, the PAO was significantly affected by temperature. A significant increase in COF over the entire Hersey number range was observed at 80 °C; see Figure 6d.

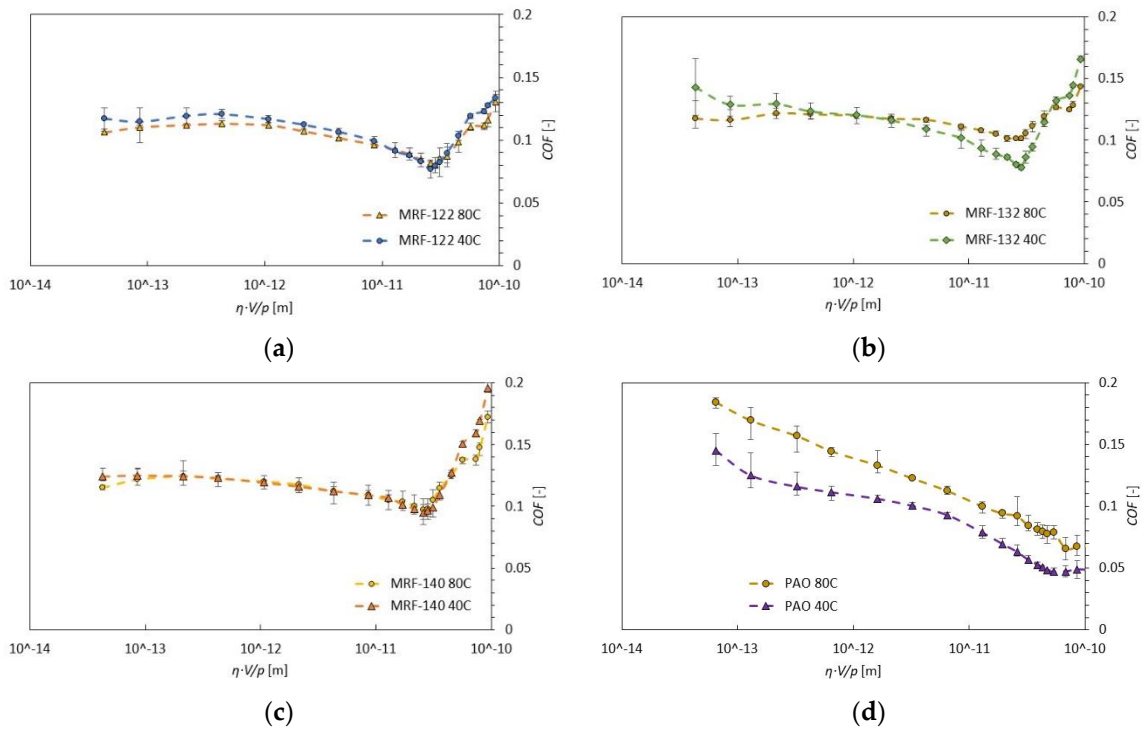


Figure 6. Comparison of individual measured fluid at temperatures 40 and 80 °C: (a) MRF-122; (b) MRF-132; (c) MRF-140; (d) PAO.

4. Conclusions

In this work, the COF measurements for three commercial MR fluids with 22–40 vol. % of CI particles from LORD company oration were done. These fluids were compared with synthetic liquid hydrocarbon PAO4, which corresponds to the base oil of MR fluids. The properties of all the fluids were measured at temperatures 40 and 80 °C. The results indicate that in the range of boundary lubrication, all the fluids exhibit similar COF, despite iron particles in the MR fluids. In the EHD area (transition between mix and hydrodynamic lubrication), where the COF is generally the lowest, the MR fluids exhibit slightly higher values of COF than PAO. The biggest difference can be observed in the hydrodynamic regime. The COF for PAO rises with a much gentler slope than MR fluids. The effect of particle concentration on COF is observable. The temperature effect on the COF of MRF is insignificant.

The results can be also used as a guide for developers of MR devices. The important result is the specification of a suitable operating range. Considering low friction and total separation of contact surfaces by lubrication film, the hydrodynamic lubrication area seems to be suitable. On the contrary, the contact flooded by MR fluid should not be operated at higher Hersey numbers, because the COF rises very steeply for specific numbers, higher than the EHD lubrication regime.

A comparison of COF measured by authors mentioned in the introduction (see Figure 7) shows quite a large variance, although only measurements with MRF132DG or fluids with similar particle concentrations are included in this figure. The majority of the values were measured in boundary and mixed regimes, where the COF is very dependent on contact surface roughness. Only a few values were measured in the hydrodynamic regime. In the HD regime, the surface roughness and geometry should have a much smaller impact on measured COF; therefore, a smaller variance can be expected. This work provided information about the COF in the usual working area of the MR damper (HD regime).

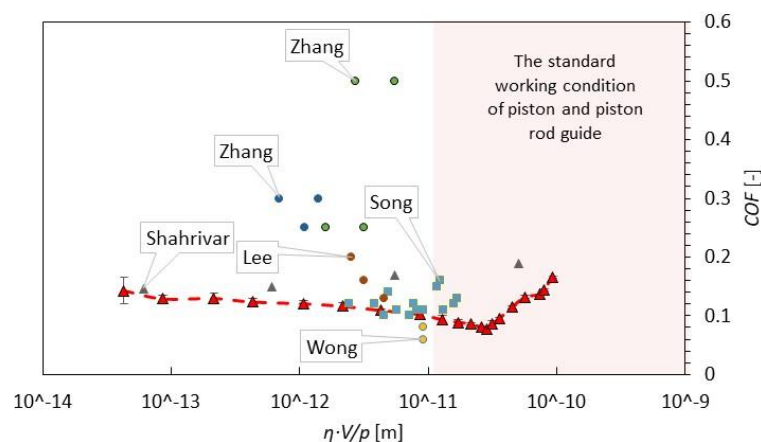


Figure 7. Comparison of results of COF from our study (red line) and results from previous works of other authors for MR fluids MRF-132DG or similar MR fluid.

Author Contributions: Conceptualization, J.R. and Z.S.; methodology, J.R. and F.J.; software, J.R.; validation, M.K, O.M. and Z.S.; writing—original draft preparation, M.K.; writing—review and editing, F.J. and Z.S.; project administration, J.R.; supervision, Z.S. All authors have read and agreed to the published version of the manuscript.

Funding: This paper and experiments have been made possible thanks to the kind sponsorship of various grants and numerous agencies. We would like to thank specifically the grant Agency of the Czech Republic (GAČR), numbers 17-10660J and 20-23261Y.

Conflicts of Interest: The authors declare no conflict of interest. The funders had no role in the design of the study; in the collection, analyses, or interpretation of data; in the writing of the manuscript, or in the decision to publish the results.

References

1. Goncalves, F.D.; Ahmadian, M.; Carlson, J.D. Investigating the magnetorheological effect at high flow velocities. *Smart Mater. Struct.* **2005**, *15*, 75–85. [[CrossRef](#)]
2. Pappas, Y.; Klingenberg, D.J. Simulations of magnetorheological suspensions in Poiseuille flow. *Rheol. Acta.* **2006**, *45*, 621–629. [[CrossRef](#)]
3. Goldasz, J. Magnetostatic study of a dual-gap MR valve. In Proceedings of the 20th International Conference on Research and Education in Mechatronics (REM), Wels, Austria, 23–24 May 2019.
4. Strecker, Z.; Kubík, M.; Vitek, P.; Roupec, J.; Paloušek, D.; Šreibr, V. Structured magnetic circuit for magnetorheological damper made by selective laser melting technology. *Smart Mater. Struct.* **2019**, *28*, 055016. [[CrossRef](#)]
5. Kubík, M.; Goldasz, J. Multiphysics Model of an MR Damper including Magnetic Hysteresis. *Shock Vib.* **2019**, *2019*. [[CrossRef](#)]
6. Chen, S.; Yang, J. Probing Slip Differential Heat of Magnetorheological Fluids Subjected to Shear Mode Operation and Its Effect on the Structure. *Materials (Basel)* **2019**, *12*, 1860. [[CrossRef](#)] [[PubMed](#)]
7. Li, W.H.; Du, H. Design and Experimental Evaluation of a Magnetorheological Brake. *Int. J. Adv. Manuf. Technol.* **2003**, *21*, 508–515. [[CrossRef](#)]
8. Park, E.J.; Stoikov, D.; Falcao da Luz, L.; Suleman, A. A performance evaluation of an automotive magnetorheological brake design with a sliding mode controller. *Mechatronics* **2006**, *16*, 405–416. [[CrossRef](#)]
9. Kubík, M.; Pavlíček, D.; Macháček, O.; Strecker, Z.; Roupec, J. A magnetorheological fluid shaft seal with low friction torque. *Smart Mater. Struct.* **2019**, *28*, 047002. [[CrossRef](#)]
10. Szczęch, M. Experimental Study on the Pressure Distribution Mechanism Among Stages of the Magnetic Fluid Seal. *IEEE Trans. Magn.* **2018**, *54*, 1–7. [[CrossRef](#)]
11. Choi, S.-B.; Hong, S.R.; Choi, Y.T.; Wereley, N.M. Vibration control of flexible structures using MR and piezoceramic mounts. In Proceedings of the Society of Photo-Optical Instrumentation Engineers (SPIE), Proceedings of Smart Structures and Materials 2004, San Diego, CA, USA, 15–18 March 2004; Flatau, A.B., Ed.; Spie-Int Soc Optical Engineering: Bellingham, WA, USA, 2004; Volume 5390, pp. 127–134.
12. Song, B.-K.; Yoon, J.-Y.; Hong, S.-W.; Choi, S.-B. Field-Dependent Stiffness of a Soft Structure Fabricated from Magnetic-Responsive Materials: Magnetorheological Elastomer and Fluid. *Materials* **2020**, *13*, 953. [[CrossRef](#)]
13. Rich, J.P.; Doyle, P.S.; McKinley, G.H. Magnetorheology in an aging, yield stress matrix fluid. *Rheol. Acta.* **2012**, *51*, 579–593. [[CrossRef](#)]
14. Roupec, J.; Berka, P.; Mazůrek, I.; Strecker, Z.; Kubík, M.; Macháček, O.; Andani, M.T. A novel method for measurement of MR fluid sedimentation and its experimental verification. *Smart Mater. Struct.* **2017**, *26*, 107001. [[CrossRef](#)]
15. Mazůrek, I.; Roupec, J.; Klapka, M.; Strecker, Z. Load and rheometric unit for the test of magnetorheological fluid. *Meccanica* **2013**, *48*, 631–641. [[CrossRef](#)]
16. Carlson, J.D. Critical factors for MR fluids in vehicle systems. *Int. J. Veh. Des.* **2003**, *33*, 207. [[CrossRef](#)]
17. Iyengar, V.R.; Robert, T. Foister Durable Magnetorheological Fluid Compositions. US Patent 6,599,439, 29 July 2003.
18. Utami, D.; Ubaidillah; Mazlan, S.; Imaduddin, F.; Nordin, N.; Bahiuddin, I.; Abdul Aziz, S.; Mohamad, N.; Choi, S.-B. Material Characterization of a Magnetorheological Fluid Subjected to Long-Term Operation in Damper. *Materials (Basel)* **2018**, *11*, 2195.
19. Jolly, M.R.; Bender, J.W.; Carlson, J.D. Properties and Applications of Commercial Magnetorheological Fluids. *J. Intell. Mater. Syst. Struct.* **1999**, *10*, 5–13.
20. Song, W.-L.; Choi, S.-B.; Choi, J.-Y.; Lee, C.-H. Wear and Friction Characteristics of Magnetorheological Fluid under Magnetic Field Activation. *Tribol. Trans.* **2011**, *54*, 616–624. [[CrossRef](#)]
21. Shahrivar, K.; Ortiz, A.L.; de Vicente, J. A comparative study of the tribological performance of ferrofluids and magnetorheological fluids within steel–steel point contacts. *Tribol. Int.* **2014**, *78*, 125–133. [[CrossRef](#)]
22. Rosa, W.O.; Vereda, F.; de Vicente, J. Tribological Behavior of Glycerol/Water-Based Magnetorheological Fluids in PMMA Point Contacts. *Front. Mater.* **2019**, *6*, 1–11. [[CrossRef](#)]
23. Zhang, P.; Lee, K.-H.; Lee, C.-H. Friction behavior of magnetorheological fluids with different material types and magnetic field strength. *Chin. J. Mech. Eng.* **2016**, *29*, 84–90. [[CrossRef](#)]

24. Leung, W.C.; Bullough, W.A.; Wong, P.L.; Feng, C. The effect of particle concentration in a magneto rheological suspension on the performance of a boundary lubricated contact. *Proc. Inst. Mech. Eng. Part J J. Eng. Tribol.* **2004**, *218*, 251–263. [[CrossRef](#)]
25. Sohn, J.W.; Choi, S.B.; Lee, C.H.; Cho, M.W. Wear Characteristics of Magnetorheological Fluid under Boundary Lubrication. *Adv. Mater. Res.* **2009**, *79*, 83–86. [[CrossRef](#)]
26. Song, W.-L.; Lee, C.-H.; Choi, S.-B. Sliding wear behavior of magnetorheological fluid for brass with and without magnetic field. *Trans. Nonferrous Met. Soc. China* **2013**, *23*, 400–405. [[CrossRef](#)]
27. Wong, P.; Bullough, W.; Feng, C.; Lingard, S. Tribological performance of a magneto-rheological suspension. *Wear* **2001**, *247*, 33–40. [[CrossRef](#)]
28. Lee, C.H.; Lee, D.W.; Choi, J.Y.; Choi, S.B.; Cho, W.O.; Yun, H.C. Tribological Characteristics Modification of Magnetorheological Fluid. *J. Tribol.* **2011**, *133*. [[CrossRef](#)]
29. Zhang, P.; Lee, K.-H.; Lee, C.-H. Reciprocating friction characteristics of magneto-rheological fluid for aluminum under magnetic field. *Trans. Nonferrous Met. Soc. China* **2014**, *24*, 171–176. [[CrossRef](#)]
30. Yakubov, G.E.; Branfield, T.E.; Bongaerts, J.H.H.; Stokes, J.R. Tribology of particle suspensions in rolling-sliding soft contacts. *Biotribology* **2015**, *3*, 1–10. [[CrossRef](#)]

Publisher's Note: MDPI stays neutral with regard to jurisdictional claims in published maps and institutional affiliations.



© 2020 by the authors. Licensee MDPI, Basel, Switzerland. This article is an open access article distributed under the terms and conditions of the Creative Commons Attribution (CC BY) license (<http://creativecommons.org/licenses/by/4.0/>).



OPEN

Transient response of magnetorheological fluid on rapid change of magnetic field in shear mode

Michal Kubík^{1✉}, Josef Válek¹, Jiří Žáček¹, Filip Jeniš¹, Dmitry Borin², Zbyněk Strecker¹ & Ivan Mazůrek¹

The transient behaviour of magnetorheological (MR) devices is an important parameter for modern semi-actively controlled suspension systems. A significant part of the MR device response time is the MR fluid response time itself. A significant factor is the so-called rheological response time. The rheological response time is connected with the structuring particle's time and the development of shear stress in MR fluid during the deformation. The main aim of this paper is to experimentally determine the rheological response time of MR fluid and evaluated the effect of shear rate, magnetic field level, and carrier fluid viscosity. The unique design of the rheometer, which allows the rapid change of a magnetic field, is presented. The rheological response time of MRF 132-DG and MRC-C1L is in the range of 0.8–1.4 ms, depending on the shear rate. The higher the shear rate, the shorter the response time. It can be stated that the higher the magnetization of the MR fluid, the lower the response time. The higher the viscosity, the higher the rheological response time. The measured data of rheological response time was generalized and one master curve was determined.

Magnetorheological (MR) fluid is the suspension of fine, non-colloidal, low-coercivity, high-magnetizable particles in a carrier fluid. These particles are usually made of carbonyl iron and have a spherical shape due to their durability and tribological properties. The continuous phase of MR fluids is typically silicon or synthetic hydrocarbon oils¹. The lowest possible viscosity of the continuous phase is required, but this significantly affects the sedimentation stability². MR fluid also contains several additives that affect rheological³, tribological⁴, or sedimentation stability⁵. When the MR fluid is energized by the magnetic field, the ferromagnetic particles are magnetized and form chain-like structures in the direction of the magnetic field⁶. The rheology of MR fluid in activated state is characterized by pre-yield and post-yield regime. In the pre-yield regime, the MR fluid exhibits viscoelastic behaviour. The complex modulus G is a magnetic field H and particle concentration dependent. The shear stress τ in the fluid can be described by the equation below

$$\tau = G\gamma, \tau < \tau_0(H) \text{ and } \dot{\gamma} = 0$$

where γ is shear strain, $\dot{\gamma}$ is shear rate and $\tau_0(H)$ is MR fluid yield stress. The post-yield regime is usually described by Bingham model as follows:

$$\tau(H) = \tau_0(H) + \eta\dot{\gamma}$$

where $\tau(H)$ is shear stress, η is Bingham viscosity, and H magnetic flux intensity. It is the simplest model that can describe this behaviour. The MR dampers^{7,8}, clutches/brakes⁹, or seals^{10,11} take advantage of the unique behavior of MR fluid.

The transient behaviour (transient response) of MR fluid is an important parameter for modern magnetorheological devices working with real-time control^{12,13}. The MR fluid response time is composed of other partial response times which are differently important depending on the operating conditions and the method of MR fluid loading. The response time of MR fluid can be divided into (1) hydrodynamic response time, (2) particle structure development response time, and (3) rheological response time.

¹Faculty of Mechanical Engineering, Brno University of Technology, Brno, Czech Republic. ²Chair of Magnetofluidynamics, Institute of Mechatronic Engineering, Technische Universität Dresden, Dresden, Germany. ✉email: Michal.kubik@vutbr.cz

The research studies of Sherman¹⁴ or Goldasz et al.¹⁵ show that MR valve pressure drop due to MR fluid yield stress decreases with the increasing gap velocity. At high velocities, this pressure drop is approaching to be zero. This statement is based on CFD (computational fluid dynamics) simulations. This phenomenon is related to transient rheology connected with the development of the velocity profile in the gap and is often referred to as the hydrodynamic fluid response time. Goncalves et al.¹⁶ experimentally determined that the hydrodynamic response time is 0.73 ms for magnetic field 100 kA/m and 0.53 ms for magnetic field 200 kA/m. The commercial MRF-132LD (Lord Corp., USA) was used in this study. Kubík et al.¹⁷ published similar study. This team measured the hydrodynamic response time of MR fluid MRF-132DG (Lord Corp., USA) and ranges from 0.4 to 1 ms for a selected gap size and a range of magnetic field stimuli. The velocity profile development mechanism is similar for MR fluid and electrorheological (ER) fluid¹⁸. However, ER fluid show faster response time than MR valve. ER fluid is the suspension of fine electrically active particles in fluid. This fluid exhibits a rapid increase of fluid yield stress under the application of an electric field. Gavin et al.¹⁹ modelled the transition from a fully developed Bingham profile to a Newtonian flow for ER fluid. The yield stress of ER fluid was assumed to drop to zero quicker than the dissipation energy due to the development of the velocity profile¹⁹. It can be stated that this hydrodynamic response time is connected with high shear rates or fast changes of the magnetic field in valve mode.

The particle structure development response time is related to the time needed for the structuring of particles in the direction of the magnetic field without the flow conditions of the MR fluid. Jolly et al.²⁰ proposed an experimental method that microstructure formation time can be deduced from the transient changes in the relative magnetic permeability of the MR fluid. The chained particles are assumed to have a higher magnetic permeability than the dispersed. Two-time responses were observed²⁰. The first attributes the connection with the transfer of particles into diverse chains (pair formation) and the second (an order of magnitude slower) connection with the migration of these initial chains into longer and stronger structures. The response time was between 5 and 10 ms. A similar measurement method was also published by Horváth et al.²¹. Pei et al.²² stated that the response time of dry MR fluid was in the order of μs by the model. This statement is based on simulation results.

The rheological response time is connected with the structuring particle's time and the development of shear stress in MR fluid during the deformation (flow). Sherman et al.²³ create a chain model of MR fluid. This model is based on one million particles. One result of this paper is the shear stress time history on the step change of a magnetic field. For this data, the rheological response time can be determined as roughly 0.4 ms. The MR fluid had a volume particle fraction of 25% and was under the shear rate of 500 s^{-1} . Laun and Gabriel²⁴ determined the response time of MR fluid of 2.8 ms. They used sinusoidal excitation and the determined time lag between magnetic flux density and shear stress. Kikuchi et al.²⁵ examined the response time to a step electric current and introduce non-dimensional response time parameter. It can be expected that the mechanism of chain formation in Electro-rheological (ER) fluids and MR fluids is similar. Koyanagi et al.²⁶ developed a method for a measurement response time of ER fluid. This team experimentally determined the response time as 0.95 ms.

The information about the transient behaviour of MR fluid is limited. This issue is becoming more important due to the development of MR devices with a short response time^{7,27}, where the limiting part is now the MR fluid itself. The current design of the MR damper achieved a response time of about 1.2 ms. In the current state of the art, more studies can be found dealing with the response time of MR fluid^{7,12} than is presented above. In these several cases, the authors measured the time constant of measuring devices instead of the time constant of MR fluid¹⁴. The rheological response time of MR or ER fluid was just experimentally determined in studies^{24,26}. Both studies presented response time just for one experimental condition. The main aim of our paper is to experimentally determine the rheological response time of MR fluid and evaluated the effect of shear rate, magnetic field level, and carrier fluid viscosity. Our results will be compared with the published analytical approach¹⁴.

Materials and methods

Description of the measured phenomenon and measuring methods. The aim of the measurement is to experimentally determine the time constant of MR fluid in the shear mode (from the increase in shear stress τ) on a rapid change in the magnetic field B . The procedure of the experiment is described in Fig. 1. At time T_1 , the MR fluid is loaded by given shear rates and the magnetic field is off. At time 0, the magnetic field is activated and, at time T_2 , the magnetic field is already at the maximum value. However, until time T_3 , the shear stress remains at the same level as at time T_1 . In the author's opinion, this delay is associated with particle structure formation in the MR fluid. In reality, there are no separate single chains. That is just a tentative simplification. At time T_4 , there is a rapid increase in shear stress in the MR fluid due to the deformation of the particle structure. This is shown as tilting chains in the shear direction but the mechanisms of structure fracture are more complex. Generally, the simplest dynamic system, that can serve as an approximation of the transient behavior of MR fluid is a first-order system. The transient response is expressed by the time constant T_{63} (primary response time), which determines the time when monitored torque (calculated shear stress) achieved 63.2% of the final controlled value (steady-state). This approximation can be used for the dynamic behaviour of MR actuators²⁸. In the case of rheology measurement, the MR fluid can be described by a simple Maxwell model and by Bingham constitutive equation. For step change on magnetic field, the expected shear stress response $\tau(t)$ would be:

$$\tau(t) = \tau_0 \left[1 - e^{-\frac{t}{T_{63}}} \right] + \eta \dot{\gamma} \quad (1)$$

where t is time. More names for a variable T_{63} can be found in the literature as switching time²⁴, response time¹⁷ or rheological response time¹⁴. However, the transient response of MR fluid exhibits different behaviour than the first-order system, see Fig. 5. Therefore, we decided to determine those time constants in our paper: (1) first-order time constant T_{63} (0–63.2%) and (2) rise time T_{90} (0–90%), see Fig. 1. This response time were so-called

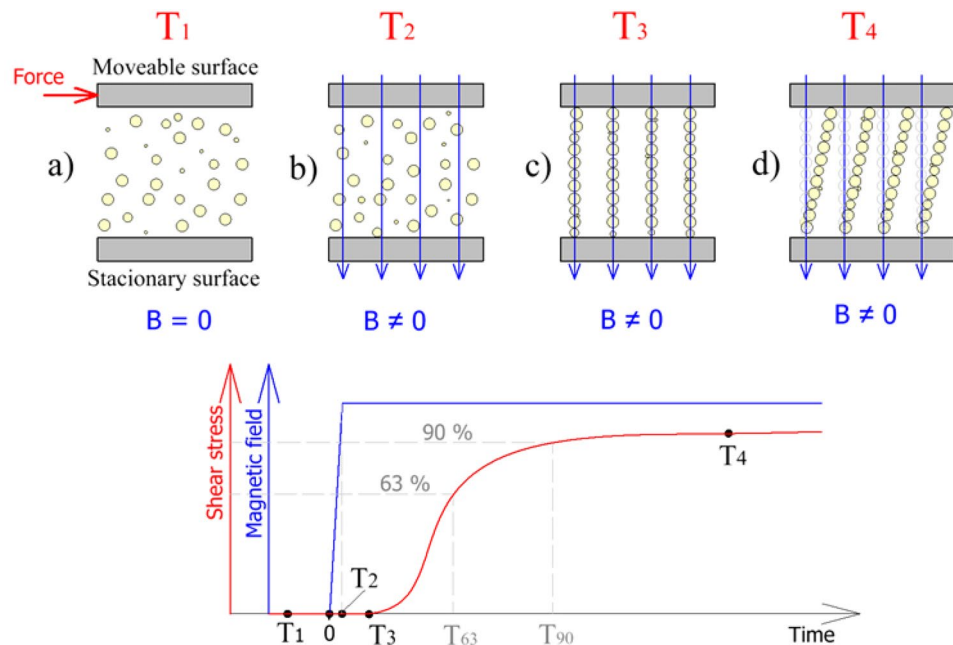


Figure 1. Demonstrating measured method and determination of time constants.

rheological response time because it is connected with changes in the rheology of MR fluid. Those time constants were selected due to a suitable comparison of our experimental data with results from published papers.

Experimental test rig. The experimental test rig is composed of an electric motor with encoder (1), developed rheometer (2), load inertia (3), lever (4), and force sensor (5), see Fig. 2A. The load inertia accumulated energy to stabilize rotation during the activation of MR fluid using the magnetic field (an increase motor load). The load inertia had 4.6 kg (moment inertia 5900 kg/mm²). The whole system is mounted rotationally and the torque is measured by a force sensor on the lever (52 mm). The homemade rheometer is composed of the rotor (a), stator (b), and MR fluid sample (c), see Fig. 2. The electromagnetic coil creates the magnetic flux (d) in the magnetic circuit (shown in grey). The gap size was 0.6 mm, see Fig. 2. The transient behaviour of the rheometer is fundamental for the precise measurement of MR fluid response time. The response time of hardware (rheometer) has to be as short as possible and two main sources were identified in the literature: (1) eddy currents in the magnetic circuit⁷, and (2) inductance of the rheometer electromagnetic coil⁷. In our rheometer, we used soft magnetic composite (SMC) material (trademark Sintex) for the magnetic circuit to eliminate eddy currents. SMC material is magnetic conductive and electric non-conductive (resistivity 280 μΩm). The suitable design of a magnetic circuit with our patented current controller allows a rapid increase of electric current on the electromagnetic coil ($T_{63} = 0.21$ ms).

Methodology measurement. The aim of the experiments was to determine shear stress in MR fluid and magnetic field over time. The shear stress τ was calculated from area and torque which was measured indirectly based on data from the force sensor (MEG20) on the lever, see Fig. 2. The force sensor measuring range was 0–200 N. The force range (deformation) was chosen to maximize system rigidity and only the first 10% of the range was used for measurement. The magnetic field in the gap corresponds with the electric current course and was measured by Fluke i30 current clamps. These two signals were recorded and conditioned with a sampling frequency of 200 kHz by the Dewetron USB-50 analyzer. The MFG-2120MA signal generator generates a square wave voltage signal which inputs to the current controller at a frequency of 1 Hz. Our developed current controller generates an electric current on the electromagnetic coil with over-voltage up to 100 V. The measurement procedure was as follows: (1) 10 s measurement without magnetic field, and (2) 10 s measurement with the application of the magnetic field. This procedure was necessary for the elimination of non-constant friction forces in the rheometer and viscous forces. Those phenomena can significantly complicate the subsequent evaluation of response time. The experiments were conducted 5 times under the same conditions. The data was not filtered but averaged from raw data. Then, the ramp data was normalized. All measurements were performed at 25 °C ± 1 °C.

Methodology evaluation of response time. The measured response time of the magnetic field (electric current) achieved a value of $\tau_{63} = 0.21$ ms and $\tau_{90} = 0.33$ ms, see Fig. 4. In several cases of the transient behaviour of MR actuators, this time can be expected as a step change. In our case, we cannot make this simplification because the expected response time of MR fluid from published models¹⁴ is in the same time scale (roughly 1.5 ms). Therefore, it was necessary to determine the transfer function between the measured magnetic field and shear stress in MR fluid. We used a process model for describing the MR fluid transient response. The process

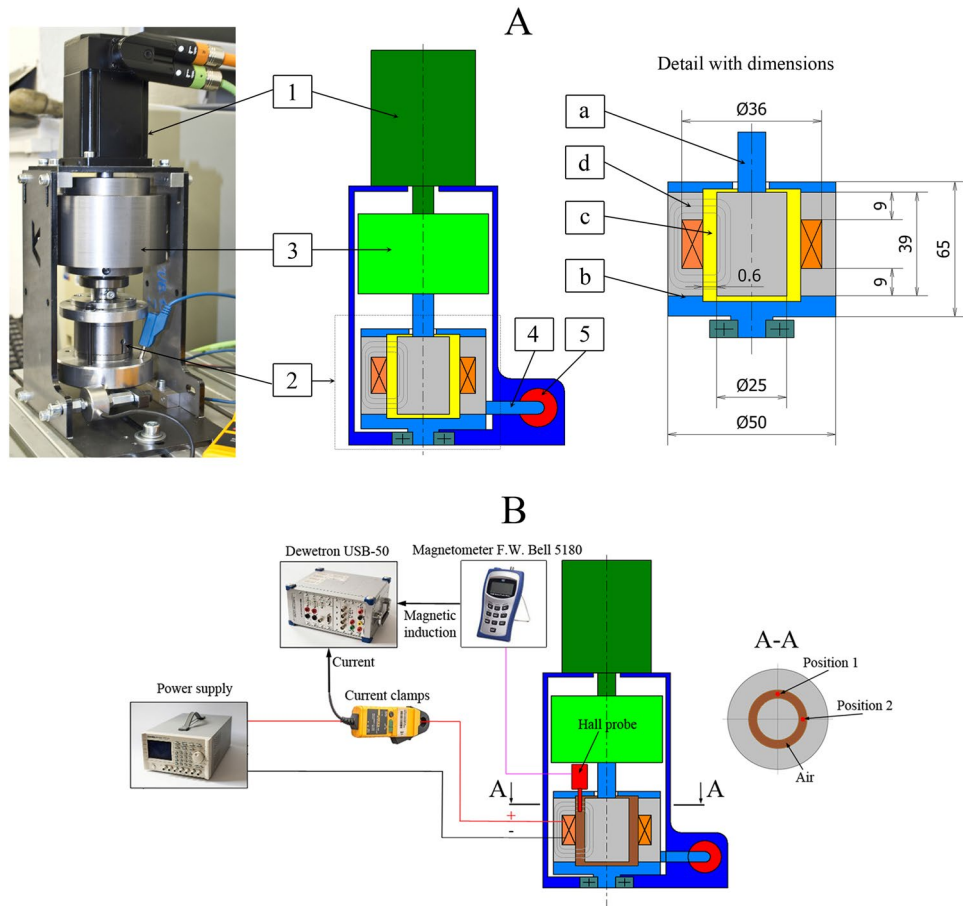


Figure 2. (A) Rheometer design with important dimensions (grey, soft magnetic composite material; orange, copper; light blue, aluminium; yellow, MR fluid sample, green, steel) and (B) magnetic flux density measurement in the gap.

	MRF-132DG	MRHCCS4-A	MRHCCS4-B	MRC-C1L
Solid content by weight (%)	80.98	70	80	80
MR fluid viscosity at 40 °C (Pa s)	0.114	0.167	0.237	0.108
Carrier fluid viscosity at 40 °C/25 °C (Pa s)	0.011/0.018	0.03/0.051	0.03/0.051	0.008/0.011
Average particle size (µm)	Spherical 2.1	Spherical 1.8	Spherical 1.8	Spherical 1–5

Table 1. MR fluid samples.

model is popular for describing system dynamics in many industrial applications²⁹. We used the so-called simple SISO (Single Input, Single Output) process model which is described by this transfer function:

$$sys = \frac{K_p}{1 + T_p s} e^{-T_d s} \tag{2}$$

where K_p is the proportional gain, T_p is the time constant, and T_d is dead time. A similar approach was used in study²⁶. The Matlab System identification toolbox was used for the identification of constants. The length of the evaluated section was 20 ms.

Magnetorheological fluid samples. The commercial MR fluid MRF-132DG supplied by Lord Corp., MR fluid MRHCCS4-A and MRHCCS4-B supplied by Liquids Research, and MRC-C1L supplied by CK Materials were chosen as the samples, see Table 1. These fluids were chosen because they have a similar particle size and a different viscosity of the carrier fluid.

The viscosity listed in the table was measured by the Haake Rotovisco 1 rheometer, and determined as a slope between 400 and 800 s^{-1} . It should be noted that carrier fluid of MR fluids exhibits Newtonian behaviour but MR

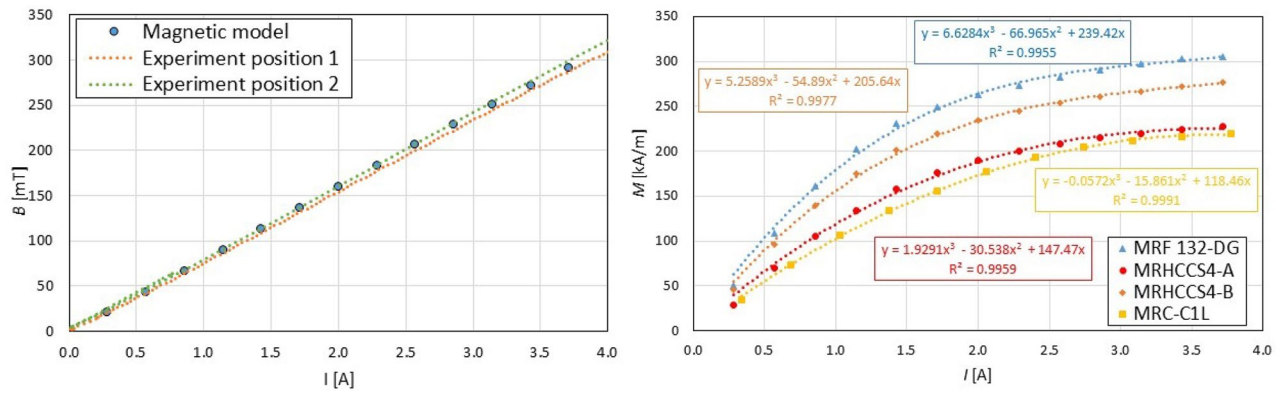


Figure 3. The results from the magnetic model and experiment for air gap (left), The calculated magnetization M dependency of electric current I on the coil for different MR fluids (right).

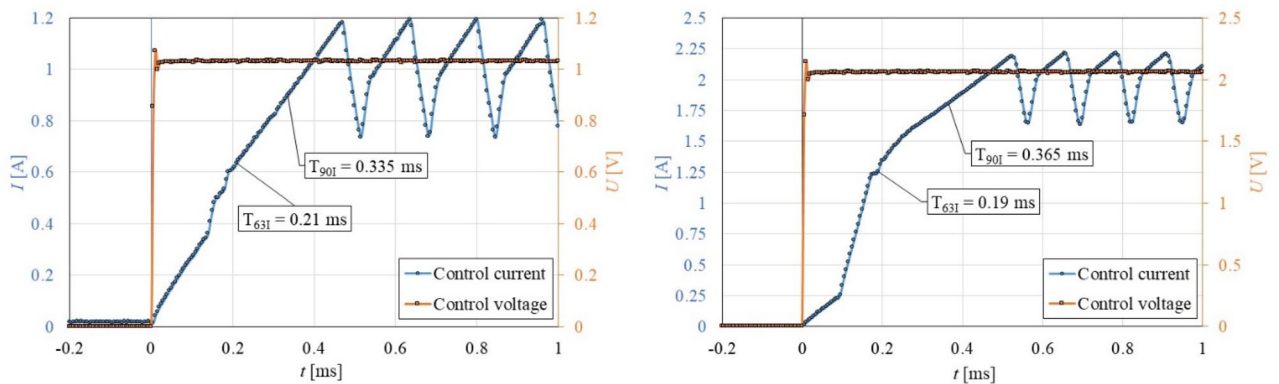


Figure 4. The course of the electric current I in the time t for the final value of electric current 1 A (left) and 2 A (right).

fluids are in general non-Newtonian. The particle sizes were measured by a scanning electron microscope, FEG SEM ZEISS Ultra Plus, and analysed by script using tools for picture analysis in Matlab. However, the information about particle size of MRC-C1L was taken from study³⁰.

Magnetic model and experimental validation settings. The data from the magnetic model are necessary for the generalization of measured response time data. The magnetic model was created in Ansys Electronics Desktop 19.2. The geometry of the magnetic circuit was simplified. The magnetization curve of the magnetic circuit material (SMC material) was extracted from the datasheet of the supplier. The electromagnetic coil (70 turns) carrier was made of plastic with relative permeability 1. The lids were made of aluminium also with a relative permeability of 1. The magnetization curve of MR fluid was taken from a MR fluid supplier datasheet. This model was necessary for the calculation of MR fluid magnetization M , which is an important input for the calculation of Mason number M_n . The Mason number M_n is the ratio of magnetic forces to viscous forces and is usually used for the description of MR fluid's behaviour at the microscopic level³¹. The magnetometer F.W. Bell 5180 with an ultrathin transverse probe (STB1X-0201) was used for magnetic measurement. The Fluke i30 current clamps were used for electric current measurement. These two signals are recorded and conditioned with a sampling frequency of 100 Hz by a front-end Dewetron USB-50-USB2-8 connected to the laptop, see Fig. 2B.

Results and discussion

Magnetic model validation. The comparison of results of magnetic flux density B over the electric current from the magnetic model and experiment with air in the gap can be seen in Fig. 3, left. Magnetic flux density measurements in the gap were performed for two positions that are perpendicular, see Fig. 2B. The agreement between model and experiment is acceptable. This experimentally verified model was used for the calculation of magnetization M in the gap with MR fluid. The results can be seen in Fig. 3 right. This data is necessary for the calculation of Mason number M_n .

Control electric current signal. First of all, it was necessary to precisely describe the excitation of MR fluid. It can be assumed that the course of magnetic flux density in the MR fluid copies the course of an electric current due to the elimination of eddy current in the magnetic circuit. This is ensured by a special design of the rheometer. The course of the electric current I in time t can be seen in Fig. 4 for two levels of electric current

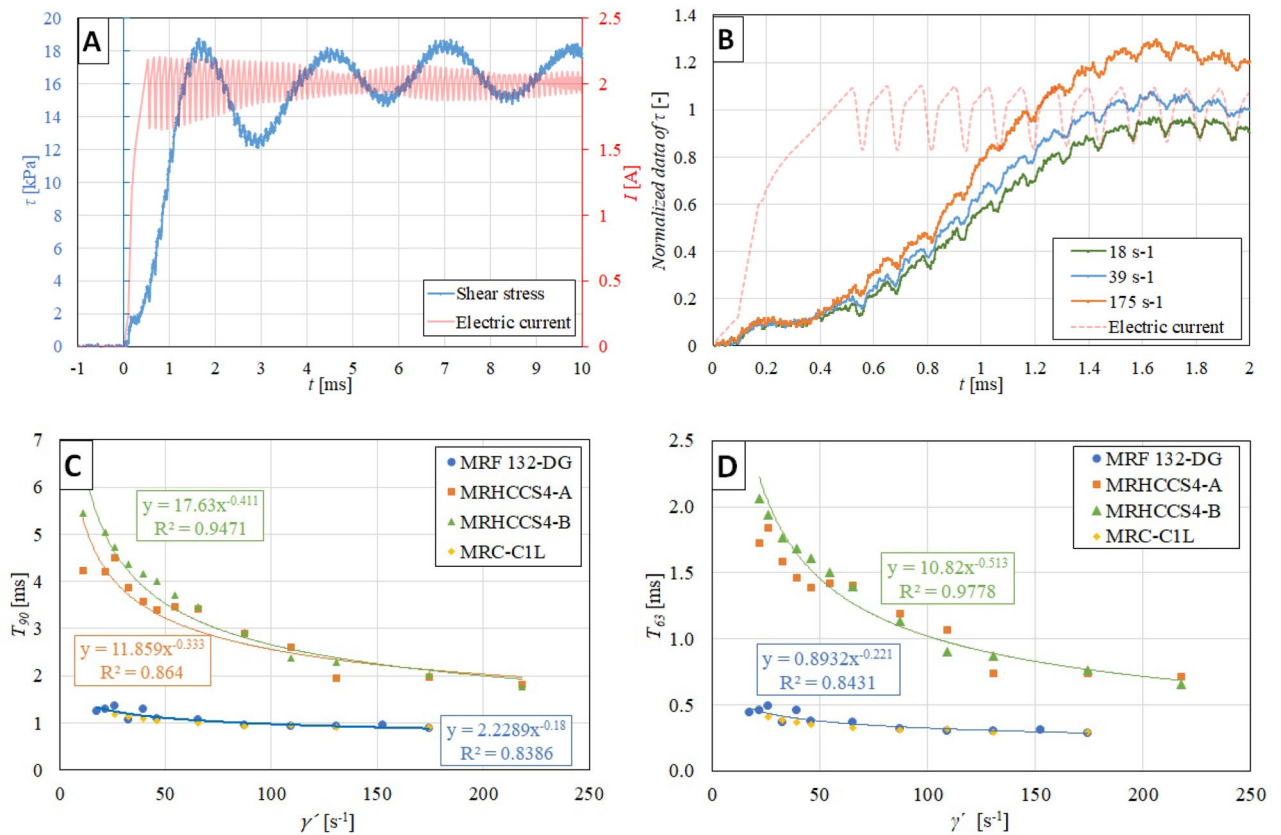


Figure 5. (A) The selected shear stress and electric current course over time for shear rate 39 s^{-1} and MRF 132-DG, (B) the effect of shear rate on the normalized course of shear stress in MRF 132-DG; The effect of shear rate on response time 90% (C), 63% (D) for different MR fluids at the same electric current excitation of 2 A.

I. A fast rise in the electric current *I* is achieved by connecting a higher voltage than results from the Ohm law (over-voltage method). When the required electric current value is achieved, the current controller starts to regulate at a frequency of 8 kHz. Therefore, the electric current exhibits oscillations in time *t* after 0.5 ms. Next, reducing the electric current response time was not possible due to the available current controller (maximum 100 V) and rheometer design (coil inductance). The response time (90%) of the electric current achieved a value of $T_{90I} = 0.335 \text{ ms}$ for electric current 1 A and a value of $T_{90I} = 0.365 \text{ ms}$ for electric current 2 A, see Fig. 4.

The selected courses of MR fluid shear stress in time. The Fig. 5A show the course of shear stress τ and electric current *I* over time *t*. The course of shear stress τ exhibits oscillations with a constant frequency of 360 Hz, which is connected with the natural frequency of some part of the rheometer. This hypothesis was verified by measurements using an accelerometer and evaluation based on FFT (Fast Fourier transform). The measured frequency was $337 \text{ Hz} \pm 4.88 \text{ Hz}$. The right of Fig. 5B the effect of shear rate $\dot{\gamma}$ on the course of shear stress τ . With the increase of shear rates $\dot{\gamma}$, the response time decreases. An initial dead time of 0.4 ms can also be seen, which is independent of the shear rate level, see Fig. 5B. It should be noted that this phenomenon may be associated with an increase in the magnetic field. The previous study²⁶ measured a dead time of 0.5 ms for ER fluids and dead time of 0.6 ms for MR fluid⁷, which is consistent with our experiments. We assume that the measured dead time of 0.4 ms is related to the chaining of ferromagnetic particles (microstructure formation) in the MR fluid.

The effect of shear rate on the rheological response time. The response times shown in Fig. 5C were determined from the experimental data and evaluated according to a process model. The relationship between response time and shear rate $\dot{\gamma}$ is nonlinear. The measured data of response time can be fitted by a power-law function, see Fig. 5C. The higher the shear rate, the shorter the response time. The data were measured for the same electric current (2 A), but the magnetization of the fluid sample was different. The response time T_{90} ranges from 5.5 to 1.9 ms for shear rate $\dot{\gamma}$ from 11 to 218 s^{-1} (MRHCCS4-A and MRHCCS4-B). Within the measurement and evaluation error, it can be stated that both fluids are identical in terms of transient response. The effect of particle concentration is therefore nonsignificant. MRF 132-DG and MRC-C1L fluids exhibit a shorter response time T_{90} than LR fluids in the range from 1.4 to 0.8 ms. This is probably due to the lower viscosity of the carrier liquid, which is about 3 times lower. The Fig. 5D shows the response time T_{63} dependent on shear rate $\dot{\gamma}$. There can be seen the same trend as in the case of 90%. Koyanagi et al.²⁶ experimentally determined the response time τ_{90} for ER fluid as 0.95 ms (dead time + time constant) which is near to our results. Lee et al.³² measured

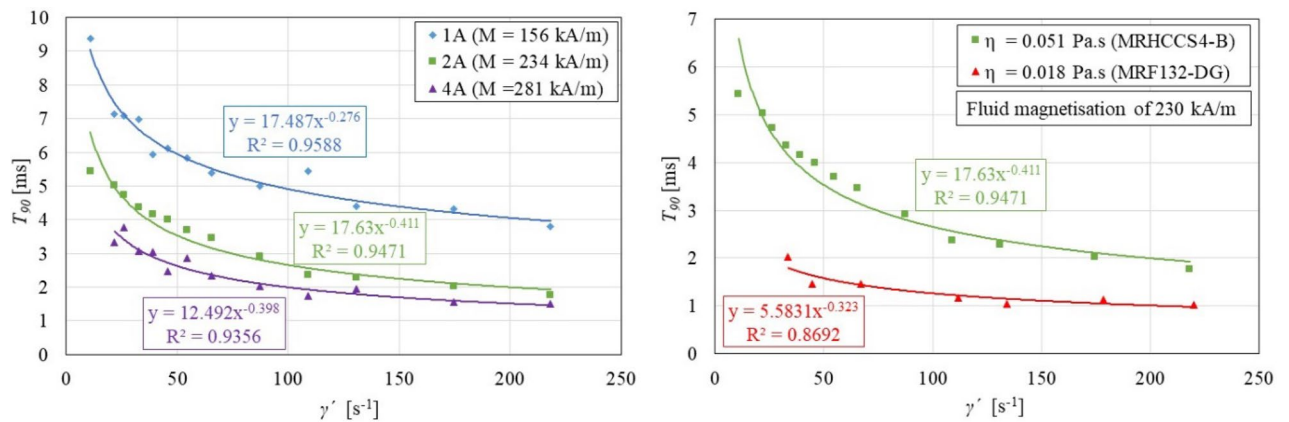


Figure 6. The effect of magnetization M (left) and carrier fluid viscosity η (right) on response time T_{90} .

response time τ_{63} as 5.1 ms and τ_{90} as 6.1 ms for ER fluid in shear mode (data estimated from the publication graph). These values are slightly higher than the presented data in this paper. Laun and Gabriel²⁴ measured the MR fluid response time based on sinusoidal excitation. The experiment determined the response time τ_{63} of MR fluid to 2.8 ms \pm 0.5 ms at a shear rate of 100 s⁻¹ at a magnetic flux density of 0.9 T. This measured value is about 3 times higher than the presented response time for Liquids Research fluids. However, it can be stated that the direct comparison of results is complicated because the measuring systems are not comparable. The studies^{24,26} used plate-plate configuration or study³² used rotating cylinder.

Effect of magnetization and carrier fluid viscosity on the rheological response time. The effect of fluid magnetization M on the response time T_{90} was demonstrated on MRHCCS4-B fluid because the effect of magnetization M was most noticeable. The fluid was measured at three levels of magnetization M , see Fig. 6, left. For all three levels of magnetization M , the dependence on the shear rate $\dot{\gamma}$ is exponential. It can be stated that the higher the magnetization M of the MR fluid, the lower the response time T_{90} . This is consistent with the theory.

The effect of carrier fluid viscosity η on response time T_{90} will be demonstrated on two selected MR fluids (MRF 132-DG and MRHCCS4-B). These fluids have similar particle concentrations and different carrier fluid viscosities η . The viscosity of the MRHCCS4-B carrier fluid is approximately 2.8 times higher than the carrier fluid of MRF 132-DG. The right of Fig. 6 shows that an MR fluid with a higher carrier fluid viscosity η shows a significantly higher response time T_{90} . It should be noted that the MR fluids had the same magnetizations M of 230 kA/m, but different electric current excitation (MRF 132-DG electric current of 1.5 A; MRHCCS4-B electric current of 2 A). The effect of additives of carrier fluid viscosity was not considered here.

Generalization of measured data. Sherman¹⁴ stated that MR fluid response time data in shear mode can be generalized using non-dimensional response time T^* and Mason number M_n . This study provided the equation for the calculation of non-dimensional response time as:

$$T^* = \frac{T_{90}}{\frac{144\eta}{M^2\mu_0}} \quad (3)$$

T_{90} is the rheological response time (90%), η is the viscosity of carrier fluid, M is MR fluid magnetization and μ_0 is vacuum permeability. The Mason number can be calculated as follow:

$$M_n = \frac{144\eta\dot{\gamma}}{M^2\mu_0} \quad (4)$$

where $\dot{\gamma}$ is shear rate. The Non-dimensional response time T^* and Mason number M_n were calculated from measured data, see Fig. 7. The master curve can be determined from measured data, see Fig. 7—red line. The results show a significant difference between the published model¹⁴ and our experiment for M_n values higher than 0.005. The T^* and M_n was also evaluated (estimated) from papers^{24,26}. This data is out of range of our measurement. However, it should be noted that the data obtained from the experiment are only from study²⁴. The difference in the results may be due to (1) the model simplification and (2) inaccuracies in the measurement and evaluation of the measured data. It has been hypothesized that the difference may be due to the deformation of the measuring device (rheometer), which is not included in the model. This would result in a significant increase in response time T_{90} at low shear rates $\dot{\gamma}$ compared to the model.

Figure 8 shows a comparison of the response time T_{90} course on shear rate $\dot{\gamma}$ from the Sherman model, proposed model (Fig. 7 red) and from the experiment for MRHCCS4-B. The carrier fluid viscosity η , magnetization M , shear rates $\dot{\gamma}$ are the same for experiments and also for the model. It can be seen that the response time T_{90} from experiments is significantly lower than that from the model. Thus, it can be stated that the possible deformation of the measuring device is not the source of the difference between the experiment and the model. The difference can be explained by certain simplifications of the model. However, both curves have an exponential

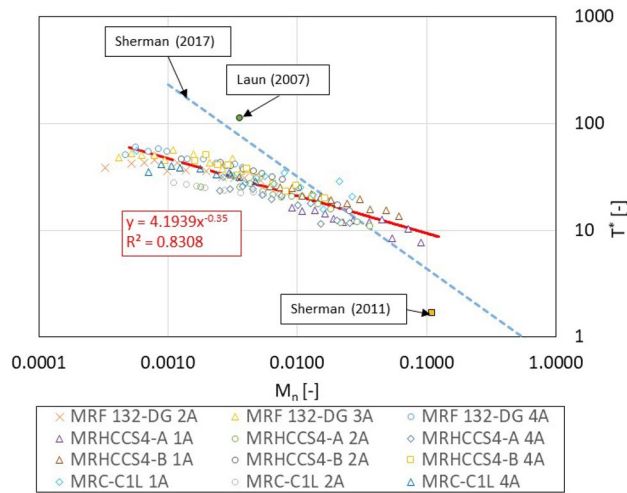


Figure 7. Dependency non-dimensional response time T^* on Mason number M_n ; Data from other publications have been estimated according to available information.

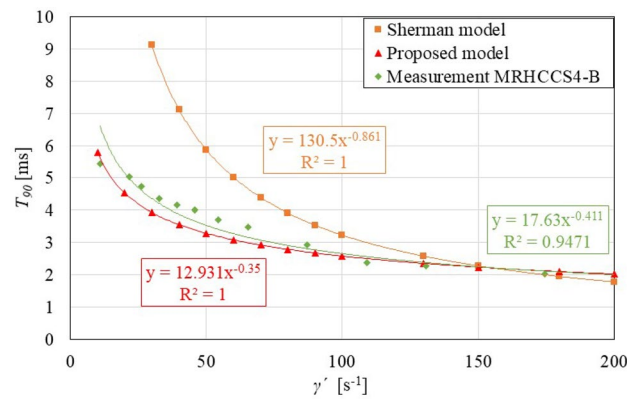


Figure 8. The comparison of model and experiment for the same inputs (MRHCCS4-B, electric current 2 A).

character and therefore the model describes trends very well. Another significant difference is that measured MR fluid contains additives that are not included in the model. The question is how significant a difference can create this simplification. The surface roughness can also affect MR fluid dynamics³³. This is also not included in the model, and can also play an important role.

Conclusion

This paper deals with the experimental determination of magnetorheological fluid transient response (rheological response time) on the rapid change of a magnetic field in shear load mode. A unique rheometer was presented that allows almost unit step of magnetic fields and also allows the measuring of the development of MR fluid shear stress over time. The transient response was determined on four MR fluids that differ in supplier, particle concentration, or carrier fluid viscosity. The paper also includes a magnetic model and its experimental verification. The most important conclusions of the paper are the following:

- The response time of the magnetic field is $T_{90I} = 0.335$ ms and slightly increases with an increasing maximum value of electric current.
- The rise of shear stress exhibits an initial dead time of 0.4 ms, which is independent of the shear rate level.
- The value of the shear rate significantly influences the rheological response time at low shear rates. The higher the shear rate, the shorter the response time. The measured data of the response time can be fitted by a power-law function. The response time T_{90} ranges from 5.5 to 1.9 ms for shear rate $\dot{\gamma}$ from 11 to 218 s^{-1} for MR fluid MRHCCS4-A and MRHCCS4-B.
- The fluid magnetization M significantly affects the rheological response time. The higher the magnetization M of the MR fluid, the lower the response time T_{90} .
- The carrier fluid viscosity also affects the rheological response time. The MR fluid with a higher carrier fluid viscosity η shows a significantly higher response time T_{90} .

- All measured data was generalized in the term of non-dimensional response time T^* and Mason number M_n . One master curve ($T^* = 4.1939M_n^{-0.35}$) can be determined from measured data independent of magnetization M , carrier fluid viscosity η , shear rates $\dot{\gamma}$, etc. This is an important conclusion because the master curve allows the determination of rheological time response for a given MR fluid and given load (shear rates).

It should be noted that the our experimentally determined master curve shows a deviation from the model¹⁴. MR fluids used in the experiment and model differ in the type or concentration of additives (the model does not include additives), which may also affect the transient response. For this reason, a plan for further research in this area is to determine the rheological response time for homemade MR fluid (full control of additives) and measurement for a higher range of Mason numbers. We also see the potential for future research in the area of a particle chaining model that allows the showing of particle motion during the step change of a magnetic field.

Data availability

The data presented in this study are available on request from the corresponding author.

Received: 29 April 2022; Accepted: 10 June 2022

Published online: 23 June 2022

References

- Zhang, Y. *et al.* Effect of base oil lubrication properties on magnetorheological fluids. *Smart Mater. Struct.* **30**, 095011 (2021).
- Roupec, J. *et al.* Influence of clay-based additive on sedimentation stability of magnetorheological fluid. *Smart Mater. Struct.* **30**, 027001 (2021).
- Gürgen, S., Li, W. & Kuşhan, M. C. The rheology of shear thickening fluids with various ceramic particle additives. *Mater. Des.* **104**, 312–319 (2016).
- Rosa, W. O., Vereda, F. & de Vicente, J. Tribological behavior of glycerol/water-based magnetorheological fluids in PMMA point contacts. *Front. Mater.* **6**, 32 (2019).
- Kumar, S., Sehgal, R., Wani, M. F. & Sharma, M. D. Stabilization and tribological properties of magnetorheological (MR) fluids: A review. *J. Magn. Magn. Mater.* **538**, 168295 (2021).
- Morillas, J. R. & de Vicente, J. Yielding behavior of model magnetorheological fluids. *Soft Matter* **15**, 3330–3342 (2019).
- Strecker, Z., Jeniš, F., Kubík, M., Macháček, O. & Choi, S.-B. Novel approaches to the design of an ultra-fast magnetorheological valve for semi-active control. *Materials (Basel)*. **14**, 2500 (2021).
- Zhang, H., Zou, Z., Choi, S.-B. & Yang, X. Active dispersing mechanism for settled magnetorheological fluid featuring with rotary blades and inductive coils in twin-tube damper. *Smart Mater. Struct.* **30**, 067001 (2021).
- Wang, H. & Bi, C. Study of a magnetorheological brake under compression-shear mode. *Smart Mater. Struct.* **29**, 017001 (2020).
- Kubík, M., Pavlíček, D., Macháček, O., Strecker, Z. & Roupec, J. A magnetorheological fluid shaft seal with low friction torque. *Smart Mater. Struct.* **28**, 047002 (2019).
- Hegger, C. & Maas, J. Smart sealing for magnetorheological fluid actuators. *J. Intell. Mater. Syst. Struct.* **30**, 689–700 (2019).
- Yoon, D.-S., Kim, G.-W. & Choi, S.-B. Response time of magnetorheological dampers to current inputs in a semi-active suspension system: Modeling, control and sensitivity analysis. *Mech. Syst. Signal Process.* **146**, 106999 (2021).
- Strecker, Z., Mazúrek, I., Roupec, J. & Klapka, M. Influence of MR damper response time on semiactive suspension control efficiency. *Meccanica* **50**, 1949–1959 (2015).
- Sherman, S. G. *Magnetorheological Fluid Dynamics for High Speed Energy Absorbers* (University of Maryland, College Park, 2017). <https://doi.org/10.13016/M21P2M>.
- Goldasz, J. & Sapiński, B. Insight into magnetorheological shock absorbers. *Insight Magnetorheol. Shock Absorbers* <https://doi.org/10.1007/978-3-319-13233-4> (2015).
- Goncalves, F. D. *Characterizing the Behavior of Magnetorheological Fluids at High Velocities and High Shear Rates* (Virginia Polytechnic Institute and State University, Blacksburg, 2005).
- Kubík, M. *et al.* Hydrodynamic response time of magnetorheological fluid in valve mode: model and experimental verification. *Smart Mater. Struct.* **30**, 125020 (2021).
- Choi, Y.-T. & Wereley, N. M. Assessment of time response characteristics of electrorheological and magnetorheological dampers. In: (ed. Inman, D. J.) *Proceedings of the Society of Photo-Optical Instrumentation Engineers, SPIE - The International Society for Optical Engineering*, 92–102 (Bellingham, WA, 2001). <https://doi.org/10.1117/12.432693>
- Gavin, H. P., Hanson, R. D. & Filisko, F. E. Electrorheological dampers, part i: Analysis and design. *J. Appl. Mech.* **63**, 669–675 (1996).
- Jolly, M. R., Bender, J. W. & Mathers, R. T. Indirect measurements of microstructure development in magnetorheological fluids. *Int. J. Mod. Phys. B* **13**, 2036–2043 (1999).
- Horváth, B., Decsi, P. & Szalai, I. Measurement of the response time of magnetorheological fluids and ferrofluids based on the magnetic susceptibility response. *J. Intell. Mater. Syst. Struct.* **33**, 918–927 (2022).
- Pei, L. *et al.* Simulations on the rheology of dry magneto-rheological fluid under various working modes. *Smart Mater. Struct.* **31**, 015031 (2022).
- Sherman, S. G., Paley, D. A. & Wereley, N. M. Massively parallel simulations of chain formation and restructuring dynamics in a magnetorheological fluid. In *ASME 2011 Conference on Smart Materials, Adaptive Structures and Intelligent Systems, Volume 1* 651–658 (ASME, 2011). <https://doi.org/10.1115/SMASIS2011-5188>
- Laun, H. M. & Gabriel, C. Measurement modes of the response time of a magneto-rheological fluid (MRF) for changing magnetic flux density. *Rheol. Acta* **46**, 665–676 (2007).
- Kikuchi, T., Noma, J., Akaiwa, S. & Ueshima, Y. Response time of magnetorheological fluid-based haptic device. *J. Intell. Mater. Syst. Struct.* **27**, 859–865 (2016).
- Koyanagi, K. & Terada, T. Time Response Model of ER Fluids for Precision Control of Motors. *J. Intell. Mater. Syst. Struct.* **21**, 1517–1522 (2010).
- Yoon, D.-S., Park, Y.-J. & Choi, S.-B. An eddy current effect on the response time of a magnetorheological damper: Analysis and experimental validation. *Mech. Syst. Signal Process.* **127**, 136–158 (2019).
- Guan, X., Guo, P. & Ou, J. Study of the response time of MR dampers. In: (eds. Leng, J., Asundi, A. K. & Ecke, W.) *Proceedings of SPIE - The International Society for Optical Engineering* 74930U (2009). <https://doi.org/10.1117/12.840217>
- The MathWorks, I. *Process Models*. <https://www.mathworks.com/help/ident/process-models.html>.
- Utami, D. *et al.* Material characterization of a magnetorheological fluid subjected to long-term operation in damper. *Materials (Basel)*. **11**, 2195 (2018).

31. Sherman, S. G., Becnel, A. C. & Wereley, N. M. Relating Mason number to Bingham number in magnetorheological fluids. *J. Magn. Mater.* **380**, 98–104 (2015).
32. Lee, H. G., Choi, S. B., Han, S. S., Kim, J. H. & Suh, M. S. Bingham and response characteristics of ER fluids in shear and flow modes. In *Electro-Rheological Fluids and Magneto-Rheological Suspensions* 523–530 (World Scientific, 2000). https://doi.org/10.1142/9789812793607_0059
33. Borin, D., Spörl, E. M., Zubarev, A. & Odenbach, S. Surface influence on the stationary shear deformation of a magnetorheological fluid. *Eur. Phys. J. Spec. Top.* <https://doi.org/10.1140/epjs/s11734-022-00527-4> (2022).

Acknowledgements

This paper and experiments have been made possible thanks to the Czech Science Foundation (GAČR) within the scope of the project No. 20-23261Y.

Author contributions

Conceptualization, Z.S., F.J., M.K.; methodology, M.K., J.V.; software, Z.S., M.K.; validation, Z.S., M.K.; formal analysis, F.J., I.M., J.Ž.; investigation, M.K., J.V.; writing—original draft preparation, M.K., D.B.; writing—review and editing, Z.S., D.B., J.Ž., I.M.; visualization, Z.S., F.J.; supervision, M.K., I.M.; project administration, M.K.

Competing interests

The authors declare no competing interests.

Additional information

Correspondence and requests for materials should be addressed to M.K.

Reprints and permissions information is available at www.nature.com/reprints.

Publisher's note Springer Nature remains neutral with regard to jurisdictional claims in published maps and institutional affiliations.



Open Access This article is licensed under a Creative Commons Attribution 4.0 International License, which permits use, sharing, adaptation, distribution and reproduction in any medium or format, as long as you give appropriate credit to the original author(s) and the source, provide a link to the Creative Commons licence, and indicate if changes were made. The images or other third party material in this article are included in the article's Creative Commons licence, unless indicated otherwise in a credit line to the material. If material is not included in the article's Creative Commons licence and your intended use is not permitted by statutory regulation or exceeds the permitted use, you will need to obtain permission directly from the copyright holder. To view a copy of this licence, visit <http://creativecommons.org/licenses/by/4.0/>.

© The Author(s) 2022

MAGNETORHEOLOGICAL FLUID DEVICES

Smart material systems or smart structures are systems that learn and adapt their behaviour in response to the external stimulation, which is provided by the environment in which it operates [82]. Those systems work on a feedback mechanism. From a technological point of view, the feedback system's function can be subdivided into (i) sensor, (ii) control, and (iii) actuator subsystems [83], see Figure 16. The main aim of the sensor system is to collect the required raw data needed for appropriate sensing and monitoring of the structure. The role of this control system is to manage and control the whole system by analyzing the data from sensors, reaching the appropriate conclusion, and determining the actions required. The main purpose of the actuators subsystem is to take action by triggering the controlling device.

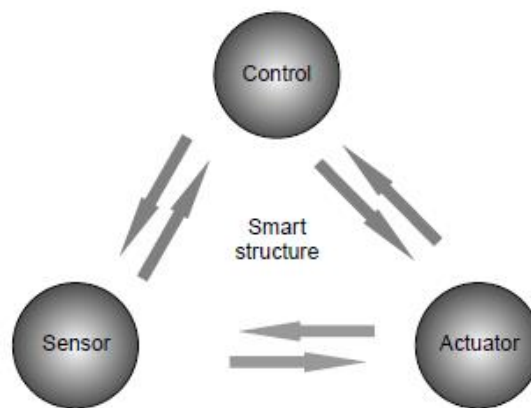


Figure 16 Feedback mechanism of the smart material system [83]

In the following chapters, the magnetorheological actuator subsystem as a part of the smart material system is described in more detail. State of the art is focused on static (quasi-static) and transient behaviour of this actuator/subsystem concerning the highlighted the author's contribution to this research field. This text does not contain the issue of control and sensor. However, it should be noted that these two subsystems also fundamentally affect the performance of the whole system.

3.1 Magnetorheological devices

Magnetorheological devices take advantage of the unique properties of MR fluid. MR devices have been developed in various sizes, configurations, and load requirements to accommodate specific application needs. MR fluid-based devices are mainly based on four operational modes of MR fluid, including flow mode, shear mode, squeeze mode, and pinch mode, which provide different benefits in various practical applications. Several devices utilize more than one operating mode and are mix-mode devices. A significant development (analysis of publications from 2021) in the field of MR devices is in engineering and medical application. The predominant applications are in dampers, clutches/brakes, or seals. However, the dominant development is in the field of dampers. In the following section, state of the art in MR dampers and seals are described in more detail.

3.1.1 Magnetorheological dampers

The MR dampers are energy-dissipating devices. Those dampers are filled with MR fluid which is controlled by a magnetic field, usually using an electromagnetic coil. The MR fluid changes apparent viscosity in the gap, which affects the hydraulic gap resistance. This allows continuously controlled damping by varying the power of the electromagnetic coil. The apparent viscosity increase as an electromagnet power increase. The main advantages of MR dampers are mechanical simplicity, low power demands, high dynamic force range, noiseless work, and great transient behaviour [6]. The MR valve does not contain the mechanical moving part (shim valve, etc.), which is also a significant advantage. The MR damper design can be categorized according to three aspects: (i) hydraulic housing, (ii) piston structure, and (iii) operating mode.

As regards of operating modes of MR dampers are divided into four categories: (a) flow mode dampers, (b) shear mode dampers, (c) squeeze mode dampers, and (d) pinch mode dampers, see Figure 17. Pinch mode dampers are quite new, and just several papers exist [84–86]. The squeeze mode dampers are suitable for damping of small amplitude in dimensions of several millimetres and achieve high damping force compared to the flow of shear mode dampers. Many different squeeze damper designs or approaches for modeling have been published [87–89]. MR rotary dampers mainly work in shear mode [90, 91]. These dampers are structurally very similar to clutches or brakes. Linear dampers operating in this mode can also be found in the papers. However, in general, these dampers achieve significantly lower damping forces than dampers operating in flow mode at the same dimensions. The advantage is that they do not need a high-pressure expansion chamber. However, the most common is the design of the MR damper working in flow mode.

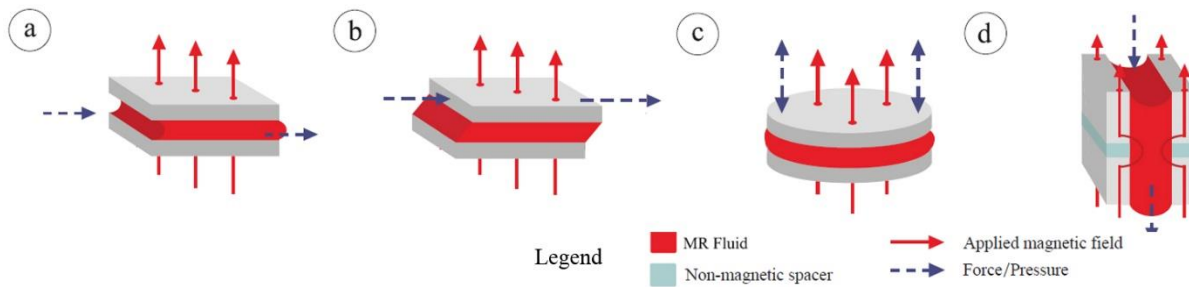


Figure 17 Operating mode of MR fluid [92]

The hydraulic housing of the damper is a mono-tube or twin-tube device. Mono-tube dampers are the most commonly used devices that utilize the MR fluid, see Figure 18. The main advantage is mechanical simplicity. In most cases, it is a gas-charged MR damper (accumulator), where high pressure is necessary. High pressure is necessary for cavitation-free operation. The damper contains a piston, MR fluid, bearing and sealing of piston rod, and hydraulic cylinder, see Figure 18. The possible modification can be an MR damper in a twin-rod configuration, where high gas pressure is not necessary (just a small compensation volume to account for fluid expansion with temperature).

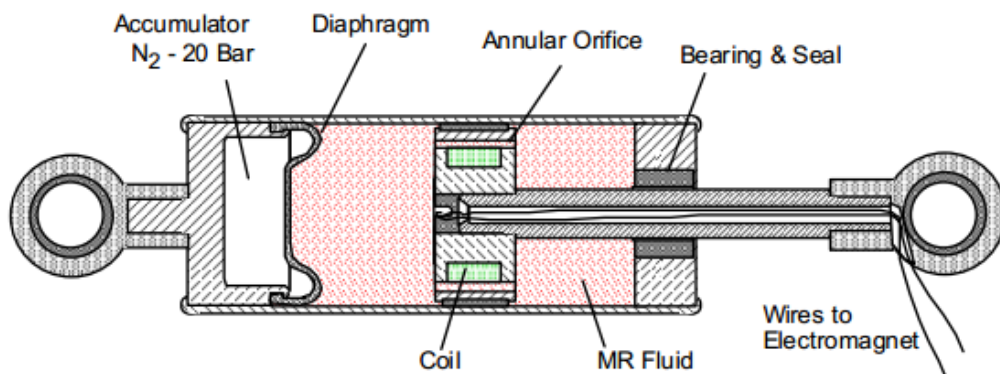


Figure 18 Mono-tube magnetorheological damper [43]

The double-tube configuration is typical for hydraulic oil dampers. Compared to mono-tube configuration, double-tube configuration features concentric hydraulic cylinders. Usually, the inner cylinder contains a piston valve and foot valve. The damper work with low gas pressure. The publications or patents of magnetorheological double-tube damper designs are rare [93–96]. These designs usually work with two MR valves, or it is necessary to use a minimum one foot/ check valve.

The MR damper piston (control valve) is composed of an electromagnetic coil or coils (2), a magnetic circuit (1), and one or more annular gaps (3), see Figure 19. The control valve modified the damping forces of the damper. The MR control valve can be categorized in terms of the number of arrangements of the flow path, coil arrangement, etc. [97]. The most common categorization is according to the number of coils as single-coil [6, 98] and multi-coil structure (Figure 19) [99, 100].

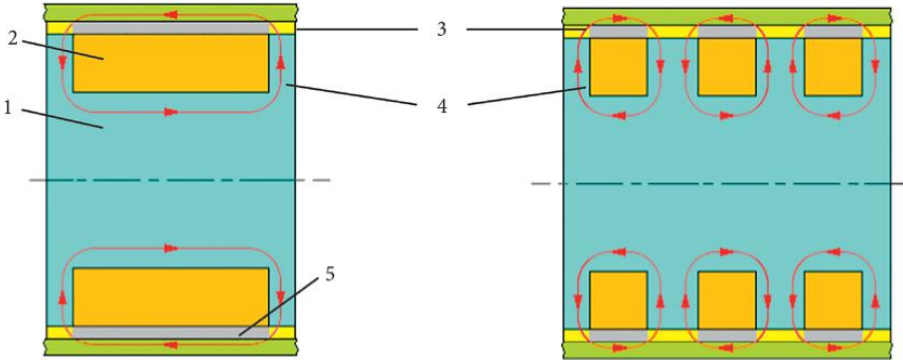


Figure 19 Single-coil structure (left); three-coil structure (right): 1, magnetic circuit; 2, electromagnetic coil; 3, annular gap; 4, magnetic flux lines; 5, non-magnetic section [97]

The single-coil structure is commonly used due to its simplicity. However, the two- or three-coil structure is becoming more common due to the improvement of dynamic force range and transient behaviour (response time) [97]. Another possible grouping is according to the arrangement of path flow. The number of parallel flow (one or multi parallel flow) [101], geometry (tapered) [102], or a change in the flow direction (meandering flow path valve) [103] can be found in papers. In the current state of the art, it can be quite often found a dual-gap variant (two parallel flows) that significantly improves the dynamic force range or MR valve with a meandering flow path which allows for designing an MR damper with a small-sized valve.

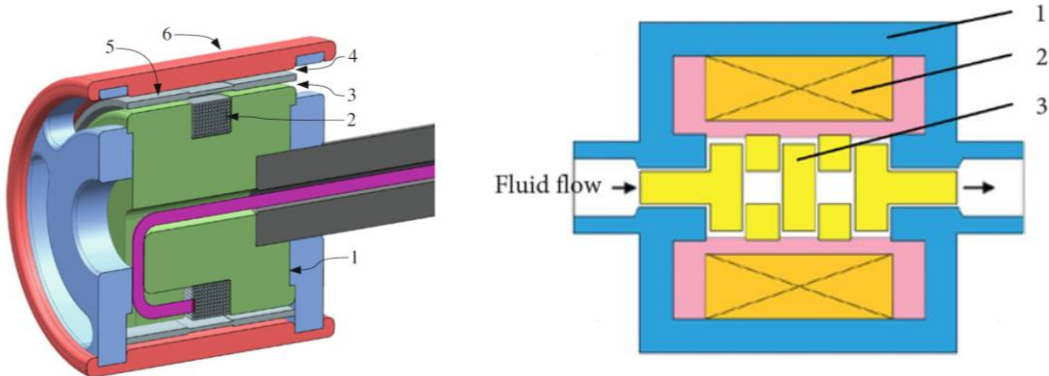


Figure 20 Dual-gap piston structure (left)[6]: 1, core coil; 2, electromagnetic coil; 3, gap 1; 4, gap 2;5, non-magnetic spacer; 6, sleeve; meandering valve (right) [97]:1, magnetic circuit; 2, electromagnetic coil; 3, meandering path

A significant problem of the MR damper is its poor fail-safe behavior. In the case of power supply is interrupted, the damper will stay at the minimum damping level. This limits the use of MR dampers in aerospace or railway. A suitable solution is to use a permanent magnet in the MR damper magnetic circuit. The permanent magnet creates a magnetic flux in the magnetic circuit, which ensures damping

during a power supply failure (fail-safe state). The damping level with no electric current and with a permanent magnet usually achieved one-third of the maximum damping force. Several different designs of MR dampers with permanent magnets were published [104–106].

3.1.2 Magnetorheological fluid seal

The magnetic fluid seal has been commonly used in industry since the 1970s. The conventional design of a seal with magnetic fluid contains a source of electromotive force, two ferromagnetic pole pieces, magnetic fluid, and a sealed shaft, see Figure 21. The magnetic fluid is usually used as Ferro fluid (FF).

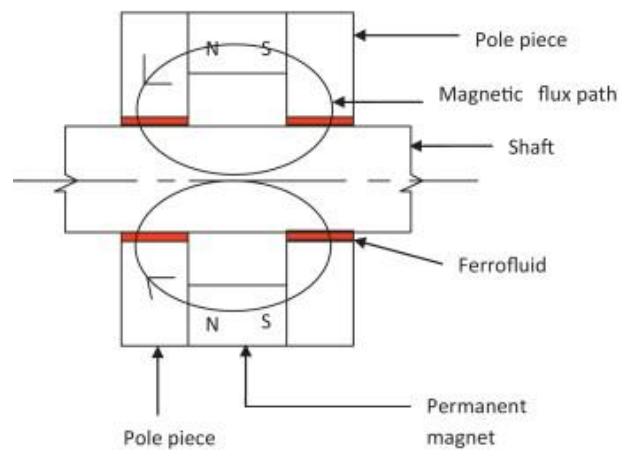


Figure 21 Conventional design of seal with magnetic fluid [107]

A FF is composed of nanoparticles and a carrier fluid. A FF seal (FFs) is characterized by a small friction torque and a high level of tightness. However, the disadvantage of FFs is the relatively low burst pressure. In recent years, several designs of magnetic fluid seal which uses MR fluid instead of FF appears [108–111]. The main advantage of MR fluid is better magnetic properties (higher magnetization) than FF, which leads to an increase in bursts pressure. The typical static burst pressure of MR fluid seal is in the hundreds of kPa. Kordonski et al. [110] published a one-step magnetorheological fluid seal and experimentally determined burst pressure and friction torque. MRFs exhibit higher burst pressure and higher friction torque than FFs. Urreta et al. [109] confirm the measurement of Kordonski et al. [110].

3.2 Transient response of magnetorheological damper

Magnetorheological dampers are often used in semi-actively controlled suspension systems. It turns out that the transient response of the controlled damping element is crucial for the performance of these systems. Yoon et al. [112] identified that the shorter the response time (better transient response) of the MR damper is, the better the vibration control of the car wheel can be achieved. They demonstrated this effect on the full car suspension model (7 DOF). Oh et al. [113] also tested the effect of MR damper response time on the comfort and driving performance of the car. They stated by the model that the shorter the response time, the better driving performance and comfort. Similar conclusions were published by Strecker et al. [114] or Macháček et al. [115].

The simplest dynamic system (transient response), which can serve as an approximation of the dynamic behaviour of the MR damper, is a first-order system, see Figure 22. The response is expressed by the time constant τ_{63} (primary response time), which determines the time when 63.2 % of the maximal controlled value is achieved. However, the response time of the MR damper is also presented as 90 % [116] or 95 % [117] of the steady-state force at a given piston velocity.

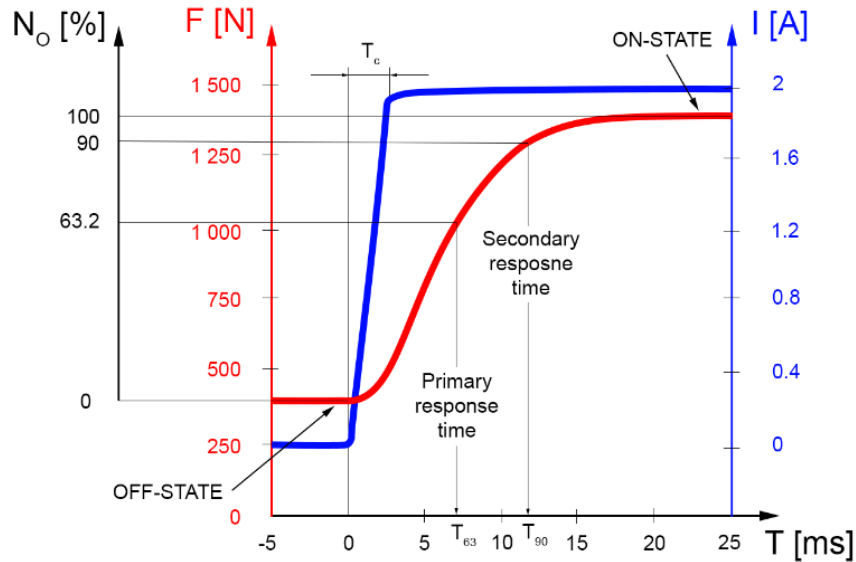


Figure 22 Response time definition

Koo et al. [118] measured the transient response of the LORD automotive MR damper. The response time of the MR damper was identified in the range of 15 – 55 ms. Guan et al. [119] measured the response time of MR damper in the range of 160 - 240 ms. Zhang et al. [120] measured MR damper response time in the range of 34.6 to 75.4 ms. The force rise was significantly faster than the force drop. They concluded that the higher the piston velocity, the higher the response time is. Takesue et al. [121, 122] published the design of the MR actuator (clutch) with a response time of 5 ms. This short response was achieved by a suitable design of a magnetic circuit based on transient magnetic simulation. Giorgetti et al. [123] developed an MR actuator (clutch) with a response time of 17 ms. The measured response time was not affected by excitation velocity. They stated that the measured time delay is a combination of power supply dynamics, magnetic circuit dynamics, fluid rheology effect, and fluid compressibility. Occhiuzzi et al. [124] tested MR damper with a response time of 10 ms. Goncalves et al. [125] measured the response time for rebound activation as 15.4 ms and rebound deactivation as 13.9 ms. Similar results also have Vivas-Lopez et al. [126] or Huang et al. [127]. It can be stated that many authors measured the response time of MR dampers and the response time differed significantly.

It can be identified *four main sources of the time lag* between damping force and control signal (response time) as (i) response time of MR fluid itself, (ii) inductance of MR damper electromagnetic coil, (iii) creation of eddy current in the magnetic circuit, and (iv) compressibility of fluid and hydraulic system. The response time of MR fluid was discussed in detail in chapter 2.3.

3.2.1 The inductance of an electromagnetic coil

The electromagnetic coil inductance creates a time delay between voltage and electric current. From the electrical point of view, the MR damper can be simplified as inductance L connected in series with resistance R . The course of electric current $i(t)$ after switching on can be expressed by the equation:

$$i(t) = \frac{U}{R} \left(1 - e^{-\frac{Rt}{L}} \right) \quad (6)$$

Where U is voltage, R is the resistance of the coil, L is inductance, t is time. The time constant is the ratio of inductance L and resistance R . This response time is significant and ranges from units to hundreds of milliseconds depending on the size of the damper (electromagnetic coil) [128]. Yang et al. [129] presented a current controller which works with the over-voltage method. The controller keeps higher voltage inputs than corresponding to Ohms law until the desired current is achieved. Using this method, Yang et al. [129] reduced the response time of the MR damper from 300 ms to 60 ms. A similar method was published by Strecker et al. [130] or Friedman et al. [131]. Zheng et al. [132] developed

current controller based on pulse width modulation (PWM) current drive technology. Goldasz et al. [6] presented lumped parameter model of the LR circuit, which was connected to the hydraulic domain and determined the transient response of electric current and damping force.

3.2.2 Eddy current in the magnetic circuit

Mass and Guth [133] found out time lag between the course of electric current and the course of damping force. They explained this lag as a result of eddy current induced in the magnetic circuit. Similar conclusions were published by Guan et al. [119], Zheng et al. [132], Farjoud et al. [134], and Takesue et al. [121, 122]. Guan et al. [119] stated that the reducing of the eddy current is the key to developed MR damper with a short response time. The main idea is the following. When the magnetic flux changes rapidly, an electromotive force is generated in the magnetic circuit according to Faraday's law (1):

$$\varepsilon = -N \frac{d\Phi}{dt} \quad (7)$$

Where ε is the electromotive force, t is time, N is the number of turns of the coil, Φ is the magnetic flux. From Ohm's law, the magnitude of eddy currents can be determined as follows:

$$\varepsilon = R_{circuit} \cdot I_{eddy} \quad (8)$$

Where $R_{circuit}$ is the electrical resistance of magnetic circuit material in the direction of eddy currents flow and I_{eddy} is the magnitude of the eddy currents. By increasing $R_{circuit}$ is possible to reduce the magnitude of I_{eddy} with the same change in magnetic flux. Therefore, the problem of eddy currents can be solved by two approaches: (i) by suitable material selection and (ii) by suitable shape.

The material selection for the magnetic circuit is a trade-off between the static and transient efficiency of the magnetic circuit. Materials like ferrites or soft material composites (SMC) generally have lower permeability or a lower magnetic saturation limit compared to pure iron. However, those materials have high electrical resistivity, thus preventing the creation of eddy currents. Other problems with these materials are their low mechanical strength, high cost, and poor machinability.

The second approach to preventing eddy currents is the shape approach. This approach is commonly used at low-frequency transformers using isolated sheets. The MR control valve with an isolated sheet was also published [6]. The magnetic circuit of the piston is similar to the magnetic circuit of the electric motor. The electromagnetic coil is wound around the outside of the core, see Figure 23. This design exhibits a short response time.

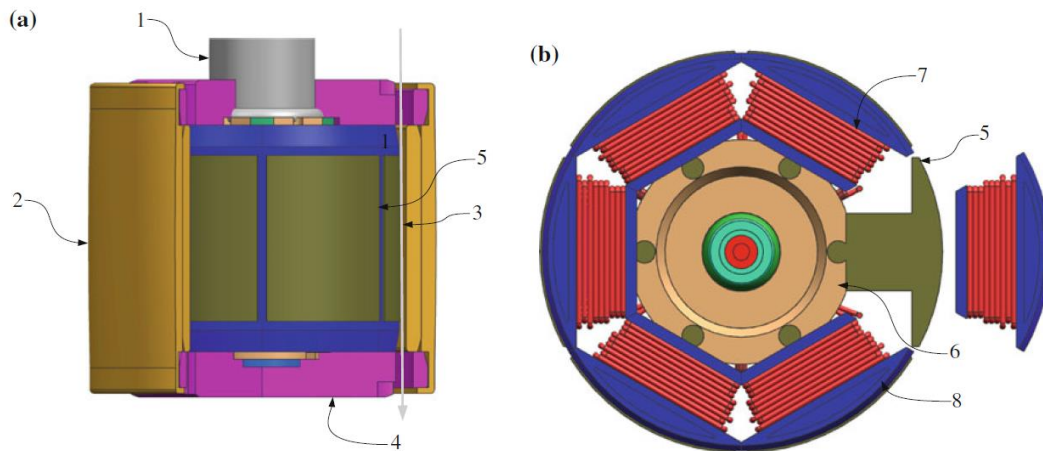


Figure 23 MR control valve with laminated magnetic circuit: 1, rod; 2, sleeve; 3, annulus gap; 4, lids; 5, magnetic poles; 6, coil core; 7, electromagnetic coil; 8, casing [6]

3.2.3 Compressibility of the damper system

Koo et al. [118] studied the effect of piston velocity on the response time. They determined that the response time decreases exponentially with increasing piston velocity. They conclude that the response time at low velocities is highly dependent on system compliance (stiffness). The compliance inputs to the system in different ways as fluid compressibility, accumulator compressibility, silent block, or load frame stiffness. The MR damper behaves as a spring in series with the damper, see Figure 24. The deformation of the MR actuator can be calculated as a ratio of force F and system stiffness K as follows [118]:

$$X = F / K \quad (9)$$

Therefore, the response time T can be calculated very simply as follow:

$$T = X / v \quad (10)$$

Where X is deformation and v piston velocity. Clearly, T becomes large as v becomes small. Giorgetti et al. [123] stated that compressibility of MR fluid is very important to the transient response of MR damper.

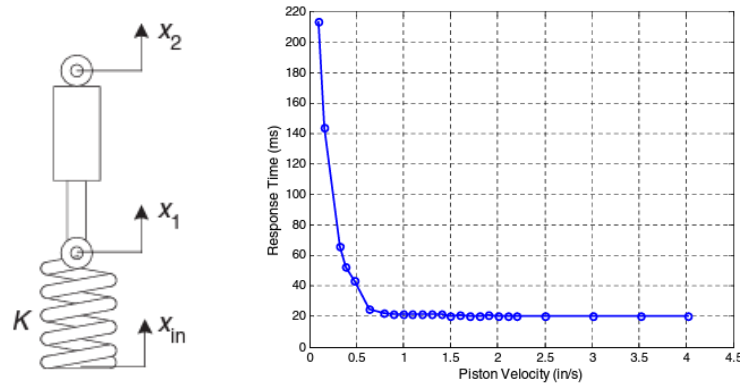


Figure 24 The effect of piston velocity on MR damper response time [118]

3.3 Knowledge gaps

In the current state of the art in the field of the transient response of MR dampers and MR fluid seals can be found several knowledge gaps.

(i) Transient response of MR damper: effect of permanent magnet

If the power supply of the MR damper electromagnetic coil is interrupted, the damper will stay at the minimum damping level. This is a significant problem for a wide range of MR damper applications (aerospace, rail, automotive, etc.). Many MR damper designs have been published that include a permanent magnet to ensure fail-safe behaviour [104–106]. These papers were focused on adjusting suitable damping. However, the *information about the permanent magnet effect on MR damper transient response is unknown*. Therefore, our study [135] deals with this knowledge gap.

(ii) Transient response of MR damper: eddy current effect

The transient behavior of the MR damper is degraded by the formation of eddy currents in the magnetic circuit. Several approaches how to improving MR damper transient response were published. However, each approach has significant limitations. *The information on how to design of MR damper which meets with a short response time, great dynamic force range, good*

mechanical properties, and low weight is unknown. In our paper [136], we decided to present this type of MR damper design.

(iii) Transient response of MR damper: fluid compressibility effect

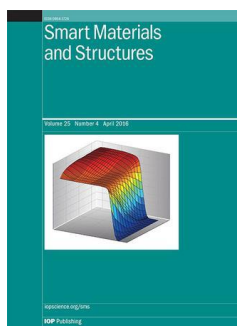
The transient response of the MR damper is probably also affected by the compressibility of the damper system [118] and the MR fluid itself. *The effect of MR fluid compressibility and MR fluid volume is unknown.* It is relatively difficult to experimentally determine the effect of fluid compressibility on damper response time. Therefore, the multiphysics model, which includes magnetic, hydraulic a mechanical domains, will be necessary create to determine MR fluid compressibility effect. Therefore, our study [137] deals with this knowledge gap.

(iv) MR fluid shaft seal

The main advantage of MR fluid seal is higher burst pressure than FF fluid seal. However, the friction torque of the MR fluid seal is significantly higher than FF fluid seal. *The design of the MR fluid seal, which combines the high burst pressure and low friction torque, is unknown.* This type of design was published in our paper [138].

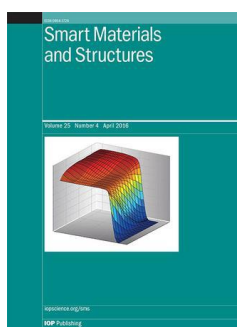
3.4 Author's contribution to the field

The author of the thesis published three papers focused on the research field of the transient response of MR damper and one paper on the research field of MR fluid seal. The *first study (i)* [135] deals with the transient response of the MR damper with a permanent magnet in the magnetic circuit. The *second paper (ii)* [136] is connected with the design of an MR damper with a short response time which is secured by a structured magnetic circuit made of 3D metal printing. The *third paper (iii)* [137] in this section deals with the multiphysics model of the MR damper. One important result is the effect of fluid compressibility on transient response. One publication **(iv)** also deals with the design of magnetorheological fluid seals with low friction torque [138]. The design is based on the pinch mode of MR fluid. All the papers were published in peer-reviewed WOS journals with IF. The list of the included papers is as follows:



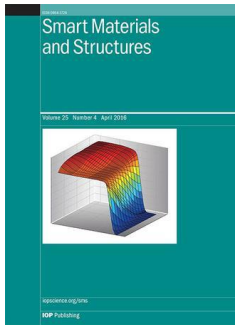
[135] JENIŠ, F, M KUBÍK, O MACHÁČEK, K ŠEBESTA a Z STRECKER. Insight into the response time of fail-safe magnetorheological damper. *Smart Materials and Structures*. **2020**, 30(1)

Author's contribution	= 45 %
Journal impact factor (IF ₂₀₂₀)	= 3.585
JIF Quartile	= Q1
Citations (WOS)	= 0 w/o self cit.



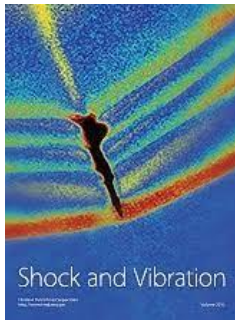
[136] STRECKER, Z, M KUBÍK, P VÍTEK, J ROUPEC, D PALOUŠEK and V ŠREIBR. Structured magnetic circuit for magnetorheological damper made by selective laser melting technology. *Smart Materials and Structures*. **2019**, 28(5)

Author's contribution	= 25 %
Journal impact factor (IF ₂₀₁₉)	= 3.613
JIF Quartile	= Q1
Citations (WOS)	= 5 w/o self cit.



[138] KUBÍK, M., D PAVLÍČEK, O MACHÁČEK, Z STRECKER and J ROUPEČ. A magnetorheological fluid shaft seal with low friction torque. *Smart Materials and Structures*. **2019**, 28(4)

Author's contribution = 50 %
 Journal impact factor (IF₂₀₁₉) = 3.613
 JIF Quartile = Q1
 Citations (WOS) = 17 w/o self cit.



[137] KUBÍK, M. and J. GOLDASZ. Multiphysics Model of an MR Damper including Magnetic Hysteresis. *Shock and Vibration*. **2019**, 2019, 1-20

Author's contribution (BUT) = 100 %
 Journal impact factor (IF₂₀₁₉) = 1.298
 JIF Quartile = Q3
 Citations (WOS) = 5 w/o self cit.

The author of the thesis is also significantly connected to applied research (projects) in this research field (Figure 25). The most important outputs of applied research are (i) the European Patent Office [139], where the main idea is based and a structured magnetic circuit made of 3D metal printing that improves magnetic circuit dynamics, and (ii) a functional sample [140] of a magnetorheological yaw damper with a short response time for the locomotive of Škoda Transportation, see figure below.

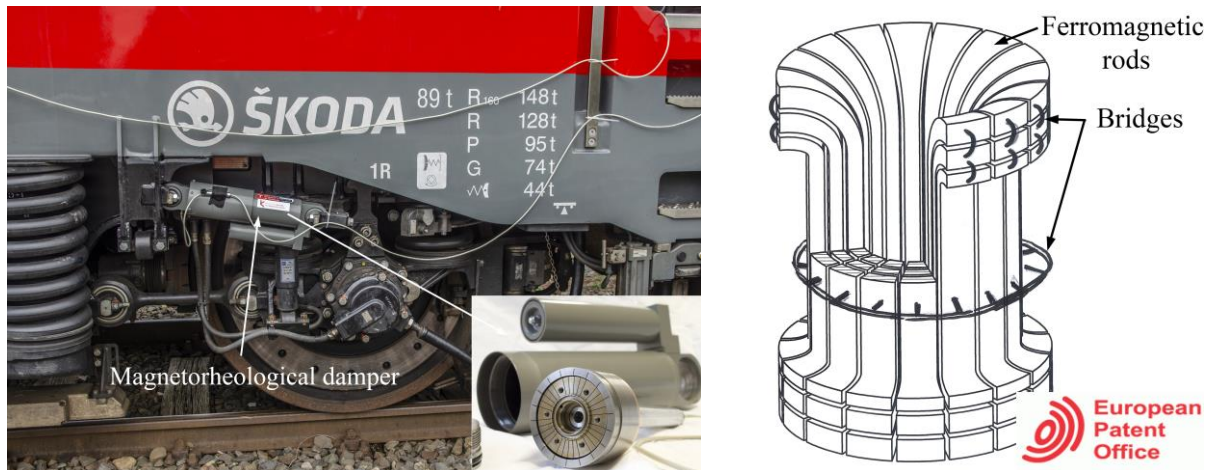


Figure 25 Developed MR damper with short response time mounted on locomotive Škoda Transportation during testing (left), the main idea of structured magnetic circuit patent (right)

A more detailed description of each publication can be found in the chapters below.

3.4.1 Insight into the response time of fail-safe magnetorheological damper [135]

The first paper is connected with the determination of the transient response of fail-safe MR damper. The significant problem of magnetorheological (MR) dampers is their poor fail-safe ability which can be solved by accommodating a permanent magnet to the magnetic circuit of the damper, see Figure 26. The effect of the permanent magnet on the transient response of the damper was unknown. The main

goal of this paper was to introduce the transient response of the MR damper with a permanent magnet. The damper design with the permanent magnet, transient magnetic simulation including magnetic hysteresis and eddy currents, and experimental evaluation were presented. The important result was that the permanent magnet significantly influences the MR damper transient response. The decrease of the damping force from a fail-safe state to off-state is significantly faster (2 ms, -1A) than the increase to on-state (12 ms, 1A), see Figure 27. The exact value depends on the electric current magnitude and piston velocity.

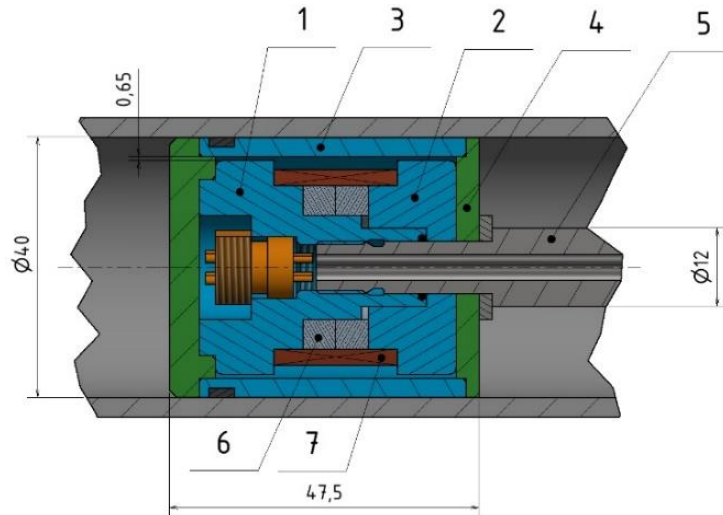


Figure 26 MR piston with permanent magnet; 1, 2, 3 magnetic circuits; 4, lids; 5, piston rod; 6, permanent magnets; 7, an electromagnetic coil [135]

Similar trends are for the electric current drop. Another important result is that this transient behaviour can be determined by transient magnetic simulation with relatively low error, see Figure 27.

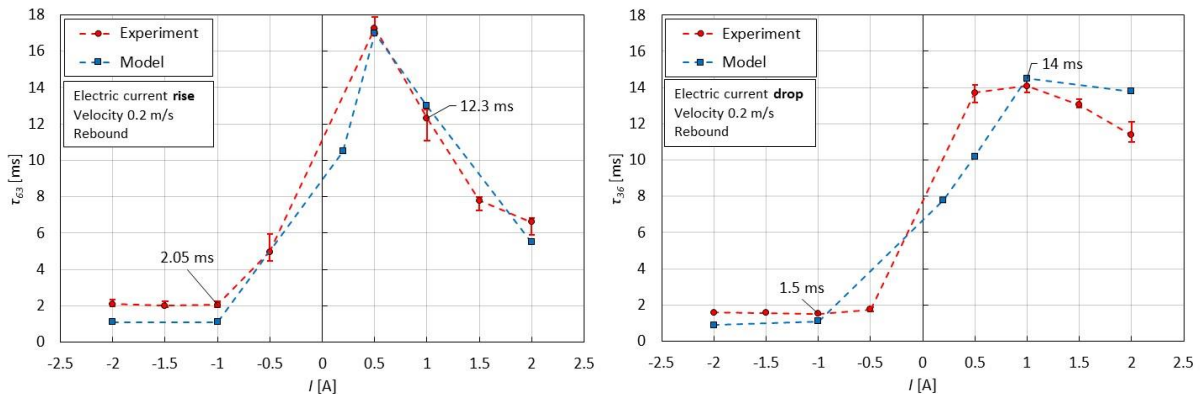


Figure 27 The course of primary response time (63 %) on orientation and magnitude of electric current for configuration with electric current step rise (left) and drop (right)

3.4.2 Structured magnetic circuit for magnetorheological damper made by selective laser melting technology [136]

This paper describes the shape approach for the elimination of eddy current in the magnetic circuit. The design and experimental evaluation of a structured core for an MR damper made of pure iron manufactured by 3D SLM print were presented, see Figure 28. The aim of the research was to create the MR damper with a short response time, great dynamic force range, good mechanical properties, and low weight. This is an experimental verification of our patented technology [139]. Based on the 3D transient magnetic simulation, the suitable geometry of the magnetic circuit was determined, see Figure 28.

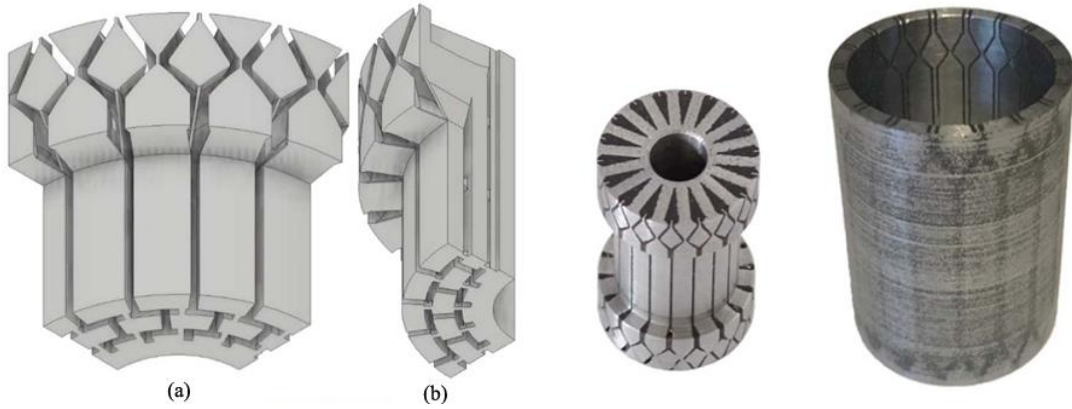


Figure 28 The structured core optimized for weight and homogenous magnetic flux density in the gap (left), manufactured structure by 3D metal printing method (right)

The results presented in the paper show that it is possible to design and manufacture magnetic circuits with a remarkable combination of low eddy-current losses (short response time), high magnetic flux (high dynamic force range), low weight, and good mechanical properties, see Figure 29.

Type of piston	Primary response time (ms)	Secondary response time (ms)	Magnetic flux density (T) (2 A, air in the gap)	Weight (g)	Dynamic force range (-)
Solid piston (11SMn30)	6.2	30.9	0.174	208	5.73
SMC piston	1.06	1.3	0.154	193	4.03
Grooved piston (11SMn30)	1.36	1.75	0.17	177	5.33
Structured piston (Fe)	1.32	1.68	0.18	156	5.12

Figure 29 Performance comparisons of MR pistons

3.4.3 Multiphysics Model of an MR Damper including Magnetic Hysteresis [137]

The paper deals with a hybrid multiphysics model of the magnetorheological damper. The electromagnetic domain is modeled using the vector hysteresis FE model (present in Ansys Maxwell) based on the extension of well-known Maxwell equations, and the hydraulic section is described through the dimensionless biplastic Bingham approach. We used lumped parameter model (in SimScape software), which was coupled with the transient FE model through the yield stress-flux density interface. The hydraulic and mechanical domains can be seen in Figure 30.

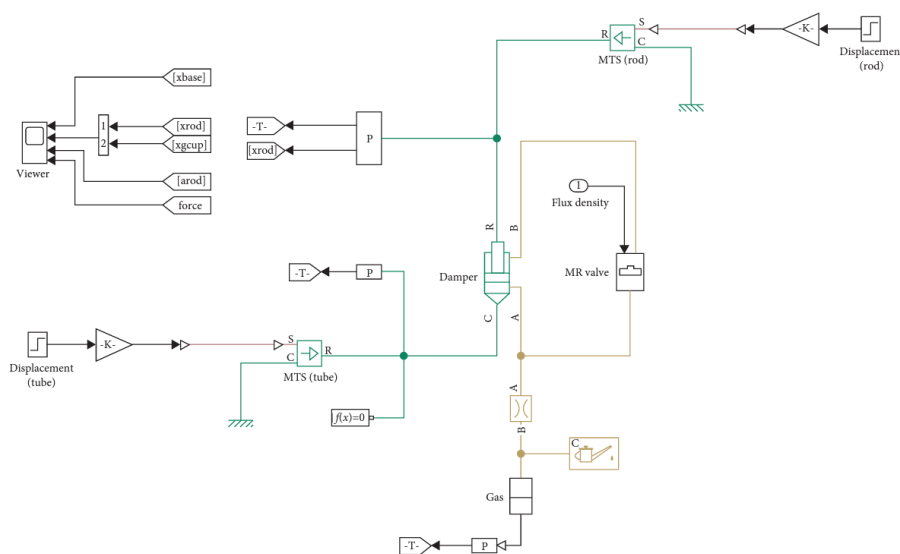


Figure 30 High-level Simscape model layout [137]

The effect of magnetic core electric conductivity, piston velocity, and MR fluid compressibility on the transient response (response time) of MR damper was also studied. As shown in Figure 31 left, as the conductivity decreases, the eddy currents are reduced, and the response of the damper becomes faster. The obtained results imply that the slower the piston velocity, the slower the magnitude of the force change rate generated (Figure 31, right).

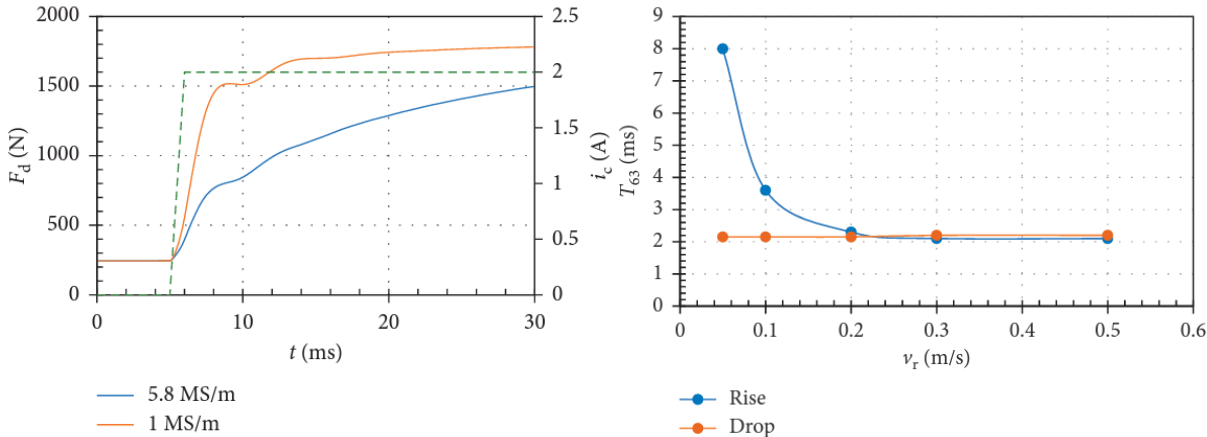


Figure 31 Effect of electric conductivity on the course of damping force (left); The effect of piston velocity of primary response time (right)[137]

3.4.4 A magnetorheological fluid shaft seal with low friction torque [138]

The last paper deals with the design and tests of a magnetorheological fluid seal using the innovative concept of the magnetic circuit, which allows the achievement of a promising trade-off between burst pressure and friction of the seal. The presented seal design is working in pinch mode of MR fluid, see Figure 32, left. A new experimental test rig and methodology measurement were developed and also presented in the paper, see Figure 32, right.

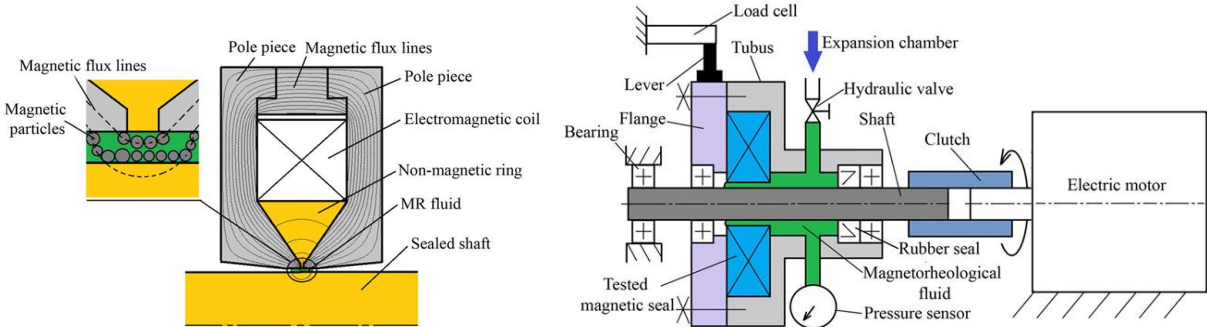


Figure 32 Function principle of a pinch magnetorheological fluid seal (left) and test rig (right)

The pinch MRFs exhibit lower friction torque than standard MRFs with one sealed zone, and static bursts pressure are comparable, see Figure 33. The burst pressure of the pinch seal significantly decreases with the increasing shaft rotation. The significant leakage of carrier fluid was observed during the measurement of standard MRFs with rotation by the same methodology. Therefore, it was not possible to determine burst pressure dependence on rotation in standard MRFs.

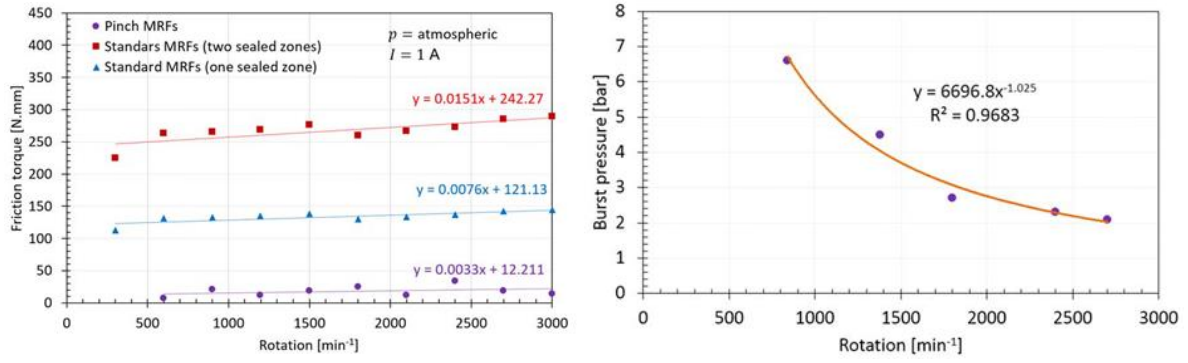


Figure 33 The effect of rotation on friction torque (left) and pinch seal burst pressure (right)

Technical Note

Insight into the response time of fail-safe magnetorheological damper

F Jeniš , M Kubík , O Macháček, K Šebesta and Z Strecker 

Brno University of Technology, Brno, Czech Republic

E-mail: filip.jenis@vutbr.cz

Received 30 June 2020, revised 23 September 2020

Accepted for publication 19 October 2020

Published 9 December 2020



CrossMark

Abstract

The significant problem of magnetorheological (MR) dampers is their poor fail-safe ability. In the case of power supply failure, the damper remains in a low damping state which is dangerous for several technical applications. This can be solved by accommodating a permanent magnet to the magnetic circuit of the damper. Currently, the MR dampers are used in progressive semiactive (S/A) control of suspension systems. The dynamics (force response time) of the damper is an important parameter that affects the performance of S/A control. The main goal of this paper is to introduce the dynamic behavior of MR damper with a permanent magnet. The damper design with the permanent magnet in the magnetic circuit, transient magnetic simulation including magnetic hysteresis and eddy currents, and experiments are presented. The magnetic field response time and MR damper force response time are measured and also determined from magnetic simulation. The permanent magnet significantly influences the MR damper dynamics. The decrease of the damping force from a fail-safe state—medium damping to off-state—low damping is significantly faster (2 ms, -1 A) than the increase to on-state—high damping (12 ms, 1 A). The exact value is depending on the electric current magnitude and piston velocity. The damper achieved fail-safe damping force approximately 1/3 of the maximum damping force. The exact value of the fail-safe force is magnetization history-dependent. The maximum dynamic force range is 8.5 which is comparable with the common design of MR damper.

Keywords: magnetorheological valve, MR damper, response time, permanent magnet, fail-safe, transient response, damper dynamics

(Some figures may appear in colour only in the online journal)

1. Introduction

The main aim of the car suspension system is to provide maximum ride comfort and handling stability. Three types of suspension systems, namely, passive, semiactive (S/A), and active are commonly used. The passive suspension system can't effectively mitigate vehicle vibration on passengers because the damping cannot be changed according to the actual situation. In the case of the active suspension system, linear electric motor or electric pump [1], are used to control vehicle body motion over a wide frequency range. The main disadvantages of the active system are their high energy consumption, high cost, or stability problem. The S/A suspension

systems offer a compromise between suspension system performance and cost. The S/A system requires low energy source and provide significantly higher ride comfort and handling stability than passive systems. Since the 1970s [2], the control strategy and suitable dampers have been widely studied for different technical applications.

The performance of S/A control of the suspension system is significantly influenced by the dynamic behavior of the damper. The response time of the damper on the control signal is a key factor [3]. A rapid increase or decrease of damping level (short response time) on the control signal is desired for all real-time S/A control applications [4]. Giua *et al* [5] simulated influence of damper response time on to S/A control

performance. The damper with response time 7 ms exhibits better results in terms of performance S/A suspension system than damping element with response time 30 ms. Similar conclusions can be found in publications [3, 6]. Suitable dampers for real-time S/A control are the hydraulic solenoid valve damper and the magnetorheological (MR) damper.

A solenoid valve damper varies the size of an orifice by an electromagnetic coil, which can give continuously variable damping characteristics. This technology offers several companies (Sachs ZF, Tenneco, etc) under various trade names such as CDC, DCC, etc. This damper can be designed with fail-safe behaviour, i.e. the maximum damping force is generated in a damper with no electric current. Qin *et al* [7] measured the dynamic behaviour of the CDC solenoid damper. The response time for the force rise (soft \rightarrow hard) was in the range 16 ms to 24 ms; the response time for the force drop (hard \rightarrow soft) was in the range 7 ms to 15 ms. The dynamic behavior of the solenoid valve damper has also been addressed in [8].

The MR damper utilizing MR fluid which, when subjected to magnetic stimuli generates yield stress thus increasing the apparent viscosity of the fluid [9]. MR fluid is a suspension of micro-sized ferromagnetic particles which are dispersed in the carrier fluid. These particles are chained in the direction of the magnetic field and cause a significant increase in the apparent viscosity and damping forces. The sedimentation stability of MR fluid (particles) is intensively addressed in [10–13]. In papers can be found several MR damper designs that differ in the number of coils [14–16], the arrangement of the magnetic circuit [17], the number of gaps [18, 19], etc. If the power supply of the coil is interrupted, the damper will stay at the minimum damping level. This is a significant problem for a wide range of MR damper applications (aerospace, rail, automotive, etc.). A suitable solution is to use a permanent magnet into the MR damper magnetic circuit. The permanent magnet creates a magnetic flux in the magnetic circuit, which ensures damping during a power supply failure—fail-safe state. In some designs, the permanent magnet is placed under the inner edge of the electromagnetic coil [20–23] or next to the electromagnetic coil on the edge of the piston gap [24, 25]. The damping level with no electric current and with permanent magnet usually achieved one-third of the maximum force. Also, a low-coercivity magnet accommodated in the magnetic circuit (e.g. Alnico, made of Aluminium–Nickel–Cobalt) can provide the MR damper with non-minimal damping forces without external power supply as mentioned in [24]. However, using a so-called switchable magnet does not ensure a full fail-safe ability of MR damper due to the possibility of magnet demagnetization.

The dynamic behavior of MR dampers dealt with only a handful of authors. Koo *et al* [4] experimentally determined the response time of a commercially available Lord Corporation's Motion Master[®] Ride Management System at approximately 17 ms (lowest measured value). However, the response time of damper is strongly dependent on the magnitude of the applied electric current and the piston velocity. Takesue *et al* [26] presented the design of the MR clutch where they improved the dynamic behavior of this actuator

by reduction of eddy current in the magnetic circuit. The same aim had Strecker [27] and Kubík [16] who published the design of MR damper with a short response time where the ferrite material of the magnetic circuit was used. Strecker [17] published MR damper with a magnetic circuit manufactured by 3D metal printing, which allowed the MR damper design with a response time of 1.68 ms and a high dynamic range. This method is based on the design of the special shape of the magnetic circuit contributing to the reduction of eddy current. The effect of eddy currents on MR damper dynamics can be also reduced using a magnetic circuit made by laminated sheets [15, 28]. Sahin *et al* [29] compared two MR valves with similar material and different geometry. Sahin *et al* showed that the response time of the MR damper is also dependent on the geometry of the MR valve. The dynamic behavior of MR damper with a permanent magnet was examined only by Lee *et al* [30]. The damping force of this damper is realized by the variation of the magnetization area (position-dependent damper), not by the electromagnetic coil.

The *main aim* of this paper is to introduce the *dynamic behavior of fail-safe MR damper with a permanent magnet*. The response time of the magnetic field and force on the step the control signal are determined experimentally and using the magnetic models.

2. Materials and methods

2.1. MR damper response time

The dynamic behavior of MR damper is usually assumed as a first-order system, where the response time is determined at 63.2% of steady-state force value [9, 16, 27]. However, in many publications, the response time of MR damper is described as 90% [31, 32] or 95% [4, 17] of the steady-state force value. The criterion of 90% is frequently used for the description of the dynamic behavior of actuators in industrial applications [30]. Response time (τ) of the system indirectly implies cut-off frequency ($f = \frac{1}{2\pi\tau}$) which is connected with the controllable frequency range of the damper [33]. The primary response time τ_{63} , τ_{36} (63.2% for the rise and 36.8% for a drop of steady-state value) and secondary response time τ_{90} , τ_{10} (90% for the rise and 10% for a drop of steady-state value) on step electric current drop and rise will be determined from measured and simulated data in this paper, see figure 1. The measured and simulated data were normalized by the non-dimensional function N_o . A detailed description of this method in paper [30].

2.2. Design of MR damper with permanent magnet

The presented MR damper is a monotube design, where the high-pressure gas (6) is separated from the MR fluid (5) by a floating piston (2), see figure 2.

The piston rod was sealed by a piston rod seal from H-PU material and guided by bearing (4). The most important part of the damper is a piston unit (1). The damper was filled by 200 ml of MRF Lord MRF 132-DG and pressurized by 30 bar. The piston unit consists of a core (1, 2), sleeve (3), plates (4),

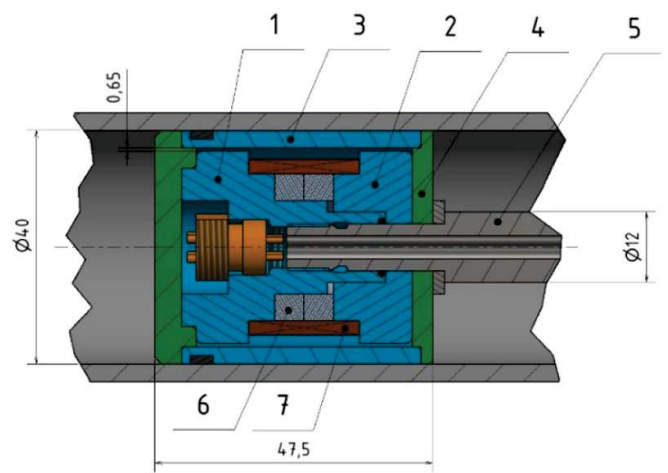
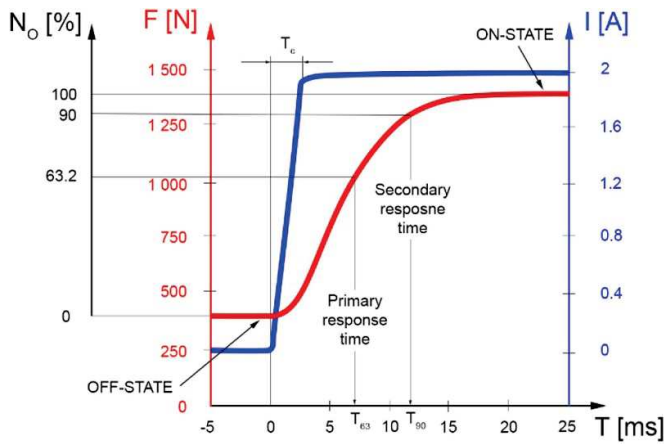


Figure 3. The detail of MR valve with permanent magnet.

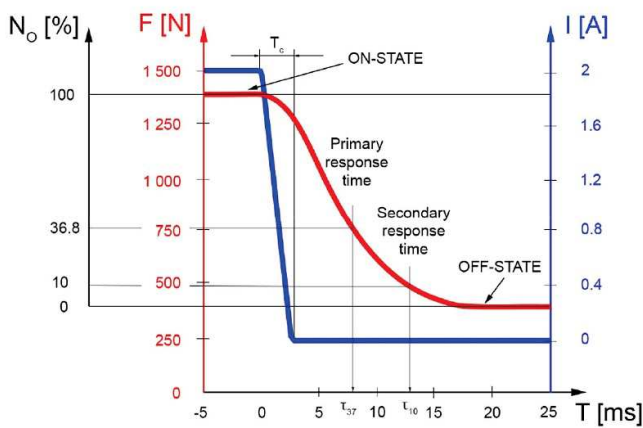


Figure 1. Definition of the response time of MR damper.

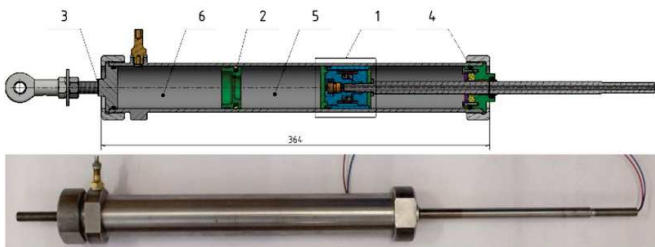


Figure 2. Design of MR damper with permanent magnet.

piston rod (5), permanent magnet (6), and an electromagnetic coil (7). The important dimensions are shown in figure 3.

The wire of the electromagnetic coil was connected to the connector integrated into the piston rod. The magnetic circuit (1, 2, 3) was made of cutting steel (11SMn30 with a carbon content of less than 1%). Two neodymium permanent magnets in the form of a ring $25 \times 16 \times 5$ mm, class N42 was used. These magnets have been selected because they were up for sale. The maximum operating temperature is 80°C .

An electromagnetic coil was wound by 190 turns of copper wire with a diameter of 0.5 mm. Figure 4 shows the main principle function idea of the damper with the magnet. In the case of the positive polarity of electric current $+I$, the magnetic flux density in the gap is $B_{\text{max}} = B_{\text{mag}} + B_{\text{coil}}$. In the case

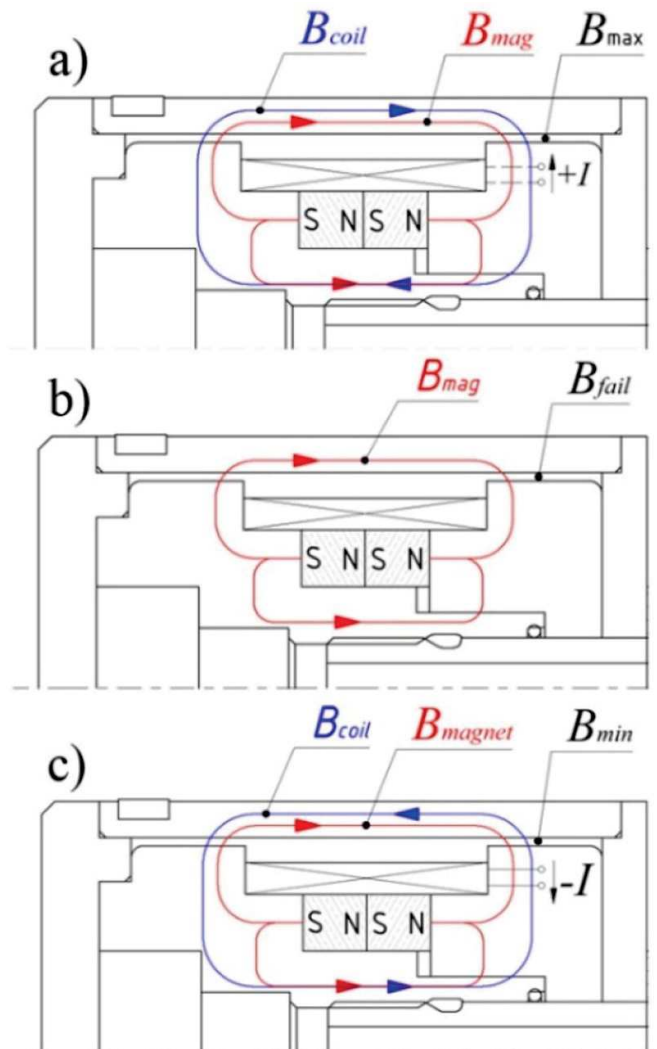


Figure 4. The main principle of MR valve function with permanent magnet; (a) current $+I$, (b) no current, (c) $-I$ current.

of the negative polarity of electric current $-I$, the magnetic flux density in the gap is $B_{\text{min}} = B_{\text{mag}} - B_{\text{coil}}$.

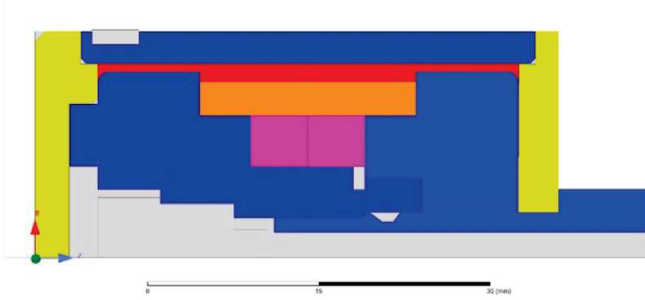


Figure 5. Simplified geometry of MR valve for the magnetic model; steel 11SMn30 (blue), MR fluid or Air (red), bronze (yellow), NdFe42 magnet (green), copper (orange) and air surrounding (white).

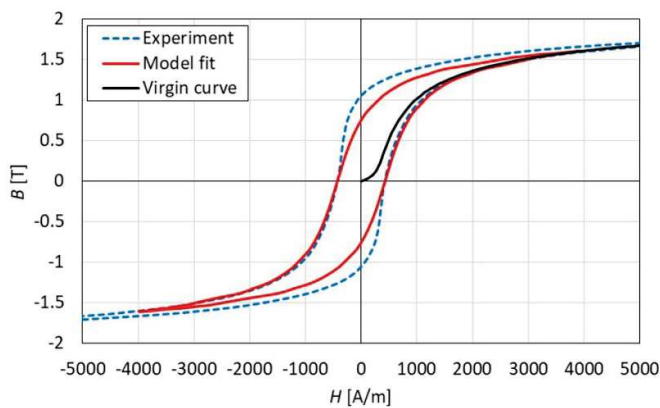


Figure 6. The virgin (black) and hysteresis magnetization curve for steel 11SMn30; experiment (blue), model fit on experimental data (red).

2.3. Magnetic model

The FE magnetic model is necessary for the calculation of magnetic circuit properties including significant non-linearities (magnetization curve, magnetic hysteresis, etc). The analytical approach is considerably inaccurate due to the model complexity. The Ansys Electronics Desktop 2018 with co-simulation of Ansys Twin Builder 2018 was used for the presented models. We assumed the MR valve in the damper as asymmetric around the centerline Z in a cylindrical coordinate system. The simplified geometry of the MR valve for magnetic simulation is shown in figure 5.

The magnetic circuit (figure 3 (1–3)) was made of cutting steel 11SMn30. The virgin and hysteresis magnetization curve was experimentally determined for sample of this steel by system Remagraph C-500. Measured data is shown in figure 6. The coercivity and remanence were determined from the measured hysteresis loop: $H_c = 427 \text{ A m}^{-1}$ and $B_r = 1.05 \text{ T}$.

The electric bulk conductivity $\sigma = 5.8 \text{ MS m}^{-1}$ was used. The lids were made of bronze with relative permeability $\mu_r = 1$ and electric bulk conductivity $\sigma = 10 \text{ MS m}^{-1}$. The MRF 132-DG was used for models. The magnetic hysteresis of MR fluid was neglected. We applied the vector hysteresis modeling feature available in system Ansys on the electromagnetic model

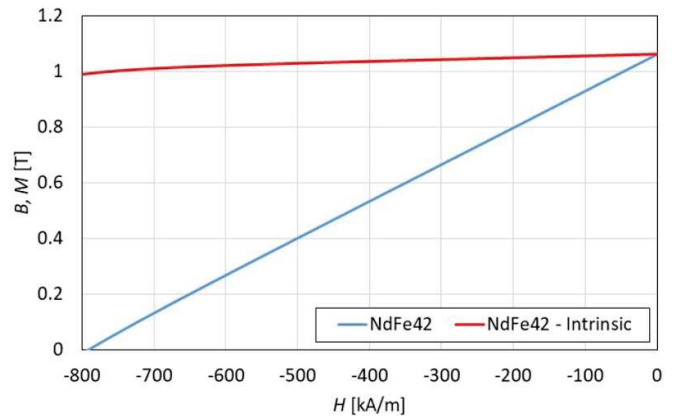


Figure 7. Magnetisation curve of NdFe42 permanent magnet.

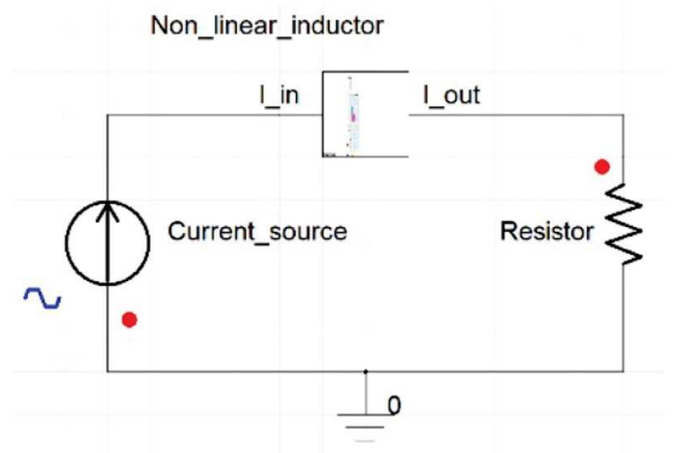


Figure 8. Lumped electric circuit (an external electric circuit).

of the MR valve. A more detailed description of this model is in the publication [9]. The curve fit to the experimental hysteresis data for the steel 11SMn30 was created by Ansys software, see figure 6. The agreement is sufficient except for low magnetic field strength. The NdFe42 permanent magnet was used in the model, see the magnetization curve from magnet manufacture in figure 7. The exact geometry and magnet type were selected for availability on the market.

The magnetic model was coupled to the external electric circuit revealed in figure 8. The lumped electric circuit is composed of an ideal electric current source (control input), resistor (with the resistance of coil winding), and MR valve object (non-linear inductor).

The proposed magnetic model was used in two cases with different time scales to determine the quasi-static section 2.3.1 and transient section 2.3.2 behavior of the magnetic circuit.

2.3.1. Quasi-static magnetic model. This model was used to determine the hysteresis behavior of a magnetic circuit in two configurations: with air in the gap and with MRF in the gap. The effect of eddy currents was neglected due to slow changes in electric current. The setting of this model was used in these configurations:

- (a) magnetic circuit with the electromagnetic coil (air in the gap; results in figure 11),
- (b) magnetic circuit with electromagnetic coil and magnet (air and MRF in the gap; results in figures 12 and 13).

This model allows us to design a proper geometry of the magnetic circuit to maximize fail-safe magnetic flux and minimize the effect of the magnet in the gap in off-state.

2.3.2. Transient magnetic model. This model calculates the magnetic induction (flux density) course in the gap on step current input. The response times are determined from these data. The final value of the electric current (T_c) was reached at $T_c = 0.2$ ms. Therefore, it is assumed that it is the step control signal in the simulation. This value has been selected due to previous experimental experiences. The waveforms of electric current were different for different settings of this simulation. The constant simulation time step was set at 0.2 ms. The mesh was generated with refinement on the edges of the magnetic circuit due to the rapid creation of eddy current on these areas. The setting of this model was used in these configurations:

- (a) magnetic circuit with electromagnetic coil and MRF in the gap (results in figure 16),
- (b) magnetic circuit with an electromagnetic coil, permanent magnet and air in the gap (results in figure 15),
- (c) magnetic circuit with an electromagnetic coil, permanent magnet, and MRF in the gap (results in figure 17).

2.4. Measurement setup of B - I map and magnetic circuit dynamics with the air gap

This measurement was carried out for verification of the modeling method. Measuring magnetic flux density with Hall probe can only be measured material in the gap with relative permeability $\mu_r = 1$ (air). It can be assumed, that the magnetic model verified with air in the gap will be valid for MR fluid in the gap as well. Four types of measurement with the almost identical configuration of measuring setup were carried out: (a) quasi-static properties of the magnetic circuit with permanent magnet and electromagnetic coil; (b) quasi-static properties of the magnetic circuit with electromagnetic coil; (c) response time of magnetic flux density on the electric current step in configuration with permanent magnet and electromagnetic coil; and (d) response time of magnetic flux density on the electric current step in configuration with an electromagnetic coil. For the response time measurement, the own patented current controller working with the overvoltage method was used [27]. The controller is supplied by laboratory supply and the input signal was generated from the Arduino control board. The increase in current took 0.2 ms. The experimental setup diagram can be seen in figure 9. The magnetic flux density was measured by a teslameter (F.W. Bell 5180) with an ultra-thin transverse probe (STB1X-0201). The course of electric current was measured by current clamp Fluke i30s. These two signal was measured with a sampling frequency of

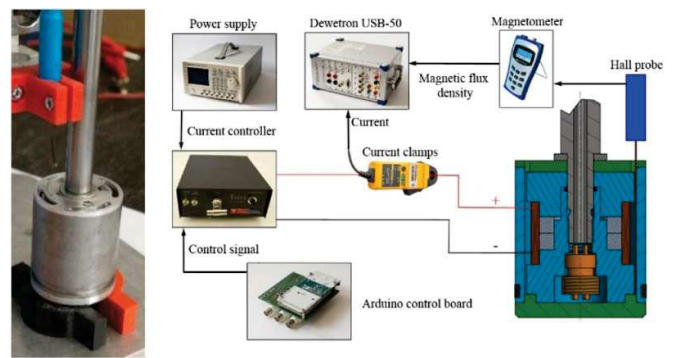


Figure 9. Experimental setup for magnetic behaviour measurement.

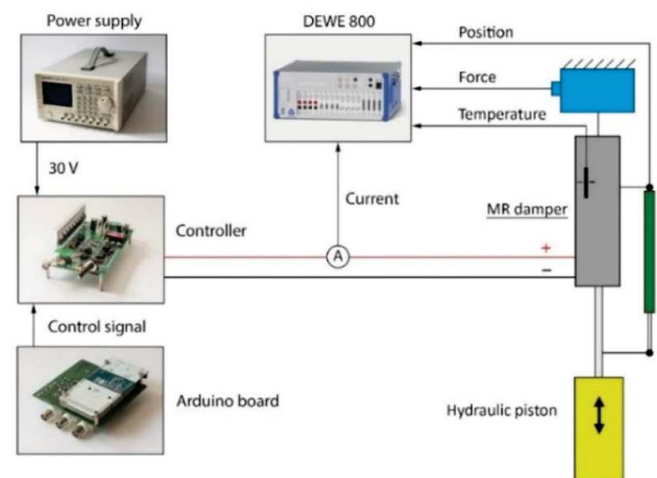


Figure 10. Experimental setup for F - v - I measurement.

200 kHz by front-end Dewetron USB-50. The measured data was processed by the software DeweSoft.

2.5. Measurement setup of F - v - I map

The measurement of the F - v - I (force-velocity-electric current) map was performed on the hydraulic pulsator Inova, see figure 10. Logarithmic sweep with a constant amplitude of 25 mm was used as an excitation signal in the frequency range 0.05–1.91 Hz, therefore, the velocity was increasing during the test. The maximum velocity was 0.2 m s^{-1} . The load gauge 1730 ACK-50 kN was used for the force measurement, the position of piston-rod was measured by resistance sensor VLP15\$A150, the current was calculated from the voltage drop on 0.1Ω power shunt, and the temperature was measured by sensor PT35. The presented temperature was measured on the hydraulic tube surface of the MR damper in the range 37°C – 43°C . These signals were recorded with a sampling frequency of 50 kHz by analyzer Dewe-800.

On the control board Arduino was set constant electric current 1 A, 2 A, 0 A(+) and with opposite polarity -1 A, -2 A, 0 A(–). The piston velocity was calculated by derivation of the piston position. The F - v - I map was calculated from measured data choosing the points with zero acceleration (center of the stroke).

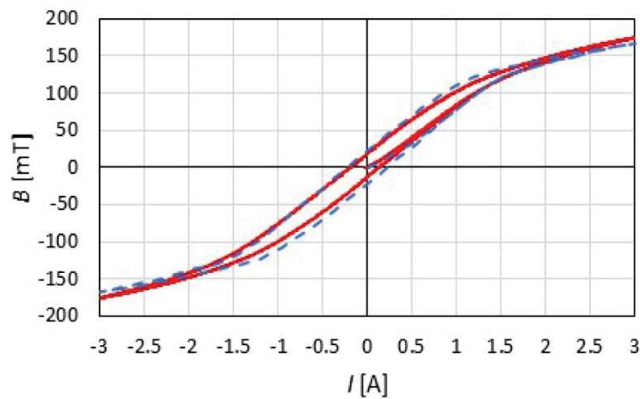


Figure 11. Comparison of the magnetic model (full line) and experiment (dotted line) for configuration without magnet and with air in the gap.

2.6. Measurement setup of MR damper dynamics (force response time)

For the force response time measurement was used load gauge HBM U2AD1/2. The configuration of the measurement was the same as in chapter 2.4. The control signal was generated by the Inova control computer. This signal was input into the Arduino board and then to the current controller. The electric current was switched always after two strokes of the MR damper in the middle of the stroke. Measurement of transient response was carried out for piston velocity 0.2 m s^{-1} and electric currents 0.5 A, 1 A, 1.5 A, 2 A, and for the same values with opposite polarity. Measurement of the rise and drop of the force was performed $5 \times$ and the response time was determined as the average of these values for each electric current.

3. Results and discussion

3.1. Quasi-static magnetic behavior

This section aims to compare the magnetic model with an experiment for configuration with and without a permanent magnet. Figure 11 shows the comparison between the magnetic model (full line) and experiment (dotted line) for configuration without magnet and air in the gap. The magnetic circuit exhibits a remanent flux density of 22 mT in the gap. The agreement between model and experiment is very good. The maximum error is 15% at zero electric currents. This difference is probably given by an inaccurate fit of the hysteresis magnetization curve, see figure 6.

Figure 12 shows the comparison between the magnetic model (full line) and experiment (dotted line) for configuration with the magnet and air in the gap. Remanent flux density 101 mT and 90 mT were measured in the gap at zero electric currents. The accuracy of the model is good except for the low electric current.

The fail-safe magnetic flux density in the gap creates roughly one-fourth of the maximum. This experimentally verified model was used to determine magnetic behavior with MRF in the gap, see figure 13. The fail-safe magnetic flux

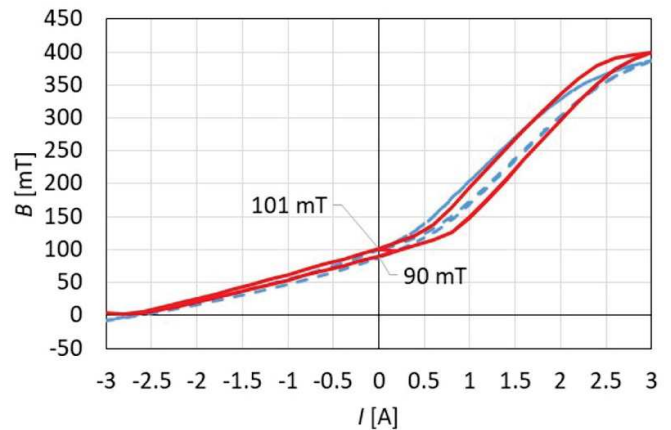


Figure 12. Comparison of the magnetic model (full line) and experiment (dotted line) for configuration with magnet and air in the gap.

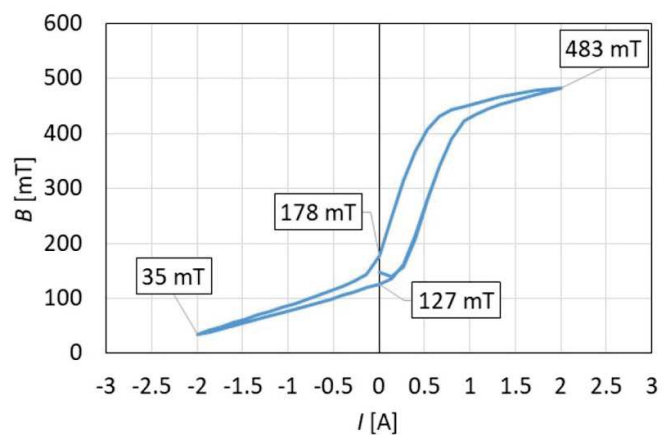


Figure 13. Hysteresis B - I curve of MR damper with MRF in the gap and permanent magnet.

density (B_{fail}) in the gap creates roughly one-third of the maximum flux density. However, the B_{fail} value is a magnetization history-dependent.

3.2. Magnetic circuit dynamics

Magnetic flux response on a different input of electric current and a different configuration of magnetic circuit were compared for the magnetic model and experiment.

3.2.1. Magnetic circuit with air in the gap (magnet and coil).

This section is important for experimental verification of the transient magnetic model. Figure 14 shows the course of magnetic flux density determined from the magnetic model (red) and experiment (blue) for the electric current step from 0 A to -1 A. Measured data were normalized in the bottom diagram.

The difference in magnetic flux density B course from the model and the experiment is probably due to the slightly different electrical conductivity of the materials used in the model. The electric conductivity was used from the datasheet of the steel suppliers. The initial and final magnetic flux density data

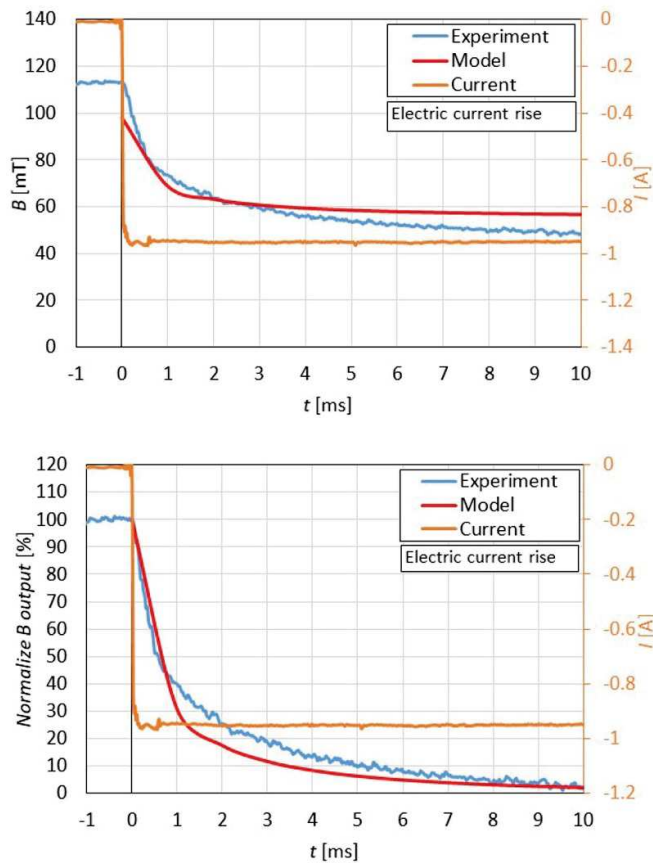


Figure 14. The course of magnetic flux density from the magnetic model and experiment.

from the model and experiment exhibits roughly 15% difference, see figure 14. This error is probably caused by the fitting of the hysteresis model to measured the hysteresis loop of magnetic circuit material, see figure 6. The accuracy of the magnetic model is very good in the context of many possible materials (slightly different chemical composition of steel, a measurement error of $B-H$ curve, etc) inaccuracies. The primary and secondary response time dependency on the electric current are shown in figure 15. All values presented in diagram labelled ‘rise’ were measured for initial current in the coil $I = 0$ A (fail-safe state). On the other hand, the data presented in diagram labelled ‘drop’ were measured for final value of current $I = 0$ A. The presented response time values in the next text sections (if are available) are always experimental data. The response time for the negative polarity ($-I$) of electric current is significantly lower than positive polarity ($+I$). The primary response time for the electric current *rise* from 0 A to -2 A is $\tau_{63} = 0.95$ ms and for electric current *drop* from -2 A to 0 A is $\tau_{36} = 0.97$ ms. The primary response time for the electric current *rise* from 0 A to 2 A is $\tau_{63} = 4.6$ ms and for a *drop* from 2 A to 0 A is $\tau_{36} = 3.6$ ms. The magnetic flux density decrease in the gap is significantly faster than the increase. The *magnet significantly influences the dynamic behavior of the magnetic circuit*. The magnetic model describes the primary response time very well. The secondary response time exhibits greater variance, especially for the electric current drop. The magnetic model can be considered experimentally verified.

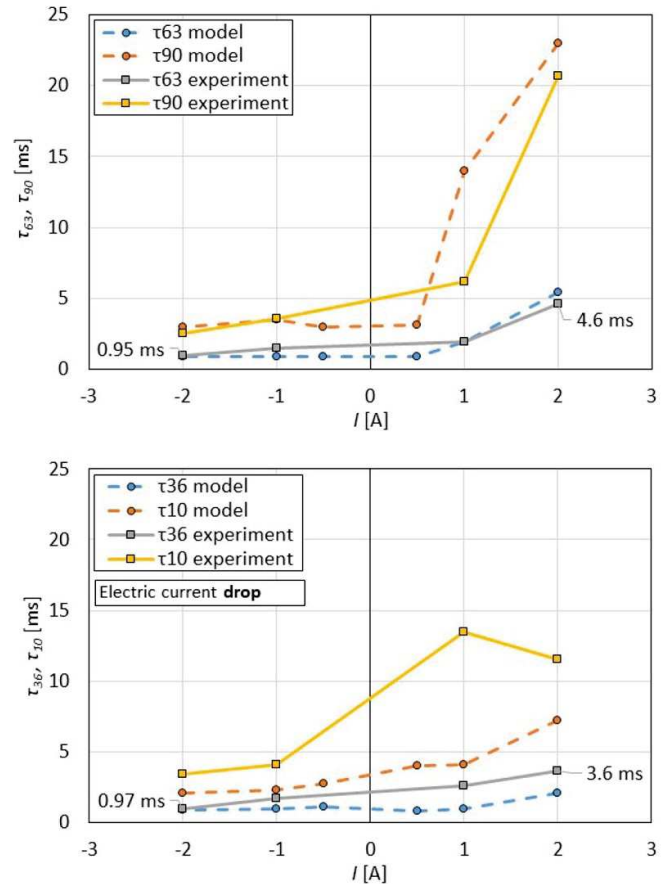


Figure 15. The primary and secondary response time for configuration with air in the gap.

3.2.2. Magnetic circuit with MRF (coil). The experimentally verified magnetic model was used to determine the dynamic behavior of the magnetic circuit with MRF in the gap (no magnet). The response time for the electric current drop and rise are presented in figure 16. The response time dependency on electric current is non-linear. For electric current rise, the lower the electric current, the greater the response time. For electric current drop, the tendency is the opposite up to 0.5 A. Then the response time is stabilized. Thus, it can be stated that the response time is dependent on the final magnitude of the electric current. Similar results are published [32]. However, this dependence is probably related to the design of the magnetic circuit (geometry) and the magnetization characteristics of the used material. These trends are supported by several simulations and publications.

3.2.3. Magnetic circuit with MRF (magnet and coil). Figure 17 shows the dependence of the response time on step electric current drop and rise input. The response time for the current rise is increasing up to 0.5 A, then significantly decreases. The response time is $\tau_{63} = 17$ ms and $\tau_{90} = 53$ ms for the electric current rise from 0 A to 0.5 A. The trends are similar as in the case of configuration without magnet. In the opposite electric current polarity ($-I$), the primary and secondary time responses are almost independent of the magnitude

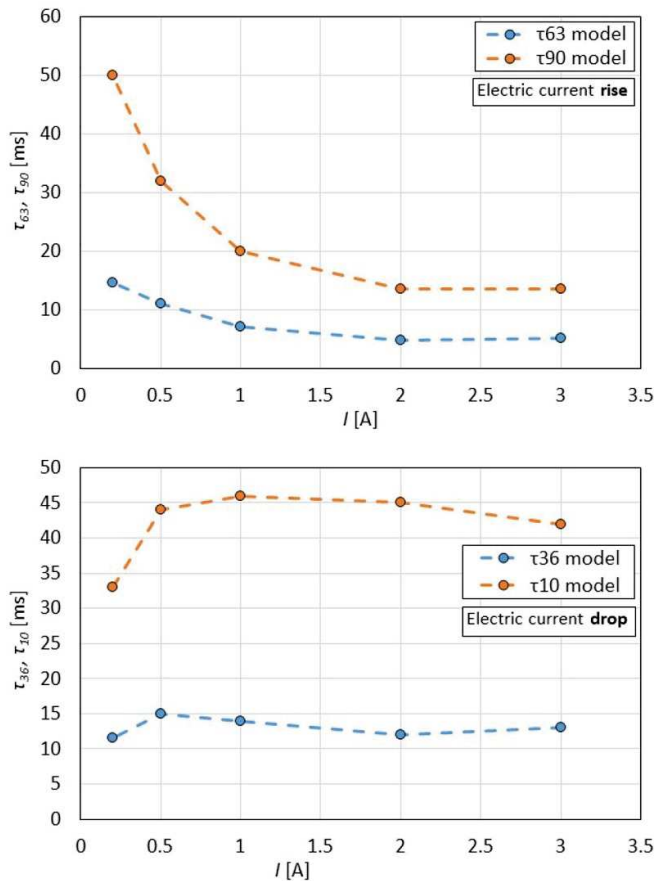


Figure 16. The response time dependency of electric current for configuration with the coil (no magnet) and MRF.

of the electric current. The response time is $\tau_{63} = 1.1$ ms and $\tau_{90} = 5$ ms for electric current rise from 0 A to -1 A. The drop of magnetic induction in the gap is 15 times faster (primary response time) and 10 times faster (secondary response time) than the rise. The magnetic circuit dynamic is almost independent of the rising or dropping of electric current in opposite electric current polarity ($-I$). However, the rise and drop for electric current have a different tendency for positive polarity. The response time is $\tau_{36} = 14.5$ ms and $\tau_{10} = 50$ ms for electric current drop from 1 A to 0 A. The response time is stabilized after achieved 1 A. It can be deduced that the short response time of magnetic field formation with the negative polarity of electric current is not related to MR fluid because this effect was observed also in the magnetic circuit without MRF, see figure 15.

3.3. F - v - I map

Based on the methodology described in chapter 2.4, the force-velocity (F - v) maps were measured for 2 A, 1 A, 0 A (+), -1 A, -2 A and 0 A(-) electric currents, see figure 18. The F - v map for no electric current is affected by magnetization history (previous orientation of electric current). The damping force for zero electric current and change from higher damping forces ($+0$ A) is higher than the switch from lower damping forces (-0 A). The damping

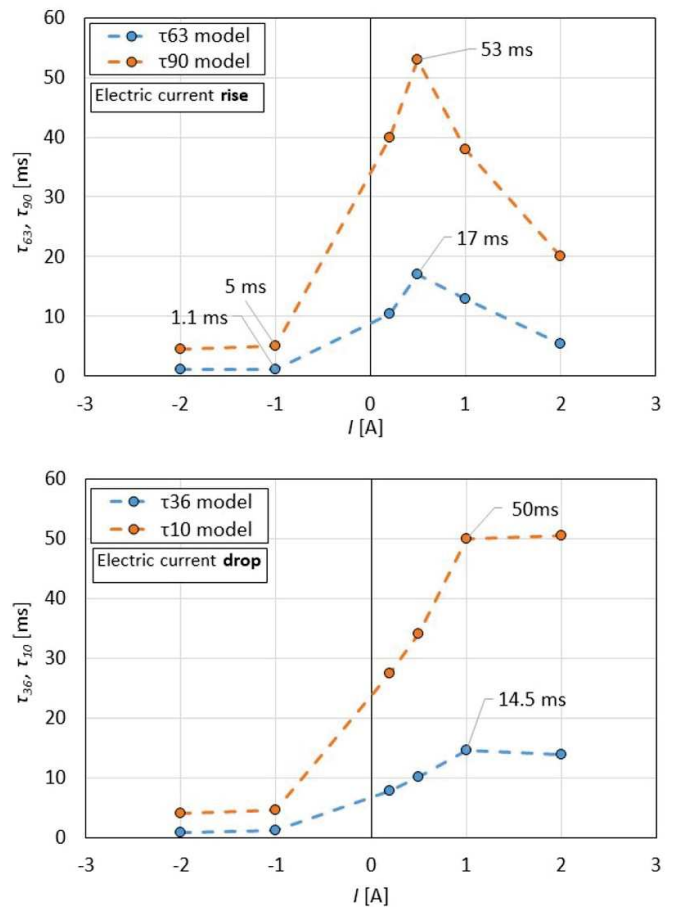


Figure 17. The response time dependency of electric current for configuration with an electromagnetic coil, magnet, and MRF.

force for $+0$ A was 592 N and for -0 A was 505 N at piston velocity 0.1 m s $^{-1}$. This is a 15% decrease. This difference is due to the hysteresis behavior of the magnetic circuit itself, as described in figure 13. The force 505 N corresponds with magnetic induction 127 mT and force 592 N with magnetic induction 178 mT. This difference could be reduced by using another material of magnetic circuit (SMC, Vacoflux, etc) or by selecting a suitable heat treatment. Fail-safe damping force is approximately 1/3 of the maximum damping force (0.1 m s $^{-1}$).

The dynamic force range of damper was calculated from the maximum ($+2$ A) a minimum (-2 A) damping forces at given piston velocity, see figure 19. The maximum dynamic force range is 8.5 at the piston velocity of 0.06 m s $^{-1}$. The presented fail-safe MR damper achieves a comparable dynamic force range as the non-permanent magnet MR damper variants [3, 9, 16]. The dynamic force range of the damper is also one of the essential parameters for efficient S/A control [6].

3.4. MR damper dynamics (force response time)

The force courses on the step current input were measured according to the methodology described in chapter 2.5. Figure 20 shows the course of force (blue) and electric current

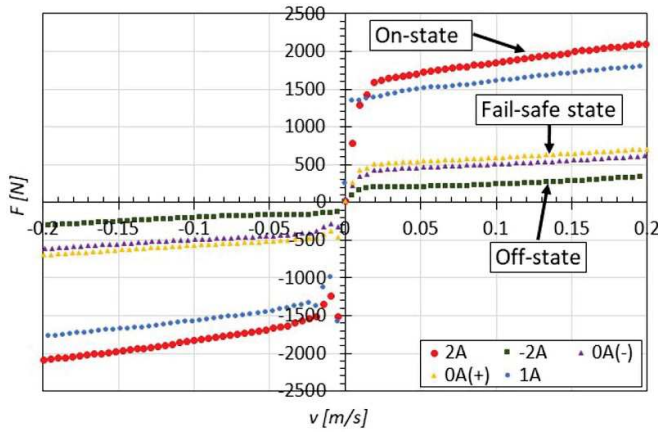


Figure 18. Force–velocity map of fail-safe MR damper.

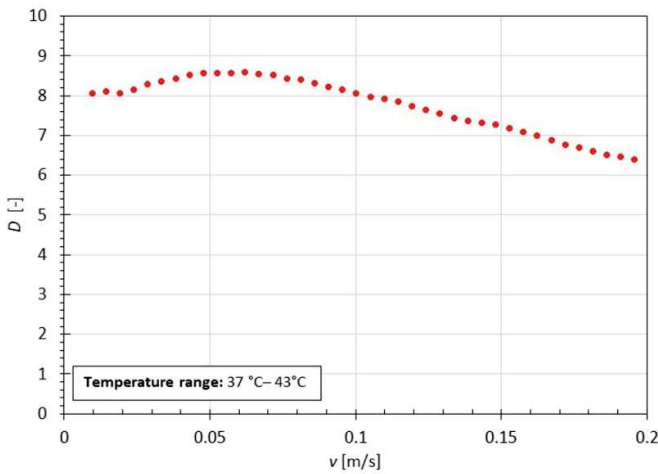


Figure 19. Dynamic force range of MR damper with magnet.

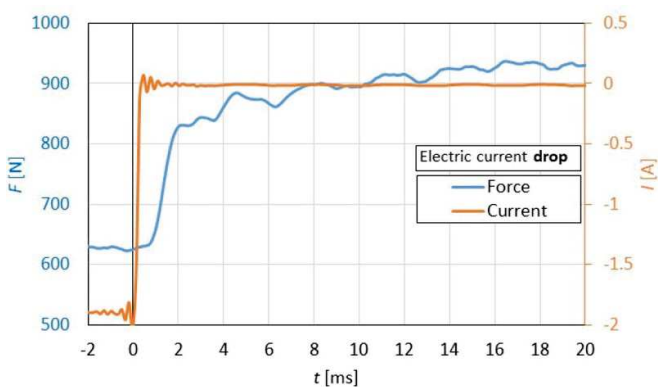


Figure 20. Example of the course of the force and electric current for unit-step electric current drop input at piston velocity 0.3 m s^{-1} .

(orange) for step current drop input from -2 A to 0 A at piston velocity 0.3 m s^{-1} . The measured force data was normalized, see figure 21. In all the measured data, it can be seen the time delay approximately $0.5\text{--}0.8 \text{ ms}$ between the course of electric current and force. This time delay was *not* observed in the

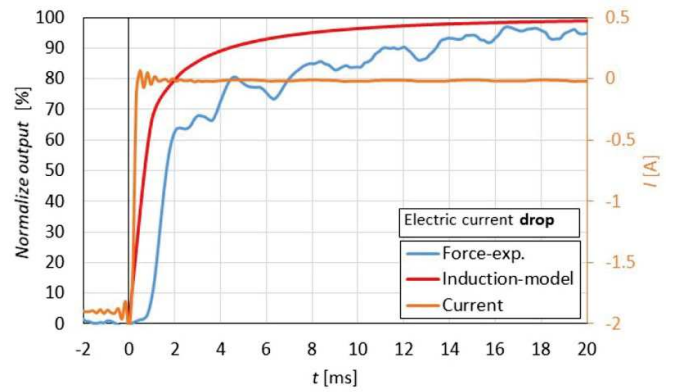


Figure 21. Normalize course of force and magnetic induction.

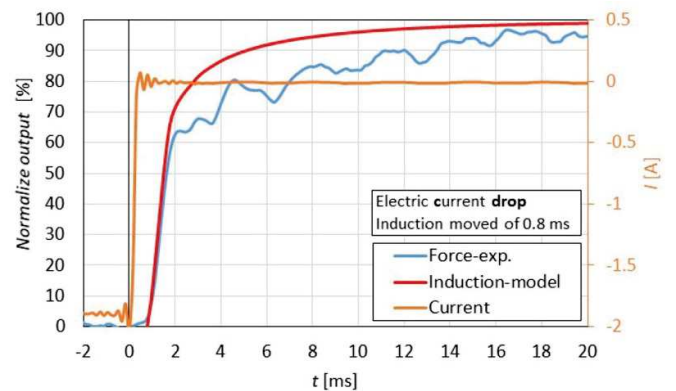


Figure 22. Normalize course of force and magnetic induction (moved of 0.8 ms).

course of magnetic induction, see figure 21, which means that it must be related to the hydraulic system.

It was checked that this time delay is not due to measurement devices or their settings. This time delay is probably caused by the response time of MR fluid itself or deformation of the rubber part of the damper (seal). Similar conclusions have been published in [17]. This phenomenon will be detailed studied in the following research.

The data from the magnetic model was moved of 0.8 ms due to the presented delay, see figure 22. The magnetic model well describes the initial course of force.

The force course exhibits significant pulsation due to the hydraulic system compliance [9]. Therefore, the determination of secondary response time is quite inaccurate and exhibits a large dispersion. The comparison of response time dependency on electric current from force measurement and magnetic model is presented in figures 23 and 24. The force measurement dispersion is presented by error bars that show maximum, minimum measured force value, and also average value.

3.4.1. Electric current step rise. The primary (τ_{63}) and secondary (τ_{90}) force response time is strongly dependent on electric current polarity and magnitude, see figure 23.

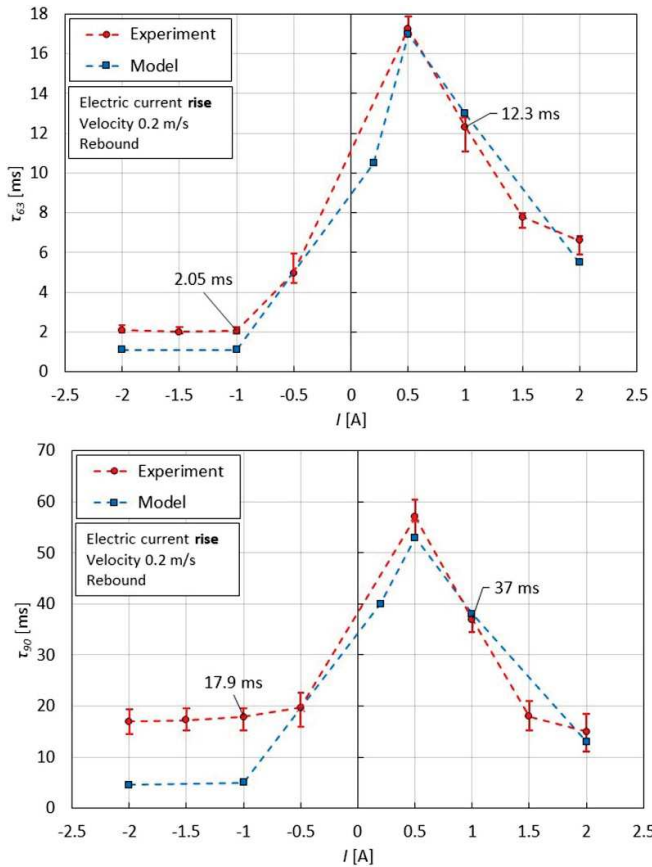


Figure 23. The course of primary and secondary response time on orientation and magnitude of electric current for configuration with electric current step rise; force data (red circle), magnetic model data (blue square).

The response time is significantly lower for the negative orientation of electric current (from 0 A to -1 A; force data $\tau_{63} = 2.05$ ms, $\tau_{90} = 17.9$ ms) than for positive orientation (from 0 A to 1 A; force data $\tau_{63} = 12.3$ ms, $\tau_{90} = 37$ ms). The drop of force is app. six times faster than rising. The primary response time determined from the magnetic model well fit experimental data, see figure 23. The secondary response time from the magnetic model also well fit experimental data except for the negative orientation of electric current. There is a significant difference.

3.4.2. Electric current step drop. The primary (τ_{63}) and secondary (τ_{90}) force response time is also strongly dependent on electric current orientation and magnitude, see figure 24.

It can be seen that negative orientation of electric current (from -1 A to 0 A; $\tau_{36} = 1.5$ ms, $\tau_{10} = 4.5$ ms) is significantly faster than positive orientation (from 1 A to 0 A; $\tau_{36} = 14$ ms, $\tau_{10} = 58$ ms). In this case, the magnetic model very well fit experimental data. It should be noted that the presented data are connected with the exact geometry and material configuration of the MR valve. It can be assumed that the exact value of response time will be dependent on the specific geometry and material configuration of the MR valve. However, the trend will be the same.

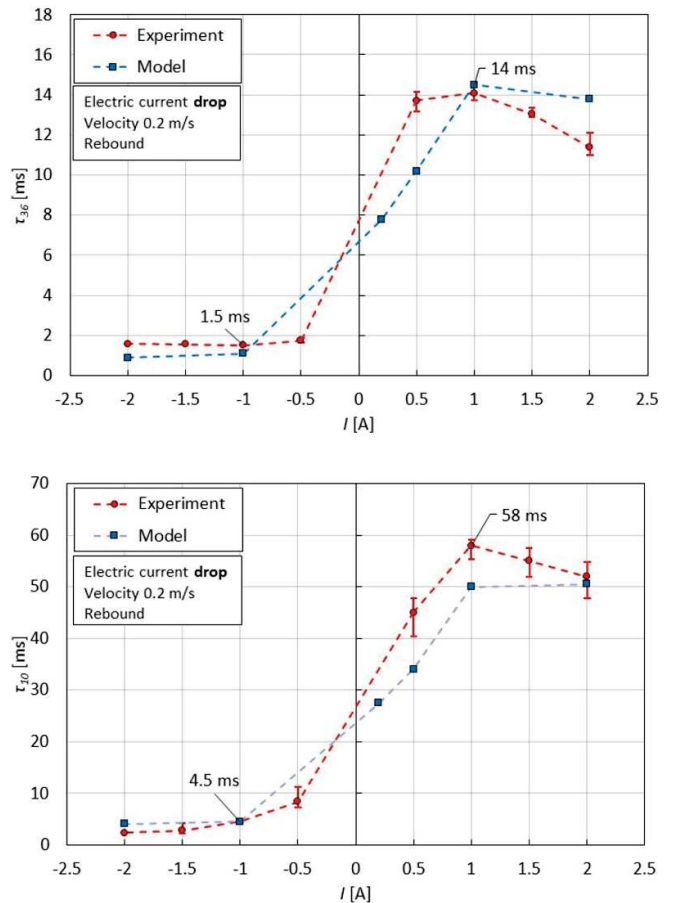


Figure 24. The course of primary and secondary response time on orientation and magnitude of electric current for configuration with electric current step drop; force data (red circle), magnetic model data (blue square).

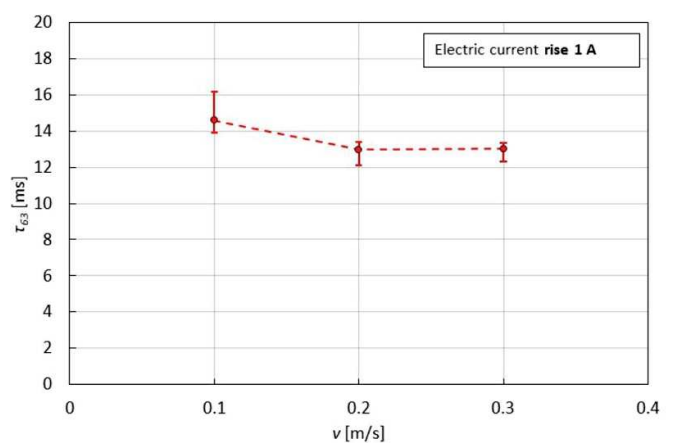


Figure 25. The influence of piston velocity on primary response time.

3.4.3. Influence of piston velocity on force response time. Figure 25 shows the influence piston velocity on primary response time for the rise of the damping force. The primary response time slightly increases at a piston velocity of 0.1 m s⁻¹. This increase is caused by the rigidity of the hydraulic system itself especially the rigidity of MR fluid. This phenomenon is also described in [9].

4. Conclusion

The optimal performance of a semi-active suspension system with fail-safe MR damper requires understanding its dynamic behavior. The knowledge of time delay between force and control signal is necessary for accurate control design study or vehicle dynamic simulations. This paper presented the dynamic behavior of MR damper with the permanent magnet. The conclusions from this paper are the following:

- The magnetic flux density in the gap at zero electric current creates roughly 1/4 of maximum and is magnetization history dependent due to hysteresis behaviour of magnetic circuit material.
- The magnetic flux density in the gap decreases significantly faster than increases on the electric current step. This is probably given by the effect of permanent magnet.
- The fail-safe damping force at zero electric current is also dependent on magnetization history and the achieved app. 1/3 of maximum damping force. The difference at fail-safe forces is due to the hysteresis behavior of the magnetic circuit.
- The dynamic force range of fail-safe MR damper achieved a value of 8.5 which similar to the common design of MR damper. The maximum damping forces are also comparable.
- The *decrease* in the *damping force* (negative polarity of electric current) from a fail-safe state to off-state is significantly faster than the increase from fail-safe state to on-state. The primary response time is roughly 2 ms. This short response time is probably given by the effect of the permanent magnet.
- The *increase* in the *damping force* (positive polarity of electric current) from fail-safe state to on-state is significantly slower than the decrease and strongly dependent on the magnitude of the electric current. The primary response time achieved roughly 12 ms at electric current 1 A.
- The initial time delay of 0.5–0.8 ms between the course of force and an electric current was observed. This delay was not observed in magnetic flux density measurement. Therefore, this delay is probably caused by hydraulic system compliance or response time MR fluid itself.
- The response time determined from the magnetic model well fitted experimental force data of MR damper. For this reason, a transient magnetic simulation is an effective tool for the determination of the dynamic behaviour of MR damper.

The following research will be focused on the durability of this type of damper and fail-safe behaviour dependency on temperature.

Acknowledgments

The authors wish to acknowledge the support of the Grant Nos. FEKT/FSI-J-20-6260, GAČR 20-23261Y and FSI-S-20-6247.

ORCID iDs

F Jeniš  <https://orcid.org/0000-0002-1753-1508>

M Kubík  <https://orcid.org/0000-0003-0105-2921>

Z Strecker  <https://orcid.org/0000-0002-1598-487X>

References

- [1] Westerhoff M 2018 ZF Vision magazine www.zf.com/site/magazine/en/home/magazine_homepage.html
- [2] Karnopp D, Crosby M J and Harwood R A 1973 Vibration control using semi-active force generators *ASME Pap.* **96** 619–26
- [3] Strecker Z, Mazůrek I, Roupec J and Klapka M 2015 Influence of MR damper response time on semiactive suspension control efficiency *Meccanica* **50** 1949–59
- [4] Koo J H, Goncalves F D and Ahmadian M 2006 A comprehensive analysis of the response time of MR dampers *Smart Mater. Struct.* **15** 351–8
- [5] Giua A, Melas M and Seatzu C 2004 Design of a control law for a semiactive suspension system using a solenoid valve damper *Proc. IEEE Int. Conf. Control Appl.* **2** pp 1467–72
- [6] Machacek O, Kubik M and Novák P 2017 A new method of magnetorheological damper quality evaluation *Eng. Mech.* **2017** 594–7
- [7] Qin Y, Zhao F, Wang Z, Gu L and Dong M 2017 Comprehensive analysis for influence of controllable damper time delay on semi-active suspension control strategies *J. Vib. Acoust. Trans. ASME* **139** 1–12
- [8] Li P X, Su M and Zhang D B 2017 Response characteristic of high-speed on/off valve with double voltage driving circuit *IOP Conf. Ser. Mater. Sci. Eng.* **220** 012028
- [9] Kubík M and Goldasz J 2019 Multiphysics model of an mr damper including magnetic hysteresis *Shock Vib.* **2019** 1–21
- [10] Roupec J, Berka P, Mazůrek I, Strecker Z, Kubík M, Macháček O and Andani M T 2017 A novel method for measurement of MR fluid sedimentation and its experimental verification *Smart Mater. Struct.* **26** 107001
- [11] Cheng H, Wang M, Liu C and Wereley N M 2018 Improving sedimentation stability of magnetorheological fluids using an organic molecular particle coating *Smart Mater. Struct.* **27** 1–10
- [12] Plachy T, Cvek M, Kozakova Z, Sedlacik M and Moucka R 2017 The enhanced MR performance of dimorphic MR suspensions containing either magnetic rods or their non-magnetic analogs *Smart Mater. Struct.* **26** 1–8
- [13] Cvek M, Mrlik M, Ilcikova M, Plachy T, Sedlacik M, Mosnacek J and Pavlinek V 2015 A facile controllable coating of carbonyl iron particles with poly(glycidyl methacrylate): a tool for adjusting MR response and stability properties *J. Mater. Chem. C* **3** 4646–56
- [14] Zheng J, Li Y and Wang J 2017 Design and multi-physics optimization of a novel magnetorheological damper with a variable resistance gap *Proc. Inst. Mech. Eng. C* **231** 3152–68
- [15] Gołdasz J 2013 Electro-mechanical analysis of a magnetorheological damper with electrical steel laminations *Prz. Elektrotechniczny* **89** 8–12 (<http://pe.org.pl/articles/2013/2a/2.pdf>)
- [16] Kubík M, Macháček O, Strecker Z, Roupec J and Mazůrek I 2017 Design and testing of magnetorheological valve with fast force response time and great dynamic force range *Smart Mater. Struct.* **26** 047002
- [17] Strecker Z, Kubik M, Vitek P, Roupec J, Paloušek D and Šreibr V 2019 Structured magnetic circuit for

- magnetorheological damper made by selective laser melting technology *Smart Mater. Struct.* **28** 1–13
- [18] Goldasz J 2019 Magnetostatic study of a dual-gap MR valve *Proc. 2019: 20th Int. Conf. Res. Educ. Mechatronics, REM 2019* **5** pp 1–5
- [19] Goldasz J 2013 Study of a magnetorheological fluid damper with multiple annular flow gaps *Int. J. Veh. Des.* **62** 21–41
- [20] Bai X X and Wereley N M 2014 A fail-safe magnetorheological energy absorber for shock and vibration isolation *J. Phys. D: Appl. Phys.* **115** 1–4
- [21] Zhang H H, Liao C R, Yu M and Huang S L 2007 A study of an inner bypass magneto-rheological damper with magnetic bias *Smart Mater. Struct.* **16** N40–6
- [22] Yan W, Ji J, Dong B and Ge H 2009 Theoretical and experimental studies on a new reversible magnetorheological damper *Struct. Control Health Monit.* **18** 1–19
- [23] Du C, Wan F and Yu G 2011 A magnetic flux leakage study of a self-decoupling magnetorheological damper *Smart Mater. Struct.* **20** 065019
- [24] Böse H and Ehrlich J 2012 Magnetorheological dampers with various designs of hybrid magnetic circuits *J. Intell. Mater. Syst. Struct.* **23** 979–87
- [25] Bose H, Ehrlich J and Trendler A-M 2009 Performance of magnetorheological fluids in a novel damper with excellent fail-safe behavior *11th Conf. on Electrorheological Fluids and Magnetorheological Suspensions* p 5
- [26] Takesue N, Kiyota Y and Furusho J 2002 Development of fast response MR-fluid actuator *Proc. 41st SICE Annual Conf. SICE* (Soc. Instrument & Control Eng. (SICE)) vol **2** pp 949–53
- [27] Strecker Z, Roupec J, Mazurek I, Machacek O, Kubik M and Klapka M 2015 Design of magnetorheological damper with short time response *J. Intell. Mater. Syst. Struct.* **26** 1951–8
- [28] Kostamo E, Kostamo J, Kajaste J and Pietola M 2012 Magnetorheological valve in servo applications *J. Intell. Mater. Syst. Struct.* **23** 1001–10
- [29] Sahin H, Gordaninejad F, Wang X and Liu Y 2012 Response time of magnetorheological fluids and magnetorheological valves under various flow conditions *J. Intell. Mater. Syst. Struct.* **23** 949–57
- [30] Lee T-H and Choi S-B 2019 On the response time of a new permanent magnet based magnetorheological damper: experimental investigation *Smart Mater. Struct.* **28** 014001
- [31] Maas J and Güth D 2011 Experimental investigation of the transient behavior of MR fluids *Conf. on Smart Materials, Adaptive Structures and Intelligent Systems (ASME)* pp 229–38
- [32] Wu G, Feng Z, Zhang G and Hou Z 2011 Experimental study on response time of magnetorheological damper *Int. Conf. on Artificial Intelligence, Management Science and Electronic Commerce (IEEE)* pp 3968–72
- [33] Yoon D S, Park Y J and Choi S B 2019 An eddy current effect on the response time of a magnetorheological damper: analysis and experimental validation *Mech. Syst. Signal Process.* **127** 136–58

Technical Note

A magnetorheological fluid shaft seal with low friction torque

M Kubík , D Pavlíček, O Macháček, Z Strecker  and J Roupec

Department of Machine and Industrial Design, Brno University of Technology, Brno, Czechia

E-mail: michal.kubik@vutbr.cz

Received 12 November 2018, revised 28 January 2019

Accepted for publication 19 February 2019

Published 20 March 2019



CrossMark

Abstract

This paper deals with the design and tests of a magnetorheological fluid seal (MRFs) using the innovative concept of the magnetic circuit, which allows the achievement of a promising trade-off between burst pressure and friction of the seal. Low friction torque and low burst pressure are typical for a ferrofluid seal (FFs). Replacement of the ferrofluid by magnetorheological fluid increases the burst pressure of the seal but the friction torque of the seal increases too. The optimum for sealing application is low friction torque and high burst pressure. The presented design is based on the pinch mode of magnetorheological fluid. The geometry of the seal was determined by a magnetostatic model. Subsequently, the chosen concept of the seal was manufactured and tested. Pinch MRFs achieved lower friction torque than common (standard) MRFs and a higher burst pressure than any FFs.

Keywords: magnetorheological fluid seal, MR fluid seal, magnetic seal, magnetic shaft seal, liquid O-ring, burst pressure

(Some figures may appear in colour only in the online journal)

Introduction

The conventional design of a seal with magnetic fluid contains a source of electromotive force (1), two ferromagnetic pole pieces (2), magnetic fluid (3), and a sealed shaft (4)—see figure 1. The magnetic fluid is located between the pole piece and the shaft made of ferromagnetic material—see figure 1 (detail). Magnetic fluid creates a liquid barrier between sealed zones; therefore, it is usually referred to as a liquid O-ring. The magnetic flux flows from the first pole piece through to a sealed shaft to the second pole piece. The magnetic field keeps the magnetic fluid in the sealed gap. The sealed effect is provided by chains of ferromagnetic particles (5) which are oriented in the direction of the magnetic field—see figure 1. Typical magnetic fluid consists of ferromagnetic particles, the carrier fluid, and additives. The first mention of magnetic fluids was in the 1940s by Jacob Rabinow [1], specifically in 1947. However, the greater development of magnetic fluids was driven in the 1960s by Steven Papell in the NASA program. He obtained a US patent in 1965 [2].

The magnetorheological fluid (MR) contains micro-particles and ferrofluids are made of nanoparticles. These liquids have different magnetic properties, sedimentation stability or apparent viscosity. The magnetic fluid seals can be divided by the type of magnetic fluid which is used for sealing as follows [3]:

- ferrofluid seals (FFs),
- magnetorheological fluid seals (MRFs).

Ferrofluid seals (FFs)

A FF uses a magnetic fluid which is composed of ferromagnetic nanoparticles. The first commercial application of a FF was in the leak-free sealing system for a computer disk drive in the 1970s [4]. A FF is characterized by a small friction torque and high level of tightness. Considering the above advantages, a FF is appropriate for sealing an ultrahigh vacuum [5], and highly clean and corrosive environments [3], etc. However, the disadvantage of FFs is the relatively low

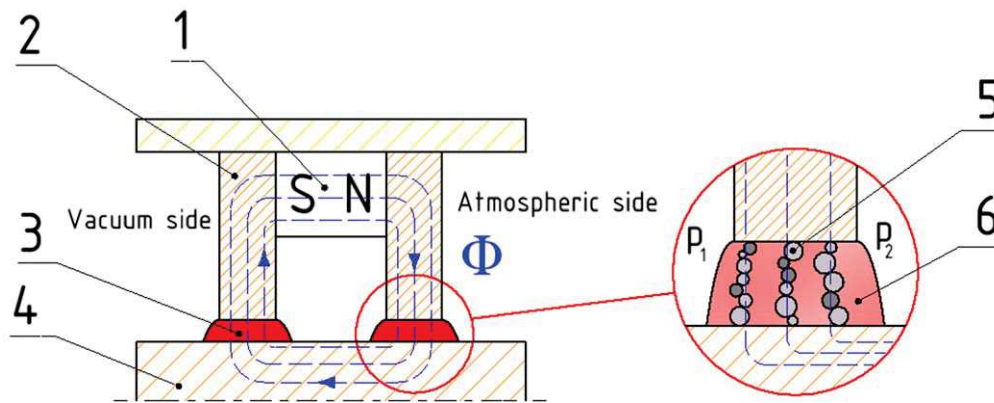


Figure 1. Standard design of a magnetic fluid seal; (1) permanent magnet, (2) pole pieces, (3) magnetic fluid, (4) sealed shaft, (5) ferromagnetic particles and (6) carrier fluid.

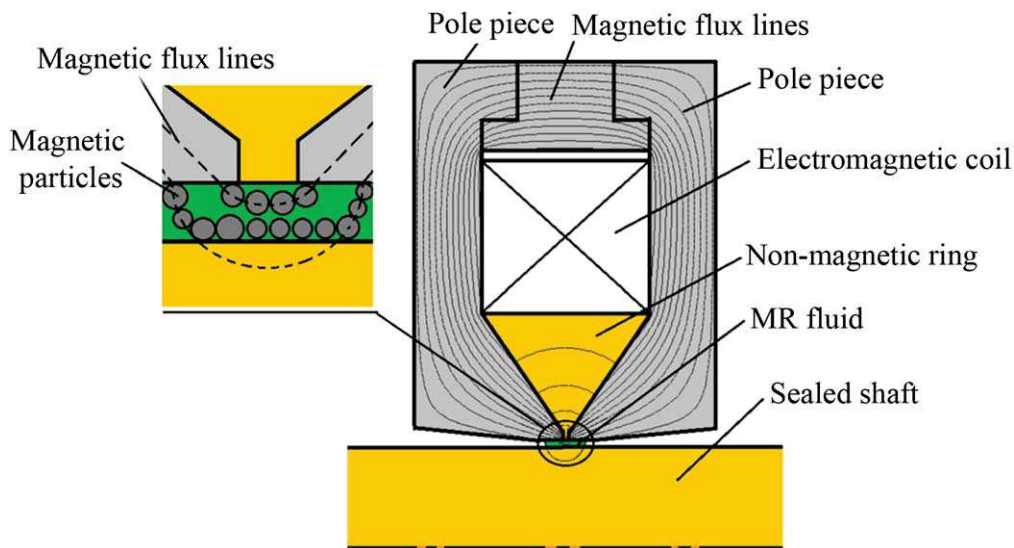


Figure 2. Function principle of a pinch magnetorheological fluid seal; ferromagnetic material (grey), non-ferromagnetic material (yellow), magnetic fluid (green).

burst pressure. The burst pressure is the maximum difference of pressures between the sealed environments over which the leakage is observed. A typical static burst pressure of FFs is in the tens of kPa; Kordonski [6] published a static burst pressure of 0.5 bar; Szezech [7] was in the range from 0.48 bar to 0.65 bar, dependent on ferrofluid type; while Tomiota [8] registered 0.3 bar. The dynamic burst pressure of FFs is usually slightly dependent on rotation [6, 8] and temperature [9]. The gap between surfaces sealed by FFs is typically in the range of 0.05 mm to 0.1 mm [6–8, 10]. Szezech [11] published a numerical study about the influences of the geometry of pole pieces on a friction torque where the friction torque was in the range of 0.05–0.5 Nm. Chen [12] published FF for reciprocating motion. The FFs system is used in a wide range of equipment worldwide, e.g. vacuum-rotary feedthrough, fluid seals for fans and blowers or hard disk drive spindle.

Magnetorheological fluid seals (MRFs)

A MRF uses magnetorheological (MR) fluid which is composed of ferromagnetic microparticles, usually in a range

from 1 μm to 2 μm . The typical application of MR fluid is for shock absorbers [13, 14], clutches [15] or engine mounts [16]. The main motivation for using bigger particles in the magnetic fluid is their higher magnetization [3], which causes stronger magnetic particle interaction. This causes the significant increase of static and dynamic burst pressure of the seal. The typical static burst pressure of MRFs is in the hundreds of kPa; Cong [5] published a static burst pressure of 26.1 bar for 4 pole pieces; Kordonski [6] 1.8 bar for one pole piece; Potoczny [17] 0.6 bar for one pole piece; and Zhang [18] 4 bar for 6 pole pieces. The dynamic burst pressure of MRFs is dependent on the speed of rotation [6]. The second motivation to use MRFs is in MR devices as a magnetorheological damper or clutch because the same fluid is used for damping and sealing. The MR fluid exhibits a settling of ferromagnetic particles in contrast with FF which are stable [19, 20]. The disadvantage of MRFs is the higher friction torque compared to FFs which causes a rapid increase in the temperature of magnetic fluid in the sealed zone (gap). Urruta [10] published that the friction torque of their design of MRFs is very high—in the range 2–8 Nm at a rotation 100 rpm.

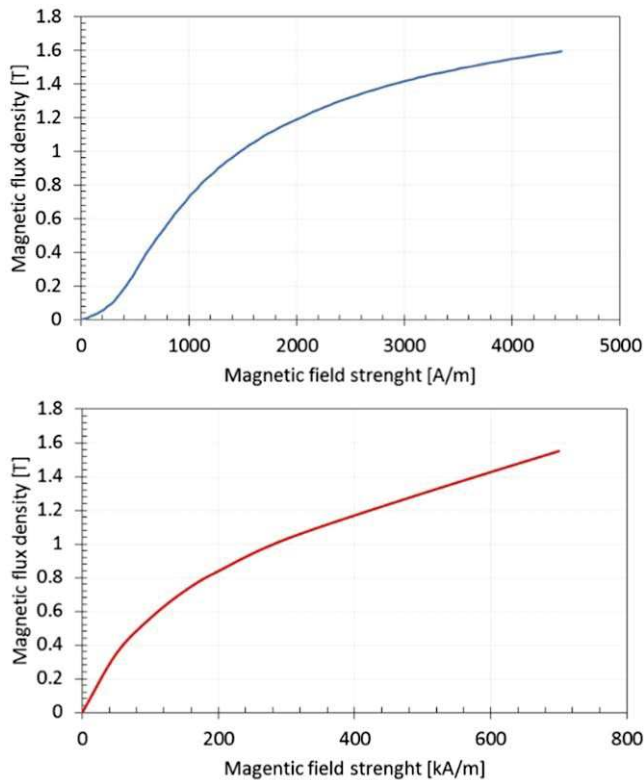


Figure 3. Virgin magnetization curve of low carbon steel S235JRG (blue), MRF-132DG made of Lord corporation (red) [25].

Hegger [21] presents MRFs of MR fluid actuator which exhibits friction torque 1.2 Nm. Such a high friction torque is obviously caused by tearing the chains of microparticles in the sealed zone during rotation.

Aim of research

The most promising area for the magnetic seal is with low friction torque and high dynamic burst pressure. The main aim of our research was to develop a new design of magnetic fluid seal which provides greater burst pressure than FFs and lower friction torque than standard MRFs.

Materials and methods

The main idea behind the new type of magnetic fluid seal

The main idea behind our new type of magnetic fluid seal with a low friction torque is based on the magnetic pinch operating mode of MR fluid, which was published by Gonçalves [22] and Goldasz [23, 24]. The main difference between the standard and magnetic pinch design of the magnetic fluid seal is the arrangement of the magnetic circuit and material of the shaft. The sealed shaft must be made from non-magnetic material—see figure 2. The magnetic circuit geometry must allow the flow of magnetic flux from one pole piece to another pole piece through a sealed zone filled by magnetic fluid. This design is specific in that the ferromagnetic particles create chain links between two pole pieces,

which is parallel to the shaft axis. There is no tearing of the particles chain and therefore, a lower friction torque is expected. The sealing effect is ensured by pressing the chains of particles on the surface of the shaft.

The MR fluid use instead of the commonly used FF should provide a greater burst pressure. In the following sections, this type of design is the so-called pinch magnetorheological fluid seal (pinch MRFs). The presented design of pinch MRFs consists of two ferromagnetic pole pieces, the electromagnetic coil, MR fluid and sealed non-magnetic shaft—see figure 2. The magnetostatic analysis was used for the proper selection of the magnetic circuit dimension respecting maximum magnetic flux density in sealed zone.

Magnetostatic model of Pinch MRFs

The magnetostatic model was created in Ansys Electronics Desktop 2017 and the geometry of the magnetic circuit was simplified to the 2D axisymmetric problem. The electromagnetic field distribution in case of magnetostatic simulation is obtained by solution of Maxwell equations below the entire domain.

$$\nabla \times \mathbf{H} = \mathbf{j}, \quad (1)$$

$$\nabla \cdot \mathbf{B} = 0, \quad (2)$$

where \mathbf{B} -magnetic flux density, \mathbf{H} -magnetic field strength, and \mathbf{j} -electric current density. The virgin magnetization curve of used low carbon steel S235JRG was set on the geometry of pole pieces—see figure 3 blue. The virgin magnetization curve of MR fluid MRF-132DG was taken from a Lord company datasheet [25].

The relative permeability $\varepsilon_r = 1.000\,021$ was set on the shaft (EN AW-2017) and ring. The geometry was discretized by 19 353 triangular elements. In the sealed zone a smooth mesh was used with average element size of 0.04 mm—see figure 4. A magnetomotive force 100 A turns was applied on the geometry of the electromagnetic coil which corresponds to an electric current of 1 A and 100 turns of the coil. The magnetostatic analysis was used for the determination of a selected dimension in the sealed zone. The magnetic flux density presented in the results is the maximum magnetic flux density on the line A–B (on the surface of the shaft)—see figure 4 left.

Calculation of burst pressure and friction torque

The internal pressure in the tested hydraulic system tends to push the MR fluid from the sealing zone to the surrounding. The MR fluid operating mode is close to the mentioned effect. In the pinch operating mode, the ferromagnetic particles are chained in a different direction than it is expected in the valve mode. Therefore, the burst pressure calculation is considered to be simplified. The burst pressure of pinch MRFs is approximately calculated by Bingham model for valve mode of MR fluid by following equation [21, 26]:

$$\Delta p = \int_{L_1}^0 \frac{c_1 \cdot \tau(B(L))}{d} dL, \quad (3)$$

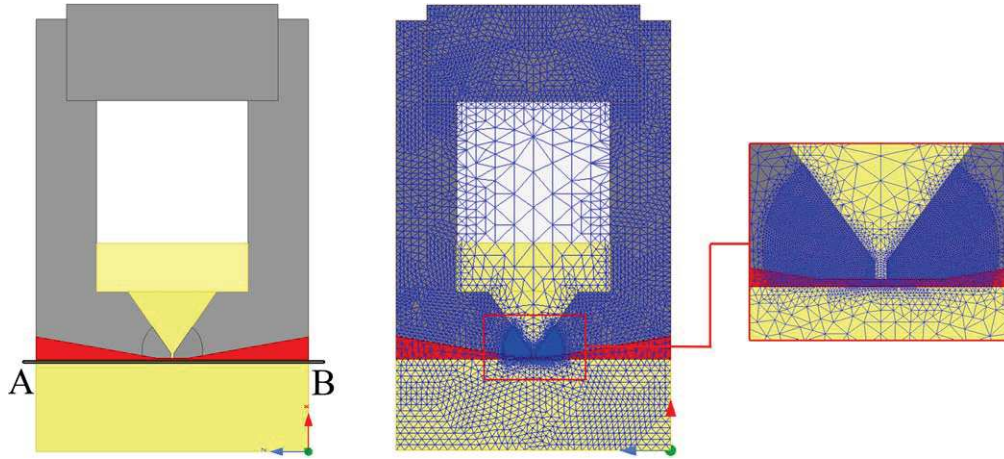


Figure 4. Geometry (left) and mesh (right) of pinch MRFs; low carbon steel (grey), aluminium alloy (yellow), MR fluid (red).

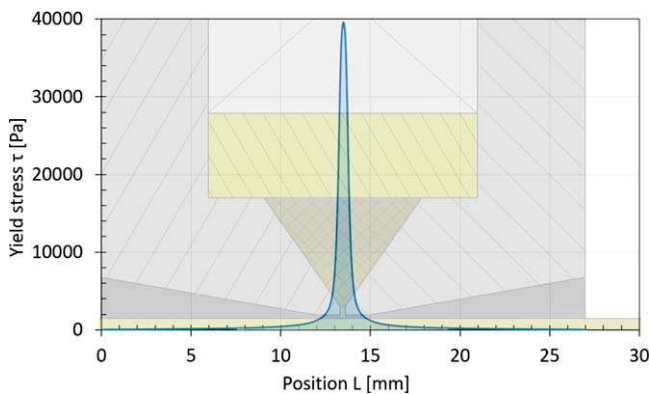


Figure 5. Yield stress of MRF on the line A–B dependency on position for electric current 1 A from magnetostatic model.

where Δp is the burst pressure of seal, d is the gap size, $\tau(B(L))$ is the yield stress of MR fluid, L_1 is the length of seal, c_1 is a parameter considered to be 3 [21].

The pole pieces are stationary and the shaft rotates during operation. This situation can be simplified by geometry of two parallel plates, one being stationary and the other in motion. This corresponds to the MR fluid shear operating mode. The friction torque calculation is based on shear mode of MR fluid by following equation:

$$M_s = \int_0^{L_1} \frac{\tau(B(L)) \cdot \pi \cdot D_2^2}{2} dL, \quad (4)$$

where M_s is the friction torque and D_2 is the sealed shaft diameter.

The shaft surface is a crucial area for burst pressure and friction torque of pinch MRFs. Therefore, the input to the equation (3) is the area under curve $\tau - L$ which corresponds to the magnetic field on shaft surface from magnetostatic model—see figure 5.

Experimental test device

The new test device was developed for testing friction torque and the burst pressure of magnetic seals—see figure 6. The

test device consists of the sealed shaft, which is supported by two bearings.

The MRF is pressured by the expansion chamber and sealed by a conventional rotational seal on the one side and by MRFs on the other side. The test device is driven by a Siemens electric motor with frequency inverter. The description of experimental test device is also presented in [27].

Friction torque measurement method

The test device was set as rotatable: it was driven by an electric motor via the clutch—see figure 6. During rotation of the shaft, the magnetic seal and the whole test device create friction torque. The value of friction torque was determined from the measured force at load cell HBM DF2SR-3 and the known length of the lever. The measured friction torque is composed of friction torque of a tested magnetic fluid seal and the friction torque of test devices (bearing, rubber seals, etc). Therefore, the friction torque of the magnetic fluid seal was determined as the difference between the measured friction torque M_m and the friction torque of the test device M_d . Every measurement had 20 s. The measured data was recorded with a sampling frequency of 100 Hz by a front-end Dewetron USB-50-USB2-8 connected to the laptop.

The first 5 s of the experiment was transitioning to the required speed of rotation. The data from the next 15 s was used for determining the average friction torque of the system—see figure 7. It was measured friction torque of test device M_d (bearings, rubber seal etc) where MRFs seal was not placed inside by presented methodology, see figure 7. This friction torque moment must be always measured after reassembling of the test device.

The friction torque of tested magnetic seal M_s was determined by the equation:

$$M_s(n) = M_m(n) - M_d(n), \quad (5)$$

where n is in rotation (1 min^{-1}). The measurements of the friction torque of the magnetic fluid seals were provided at a frequency of rotation of 20 Hz (1200 min^{-1}) for different electric currents in the range 0.3–2 A and also for rotational

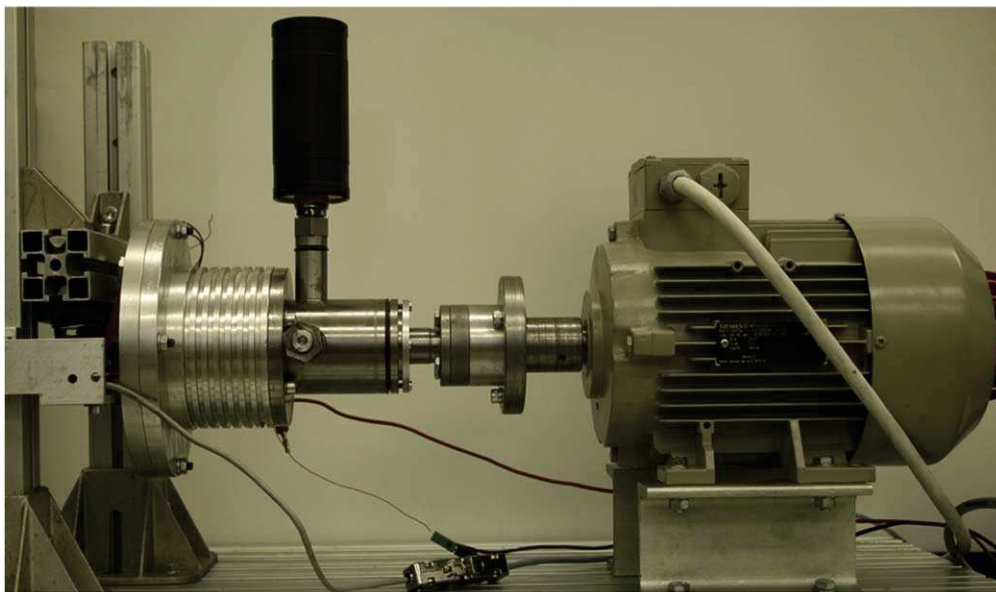
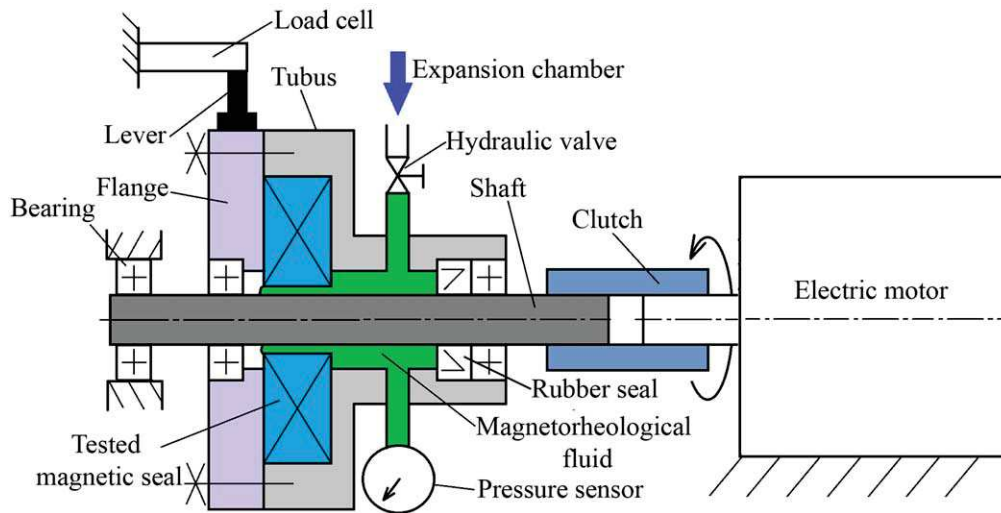


Figure 6. New experimental test devices: function principle, test devices during experiment.

speed in the range from 10 to 50 Hz for atmospheric pressure at constant electric current 1 A.

Burst pressure measurement method

The expansion chamber with the hydraulic valve and pressure sensor HBM P8AP/20 bar were connected to the test device. The hydraulic system with the tested magnetic fluid seal was pressurized by the expansion chamber with an external pump. The pressure in the hydraulic system was increased step by step during the experiment. The hydraulic valve connecting the hydraulic system and the expansion chamber was closed before the experiment because of the elimination of a gas spring, which allows the detection of an MRF leakage by the pressure drop. The burst pressure was measured as a maximum of pressure before the MR fluid leakage occurred, which was detected as the sharp pressure drop in hydraulic system—see figure 8. The pressure in the hydraulic system and rotation was measured during the experiment. An

example of the internal pressure increasing in the hydraulic system and burst pressure are shown in figure 8.

The burst pressure of the tested magnetic fluid seal was measured in static mode (0 Hz) for a different current applied on the coil in the range from 0 to 1 A. The influence of the shaft rotation on the burst pressure was measured with a constant electric current of 2 A in the coil with 100 turns.

Results and discussion

Pinch MRF

Magnetic flux lines (left) and magnetic flux density (right) from the magnetostatic analysis for an electric current of 1 A are shown in figure 9. The magnetic flux flows from one pole piece to another through the sealed zone where a sealed plug is formed. The sealed plug is a region with a high concentration of magnetic flux density in MR fluid causes high

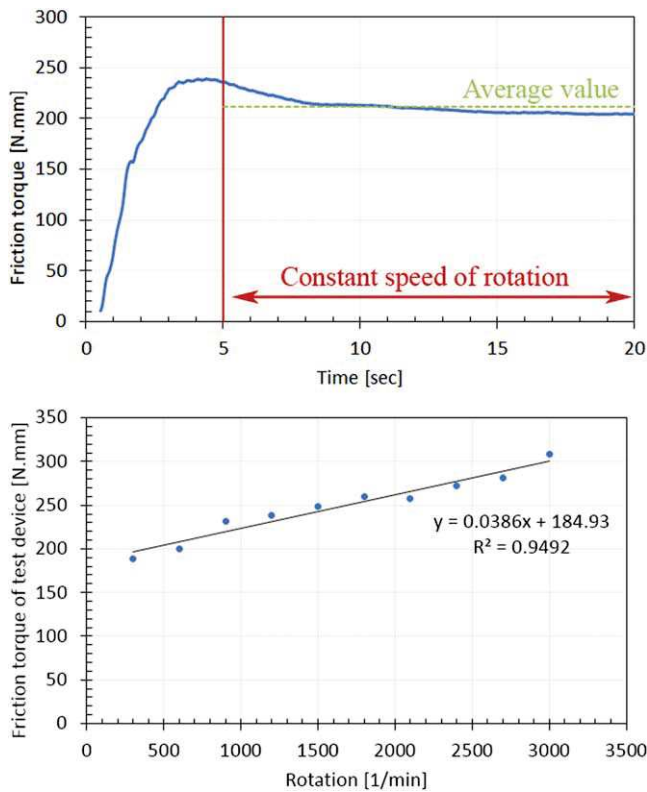


Figure 7. Example of friction torque measurement and evaluation of average friction torque of test devices (upper); friction torque of test device.

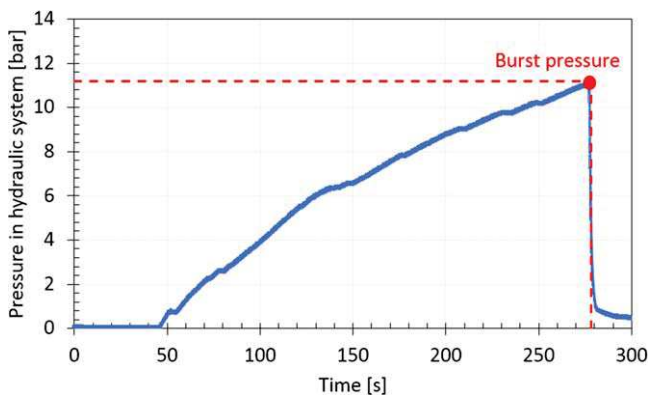


Figure 8. Example of increasing internal pressure and determination of bursts pressure; static burst pressure of pinch MRFs at electric current 1 A.

level of yield stress of MR fluid which creates the sealing effect.

The dependency of maximum flux density on the line A–B (figure 4) on an electric current is shown in figure 10. The position of line A–B is on the surface of the shaft because it is the critical area for sealing. The magnetic flux map for each point is shown in figure 10. The red colour refers to a magnetic flux density of 1 T which corresponds to the yield stress 45 kPa of MRF-132DG.

The important dimensions of the final design of pinch MRFs were determined from the magnetostatic model—see figure 11 and table 1. The influence of each dimension (b , c ,

d , α , β) on the maximum magnetic flux density on the line A–B while keeping others dimensions was tested. The most important dimensions are β , d , and c . The higher are the parameters d and c , the lower is the magnetic flux density. The higher is the parameter β , the higher is the magnetic flux density. The geometry presented in table 1 was manufactured and tested.

The standard design of MRFs (figure 1), in the next sections named standard MRFs, was also designed and manufactured for comparison of the standard and pinch version of the seal by the same methodology measurement and with the same magnetic fluid. The standard MRFs has the same packaging geometry and number of coil turns. The length of the pole piece is 6 mm. The standard MRFs contains two sealed zones compared to one sealed zone of pinch MRFs. Therefore, the friction torque and burst pressure are presented for two and one sealed zones in standard MRFs.

Friction torque of seals

The friction torque dependency on an electric current was measured for standard and pinch MRFs—see figure 12. The friction torque rapidly increases with the increasing electric current in standard MRFs. The level of friction torque 120 N mm was measured in standard MRFs at the electric current of 0.6 A (red square), which corresponds with a power loss of 15 W at a rotation of 1200 min^{-1} . For standard MRFs with one sealing zone, the friction torque is determined as half of the measured value—see figure 12 (blue triangle). The pinch MRFs exhibits constant friction torque (independent on electric current) which oscillate around 12 N mm for the whole range of the electric current (purple circle), which corresponds with a power loss of 1.5 W at a rotation of 1200 min^{-1} .

The pinch MRFs exhibits 10 times lower friction torque than standard MRFs with two sealed zones and 5 times lower friction torque than standard MRFs with one sealed zone at an electric current of 0.6 A. This ratio significantly increases with the increase of the electric current. It should be noted that the friction torque was measured with no internal pressure in the MRF. The difference between the presented friction torque model and experiment at the electric current 0.6 A was 40%. The measured data oscillates around calculated data. The oscillations are probably due to the accuracy of the measurement method of friction torque itself. The friction torque dependency on rotational speed was also measured for standard and pinch MRFs at the electric current 1 A—see figure 13. The friction torque rapidly increases with the increasing rotation for each MRFs. However, the rotation increase is less significant than the electric current.

Static burst pressure of seals

The static burst pressure dependency on an electric current was measured for standard and pinch MRFs—see figure 14.

The static burst pressure increases with the increasing electric current in both MRFs. However, the increase of burst pressure of pinch MRFs between 0 and 0.4 A is significantly

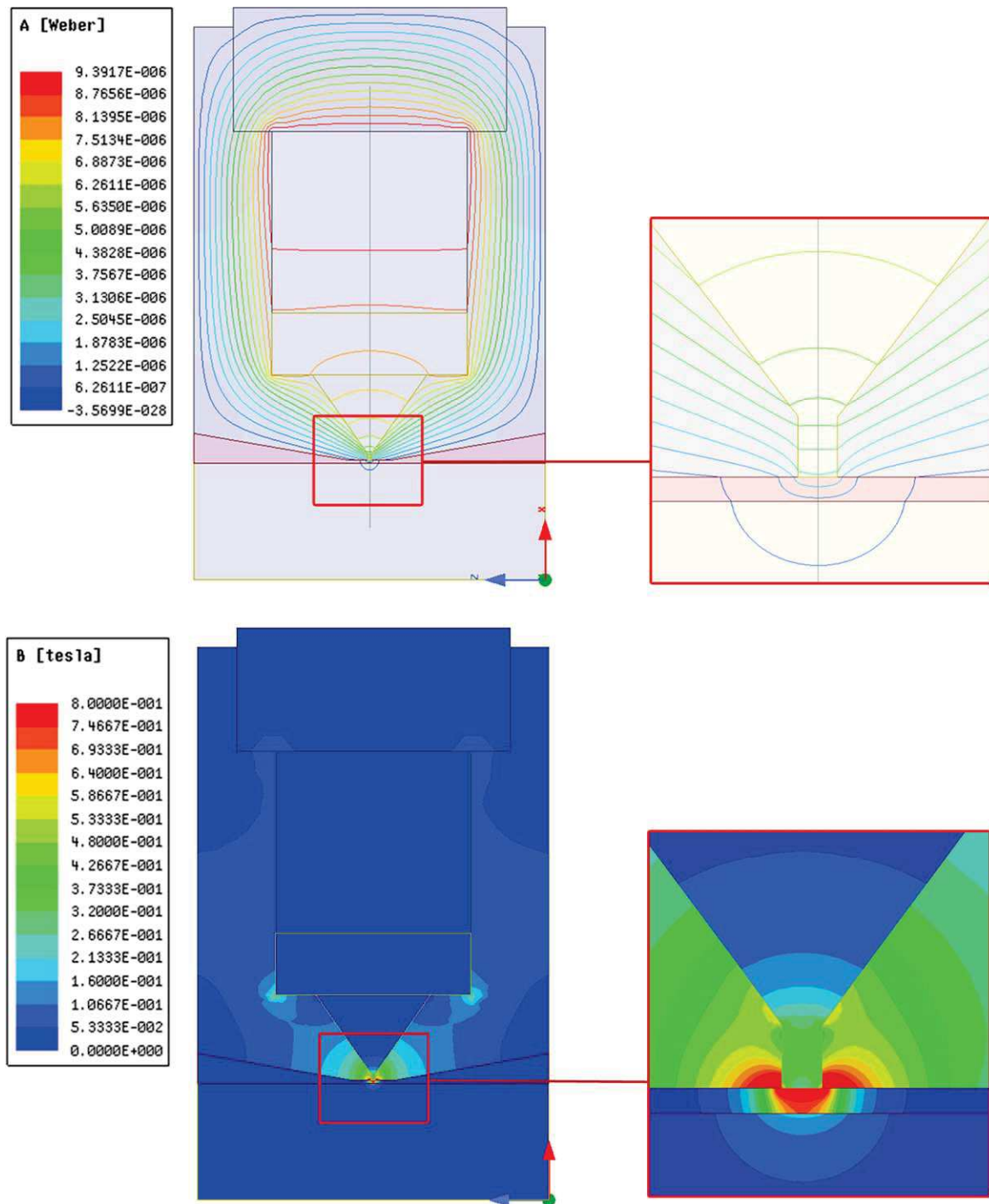


Figure 9. Magnetic flux lines (up); magnetic flux density (down).

lower in comparison to the burst pressure increase in standard MRFs.

Presumably, the ferromagnetic particles are not sufficiently pressed on the shaft surface at low electric current. After exceeding 0.4 A, a significant increase in burst pressure was observed. The standard MRFs with one sealed zone achieved approximately 1.8 times higher burst pressure than pinch variant at electric current 0.6 A. The static burst pressure is similar between standard MRFs with one sealed zone and pinch MRFs at electric current 0.8 A. Presented static

burst pressure model describes well measured data in the range 0.5–0.7 A. However, the model is inaccurate in other cases of electric current. This big difference is probably due to neglecting the direction of the ferromagnetic particle chaining in the model.

The problem of carrier fluid leakage in standard MRFs through the sealed zone was observed—see figure 15.

Similar observation presented Hegger [21]. The leakage causes a gradual decrease in internal pressure in the tested system during measurement. The first small volume of leakage

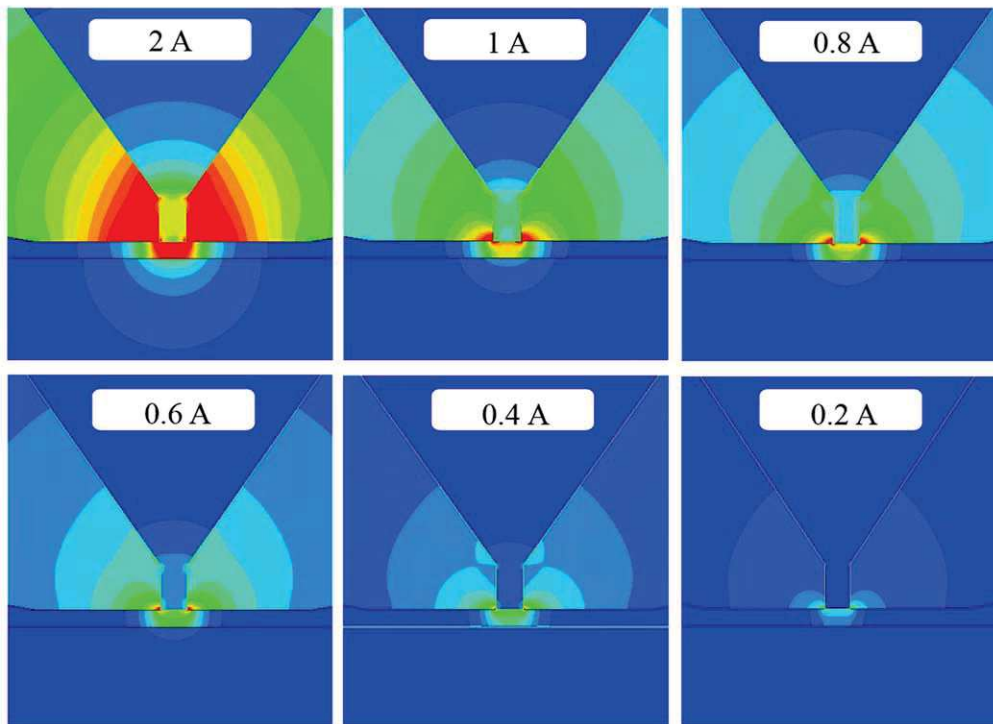
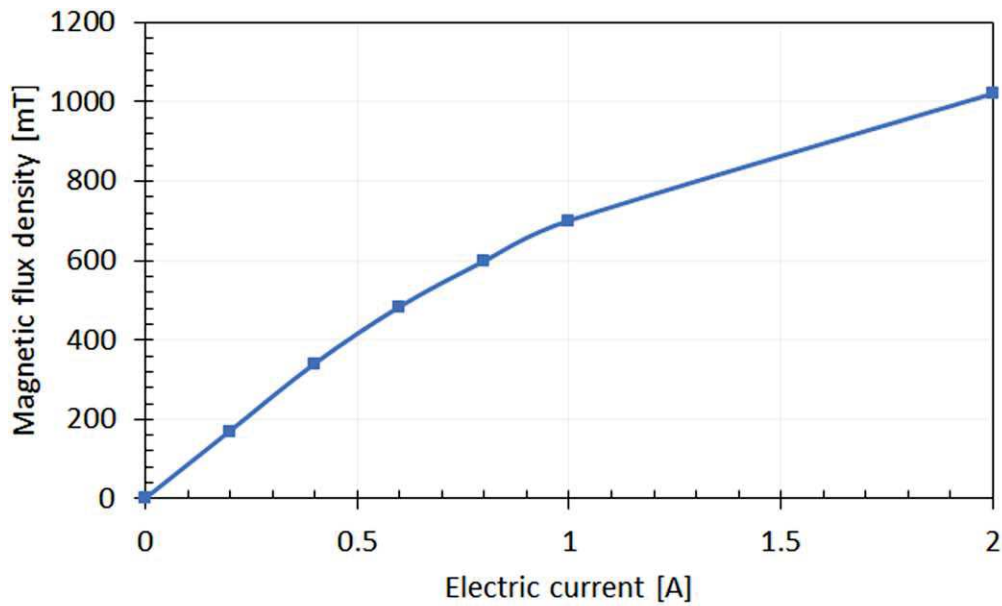


Figure 10. Maximum magnetic flux density on the surface of shaft dependency on electric current (left), magnetic flux density map for different current with constant scale (right).

fluid was observed after 3 min of the experiment. The fluid was accumulated at the bottom of the gap due to gravitation. The significant fluid volume leakage was observed after 9 min. In this case, the internal pressure gradually decreases from 7 to 0 bar. The pinch MRFs exhibit no leakage of carrier fluid in contrast with standard MRFs. The carrier fluid in the standard MRFs percolated through the sieve of chained ferromagnetic particles. The carrier fluid is held in spaces between the particle chains by capillary forces [21]. For the leakage reduction it is possible to use the lower size of the ferromagnetic particles,

increase the viscosity of the carrier fluid or the addition of nanoparticles. However, the leakage of carrier fluid is a major problem for long-term operation of MRFs and there is no mechanism to re-mix MRF.

Dynamic burst pressure

Figure 16 shows the measured influence of the shaft rotation on burst pressure of pinch MRFs at an electric current of 2 A. The burst pressure significantly decreases with the increasing

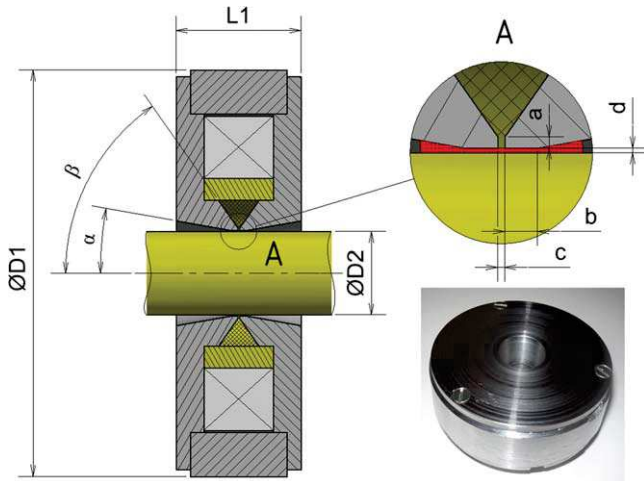


Figure 11. The important dimensions of pinch MRFs.

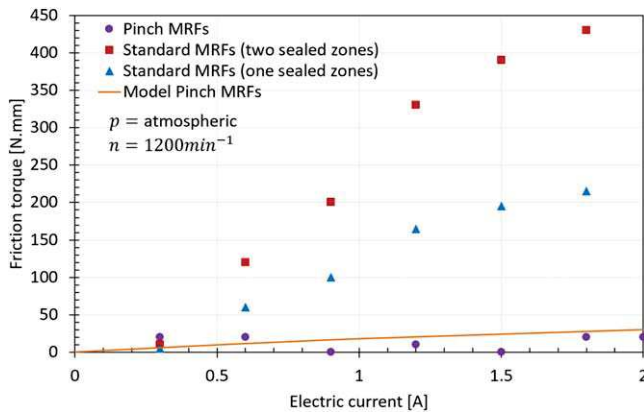


Figure 12. Friction torque of standard and pinch MRFs dependency on electric current.

Table 1. The dimension of pinch MRFs from magnetostatic model.

Name	Value	Unit	Name	Value	Unit
<i>a</i>	0.3	mm	<i>D</i> ₂	18	mm
<i>b</i>	1.4	mm	<i>L</i> ₁	27	mm
<i>c</i>	0.5	mm	<i>α</i>	10	deg
<i>d</i>	0.2	mm	<i>β</i>	55	deg
<i>D</i> ₁	88	mm			

rotation of the shaft. The measured data was approximated by the power function with exponent -1.025 .

The presented burst pressure of pinch MRFs at a high-speed rotation is significantly higher than the published design of FFs. The second advantage is that the pinch MRFs are not sensitive to magnetic shunt, which is dangerous especially in the design with the small sealing gap, as with standard MRFs or FFs. The significant leakage of carrier fluid was observed during the measurement of standard MRFs with rotation by the same methodology. Therefore, it was not possible to determine burst pressure dependence on rotation in standard MRFs.

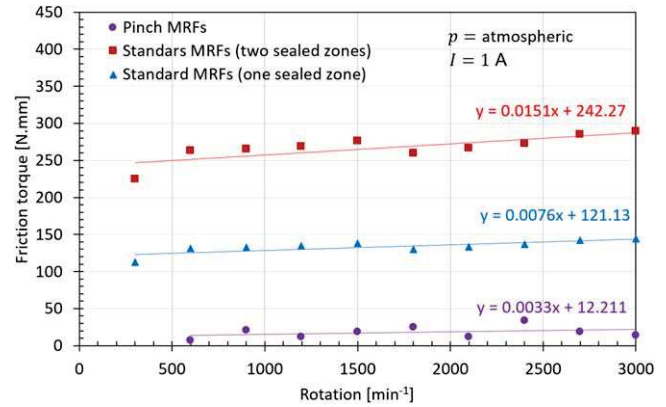


Figure 13. Friction torque of standard and pinch MRFs dependency on rotation.

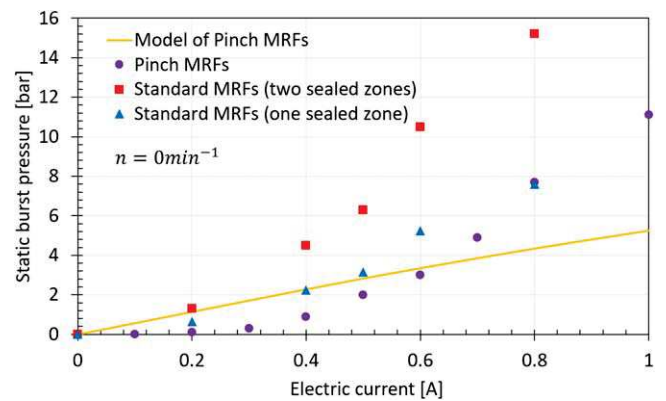


Figure 14. Static burst pressure of standard and pinch MRFs dependency on electric current.

Conclusion

In this paper, the novel MRF with low friction torque was designed and tested. The presented novel design of MRFs is based on the pinch mode of MRF and combines advantages of FFs and standard MRFs. The results are summarized in the following points:

- The presented pinch version of MRFs exhibits much lower friction torque (12 N mm) than standard MRFs (two sealed zones 120 N mm and one sealed zone 60 N mm) at the same rotation (1200 min^{-1}) and electric current (0.6 A). The friction torque of pinch MRFs is independent on the magnetic field in the sealed zone because it is caused only by liquid friction.
- The static burst pressure of pinch MRFs is lower (1.8 times) than standard MRFs with one sealed zone at the same electric current (0.6 A). However, the static pressure of pinch MRFs is higher than any pressure burst measured with FFs.
- The burst pressure of pinch MRFs is influenced by shaft rotation, according to experiments.
- The pinch MRFs allows sealing of a shaft made of non-magnetic material.

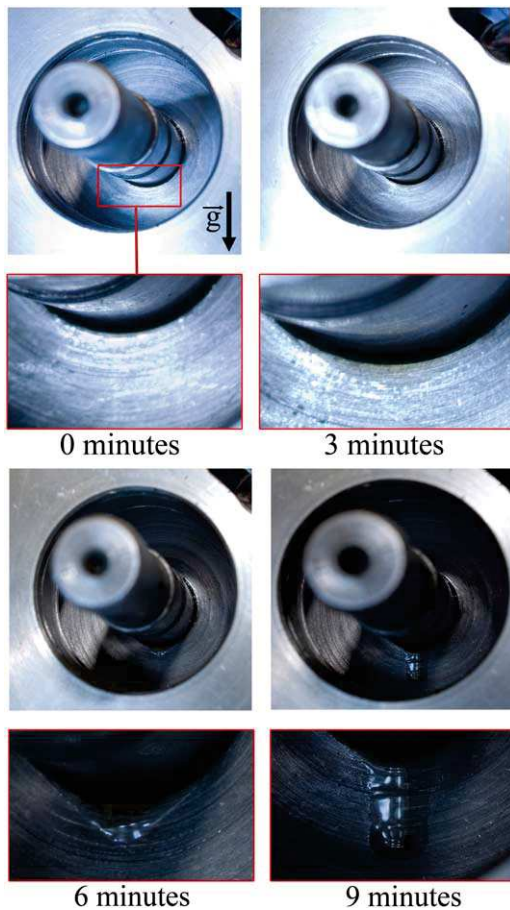


Figure 15. Leakage of carrier fluid through the sealed zone in standard MRFs.

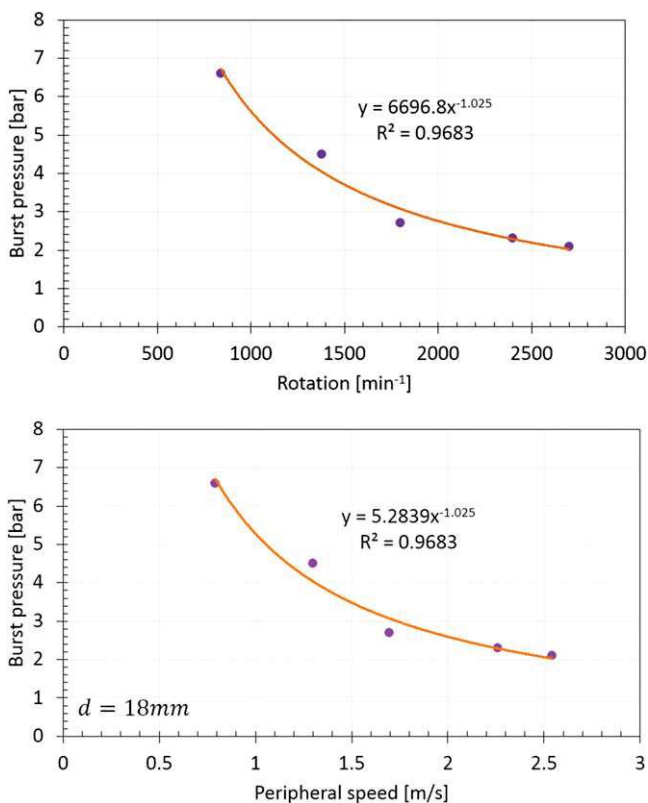


Figure 16. Influence of rotation to burst pressure of pinch MRFs.

- The leakage of carrier fluid of standard MRFs was observed visually and by a pressure drop in the tested system. The leakage was observed in static mode; however, it was more intense with the shaft rotation. This problem was not observed in pinch MRFs.

The future research will be focused on testing pinch MRFs for the sealing of sliding movement. The influence of surface roughness or wear of the shaft on the friction torque and burst pressure or a new model that will more accurately describe the burst pressure of the pinch MRFs will also be the subject of future research.

Acknowledgments

This paper and experiments have been made possible thanks to the kind sponsorship of various grants and numerous agencies. We would like to thank specifically the GAČR 17-10660 J, GAČR 17-26162 S and FSI-S-17-4428.

ORCID iDs

M Kubík <https://orcid.org/0000-0003-0105-2921>

Z Strecker <https://orcid.org/0000-0002-1598-487X>

References

- [1] Rabinow J 1948 The magnetic fluid clutch *Trans. Am. Inst. Electr. Eng.* **67** 1308–15
- [2] Papell S 1965 Low viscosity magnetic fluid obtained by the colloidal suspensions of magnetic particles *US Patent* 31509663A
- [3] Matuszewski L and Szydło Z 2008 The application of magnetic fluids in sealing nodes designed for operation in difficult conditions and in machines used in sea environment *Pol. Marit. Res.* **3** 49–58
- [4] Ferrotec (USA) Corporation 2001 FerroTec history
- [5] Cong M, Dai P and Shi H 2009 A study on wafer-handling robot with coaxial twin-shaft magnetic fluid seals *Intell. Robot. Appl.* **1123–37**
- [6] Kordonski W I and Gorodkin S R 1996 Magnetorheological fluid-based seal *J. Intell. Mater. Syst. Struct.* **7** 0–3
- [7] Szczęch M and Horak W 2015 Tightness testing of rotary ferromagnetic fluid seal working in water environment *Ind. Lubr. Tribol.* **67** 455–9
- [8] Tomioka J and Miyanaga N 2017 Blood sealing properties of magnetic fluid seals *Tribol. Int.* **113** 338–43
- [9] Szczęch M 2018 Experimental study on the pressure distribution mechanism among stages of the magnetic fluid seal *IEEE Trans. Magn.* **54** 1–7
- [10] Urreta H, Aguirre G, Kuzhir P and Lopez de Lacalle L N 2018 Seals based on magnetic fluids for high precision spindles of machine tools *Int. J. Precis. Eng. Manuf.* **19** 495–503
- [11] Szczęch M and Horak W 2017 The influence of selected parameters on magnetic fluid seal tightness and motion resistance *Tribologia* **4** 71–6
- [12] Chen Y, Li D, Zhang Y and He C 2018 Numerical analysis and experimental study on magnetic fluid reciprocating seals *IEEE Trans. Magn.* **55** 1–6

- [13] Kubík M, Macháček O, Strecker Z, Roupec J and Mazůrek I 2017 Design and testing of magnetorheological valve with fast force response time and great dynamic force range *Smart Mater. Struct.* **26** 1-9
- [14] Strecker Z, Roupec J, Mazurek I, Machacek O, Kubik M and Klapka M 2015 Design of magnetorheological damper with short time response *J. Intell. Mater. Syst. Struct.* **26** 1951-8
- [15] Ubaidillah U, Imaduddin F, Nizam M and Mazlan S A 2015 Response of A Magnetorheological Brake under Inertial Loads *Int. J. Electr. Eng. Inform.* **7** 308-22
- [16] Goldasz J and Sapiński B 2011 Modeling of magnetorheological mounts in various operation mode *Acta Mech. Autom.* **5** 29-39
- [17] Potoczny M and Zachara B 2012 Influence of magnetorheological fluid volume onto obtained critical pressures on rotary shaft seals *Key Eng. Mater.* **490** 119-27
- [18] Zhang Y and Chen Y 2018 A comparative study of ferrofluid seal and magnetorheological fluid seal *IEEE Trans. Magn.* **54** 1-7
- [19] Niu F H, Hu Z D, Yan H, Zhang H S and Yang J J 2018 Sedimentation and redispersibility of magnetorheological suspensions while settling under gravity *Smart Mater. Struct.* **27** 12
- [20] Roupec J, Berka P, Mazůrek I, Strecker Z, Kubík M, Macháček O and Andani M T 2017 A novel method for measurement of MR fluid sedimentation and its experimental verification *Smart Mater. Struct.* **26** 107001
- [21] Hegger C and Maas J 2018 Smart sealing for magnetorheological fluid actuators *J. Intell. Mater. Syst. Struct.* **1-12**1045389X1775426
- [22] Goncalves F D and Carlson J D 2009 An alternate operation mode for MR fluids—Magnetic Gradient Pinch *J. Phys.: Conf. Ser.* **149** 4
- [23] Goldasz J and Sapiński B 2017 Magnetostatic analysis of a pinch mode magnetorheological valve *Acta Mech. Autom.* **11** 229-32
- [24] Goldasz J and Sapiński B 2015 *Insight into Magnetorheological Shock Absorbers* (Cham: Springer International Publishing) (<https://doi.org/10.1007/978-3-319-13233-4>)
- [25] LORD corporation 2011 *MRF-132DG Magneto-Rheological Fluid* Lord technical data Lord corporation 2
- [26] Zhao S, Sheng Q, Lin S, Zhang F and Jiao L 2016 The model of seal mechanism for magnetic fluid and related experimental study *Mechanika* **22** 260-4
- [27] Kubík M, Macháček O and Mazůrek I 2018 Magnetorheological fluid seal with minimum friction torque *Eng. Mech.* **2018** 445-8

Structured magnetic circuit for magnetorheological damper made by selective laser melting technology

Zbyněk Strecker[✉], Michal Kubík[✉], Petr Vítek, Jakub Roupec, David Paloušek and Vít Šreibr

Faculty of Mechanical Engineering, Brno University of Technology, Brno, Czech Republic

E-mail: strecker@fme.vutbr.cz

Received 2 January 2019, revised 13 February 2019

Accepted for publication 28 February 2019

Published 5 April 2019



CrossMark

Abstract

Eddy currents are the main reason causing for the long response time of a magnetorheological (MR) damper. Eddy currents are often unwanted parasitic phenomenon for many electromagnetic machines working with an alternating magnetic field. Their reduction can be secured by the use of material with high electrical resistivity such as ferrites or soft magnetic composites. These materials, however, exhibit bad mechanical properties and cannot be used in mechanically loaded parts. Eddy currents can also be reduced by the appropriate structure which must secure high conductivity for the magnetic flux but low electrical conductivity for the electric current flowing perpendicularly to the magnetic flux. This leads to complex structures which, in most cases, cannot be manufactured by conventional methods. This paper describes the design, manufacturing and verification of simulations of the magnetic circuit for a MR damper. Structured magnetic cores printed by selective laser melting technology connects the benefits of low-carbon steel (good mechanical properties, high magnetic saturation and high relative permeability) with benefits of sintered materials (high electric resistivity). The results proved that using the potential of additive manufacturing can not only reduce the eddy currents (and thus shorten the response time and reduce losses), but significantly reduce the weight as well. This technology enables the combination of performance parameters of electromagnetic machines, which cannot be reached by any other existing method.

Keywords: selective laser melting, eddy currents, magnetorheological damper, magnetic circuit, beam structures, response time

(Some figures may appear in colour only in the online journal)

1. Introduction

The magnetic design of a magnetorheological (MR) damper piston determines the two main performance features of the MR damper—response time and dynamic force range. Many designs of MR dampers were focused on maximizing the dynamic force range [1–4]. The measurements of a commercial MR damper's secondary response time (0%–95%) quantified it to 20 ms [5]. The overall response time of MR damper is also strongly dependent on the power supply type for the coil. The use of current controller instead of the voltage controller can significantly reduce the overall

response time [6]. Although many studies simulating suspension systems with MR dampers controlled by semi-active algorithms do not take into consideration the response time of MR dampers [7–9], papers [10–12] showed the considerable influence of the MR damper response time on suspension efficiency. The simulations and measurements showed that for a passenger car with a typical unsprung mass natural frequency of 18 Hz, the primary response time (0%–63%) must be much shorter than 8 ms. The use of an MR damper with a longer response time in the suspension system controlled by a modified groundhook algorithm can not improve the grip of the wheel.

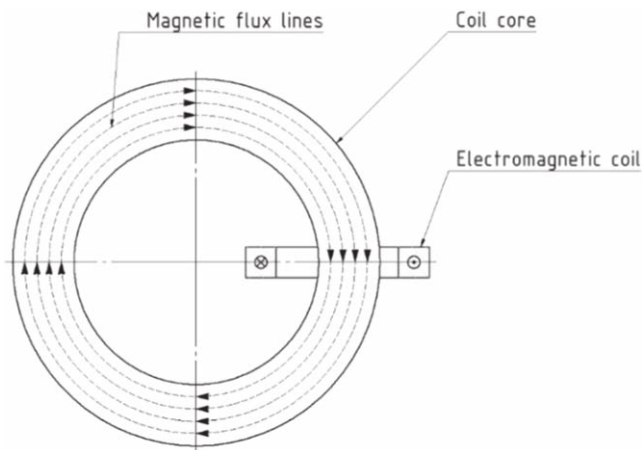


Figure 1. Magnetic flux lines in toroid core.

There are, therefore, efforts to develop the MR damper with a shorter response time. The main reason for the MR damper's long response time is that the pistons are usually made of steel, thus the eddy currents are induced in the piston during rapid changes of magnetic field. One way of achieving the short response time is the use of material with high electric resistivity such as ferrite N87 [13], or soft magnetic composites [14]. Such constructions can secure the overall response time of the damper up to 1.5 ms. Dampers with pistons made of ferrite or SMC material, however, exhibit smaller magnetic saturation or smaller relative magnetic permeability causing a reduced dynamic force range. Other disadvantages are the bad mechanical properties and poor machinability. It is also possible to use cobalt alloys like Vacoflux with several times higher resistivity than constructional steel [15] and with good mechanical properties. The eddy currents are, however, reduced only partly in this case. The second way is the shape approach. Axial grooves intersecting the path of eddy currents can significantly reduce their magnitude [16]. There are, however, technological limitations for fabrication of the grooves.

Simple grooves are not the most advantageous shape of insulation. There is a more efficient way of reducing the eddy currents, as described in the patent [17]. The principle of the structured core design can be explained on a simple toroid core. Figure 1 shows the shape of magnetic flux lines in the toroid core. Figure 2 shows the vector of magnetic flux density in the cross-section plane and figure 3 shows the vectors of generated eddy currents, which are always in a perpendicular plane to the magnetic flux lines. The structure consisting of rods following the magnetic flux lines in the steady state and isolated from each other (as shown in figure 4) should significantly reduce the eddy currents. The optimization of structures can also provide further benefits in the lower weight and better cooling of the core. Such a structure has been either very difficult or impossible to manufacture by conventional machining.

Such structures can be, however, fabricated by additive manufacturing. Selective laser melting (SLM) processing strategy for strut-lattice structure production was described by Vrána [18]. Different process parameters must be used for

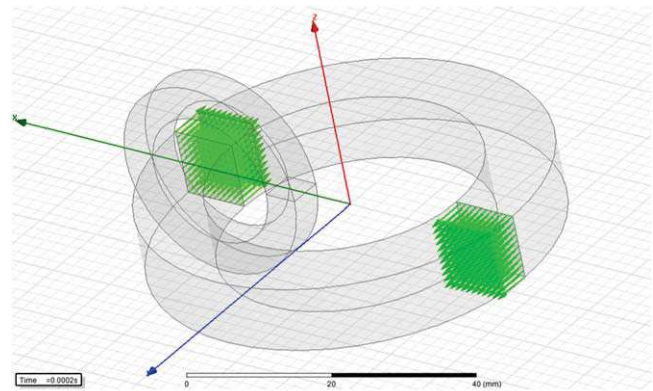


Figure 2. Visualization of magnetic flux on the cross-section plane.

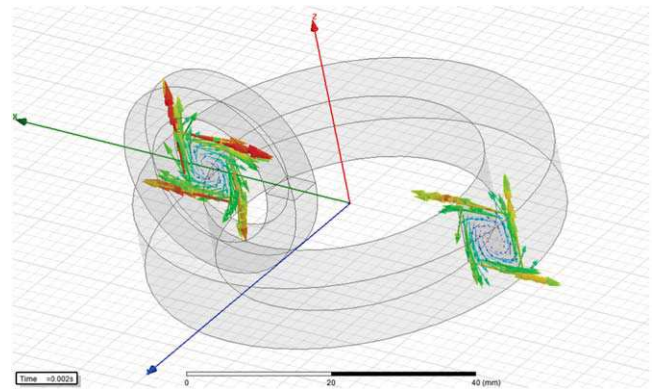


Figure 3. Visualization of eddy currents generated cross-section plane.

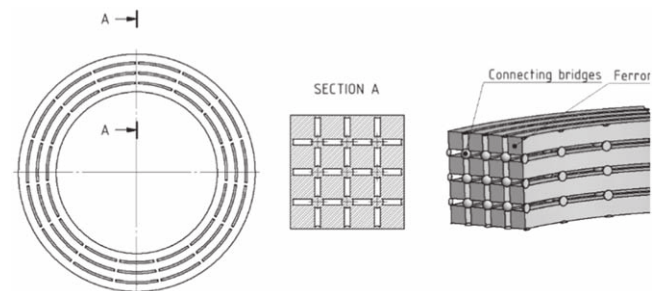


Figure 4. Structure advantageous in elimination of eddy currents.

structures and solid material. Recently, the possibility of printing from magnetically conductive materials was presented by several teams. Zhang *et al* [19–21] described and experimentally evaluated printing parameters of Fe–Ni alloy. Palousek *et al* [22] demonstrated the possibility of print from pure iron. Garibaldi [23] was able to print parts from Fe–Si steel, which is very suitable for the magnetic circuit.

This paper describes the design and experimental evaluation of a structured core for an MR damper made of pure iron manufactured by 3D SLM print. The aim of the research was to create the MR damper with a short response time, great dynamic force range, good mechanical properties and low weight.

Table 1. Particle size distribution of ATOMET FeAM powder.

D10%	15 μm
D50%	28 μm
D90%	44 μm
D99%	60 μm

2. Materials and methods

2.1. Material properties

The structured cores were designed and printed from >99.8 % pure iron. Although silicone steel has better properties for magnetic circuits working with AC magnetic fields, the pure iron was selected because of good SLM manufacturability and availability of powdery state. ATOMET FeAM powder with size distribution according to the table 1 was supplied by the Rio Tinto company.

This material is, however, not advantageous for electromagnetic circuits because of its high electric conductivity. For future application, silicone steel or cobalt iron alloy promises much better performance. However, excessive research in printing parameters must be performed.

Magnetic material properties were measured on 4 toroid samples (inner diameter 34 mm, outer diameter 40 mm and thickness 5 mm) on a Remagraph machine. The printing parameters were according to the table 2.

Magnetic properties, especially relative permeability, may be affected by heat treatment during the manufacture. Therefore, the set of two sample toroids were printed for each set of printing parameters. One toroid from the set was annealed, one of them not. Subsequently, magnetic properties of the samples were compared. The heat treated samples were firstly packed into the austenitic foil and inserted into annealing furnace. The samples were annealed at 950 °C for 4 h, consequently slowly cooled down in the closed, turned off annealing furnace.

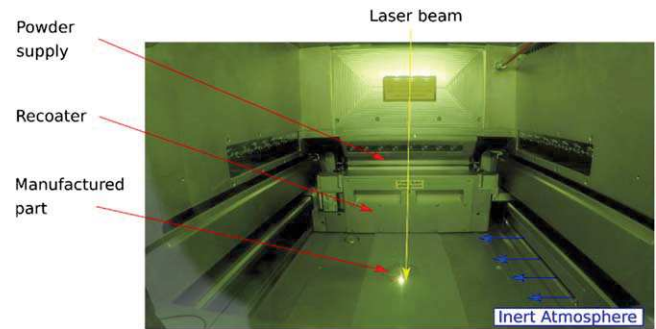
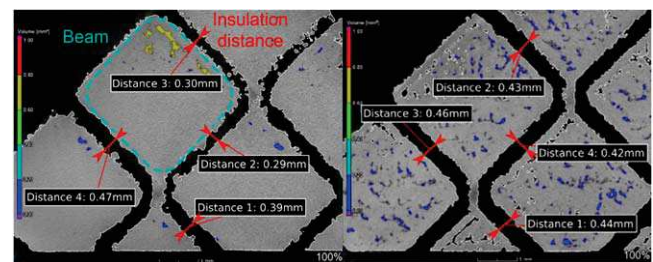
The electric resistivity of the printed material was measured on block samples with dimensions 5 × 5 × 90 mm. The measured ultimate tensile strength of heat treated samples was 315 MPa.

2.2. Principle and limitations of SLM printing

The principle of SLM printing is shown in figure 5. The printed part is sliced into layers with a defined thickness, which are printed separately. As a first step, the recoater spreads the defined thickness of the metal powder from the powder supply container to the build chamber. Consequently, the laser beam is focused on the places with final geometry and melts the powder. After melting all the geometry in the processed layer, the base plate moves one step down and the recoater spreads the next layer and the whole process is repeated. The printing chamber is pre-heated and filled with an inert atmosphere. Although in theory this principle enables the printing of almost any shape, in reality the final print quality has many limitations. The biggest limitation is

Table 2. Printing parameters of samples for *B–H* curve measurement.

	Annealing	Power	Scanning velocity	Hatch distance
Sample A	No	400 W	750 mm s ⁻¹	90 μm
Sample B	Yes	400 W	750 mm s ⁻¹	90 μm
Sample C	No	200 W	300 mm s ⁻¹	117 μm
Sample D	Yes	200 W	300 mm s ⁻¹	117 μm

**Figure 5.** The principle of 3D SLM print.**Figure 6.** Dimension analysis of samples printed with different printing parameters (cross section of beams).

probably the deformation of layers due to thermal expansion. The layer cools down unequally, which develops the mechanical stress. This stress causes shape deformation in the printed part. In order to minimize this effect, the processed layer must be connected to the previous layer or to the base plate or the heat is dissipated through supports. The various heat conductivity in specific points of a printed part also influences the temperature of melting. The forming of the weld is influenced not only by laser power and scanning velocity (and therefore energy), but by the speed of the heat transfer from the melt pool as well. The heat from the laser is transferred to the platform, to the powder and to the supports. Thin walls transfer heat faster than volumetric parts, which thus keeps a higher temperature inside. Therefore, different process parameters have to be set for thin walls and for volumetric parts. Figure 6 shows the magnified section of the same geometry printed with different laser parameters. The section from the left picture shows lower porosity, but the surface roughness is inappropriate for thin walls. Based on the results, process parameters of the hatching of the first sample and border settings of the second sample were combined. Values of the chosen parameters are described in table 3.

Table 3. Process parameters used for 3D printing of the core.

<i>Hatching</i>	
Laser power	200 W
Scanning velocity	300 mm s ⁻¹
Hatch distance	117 μm
Layer thickness	50 μm
<i>Borders</i>	
Laser power	100 W
Scanning velocity	400 mm s ⁻¹

Table 4. Definition of current for transient simulation.

Current rise		Current drop	
Time (ms)	Current (A)	Time (ms)	Current (A)
0	0	0	2
1	0	1	2
1.3	2	1.3	0
25	2	25	0

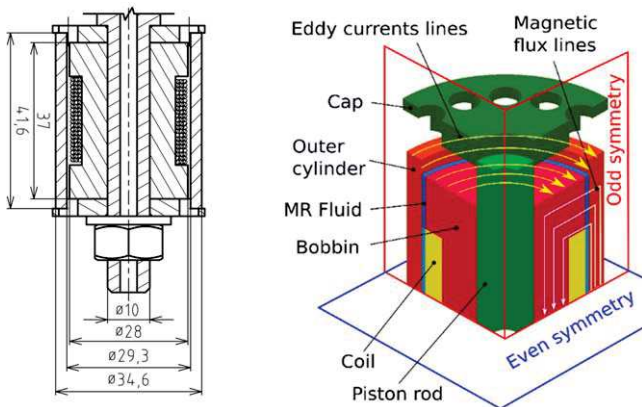


Figure 7. Geometry of the simulated piston (a) dimensions, (b) 1/8 section used for simulations—full variant.

Based on empirical results of the 3D print, the minimal insulation distance (figure 6) in the virtual model for the beams was chosen at 0.5 mm, the thinnest wall was chosen at 0.2 mm. It is clear that a decrease in the insulation distance would cause individual beams to meet in some places and therefore the degradation of eddy currents elimination.

2.3. Magnetic simulation of the piston

The magnetic model was created in Ansys Electronics 17.1. Due to the nature of the task, the simulation model was performed in 3D. Thanks to the geometrical symmetry of the MR damper piston, the simulation model has been simplified to 1/8 as is shown in figure 7. The gap was filled with air or MR fluid LORD MRF-132DG (*B–H* curve from datasheet).

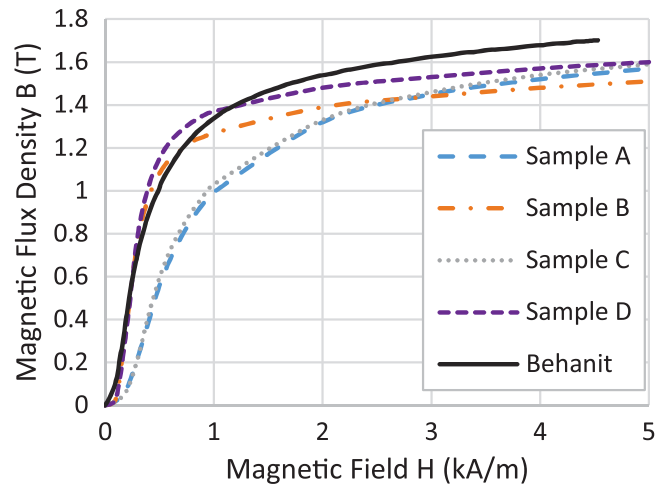


Figure 8. Electric circuit used for magnetic simulations.

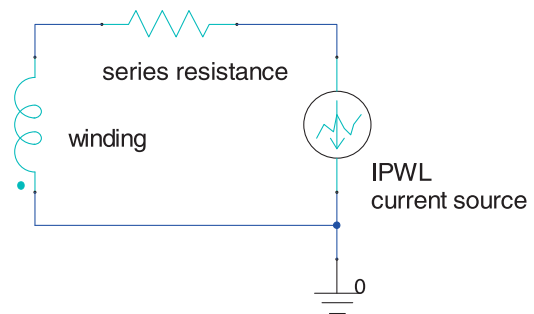


Figure 9. Measured *B–H* curves.

The piston-rod is made of steel S235JRG. The *B–H* curves for the bobbin and outer cylinder correspond to the pure iron (commercial name Behanit) (figure 8). The winding consisted of 120 turns. The coil was excited by the electric circuit (figure 9) with piecewise linear current supply (IPWL) with the course of current according to table 4. The electric rise and drop of the electric current were chosen according to the measured real currents. The series resistance was 1.1 Ω. Two types of simulations were performed—static simulations to determine *B–I* dependency and transient simulations to determine the response of magnetic flux density in the gap. The time step of transient analysis was time-dependent and varied from 0.05 to 2 ms, the length-based mesh consisted of 29 892 elements in the case of the solid MR piston and 213 372 elements in the case of the geometrically optimized MR piston. The static simulations were done for currents between 0 and 5 A. The transient simulations were done for current decrease linearly from 2 to 0 A during 0.3 ms.

2.4. Design of the structure

The structures were designed according to the patent [17]. Firstly, the magnetostatic model of the solid piston was done and the shape of the magnetic flux lines was found (figure 7(b), figure 10). Consequently, the individual beams were created by

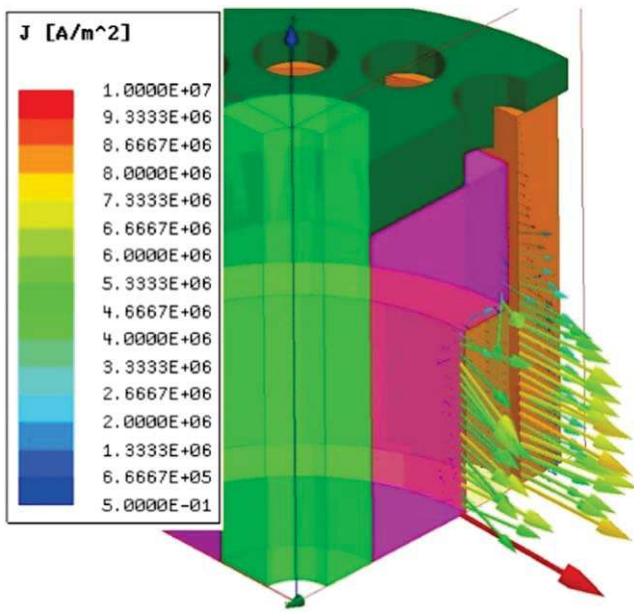


Figure 10. The vector of current density 1 ms after turning the current off.

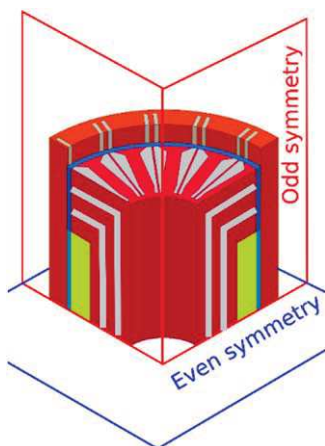


Figure 11. Initial structured variant.

sweeping the profile curve along the magnetic flux line curve (figures 11 and 12). The eddy currents generated during the rapid change of the magnetic flux are always in a perpendicular plane to the magnetic flux, as is also shown in figure 7(b). This figure, however, shows only the assumed direction in the piston geometry. The exact density of the electric current in time is, in the case of complex geometry, impossible to calculate analytically and therefore, the FEM model must be used. Figure 11 shows the initial design of the structure which should decrease the flow of eddy currents. Without an FEM model, it is not possible to quantize the reduction of eddy currents and also to determine the reduction of the response time.

The simulated magnetic flux distribution of a full piston version is shown in figure 13, the current density in the time

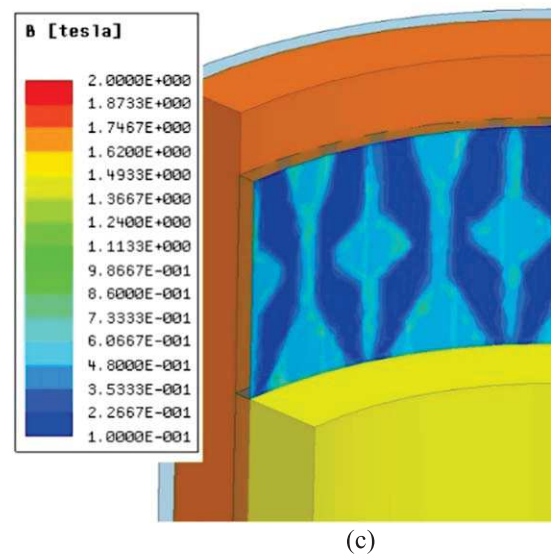
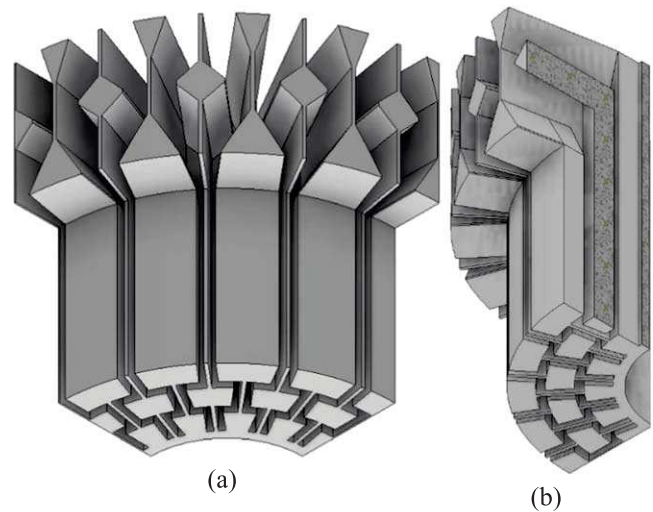


Figure 12. Structured core 2—constant cross-section for magnetic flux.

of 1 ms after turning off the electric current to the coil is shown in figure 10. It is obvious that eddy currents are not distributed homogeneously. The majority of eddy currents flow close to the surface of the bobbin and outer cylinder.

With the help of the model, it is possible to tune the structure according to the main demands. If the response time is preferred, the structure will consist of many thin beams. Isolation distances around the beams will, unfortunately, reduce the cross-section of material usable for magnetic flux which will decrease the dynamic force range. If the dynamic force range is preferred, the structure will consist of beams with a bigger cross-section or from a structure with beams only in places with a high eddy-current density. The minimization of weight is possible by keeping the same cross-section for the magnetic flux equal within the whole magnetic circuit. This cross-section is given by the plane with the smallest

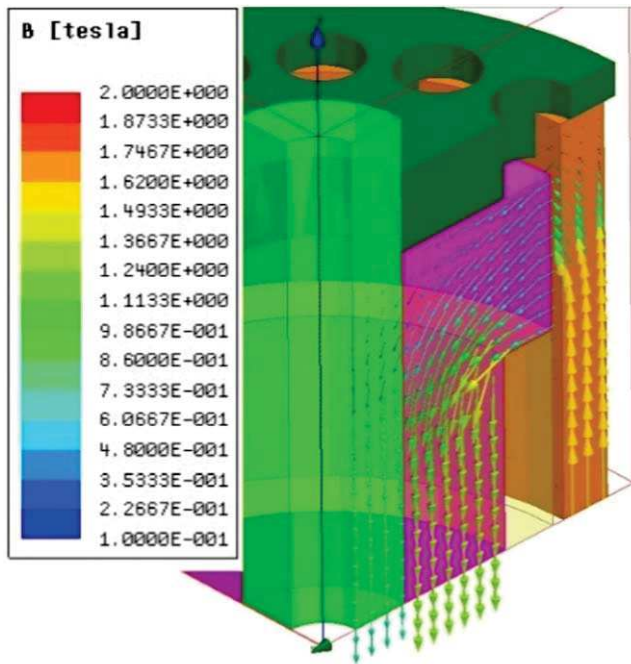


Figure 13. The vector of magnetic flux density (steady state).

cross-section (in full material model). The final design of the structure is always a trade-off between response time, dynamic force range and the weight of the MR damper's magnetic circuit.

The smallest insulation distance and the thinnest wall in the model were chosen as 0.3 mm. The space between the beams was filled by two-component plastic—PR751.

2.5. Experimental setup for measurement of response time and B - I curve on air

This measurement was carried out for the verification of the simulation model. The output from the model was a magnetic flux density in the gap at various times after the electric current to the coil was switched on or switched off. The simulations were calculated with the MRF in the gap. However, for comparison of the model and the measurement, air was used in the gap instead of the MRF. The measurement of magnetic flux density by a Hall probe can only be conducted in environment with relative permeability $\mu_r = 1$. It can be assumed that the model verified with an air-filled gap will be valid for a gap filled with MR fluid. Two types of measurement with almost identical configuration were carried out: (a) measurement of static properties of the magnetic circuit (dependence of magnetic flux density on input current to the coil); and (b) response of the magnetic flux density on the electric current step (see figure 14). For the response time measurement, our own patented current controller was used instead of the common power supply. The controller drives the rise and drop of a current using the overvoltage technique described in paper [13]. The controller is supplied by 30 V and the input signal is generated from an Arduino Due board.

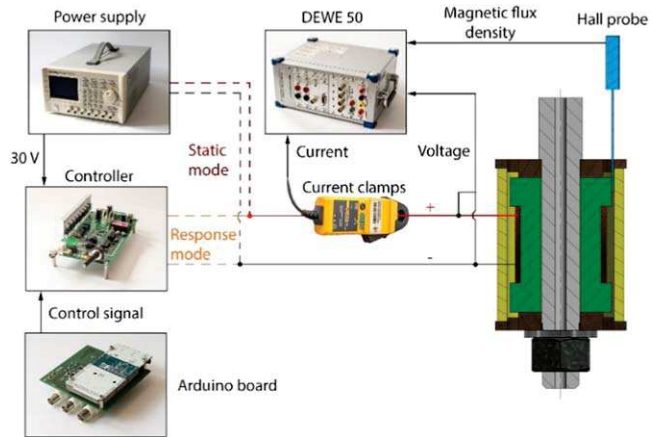


Figure 14. Scheme of measurement configuration.

The current drop from 2 to 0 A took up to 0.2 ms. The magnetic flux density was measured by a teslameter F W Bell 5180 with an ultra-thin transverse probe STB1X-0201 (see figure 15). The magnitude of the electric current in the coil was obtained by measuring with a Fluke i30s current clamp. These two signals together with the voltage on the coil contacts were recorded and conditioned with a sampling frequency of 200 kHz by a front-end Dewetron USB-50-USB2-8 connected to the laptop.

2.6. Experimental setup for measurement of response time of the MR damper

The MR cross-section of the MR damper used for measurement is shown in figure 16. The dimensions of the piston are shown in figure 7(a).

For the measurements, a hydraulic damper tester produced by the Inova company was used (see figure 17). The damping force was measured by load gauge HBM U2AD1/2, the position of the piston-rod by resistance sensor VLP15 \$A150, and the current was calculated from the voltage drop on 0.1 Ω power shunt. These three signals were recorded and conditioned with a sampling frequency of 50 kHz by the analyser Dewe-800 (see figure 18). The piston velocity was calculated by derivation of the piston position. The temperature was monitored in order not to exceed 40 $^{\circ}\text{C}$.

Firstly, the F - v - I curves were measured (dependence of damping force on piston velocity for different currents). The dynamic force range of the damper was also calculated from this dependency as a rate between the force in activated to the force in non-activated state.

The piston movement was excited by a triangle signal of position ensuring the unchanging velocity during the whole stroke. The control signal was generated directly by the Inova control computer. This control signal was connected as an input into the current controller used in section 2.5. The current was switched on and switched off alternately always after two strokes. The exact moment of switching on or off was in the centre of the stroke, see figures 17 and 18.



Figure 15. Testing device for the measurement of the overall response time of the damping force.

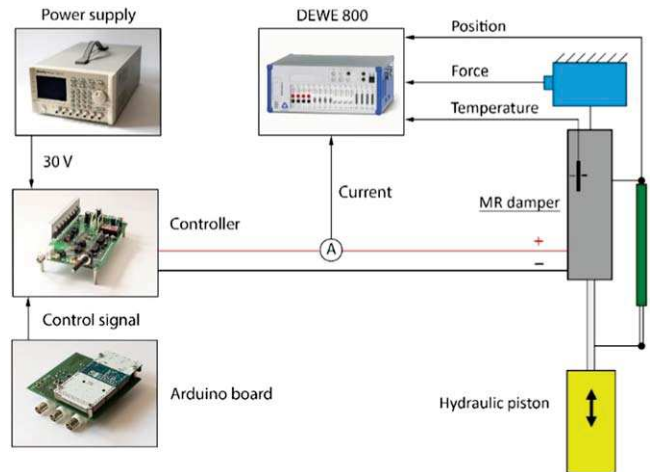


Figure 18. Measurement of damping force on tester Inova.

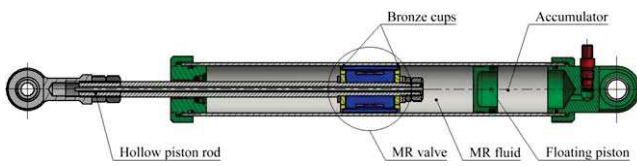


Figure 16. Detail from measurement of MR valve with Hall probe.

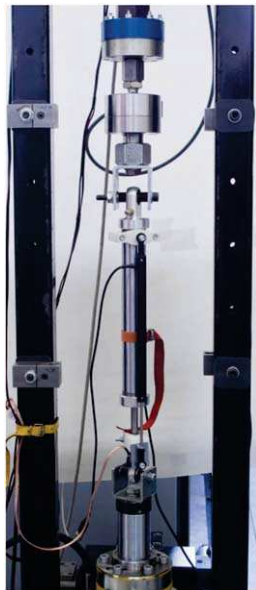


Figure 17. Tester with tested MR damper.

The measurement of the transient response was carried out for piston velocities 0.1, 0.2, 0.3 m s⁻¹ and for currents in the range from 0 to 2 A.

3. Results and discussion

3.1. Material properties

The comparison between the measured *B-H* curves of samples from table 2 is shown in figure 8: although the samples A

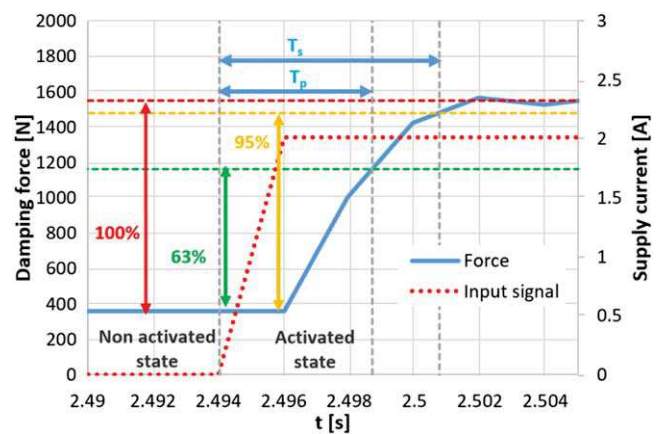


Figure 19. Detail of damper's force response on electric current step 0–2 A with determination of primary response time T_p and secondary response time T_s .

and C are printed with different printing parameters, the *B-H* curves are practically the same. Samples B and D are following heat treatment. It is obvious that heat treatment significantly increases relative permeability μ_r . The initial part of the *B-H* curve is almost the same, but the magnetic saturation differs up to 8%. This difference is probably caused not by different printing parameters, but by corrosion of sample B during heat treatment. Although the heat treated parts were packed in austenitic foil, the air closed in the package reacted with iron. The corrosion decreased the cross-section on part of the toroid. The *B-H* curves of heat treated samples printed by the SLM method also show that for magnetic intensity up to 0.4 kA m⁻¹, they correspond to the *B-H* curve for Behanit. For intensities between 0.4 and 1 kA m⁻¹, the relative permeability is even higher than in the case of Behanit. The magnetic saturation for SLM printed material is around 10% lower than for Behanit.

The measured electric resistance of the printed iron samples was $0.101 \times 10^{-6} \Omega\text{m}$. This value was also used for magnetic simulations

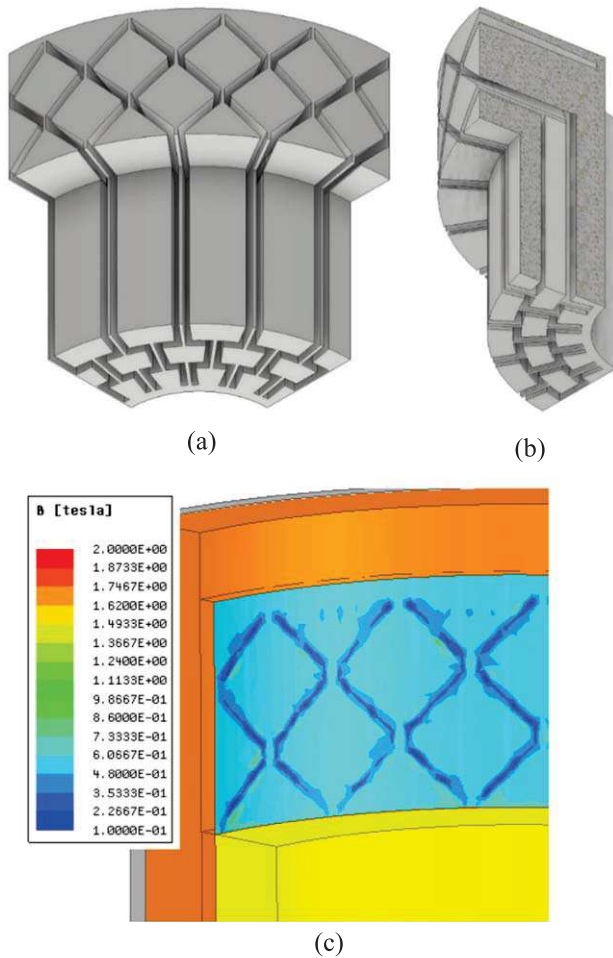


Figure 20. Structured core 1—with constant isolation distances.

3.2. Structures suitable for MR damper piston

Figure 20 shows the first structured design of the core. This design consists of beams with a variable cross-section isolated by gaps with a constant thickness of 0.3 mm. This secures the low response time and high dynamic force range, but it is not optimal from the point of view of weight because the cross-section of the magnetic circuit is not constant. The maximal flux density is limited by the place with the smallest cross-section. In all the other parts, the cross-section can be reduced with only a small drop of maximum magnetic flux in the magnetic circuit (figure 12). This design maintains the overall cross-section of beams for the whole path of magnetic flux. The disadvantage is visible in figure 12(c) which shows the magnetic flux density distribution in the gap (simulation with MR fluid Lord MRF132-DG and current 2 A). The insulation around the beams causes non-homogeneous distribution in the active zone (however, this design may also advantageously be used to create a bypass slot). Therefore, the design in figure 21 was made. The cross-section of beams remains the same except for the small region around the active zone where the beams are widened (figure 21). Table 5 compares the average magnetic induction in the gap, the response time and the weight of the three variants. The simulations were conducted with MR fluid in the gap and with the outer cylinder without

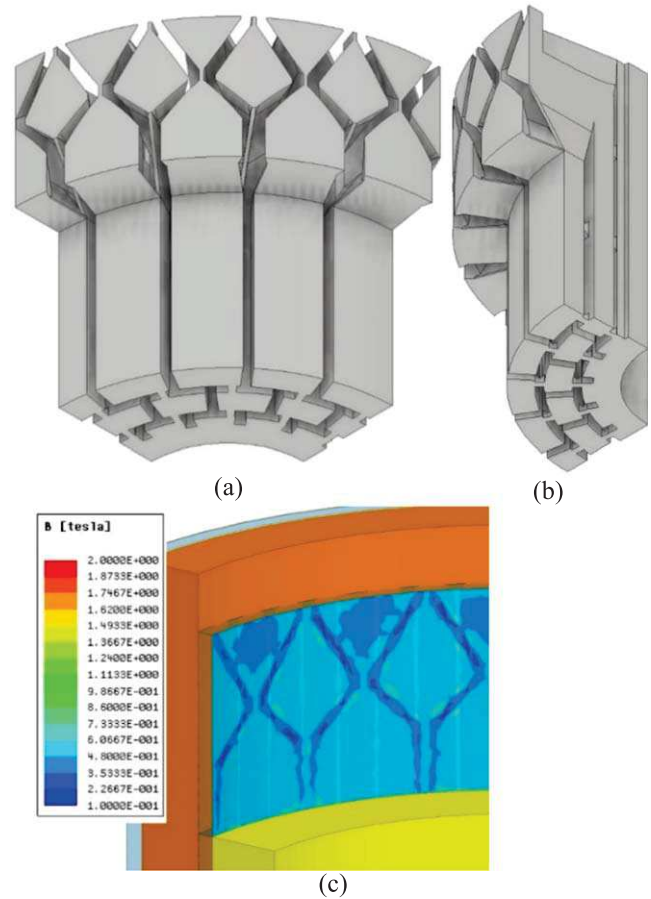


Figure 21. Structured core 3—optimization for low weight and homogeneous magnetic flux density in the gap.



Figure 22. The printed bobbin and outer cylinder with plastic material in the isolation distances.

structures. Due to the generation of eddy currents in the outer cylinder, the response times are longer than the responses measured with the structured outer cylinder.

3.3. Measured B–I curve and time response with air in the gap

The comparison of the measured and simulated B–I curve of the structured piston, version 3 (figure 22) is shown in

Table 5. Comparison of parameters of designed structures.

Type of design	Magnetic induction in the gap (T)	Primary response time (ms)	Weight (g)
Constant isolation distances	0.47	4.89	80.8
Constant cross-section	0.39	3.54	60.8
Homogenous magnetic flux	0.42	4.64	61.6

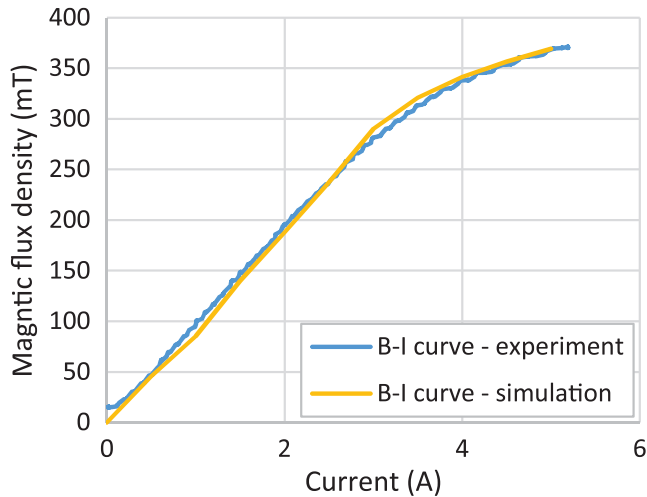
**Figure 23.** B - I curve of the structured piston.

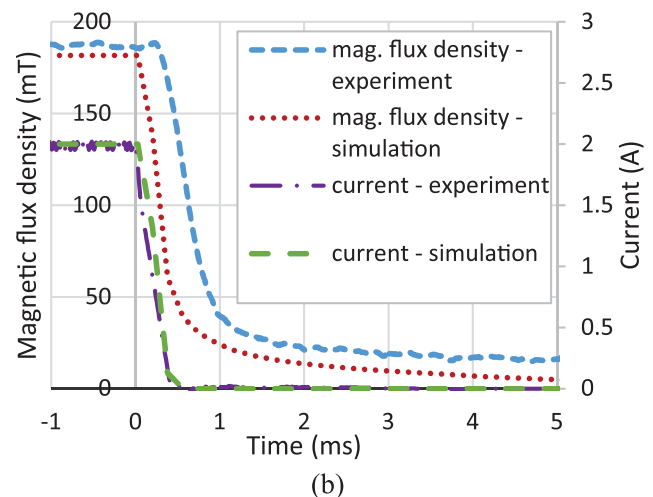
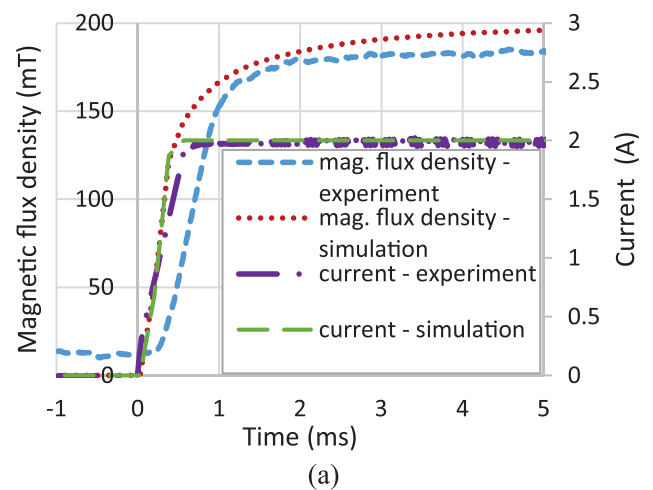
figure 23. The difference between the simulation and measured values is minimal.

The comparison between transient responses of magnetic flux density in the air-filled gap is shown in figure 24. The difference between simulation and measurement for the zero current can be explained by the remanence, which is not taken into consideration in simulation. The measured response time is slightly longer than the simulated one. The shape of the curves is very similar, but there is a time delay (0.2 ms) in the case of the measurement. This delay is probably caused by the digital filtering of the magnetic flux meter F W Bell 5180. This delay can be observed also in the case of the response of the magnetic flux density to the electric current drop (figure 24(b)).

3.4. Measurement of dynamic force range and response time of structured MR damper

The F - v - I dependencies are shown in figure 25(a). It is obvious that the piston is magnetically saturated for currents above 2 A. Applying a current above this limit has minimal impact on force increase. From these curves the dynamic force range can be derived. The dynamic force range for the given current was calculated as the ratio between the force measured for given current in activated state and force for the same piston velocity in non-activated state (zero current).

Figure 26 shows the course of the damper's force in response to the step of the control signal. The response time for turning on is 1.6 ms, while the response time for the falling edge is slightly shorter – 1.3 ms. This figure also

**Figure 24.** The magnetic flux density in the air-filled gap—comparison between simulation and measurement (a) electric current rise (b) electric current drop.

shows that there is always a delay of approximately 0.5 ms after switching the current on or off when the force remains almost the same. We observed that this delay is independent of the material of the piston. This delay is probably caused by the response time of the MR fluid itself. It can be anticipated that the response time of the MR damper can not be reduced by the elimination of eddy currents under this value. In figure 26, the rise of the force between the second and the third millisecond can be observed, although the electric current to the coil is turned off. This is probably caused by the resonance oscillations of the MR fluid inside the MR damper.

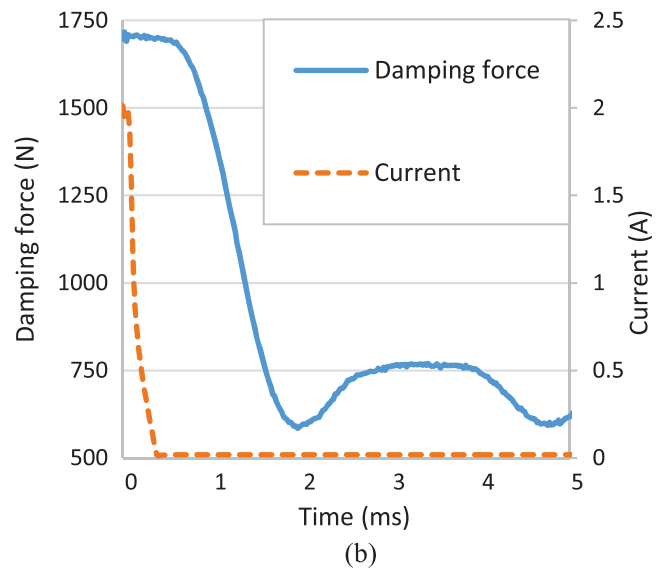
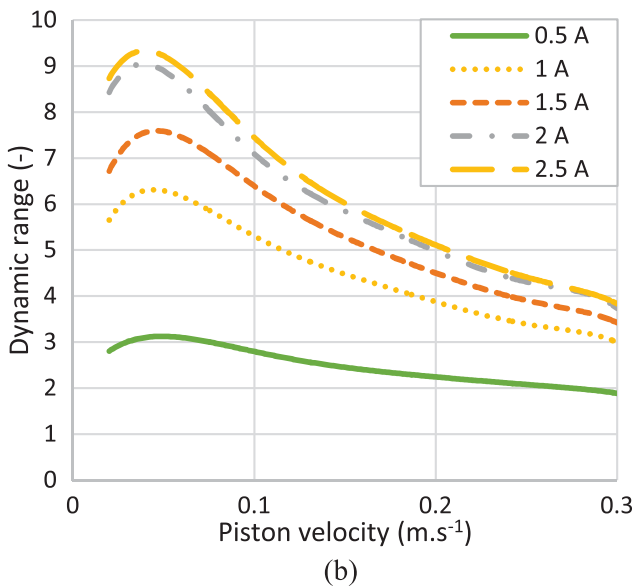
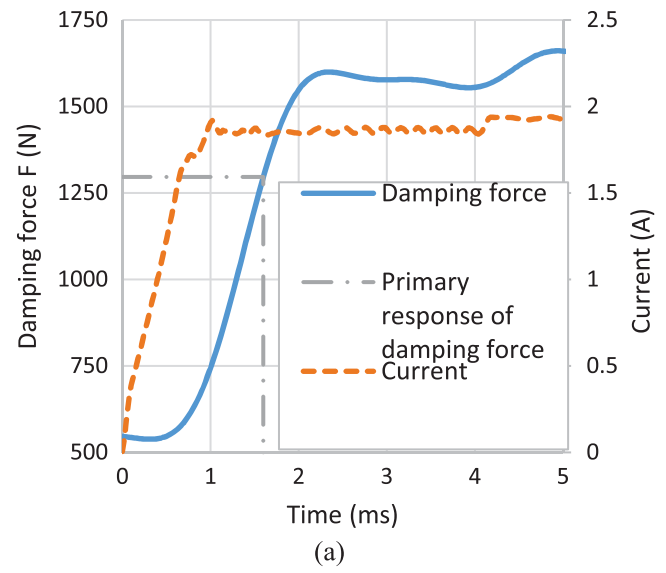
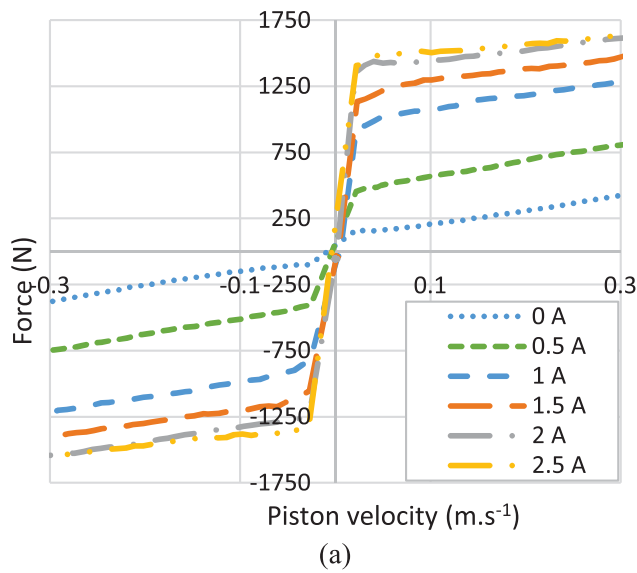


Figure 25. (a) $F-v$ dependency of MR damper with the structured piston and (b) dynamic force range.

Figure 26. The response time of force on step of control signal (a) rising edge (b) falling edge.

Figure 27(b) shows the response time of the force for the rising edge of the control signal. Although the rise of the current is shorter for the piston velocity of 0.1 m s^{-1} , the force response time is significantly longer. For a piston velocity higher than 0.2 m s^{-1} , the response time of the damper’s force is practically independent of piston velocity or the exciting current.

The shorter rise of the electric current for the piston velocity implies the lower inductance of the magnetic circuit. The only part which can influence the inductance of the magnetic circuit is the concentration of iron particles in the gap of the MR damper. The magnetic field probably causes the catching of particles from the flowing MR fluid, which raises the concentration of the MR particles in the gap. When the piston velocity (and hence the flow of MR fluid through the gap) is small, the process of collecting particles is slower, which extends the response time (figure 27). So for small

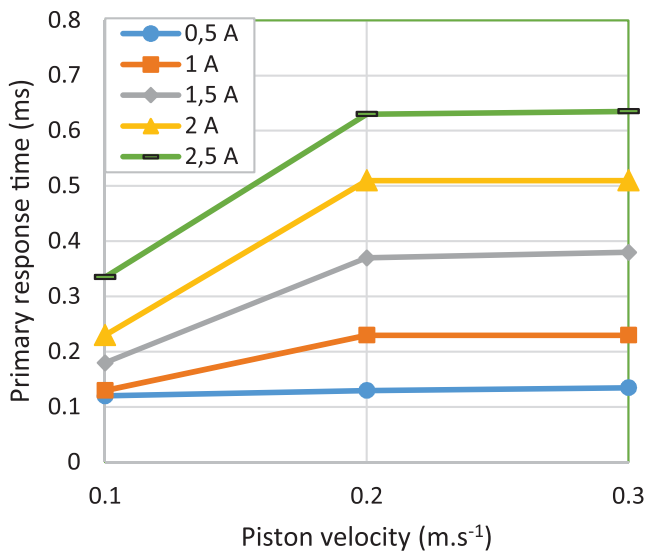
piston velocities, the average concentration of the iron particles is smaller than in case of higher piston velocity. The lower iron particles concentration causes lower inductance of the coil. Lower inductance causes faster rise of the electric current, in case of the constant supply voltage.

4. Conclusions

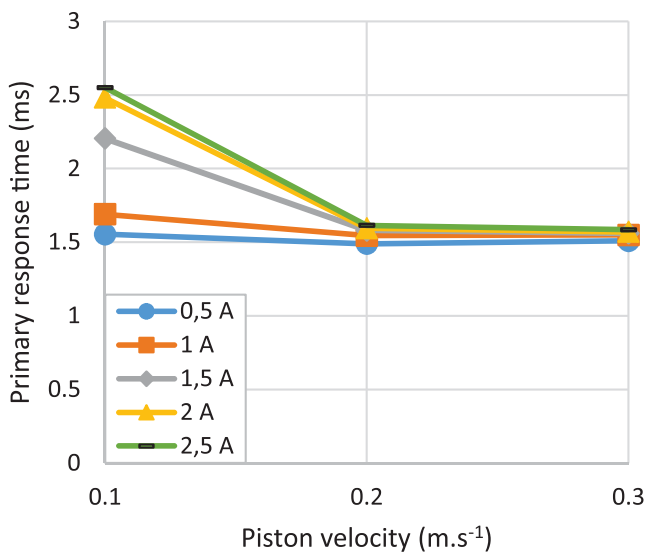
An SLM print of magnetic structured magnetic cores promises great potential for the development of electromagnetic machines. The presented results show that it is possible to design and manufacture magnetic circuits with the remarkable combination of low eddy-current losses (short response time), high magnetic flux (high dynamic force range), low weight and good mechanical properties. Such a combination of features has only recently been manufactured and only by 3D printing. Table 6 illustrates the comparison of MR dampers

Table 6. Performance comparison of pistons.

Type of piston	Primary response time (ms)	Secondary response time (ms)	Magnetic flux density (T) (2 A, air in the gap)	Weight (g)	Dynamic force range (–)
Solid piston (11SMn30)	6.2	30.9	0.174	208	5.73
SMC piston	1.06	1.3	0.154	193	4.03
Grooved piston (11SMn30)	1.36	1.75	0.17	177	5.33
Structured piston (Fe)	1.32	1.68	0.18	156	5.12



(a)



(b)

Figure 27. The dependency of response time on piston velocity and electric current (a) response time of electric current (b) response time of damper's force.

with pistons made of various materials or various technologies for a piston velocity 0.2 ms^{-1} and a falling edge of the control signal. The magnetic flux density was measured for an electric current of 2 A and with an air-filled gap. The structured version is almost as fast as the MR damper with a piston made of SMC, but the dynamic force range is more than 20 % higher. The dynamic force range of an MR damper with a structured piston is almost the same as the MR damper with a grooved piston, but the response time is shorter and the weight is 13% reduced. It is also important to remember that the structured piston was made of pure iron, which is an unsuitable material for a magnetic circuit with fast changes of magnetic field due to the low electrical resistivity and hence a high level of eddy-current generation. Printing from low-carbon steel, silicone steel or Vacoflux would enable the ability to increase the size of the beams and so reduce the

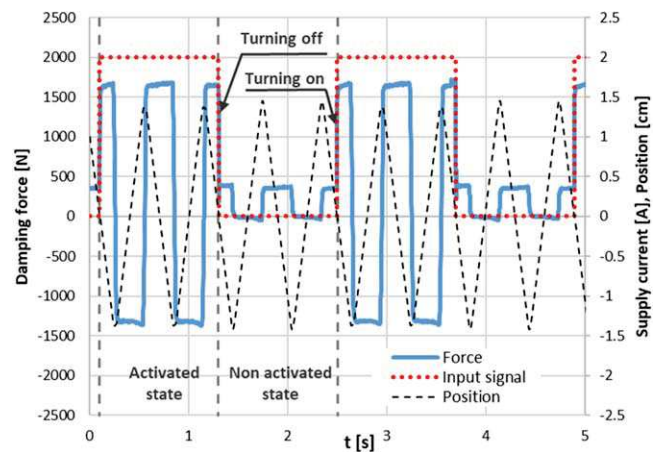


Figure 28. Course of force in dependency on control signal.

number of isolation gaps. This would increase the dynamic force range while maintaining the low response time. The same effect can also be achieved by tuning the printing process. Improving the surfaces will enable the ability to reduce the thickness of insulation.

The structured cores can be used for all electromagnetic machines working with AC fields. For electromagnetic valves, it can shorten the response time by two effects—reduction of the weight (and thus increasing the resonance frequency) and reduce of eddy currents. Reduction of weight will decrease the inertia moment of electromotor rotors, which will shorten the response time of the motor. Moreover, the reduction of eddy currents will increase the efficiency and reduce the need of cooling.

This technology enables the ability to reach the combination of performance parameters of electromagnetic machines, which cannot be reached by any other existing method.

Acknowledgments

The study was supported by the ESIF, EU Operational Programme Research, Development and Education within the research project 'Architected materials designed for additive manufacturing', Reg. No.: CZ.02.1.01/0.0/0.0/16_025/0007304, the FSI-S-17-4428 GAČR 17-10660 J and GAČR 17-26162 s.

ORCID iDs

Zbyněk Strecker <https://orcid.org/0000-0002-1598-487X>

Michal Kubík <https://orcid.org/0000-0003-0105-2921>

References

- [1] Nguyen Q-H and Choi S-B 2009 Optimal design of MR shock absorber and application to vehicle suspension *Smart Mater. Struct.* **18** 035012

- [2] Yang B, Luo J and Dong L 2010 Magnetic circuit FEM analysis and optimum design for MR damper *Int. J. Appl. Electromagn. Mech.* **33** 207–16
- [3] Gavin H, Hoagg J and Dobossy M 2001 Optimal design of MR dampers *Proc. US-Japan Work. Smart Struct. Improv. Seism. Perform. Urban Reg.* pp 225–36
- [4] Nam Y-J and Park M-K 2009 Electromagnetic design of a magnetorheological damper *J. Intell. Mater. Syst. Struct.* **20** 181–91
- [5] Koo J-H, Goncalves F D and Ahmadian M 2006 A comprehensive analysis of the response time of MR dampers *Smart Mater. Struct.* **15** 351–8
- [6] Sahin H, Gordaninejad F, Wang X and Liu Y 2012 Response time of magnetorheological fluids and magnetorheological valves under various flow conditions *J. Intell. Mater. Syst. Struct.* **23** 949–57
- [7] Poussot-Vassal C, Spelta C, Sename O, Savaresi S M and Dugard L 2011 Survey on some automotive semi-active suspension control Methods: a comparative study on a single-corner model *IFAC Proc.* **44** 1802–7
- [8] Yao G Z, Yap F F, Chen G, Li W H and Yeo S H 2002 MR damper and its application for semi-active control of vehicle suspension system *Mechatronics* **12** 963–73
- [9] Kim R-K and Hong K-S 2007 Skyhook control using a full-vehicle model and four relative displacement sensors *2007 Int. Conf. on Control, Automation and Systems* (Seoul, South Korea: IEEE) pp 268–72
- [10] Eslaminasab N and Golnaraghi M F 2008 The effect of time delay of the semi-active dampers on the performance of on-off control schemes *2007 Proc. ASME Int. Mechanical Engineering Congress and Exposition* vol 9, pp 1911–8 Pts a-C
- [11] Strecker Z, Mazurek I, Roupec J and Klapka M 2015 Influence of MR damper response time on semiactive suspension control efficiency *Meccanica* **50** 1949–59
- [12] Machacek O, Kubik M and Novák P 2017 A new method of magnetorheological damper quality evaluation *Engineering Mechanics 2017* Svratka ed C Fischer and J Náprstek (Prague: Institute of Theoretical and Applied Mechanics of the Czech Academy of Sciences) pp 594–7
- [13] Strecker Z, Roupec J, Mazurek I, Machacek O, Kubik M and Klapka M 2015 Design of magnetorheological damper with short time response *J. Intell. Mater. Syst. Struct.* **26** 1951–8
- [14] Strecker Z, Strmiska T, Roupec J, Kubík M and Macháček O 2017 Design of fast magnetorheological damper using soft material composites *Engineering Mechanics 2017* Svratka ed C Fischer and J Náprstek (Prague: Institute of Theoretical and Applied Mechanics of the Czech Academy of Sciences) pp 934–7
- [15] Goldasz J 2017 Study of a modular magnetorheological valve *2017 18th Int. Carpathian Control Conf. (ICCC)* vol 63 (Sinaia, Romania: IEEE) pp 306–9
- [16] Omekanda A M, Nehl T W, Namuduri C S and Gopalakrishnan S 2015 Electromagnetic actuator structure *Int. Patent* WO2015143107
- [17] Kubík M, Daniel K, Paloušek D, Macháček O, Strecker Z, Mazurek I and Roupec J 2018 A core skeleton made of rods of a ferromagnetic material *Cz. Patent CZ307249 B6*
- [18] Vrána R, Koutný D, Paloušek D, Pantělejev L, Jaroš J, Zikmund T and Kaiser J 2018 Selective laser melting strategy for fabrication of thin struts usable in lattice structures *Materials* **11** 1763
- [19] Zhang B, Fenineche N E, Liao H and Coddet C 2013 Microstructure and magnetic properties of Fe-Ni alloy fabricated by selective laser melting Fe/Ni mixed powders *J. Mater. Sci. Technol.* **29** 757–60
- [20] Zhang B, Fenineche N E, Liao H and Coddet C 2013 Magnetic properties of *in-situ* synthesized FeNi₃ by selective laser melting Fe-80%Ni powders *J. Magn. Magn. Mater.* **336** 49–54
- [21] Zhang B, Fenineche N E, Zhu L, Liao H and Coddet C 2012 Studies of magnetic properties of permalloy (Fe30%Ni) prepared by SLM technology *J. Magn. Magn. Mater.* **324** 495–500
- [22] Palousek D, Pantelejev L, Zikmund T and Koutny D 2017 Processing of nearly pure iron using selective laser melting-initial study *MM Sci. J.* **2017** 1738–43
- [23] Garibaldi M, Ashcroft I, Simonelli M and Hague R 2016 Metallurgy of high-silicon steel parts produced using selective laser melting *Acta Mater.* **110** 207–16

Research Article

Multiphysics Model of an MR Damper including Magnetic Hysteresis

M. Kubík ¹ and J. Goldasz ^{2,3}

¹Faculty of Mechanical Engineering, Brno University of Technology, Brno, Czech Republic

²Faculty of Electrical and Computer Engineering, Cracow University of Technology, Kraków, Poland

³Technical Center Kraków, BWI Group, Kraków, Poland

Correspondence should be addressed to M. Kubík; michal.kubik@vutbr.cz

Received 12 April 2019; Revised 31 May 2019; Accepted 9 June 2019; Published 26 June 2019

Guest Editor: Efrén Díez-Jiménez

Copyright © 2019 M. Kubík and J. Goldasz. This is an open access article distributed under the Creative Commons Attribution License, which permits unrestricted use, distribution, and reproduction in any medium, provided the original work is properly cited.

Hysteresis is one of key factors influencing the output of magnetorheological (MR) actuators. The actuators reveal two primary sources of hysteresis. The hydro(mechanical) hysteresis can be related to flow dynamics mechanisms and is frequency- or rate-dependent. For comparison, the magnetic hysteresis is an inherent property of ferromagnetic materials forming the magnetic circuit of the actuators. The need for a good quality hysteresis model has been early recognized in studies on MR actuators; however, few studies have provided models which could be used in the design stage. In the paper we reveal a hybrid multiphysics model of a flow-mode MR actuator which could be used for that purpose. The model relies on the information which can be extracted primarily from material datasheets and engineering drawings. We reveal key details of the model and then verify it against measured data. Finally, we employ it in a parameter sensitivity study to examine the influence of magnetic hysteresis and other relevant factors on the output of the actuator.

1. Introduction

Magnetorheological (MR) dampers are fairly well-known devices utilizing MR fluids which, when subjected to magnetic stimuli of sufficient strength, generate yield stress [1]. So far, the unique technology has been commercialized in semiactive passenger vehicle suspensions, powertrain mounts [2], or optical finishing [3]. Low power consumption, fast and reversible responses, and high dynamic range have made the devices attractive for use in vibration control systems in particular [4]. As MR dampers are generally operated in real-time control systems, their dynamic performance is equally important as or more important than their steady-state characteristics. Steady-state characteristics only provide the evidence of an actuator or a damper meeting the required force/torque range (or force/torque) targets. Their dynamic behaviour needs to be quantified at the same time if it is used in a real-life control process. Thus, understanding the contributions of various factors complicating the force or torque build-up dynamic process is critical for the development of a realistic application. Briefly,

with MR actuators, there is ample evidence of several factors complicating the force/torque generation process, namely, mechanical/hydraulic hysteresis, magnetic hysteresis, control circuit dynamics such as eddy currents, driver dynamics, temperature, flow losses, friction, and nonlinear relationship between the material's yield stress and the induced flux [5–7]. These factors influence the device's ability to generate the output force/torque and need to be accounted, for instance, for in the control algorithm development process.

In this study, we pay particular attention to modeling the damper's hysteretic behaviour. In general, MR devices reveal two primary sources of hysteresis. The (hydro-)mechanical hysteresis can be related to the damped dynamics of a heavy slug of MR fluid (MRF) bouncing against compliant columns of MRF in fluid chambers. The effect is rate- or frequency-dependent, and its magnitude varies with the current applied, too. It disappears as the mechanical excitation frequency approaches zero [8]. The magnetic hysteresis is different. It is present in all electromagnetic devices, e.g., electromagnetic solenoids [9], motors [10], and magnetorheological actuators [11]. First of all, it is the inherent

property of ferromagnetic materials forming the magnetic circuit of the MR valve; the hysteresis of carbonyl iron (CIP-) based MFRs is virtually nonexistent [12]. Next, it does not vanish as the inducing current frequency approaches DC limit. Also, temperature, load history, and mechanical stresses have a negative influence on the hysteresis and magnetization characteristics of ferromagnetic materials [13]. For instance, it is a common practice to subject machined ferromagnetic components to heat treatment for internal stress and hysteresis as well as coercive force reduction.

The need for a good quality hysteresis model has been early recognized in studies on MR actuators, and the reader should refer, e.g., to Zheng et al. [14] for a review of suitable phenomenological models as well as to the well-known study of Spencer et al. [15]. In general, the posteriori parametric models were obtained by examining the force-position and force-velocity relationships by fitting by model response to the actuator's output. Such models are suitable for control studies only. In the device's development process, other approaches are required. In that aspect, many MR-related research studies neglected the particular contributor's presence. The topic, however, has been well identified in the field of conventional solenoid actuators where various models were developed to copy the hysteretic behaviour of the actuators. For instance, Mayergoyz [16] applied the Preisach model to model the hysteretic behaviour of a solenoid actuator. In the Preisach model, the hysteresis is the sum of elementary hysteresis loops. Next, Coleman and Hodgdon [17] developed a first-order differential equation that links the field strength H and the flux density B . One model whose parameters can be related to physical properties of ferromagnetic materials is the Jiles–Atherton (J–A) model [18, 19]. The model was extended to include both the impact of eddy currents and temperature on hysteresis and magnetisation curves [20, 21]. All of the above models can be vectorized. Tellinen [22] proposed a simple scalar model for handling the hysteresis based on the limiting hysteresis loop from physical measurements of ferromagnetic materials. With MR actuators, however, although the significance of a good quality hysteretic model has been recognized early, the topic does not seem to have deserved enough attention. Significant contributions include Han et al. [23] who examined the field dependent hysteresis of ER fluids. The authors used the familiar Preisach approach. Moreover, Han et al. [7] used the Preisach model to identify the hysteresis of an MR fluid. Yadmellat and Kermani developed a model of an MR clutch in which the developed hysteresis model was assessed against the Preisach operator [24]. For comparison, in their early study using the Coleman-Hodgdon model, An and Kwon modelled the hysteretic behaviour of an MR clutch, and by examining the torque-current loops showed that the hysteresis is an important contributor to the device's output [25]. The model parameters were identified from physical measurements (of magnetisation characteristics) of the materials forming the magnetic circuit of the clutch. Next, Jędrzycka et al. presented a finite-element (FE) model of an MR clutch based on the J–A approach [26]. Moreover, Guo et al. presented a transient multidomain model of a

flow-mode damper based on the J–A approach and then verified it against the novel FE vector hysteresis technique [27]. The inverse J–A model was recently examined by Zheng et al. [14] to copy the transient behaviour of an MR flow-mode damper. Goldasz et al. [28] proposed an extension of the Bouc–Wen model in an attempt to separate the magnetic hysteresis from the mechanical one. The authors proposed a simple lumped parameter model of the actuator including a hysteretic operator. The model was verified against selected sinusoidal AC excitation inputs and provided acceptable accuracy for practical purposes. Still, when compared to the vast number of research studies using parametric phenomenological hysteretic models, the topic does not seem intensively studied as already mentioned. That may be due to few existing comprehensive electromagnetic models of such actuators.

Another aspect is dynamics. Clearly, the insight into the dynamics of MR actuators should be provided through transient models. Such a comprehensive model would attempt to copy not only the dynamics of the fluid flow through the valve and the flux dynamics but account for the physics outside the control valve as well. Suitable lumped parameter models usually utilize a network of elements representing physical domains of interest (hydraulic, thermal, electric, and magnetic) and connections (interfaces) between them [2]. For example, the electrical circuit of the actuator can be represented in the form of a resistor-non-linear inductor network model [5]. Their main disadvantage is the necessity of using various simplifying assumptions, e.g., uniform yield stress/flux, fully developed flow, etc. On the contrary, continuum multiphysics (magnetics and flow dynamics) models utilize fewer assumptions and can be exercised on realistic geometries, however, at a significant computational expense [29].

As such, in the paper, we propose a hybrid multiphysics model of the magnetorheological damper which separates the magnetic hysteresis of the magnetic circuit of the actuator from that of the mechanical hardware. Briefly, the electromagnetic domain is modelled using the vector hysteresis FE model (present in Ansys Maxwell) based on the extension of well-known Maxwell equations [30], and the hydraulic section is described through dimensionless biplastic Bingham approach [31].

The paper is organized as follows. First, we present an MR damper geometry and key material properties. Then, in the following section, we reveal key details of the FE model of the actuator such as magnetic hysteresis and the coupled lumped parameter hydromechanical model. Next, we show measurements of magnetic hysteresis loops and a comparison of the measurements against the FE electromagnet model. Finally, we show results of a parametric study (also involving the hybrid model) in an attempt to examine the hysteresis influence on the output of the MR actuator and then draw conclusions.

2. Magnetorheological Damper

In the study, an MR flow-mode damper configuration having a single coil assembly in the electromagnet and one annular

flow path in the control valve is of research interest. The damper is presented in Figure 1. The hydraulic tube houses (1) the piston (2), the piston rod (3), the floating piston (4) and the rod guide assembly (5). The piston separates the MR fluid volume into rebound chamber volume and the compression chamber volume. The floating piston separates the fluid from the gas chamber. The MR valve located in the piston control controls the fluid flow between the rebound and compression chamber and vice versa. The MR valve is a conventional control valve by design. It consists of the piston core (6), the sleeve (7), the nonmagnetic flanges or plates (8), the coil assembly (9), and the connecting wires (10) for connecting to an external power supply. It is the most common single-tube MR damper configuration.

The MR valve's magnetic circuit (6, 7) is manufactured out of annealed low-carbon steel 11SMn30 (see the components in blue in Figure 1). The bronze (yellow) flanges (8) define the mutual position of the piston core and sleeve. The distance between the outer diameter of the annulus and the inner diameter of the sleeve defines the annular gap height. The coil assembly (9) incorporates $N = 120$ turns of copper (purple) wire (0.5 mm diameter).

The connecting wires are routed through the thru-hole in the piston rod (3) made of steel 42CrMo4 (AISI 4140). The floating piston, the rod guide, and the remaining components are manufactured out of steel S235JR (green). The MR damper is filled with the fluid MRF132-DG by Lord Corp; see the magnetisation curve in Figure 2(c). The damper key dimensions, rheological properties of MR fluid, and gas chamber details are shown in Table 1. The magnetisation curves of the annealed low-carbon steel 11SMn30 were determined using the measurement system Remagraph C-500. The obtained virgin & hysteresis data can be seen in Figures 2(a) and 2(b).

The coercivity and remanence of the 11SMn30 material sample were determined from the measured hysteresis: $H_c = 209$ A/m and remanence $B_r = 1.09$ T. The material's bulk conductivity was set at 5.8 MS/m. Based on similar measurements of the rod material (42CrMo4), we set its coercivity to $H_c = 1250$ A/m and the bulk conductivity to 4.5 MS/m.

3. Modeling

In the section, we present modeling details. Specifically, we highlight the transient magnetic FE model of the MR valve including hysteresis followed by a description of a monotube damper lumped parameter model. The lumped parameter model is coupled with the transient FE model through the yield stress-flux density interface. We consider the integrated model as illustrated in Figure 3. In the presented layout, the electromagnetic circuit (described in Section 3.1) is driven by the voltage u supplied by the current driver. The resulting output flux density B_g is then converted into the materials' (fluid) field-induced yield stress τ_0 (extracted from the material's datasheet or rheological measurements). Given the input velocity v_r or displacement and the yield stress, we then calculate the output force according to the equations in Section 3.2.

3.1. Transient Magnetic Model with Magnetic Hysteresis. To model the electromagnetic circuit of the MR valve, we applied the vector hysteresis modeling feature available in Ansys Maxwell R19. For isotropic material and 2D/3D problems, the vector play model was recognized to be more computationally efficient than a vector Preisach model [30, 33]. In general, the play model assumes a decomposition of the applied field H into the reversible component H_{re} and the irreversible one H_{ir} . Then, the resulting flux density

$$B = B_{re} + B_{ir} = \mu_0 M(H_{re}) + \mu_0 H_{ir}, \quad (1)$$

where B_{re} is the reversible component of flux density and B_{ir} is the irreversible component. The magnetization M varies with the reversible field component along an anhysteretic curve. The process can be visualized as in Figure 4. The parameters for the model can be identified from the major hysteresis loop. The major hysteresis loop incorporates two branches, the ascending branch and the descending branch, and they can be calculated from each other, the Maxwell model utilizes only one branch of particular B - H loops. The algorithm for constructing the major and symmetric minor hysteresis loops is given in [34].

To develop the FE model, we assumed the valve to be axially symmetrical around the centerline in a cylindrical coordinate system. The geometry of the MR damper piston (valve) was simplified for the transient simulations (Figure 5(a)). The discretized model can be observed in Figure 5(b). As shown, the geometry was discretized using triangular elements. The element length-based refinement with the maximum length of 0.5 mm was applied to the coil core and the sleeve. Next, the value of 0.7 mm was applied to the piston rod and the hydraulic tube, and the criterion of 0.2 mm was applied to the MR fluid region in the active zone.

To accomplish transient field simulations, the FE model was coupled to the external circuit revealed in Figure 6(a). The lumped circuit documents an ideal current source (input) in series with a resistor (coil winding) and the FE valve object (as represented by the nonlinear inductor). The model is subjected to prescribed current waveforms, and the resulting flux density in the annulus B_g is extracted from the simulation results. The flux density B_g presented in the next sections was calculated by averaging flux density of the middle of the annulus. The information is required for coupling the FE model with the damper hydraulics.

The figure also shows the curve fit to the experimental data for the steel 11SMn30 (Figure 6(b)). The agreement is satisfactory except for low magnetic field strength and on the initial magnetization curve only. The core and sleeve components were assigned the B - H properties of the 11SMn30 alloy and the MRF component that of MRF132-DG available from Lord Corp. Also, the rod component was assigned the material properties of the 42CrMo4 steel alloy as mentioned above. Finally, all data in subsequent simulations were obtained using the fixed step-size solver with the following settings: constant time step was 0.05 ms, nonlinear residual was $1e-7$, time integration method was Backward Euler.

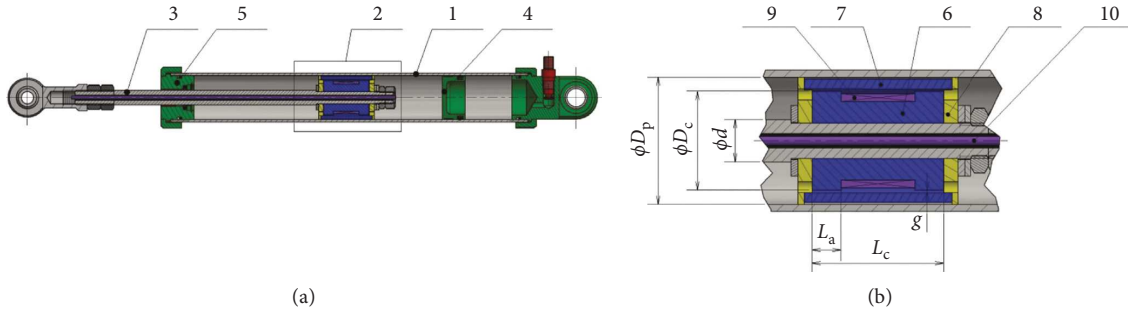


FIGURE 1: Magnetorheological damper. (a) MR damper. (b) Piston (control valve).

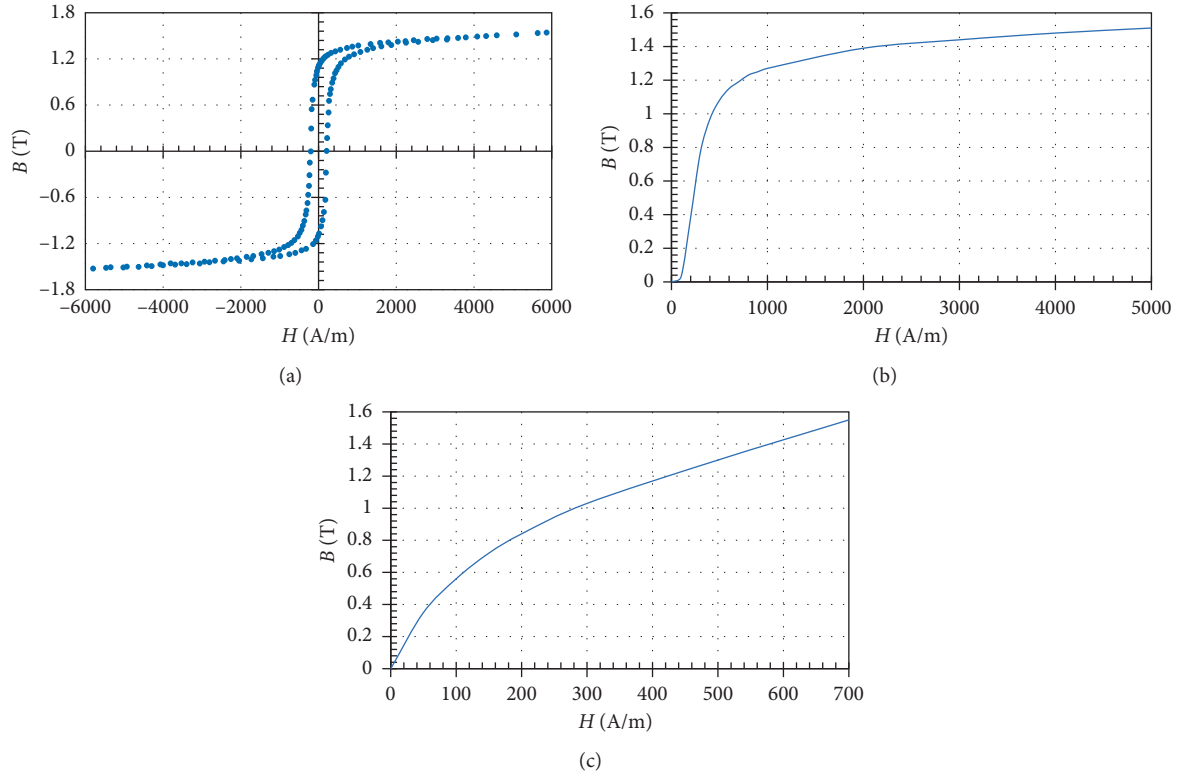


FIGURE 2: Virgin and hysteresis magnetization curves. (a) Hysteresis curve of 11SMn30. (b) Static curve of 11SMn30. (c) Static curve of MRF 132-DG [32].

TABLE 1: MR damper dimensions and material properties.

Name	Value	Symbol	Unit
<i>Geometry and weight</i>			
Piston rod outer diameter	12	d	mm
Piston outer diameter	36	D_p	mm
Annular gap height	0.65	h	mm
Active zone length	16	L_a	mm
Core length	37	L_c	mm
Piston stroke	150	L_s	mm
Internal diameter of the gap	28	D_c	mm
Floating piston weight	0.07	m_f	kg
<i>MR fluid properties (MRF-132DG [32])</i>			
MR fluid viscosity at 40°C	0.114	μ	Pa·s
MR fluid isothermal bulk modulus	1500	β	MPa
MR fluid density	3090	ρ	kg·m ⁻³

TABLE 1: Continued.

Name	Value	Symbol	Unit
Air content in the MR fluid	0.01	α	—
<i>Gas chamber</i>			
Gas volume (at midstroke)	46000	V_{g0}	mm ³
Gas temperature	40	T^0	°C
Initial gas pressure	30	P_{g0}	bar
Initial floating piston position	20	x_g	mm
<i>Others</i>			
Initial rebound chamber (upper) MR fluid volume	63333	V_{r0}	mm ³
Initial compression (lower) chamber MR fluid volume	71250	V_{c0}	mm ³
Coil turns	120	N	—
Coil resistance	1.0	R_c	Ω
Nondimensional viscosity ratio (est.)	0.1	γ	—
Yield stress number (est.)	0.5	δ	—

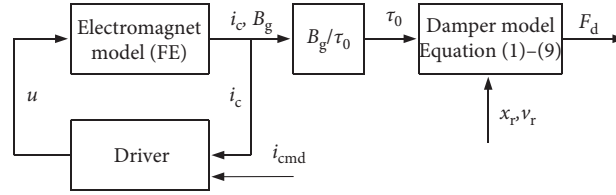


FIGURE 3: Block diagram of the proposed model.

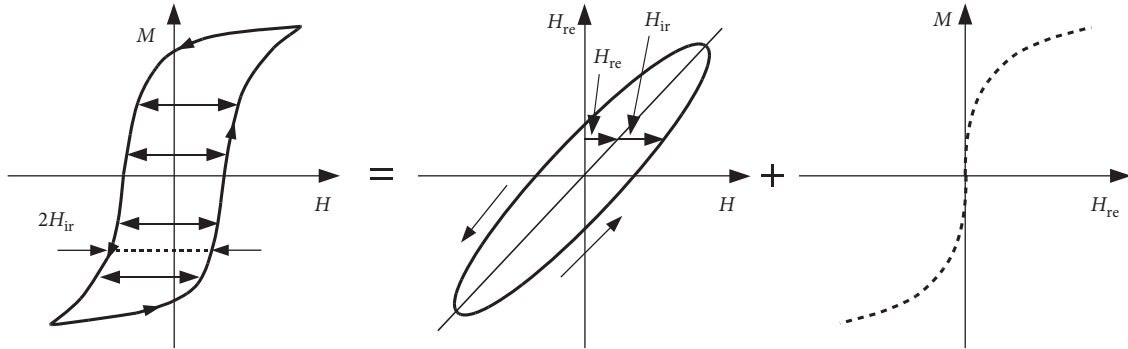


FIGURE 4: Magnetic field decomposed into reversible/irreversible components [35].

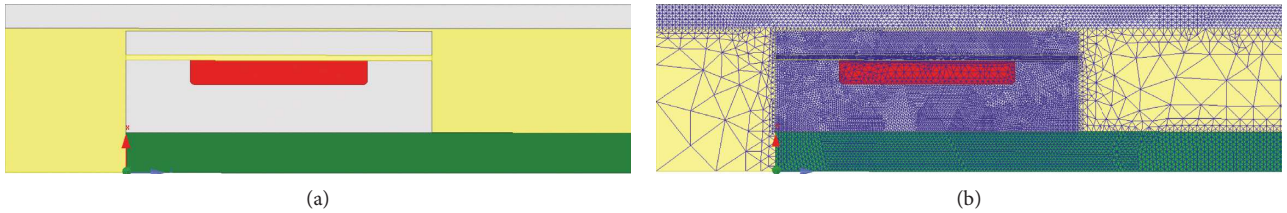


FIGURE 5: Simplified geometry of the piston unit and mesh. (a) Geometry. (b) Mesh.

3.2. Hydromechanical Model. To illustrate or reveal the effect of fluctuating (transient) magnetic field on the output of the actuator, a capable damper model is required. Modeling the behaviour of MR dampers has been clearly the subject of intensive research, to name only [36–38]. However, we chose to proceed further with the model of Goldasz and Sapinski in [2]. The approach is flexible, incorporates most key physical

phenomena occurring in the MR valve and outside of it, and was successfully verified against several MR piston valve configurations (monotube damper, valve: single coil, single annular flow path, magnetic flux bypass feature). Therefore, in the sections that follow, we describe details of the lumped parameter model of the damper and the coupling method with the FE transient model.

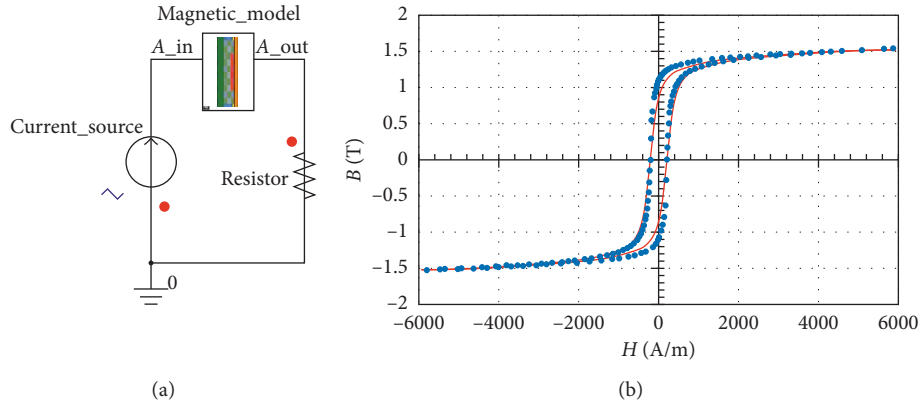


FIGURE 6: External circuit model and magnetisation curve: 11SMn30 (curve fit vs data). (a) External circuit. (b) B - H plot.

3.2.1. MR Damper Model: Theoretical Background. The schematic geometry of the damper is revealed in Figure 7. In the presented illustration, the piston separates the upper (rebound) fluid chamber from the fluid below it (compression chamber). The pressure in the upper chamber is P_r , and its (initial) volume is V_r (V_{r0}). Accordingly, the pressure in the compression chamber is P_c , and its (initial) volume is V_c (V_{c0}). The gas pressure is P_g (P_{g0}), and the (initial) gas volume below the floating piston is referred to as V_g (V_{g0}). At static conditions, the pressure in each chamber is equal to P_{g0} . The cross-sectional area of the piston is A_p and that of the rod A_r . As the piston rod moves, it displaces the floating piston (separating the lower fluid chamber and the pressurised gas). The floating gas cup mass is m_g , and its displacement is x_g . The friction forces against the rod guide and the floating piston are F_{fg} and F_{fr} , respectively. We assume one annular flow path in the MR valve; dimensions: h is the gap height; w is the circumferential width (at perimeter); $A_g = wh$ is the flow channel area. The flow rate through the annulus is referred to as Q_a . Finally, we refer to the displacement of the piston rod as x_r and to that of the cylinder tube as x_t (not shown).

The fluid's behaviour is quantified with the viscosity μ , the density ρ , the compressibility β , and the field-induced yield stress τ_0 . The non-Newtonian rheology of the MR fluid is described using the biplastic Bingham model [31].

We assume that the damper model would account for the following phenomena: MR effect (using the biplastic Bingham model mentioned above), compressibility of fluid, dynamics of the fluid element ("slug") motion when forced through the annulus, entrance and exit losses in the annulus, floating piston mass inertia, and seal friction. Elasticity of the cylinder tube, various effects due to heating, and the dependency of seal friction on the damper internal pressure are not accounted for.

First, the gas pressure in the volume below the floating piston can be modeled by assuming the adiabatic process ($n=1.4$). The gas pressure P_g is then dependent on the position of the floating piston x_g in the following manner:

$$P_g = P_{g0} \left(\frac{V_{g0}}{V_{g0} + A_p x_g} \right)^n. \quad (2)$$

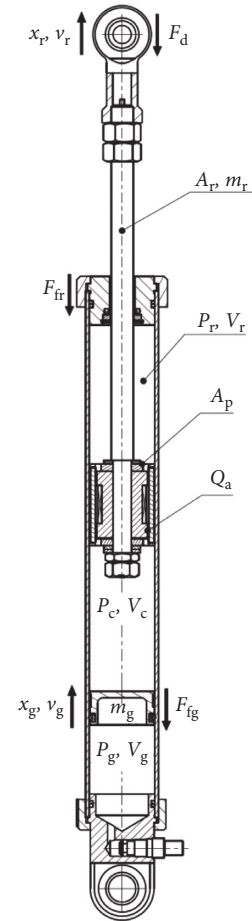


FIGURE 7: Damper model schematic layout.

The pressure variation in the chambers below/above the piston is modeled assuming isothermal processes and the conservation of mass approach [39]. Next, the dynamics of the mass of fluid is considered by examining the motion of the fluid mass in the annular channel. The resulting system of ordinary differential equation in the state-space form which describes the mutual relationships between the rebound pressure chamber P_r , the compression chamber pressure P_c , the floating piston motion velocity v_g , and the

volumetric flow rate through the annulus Q_a is shown below

$$\dot{P}_r = \beta \frac{(A_p - A_r)v_p - Q_a}{V_r}, \quad (3)$$

$$\dot{P}_c = \beta \frac{(v_g - v_p)A_p + Q_a}{V_c}, \quad (4)$$

$$\dot{v}_g = \frac{1}{m_g} [A_p(P_c - P_g) - F_{fg} \text{sign}(v_g)], \quad (5)$$

$$\dot{Q}_a = \frac{A_g}{\rho L} (P_r - P_c - \Delta p_a). \quad (6)$$

As already mentioned, the behaviour of the energized MR fluid is described by incorporating the field-dependent losses into the pressure drop Δp_a which is described in detail in Section 3.2.3; the reader should refer to [2, 39] for a more detailed derivation of the equations and the experimental verification method. The pressure term also incorporates the local flow losses Δp_e . The local flow losses as the fluid enter/exits the annulus are accounted for using the semiempirical equation [40]:

$$\Delta p_e = K \frac{\rho Q_a}{2A^2} |Q_a|, \quad (7)$$

$$K_{SE} = K_{cor} \left(1 - \frac{A_g}{A_p}\right)^2, \quad (8)$$

$$K_{SC} = K_{cor} \left(1 - \frac{A_g}{A_p}\right)^{0.75}, \quad (9)$$

where K/K_{SE} is the pressure loss coefficient for the sudden enlargement (exit from the gap), K/K_{SC} is the pressure loss coefficient for the sudden contraction (entrance to the annular gap), and K_{cor} is the correction factor. Finally, considering the forces acting on the piston yields the following relationship:

$$F_d = (A_p - A_r)P_r - P_c A_p + F_{fr} + F_{fg}. \quad (10)$$

The friction force in MR damper is assumed to be the sum of Stribeck, Coulomb, and viscous components [40]. As already mentioned, the effects of viscosity change with temperature (heating) are not included.

We solve the system of equations (2)–(10) using the multidomain modeling package Simscape which extends Simulink with tools for object oriented modeling and simulating multiphysics systems [40]. Our model as shown in Figure 8 consists of mechanical, hydraulic, and physical signals domains. Using that environment, the MR damper model was developed with isothermal hydraulic double-acting cylinder components, adiabatic gas blocks, and friction components. The MR fluid behaviour as copied specifically by equation (6) was defined by means of a custom component based on the biplastic

Bingham model approach [31] in series with the local loss model.

To allow simulations of the transient performance of the damper, the model was coupled to the FE model in Ansys Maxwell through the magnetic flux density vs yield stress relationship, $\tau_0 = \tau_0(B_g)$. The interface assumes zero delay between the electromagnetic response of the circuit and the MRF response. MRF measurements indicate the response time of the fluid to be below 0.6 ms; therefore, that particular contribution is omitted in the developed equation set.

3.2.2. Magnetorheological Valve Model. In this section, we describe the biplastic Bingham computing scheme for determining the pressure drop across the magnetorheological valve. Specifically, the relationship between the flow rate through the annulus Q_a and the pressure drop Δp_a is needed. The biplastic scheme is preferred rather than the conventional Bingham approach as it is more flexible and allows for a more effective modeling of low velocity features in the annulus, e.g., magnetic bypass [2]. Using the dimensionless representation of the scheme in terms of the pressure number G and the plasticity S , we express the relationship between the flow rate Q_a and the pressure drop across the annulus Δp_a as

$$\Delta p_a = \frac{2\tau_2 L_a}{h} G(S) = \frac{2\tau_0 L_a}{h(1-\gamma(1-\delta))} G(S), \quad (11)$$

where

$$\begin{cases} G = -\frac{h\Delta p_a}{2L_a\tau_2}, \\ S = \frac{12\mu Q_a}{wh^2\tau_2}. \end{cases} \quad (12)$$

The two additional parameters, γ and δ , are referred to as the artificial viscosity ratio and the (nondimensional) bypass number (yield stress ratio), respectively. As the biplastic model was well studied in prior research papers, the reader should refer there for in-depth details and the parameter estimation method. Briefly, δ controls the intercept force at the zero piston velocity, and γ influences the curve's slope below the knee-point of the force-velocity characteristics [2]. The two parameters of the biplastic model are related to the valve's geometry rather than material properties. The estimation procedure was highlighted, e.g., in [36]. For example, based on prior knowledge, the value of δ (0.5) was selected for a valve with no leakage flow path in the annulus. Using the model, we classify the valve's behaviour into two flow regimes: preyield ($G \leq 1$) and postyield ($G > 1$). The transition point coordinates at which the behaviour of the pseudomaterial changes from the preyield regime to the postyield regime are equal to $G = 1$, $S_0 = \gamma(2 - 3\delta + \delta^3)$. Briefly, when in the postyield regime, the relationship between G and S can be expressed as

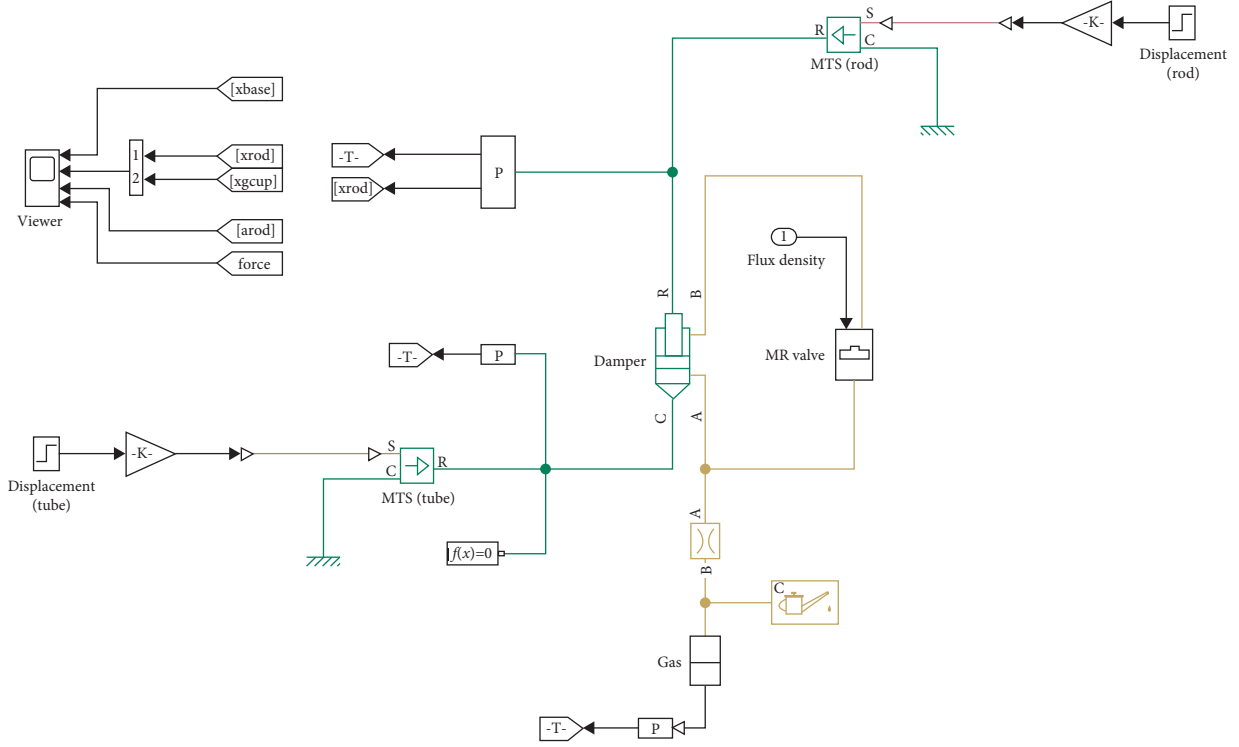


FIGURE 8: High-level Simscape model layout.

$$G = \frac{1}{6} [3(1 - \gamma(1 - \delta)) + S] \left[2 \cos\left(\frac{1}{3}a \tan 2(y, x)\right) + 1 \right], \quad (13)$$

$$\begin{cases} y = 12\sqrt{-81b^2 + 12ba^3}, \\ x = -108b + 8a^3, \\ a = \frac{3}{2}(1 - \gamma(1 - \delta)) + \frac{1}{2}S, \\ b = \frac{1}{2}(1 - \gamma(1 - \delta^3)), \end{cases} \quad (14)$$

whereas in the preyield regime, the relationship between the pressure drop and the flow rate through the annulus is governed by the following formula:

$$G = \delta \frac{1}{6} \left[\frac{S}{\gamma\delta} + 3 \right] \left[2 \cos\left(\frac{1}{3}a \tan 2(y_1, x_1)\right) + 1 \right], \quad (15)$$

where

$$\begin{cases} y_1 = 6\sqrt{3} \sqrt{27 \frac{S}{\gamma\delta} + 9 \left(\frac{S}{\gamma\delta}\right)^2 + \left(\frac{S}{\gamma\delta}\right)^3}, \\ x_1 = -27 + 27 \frac{S}{\gamma\delta} + 9 \left(\frac{S}{\gamma\delta}\right)^2 + \left(\frac{S}{\gamma\delta}\right)^3. \end{cases} \quad (16)$$

The two model parameters (γ , δ) can be identified from real damper experimental data or CFD (computational flow dynamics) simulations. Finally, equation (11) can be modified to include the contribution of the nonenergized region above the coil of the length $L_c - L_a$ through

$$\Delta p_a = \frac{2\tau_2 L_a}{h} G(S) + \frac{12\mu(L_c - L_a)Q_a}{wh^3}. \quad (17)$$

4. Magnetic Flux Measurements

For the specific electromagnet geometry, we performed a series of measurements for extracting the flux density information with respect to the control (exciting) current input. The goal was to verify the FE model. Therefore, in this section, we reveal the experimental procedure for acquiring the magnetic flux relationship against the exciting current and present the obtained data.

4.1. Test Rig Configuration. The magnetic flux density was measured in the middle of the air gap with the ultrathin Hall transverse probe (STB1X-0201) and the magnetometer F. W. Bell 5180 at the sampling frequency of 100 Hz. The coil current magnitude coil was simultaneously acquired by means of the Fluke i30s current clamp. The MR damper coil was excited using two laboratory power supplies: (1) Manson SDP2603 device for lower amplitude current excitations and (2) G. W. Instek PST-3202 power supply for higher current inputs. The two signals are recorded simultaneously using the front-end Dewetron USB-50-USB2-8 data acquisition module connected to the laptop (Figure 9).

The procedure was performed as follows: (1) current increase up to the maximum prescribed current I_{\max} , which was followed by decreasing the current down to 0 A, (2) input voltage polarity change, (3) repeat Step 1, (4) repeat

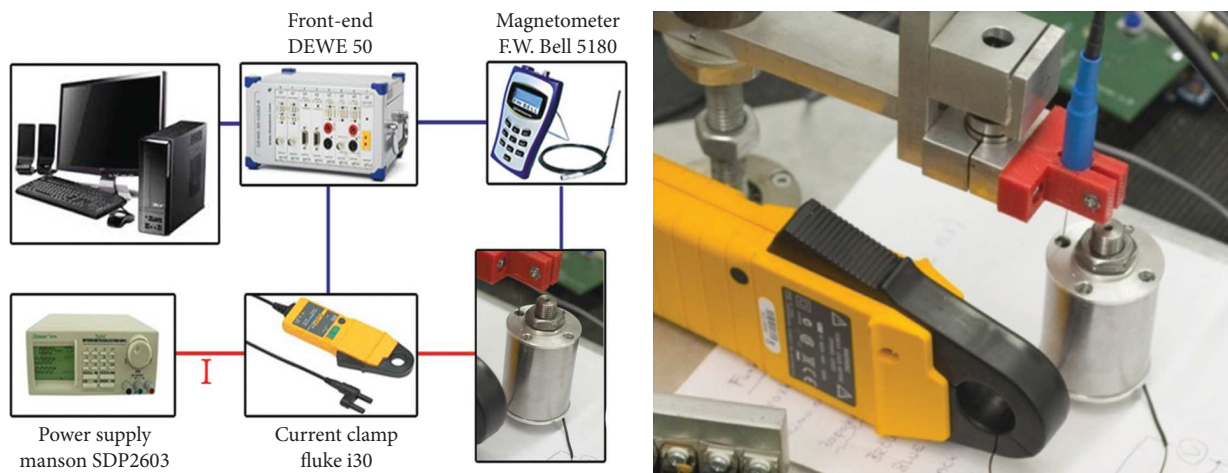


FIGURE 9: Test rig configuration.

Step 2, and (5) repeat Step 1. Using the highlighted procedure, the magnetic flux density was measured for the maximum current levels $I_{\max} = \{0.5, 1, 2, 3, 4, 5\}$ A, respectively.

The measurements of magnetic flux in the annular gap were performed without the MR fluid. Note that the relative permeability of the Hall sensor ($\mu_r = 1$) placed in the thin annulus with MR fluid would distort the accuracy of the experiment as the flux flows around the probe as illustrated in Figure 10. In the simulations, we assume the presence of MR fluid would not degrade the accuracy of the model.

4.2. Results. The obtained data are revealed in Figure 11 as plots of flux density vs coil current.

Observations of the plots of flux density vs current reveal the presence of hysteresis and nonlinear behaviour with the actuator approaching the saturation at the highest current level ($I_{\max} = 5$ A).

5. Modelling Results

The series of modelling experiments was split into two stages. First, we validate the transient FE model against the experimental data, and then we study the behaviour of the hydraulic model.

5.1. FE Model Verification: Air Gap, No MR Fluid. Here, the FE model of the damper described in Section 3.1 was verified against the obtained air gap flux density measurements. The comparison of the obtained data against the model output can be observed in Figure 12 as plots of flux density vs coil current. Due to the low current change rate, the eddy currents were neglected in the model, and only the hysteresis contribution was studied.

Again, observations of the plots reveal satisfactory agreement with the model anywhere except for the smallest exciting current. Overall, the plots prove the rationality of the proposed approach.

5.2. Hysteresis Assessment of the MR Valve. Due to reasons explained in Section 4.1, direct assessment of the hysteretic behaviour of the MR valve with the fluid in the annulus was not possible with the available laboratory equipment. However, CIP- (carbonyl powder iron-) based MR fluids show virtually zero hysteresis [12]. Therefore, the presence of the fluid in the annulus only modifies the flux density-current relationship through its (nonlinear) magnetisation characteristics. Hence, it is reasonable to proceed further under the assumption that electromagnet model of the actuator was validated, and it would be accurate also in the scenarios in which the MR annulus would be filled with the fluid. Due to the magnetic circuit saturation above 2 A, we reveal the results for the exciting currents up to 2 A (Figure 13). The nonlinear contribution of the fluid is evident in the presented results.

Next, we examine the behaviour of the valve model for the two following variants:

- (i) Hysteresis (core loss) ON, eddy currents ON (solid line)
- (ii) Hysteresis (core loss) ON, eddy currents OFF (dashed line)

The hysteresis model was applied to all 11SMn30 components (core, sleeve). As presented in Figure 14, the calculated remanent flux density is relatively independent of the previous magnetic history within the examined coil current range from 0.5 A to 2 A, and the effect of eddy currents is rather insignificant in the examined case as already revealed in Figure 14.

Furthermore, we repeated the flux density calculations for one selected electric current level ($I_{\max} = 2$ A) for the following three model variants:

- (i) Hysteresis switched OFF, eddy currents switched OFF (dashed line)
- (ii) Hysteresis ON, eddy currents OFF (dotted line)
- (iii) Hysteresis ON and eddy currents ON (solid line)

The results are revealed in Figure 15. It is now apparent that the hysteresis has the biggest impact on the initial

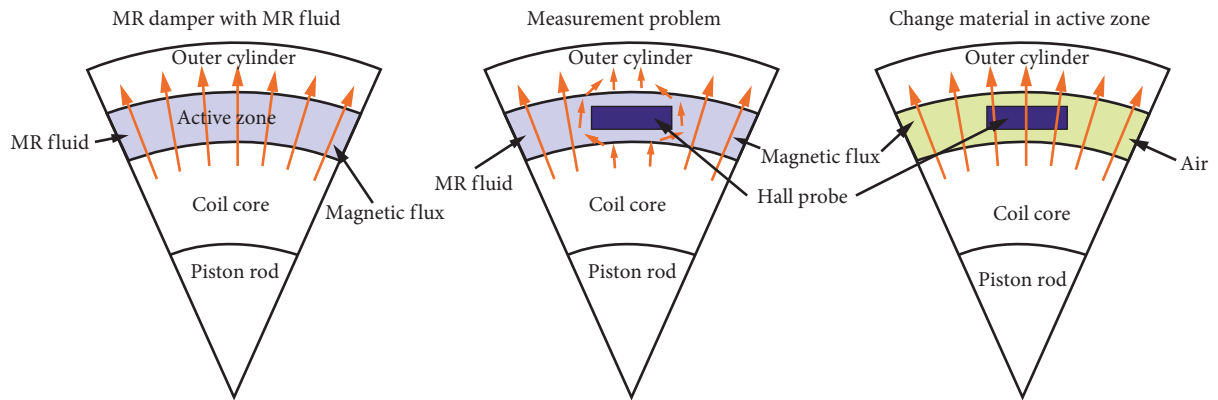


FIGURE 10: Illustration of the measurement problem with Hall sensor in the annular gap in the presence of MR fluid [41].

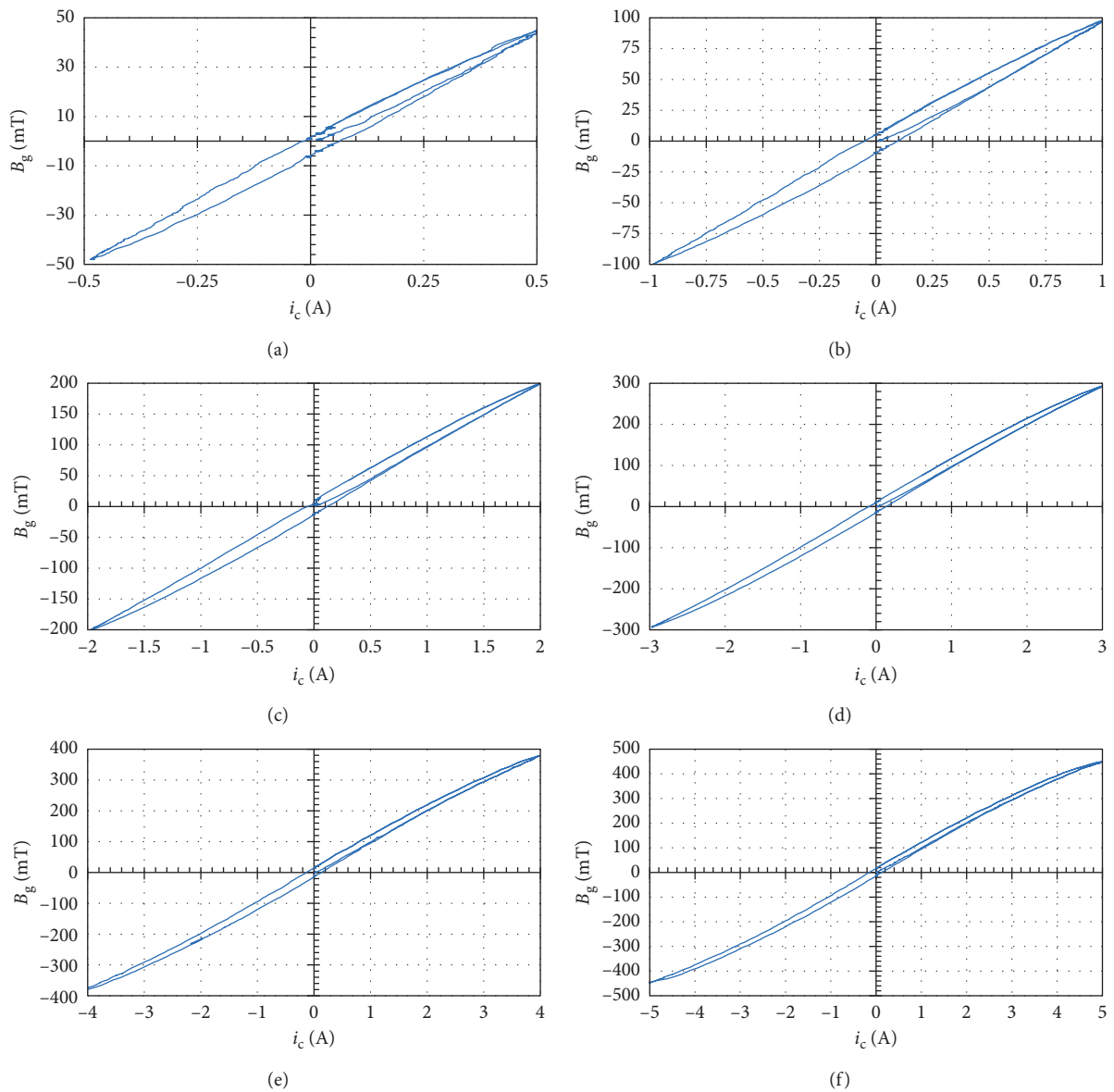


FIGURE 11: Flux density measurements: air gap, no MR fluid. (a) $I_{\max}=0.5$ A. (b) $I_{\max}=1.0$ A. (c) $I_{\max}=2.0$ A. (d) $I_{\max}=3.0$ A. (e) $I_{\max}=4.0$ A. (f) $I_{\max}=5.0$ A.

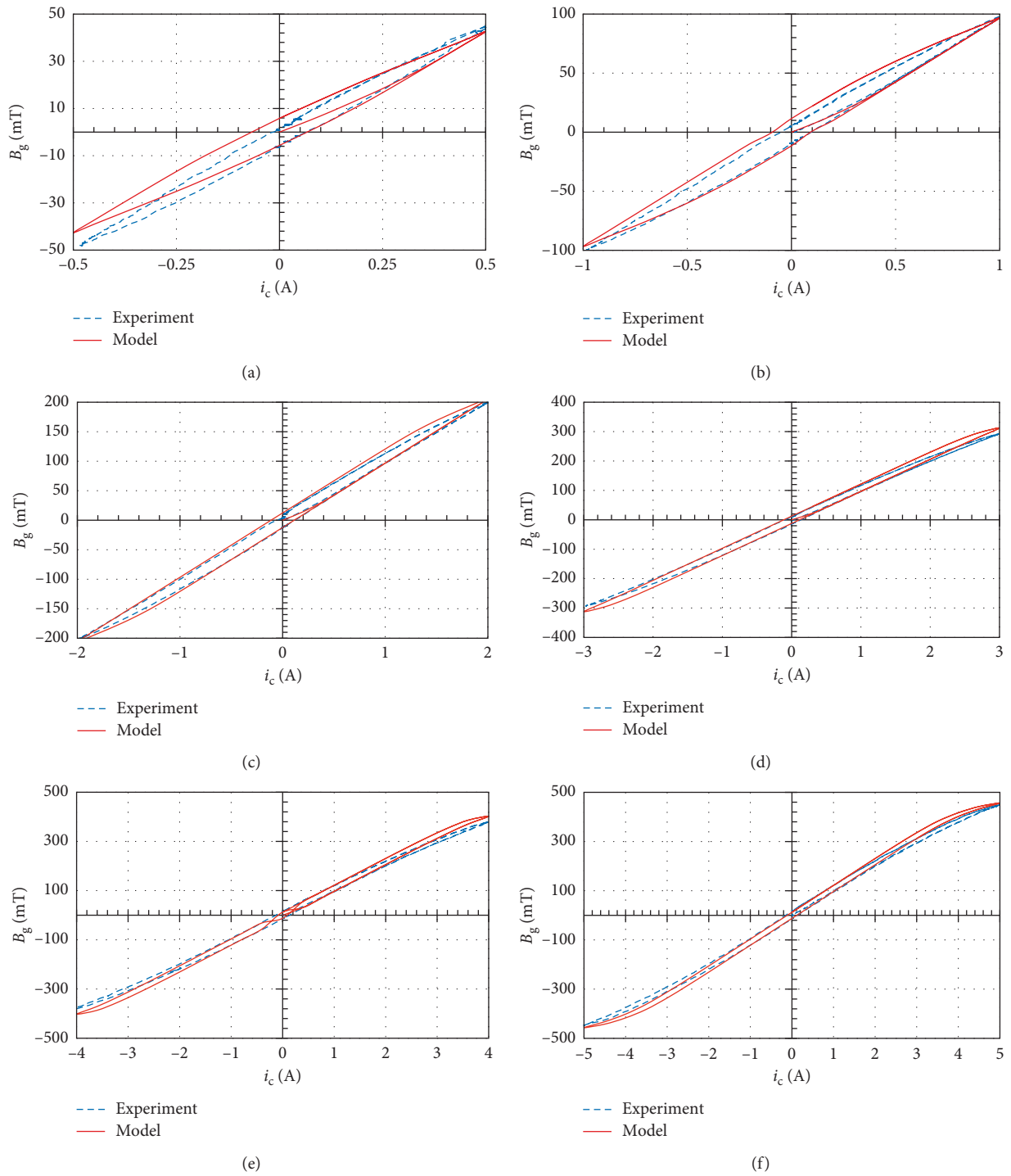


FIGURE 12: Air gap flux density: measurements vs FE model. (a) $I_{max} = 0.5$ A. (b) $I_{max} = 1.0$ A. (c) $I_{max} = 2.0$ A. (d) $I_{max} = 3.0$ A. (e) $I_{max} = 4.0$ A. (f) $I_{max} = 5.0$ A.

output of the actuator (up to 100 mT), and the contribution of the eddy currents is negligible within the examined time scale. The eddy currents have little effect on the output flux density in the examined case (Figure 15). Clearly, the first and second scenarios are only hypothetical ones and unseen

in real MR devices. However, they were included in the simulation for the purpose of isolating the contribution of a specific phenomenon.

Now, the obtained flux density output can be converted into the resulting yield stress and then used in all subsequent

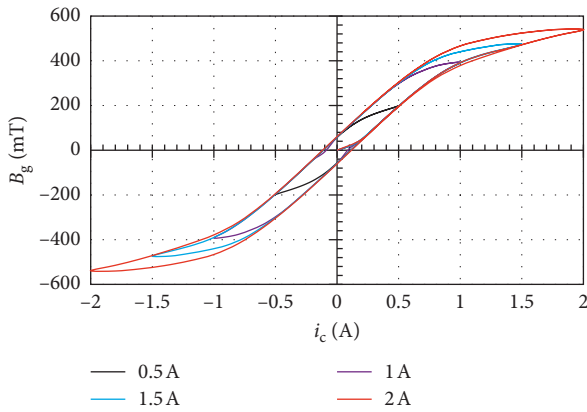


FIGURE 13: MR fluid contribution: calculated flux density vs. exciting current.

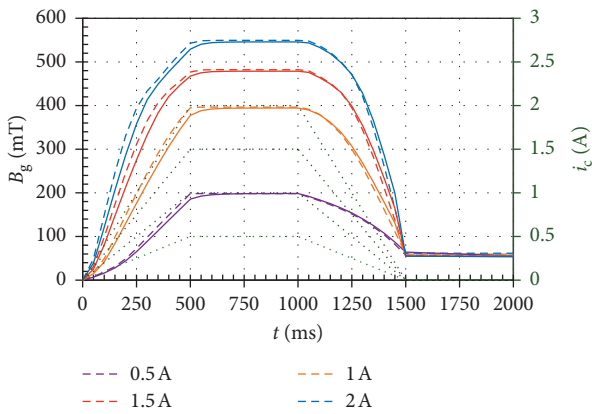


FIGURE 14: Time history of (gap) magnetic flux density: hysteresis ON (dashed line), hysteresis ON and eddy currents OFF (solid line), and electric current (dotted line).

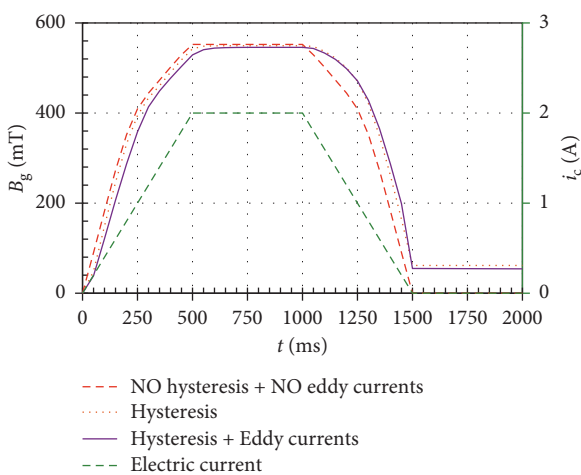


FIGURE 15: Time history: (gap) magnetic flux density, $I_{\max} = 2$ A.

damper simulations (Figure 16). As seen in the calculated data, the residual flux results in the field-induced yield stress of appr. 2.23 kPa.

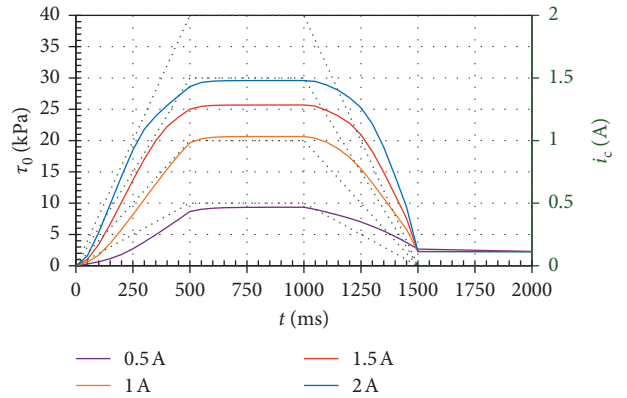


FIGURE 16: Time history: yield stress (full line) and electric current (dotted green line).

5.3. Damper Response to Sinusoidal Displacement Inputs.

Using the set of equations (1)–(9) in Section 3.2.1 and (10)–(16) in Section 3.2.2 as well as the above yield stress map in Figure 16, we then modelled the response of the damper subjected to sinusoidal displacement inputs at fixed (constant) current levels. This was merely for demonstrating the force output of the damper corresponding to the prescribed current levels. The calculated results are highlighted as plots of force vs velocity and force vs displacement for the peak velocity $V_r = 0.3$ m/s in Figure 17. In the calculated example, the stroking amplitude X_r was 30 mm. Note that the data are shifted by the gas force proportional to the product of the gas pressure P_g and the piston rod area A_r (equal to 339 N). Hysteresis due to compressibility of the fluid (increasing with the current/flux level), force oscillations at piston motion reversal points, can be also observed in the generated plots, too.

Moreover, the influence of remnant flux can be seen in Figure 18. In the figure, we present the results of off-state (zero current) simulations with and without demagnetization cycle. In the revealed example, the damper was subjected to a sinusoidal displacement input at the peak velocity $V = 0.3$ m/s. The blue loops reveal the damper response after demagnetization, and the red loops copy the off-state behaviour of the damper which was previously excited at $I_{\max} = 2$ A. The presence of the remanent flux (appr. 54 mT) results in the contribution of 140 N.

5.4. Damper Response to Control Current Step Inputs.

The optimal performance of a S/A (semiactive) control system with an MR damper requires understanding its dynamic behaviour. In controller design studies as well as vehicle simulation, a need for modeling the MR damper system dynamics arises quite often; the time delay between the force and the control signal due to, e.g., eddy currents degrades the system performance. Therefore, in this section, we reveal the results of a series of simulations in which the influence of eddy currents, magnetic hysteresis, and hydromechanical hysteresis (due to compressibility of the fluid) is considered. In the simulations, we assumed a fast controller [6] capable of driving the coil to within 2 ms of the commanded values.

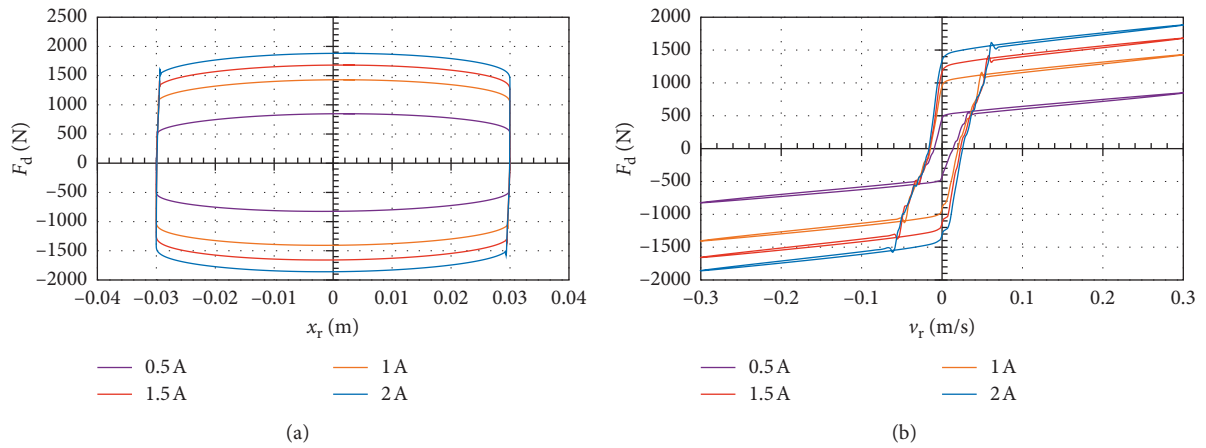


FIGURE 17: Fixed current: force vs. velocity and force vs. stroke, $V_r = 0.3$ m/s. (a) F_d vs x_r . (b) F_d vs v_r .

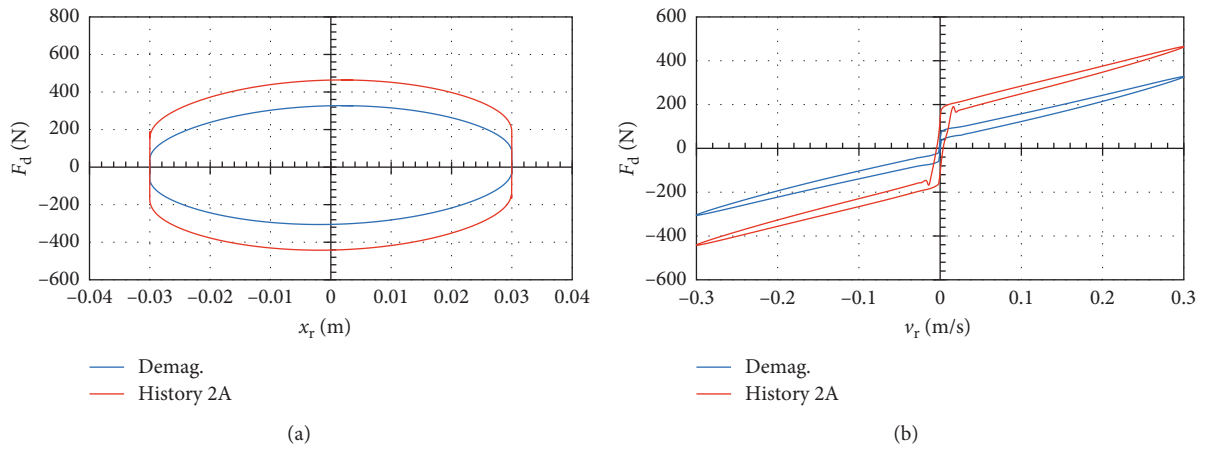


FIGURE 18: Off-state force: demagnetized (blue) and following 2 A current excitation, no demagnetization (red). (a) F_d vs x_r . (b) F_d vs v_r .

The output is highlighted in Figure 19. As seen, the actuator’s off-state output is degraded by the presence of a static (residual) flux. The actuator is capable of reaching zero flux only in the hysteresis-free scenario.

In Figure 20, we further examined the force output varying the coercivity from 0 A/m to 200 A/m. It has no effect on the force output in the current (flux) rise stage; however, in the current drop case (Figure 20(b)), its contribution became evident as the actuator never reached the initial force of 240 N (prior to the current excitation).

5.5. Sensitivity to Gap Height: Parametric Study. Next, the following series of numerical experiments involved studying the contribution of the MR valve’s geometry on the residual force (and flux) output. The model setup incorporated the hysteresis loss model only and no eddy current mechanism. Throughout the experiment series, the coercivity H_c was varied from 120 A/m to 600 A/m, and the gap size h from 0.65 mm to 1.0 mm. The generated B - H loop set (core material) is revealed in Figure 21.

The calculated results are shown in Figure 22 for the maximum electric current of 2 A. The exciting current input

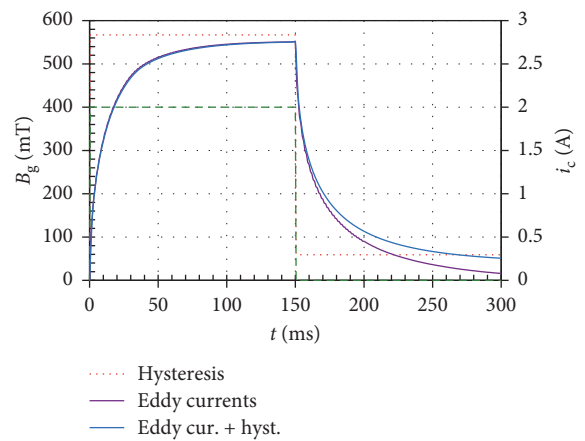


FIGURE 19: Transient FE model: time history of magnetic flux density and electric current (dashed green line).

is identical with that in Figure 14. The coercivity influences the course of the magnetic flux density over time. The greater the coercive force applied, the slower the slope of magnetic induction observed. Moreover, the material coercivity also affects the maximum achievable magnetic flux induction.

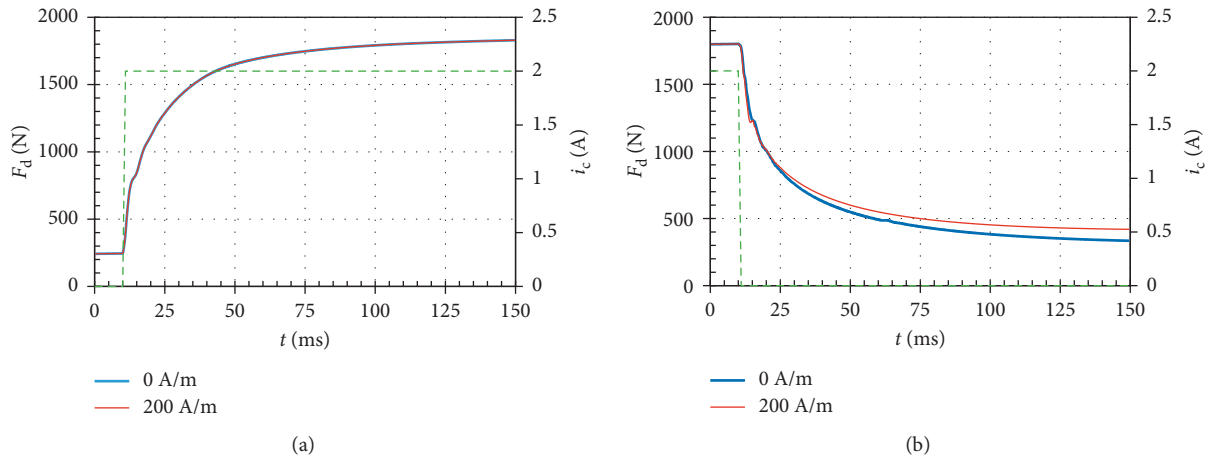


FIGURE 20: Force time history: damper response to current step input, $I_{\max} = 2$ A (electric current course highlighted by the green dashed line). (a) Current rise. (b) Current drop.

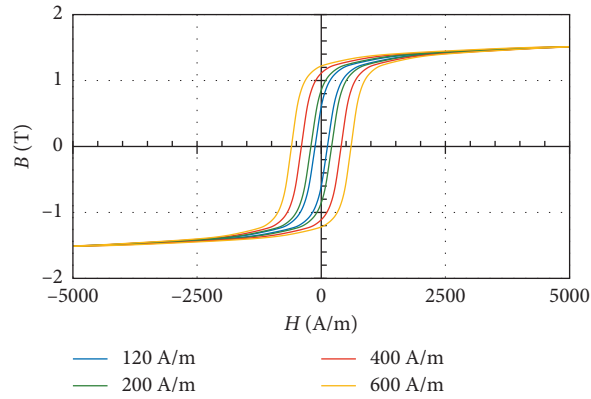


FIGURE 21: Coercivity: impact on the core material magnetisation characteristics (11SMn30).

Note that the greater the coercive force, the lower the maximum magnetic flux density generated. However, the difference is minor on the order of several percent. The difference in maximum magnetic flux density can also be due to the different shape of the generated hysteresis B - H curve by Ansys Electronics. This effect will have to be further studied in follow-up research. However, one other conclusion can be drawn: the remanent flux density follows the coercivity change. The greater the coercivity, the greater the remanent flux density induced.

The relationship of the remanent flux density vs coercivity within the range from 120 to 600 A/m is linear (Figure 23). The remanent flux density decreases as the annular gap height is increased.

Furthermore, it was of research interest to compare the impact of the material coercivity on the ratio B_{\max}/B_{rem} , where B_{\max} is the gap maximum flux density, as there is a significant influence of the annular gap size on the calculated flux density ratio at low material coercivity levels (Figure 24). It is evident that the gap height does not affect the flux density ratio at higher coercivity levels. This ratio follows the turn-up ratio change of the MR damper (Figure 25). The increase of gap size and the coercivity degradation

significantly increase the turn-up ratio K_f of MR damper. However, the maximum damping forces decrease at the same time as illustrated in Figure 26.

5.6. Parameter Sensitivity Study: Transient Response. In this section, we present the results of a parameter sensitivity study. Here, we examine the influence of the coercive force H_c , the electric conductivity σ , and the piston velocity v_r on the damping force under constant velocity excitation ($V_r = 0.3$ m/s) and current step inputs.

5.6.1. Influence of Material Coercivity. To examine the contribution of the coercivity H_c , we simulated the damper model response to current step inputs within the range from 120 A/m to 600 A/m. In each scenario, we assumed the material's electric conductivity σ equal to 1 MS/m (which is typical to some silicon steel alloys or soft magnetic composites) and the presence of eddy currents. The FE results from the transient model are shown in Figure 27. The coil current step input is also shown in Figure 27 (green dashed line).

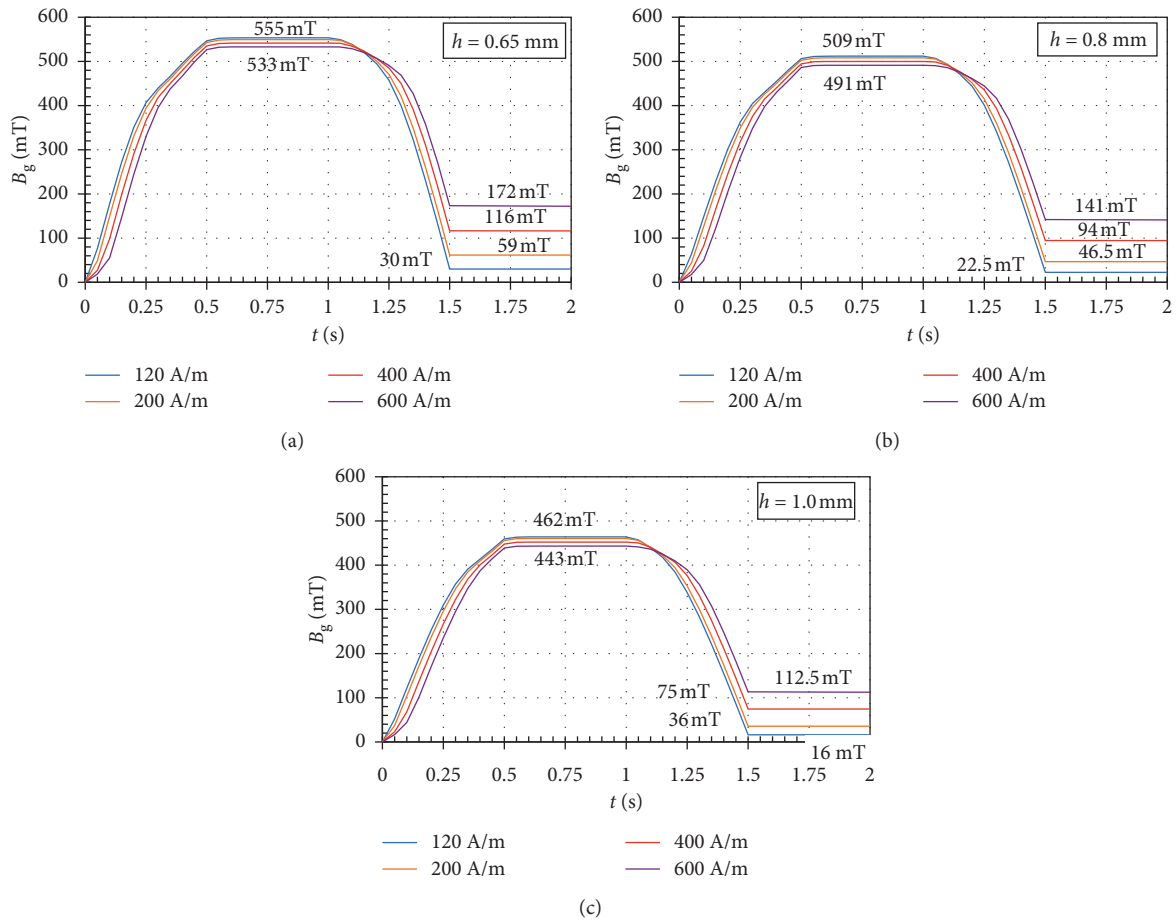


FIGURE 22: Influence of gap height and coercivity on magnetic flux density. (a) $h = 0.65$ mm. (b) $h = 0.8$ mm. (c) $h = 1.0$ mm.

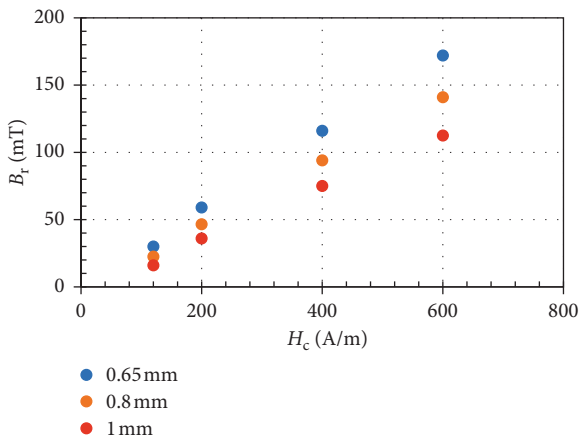


FIGURE 23: Remanent flux density variation with coercivity and gap size.

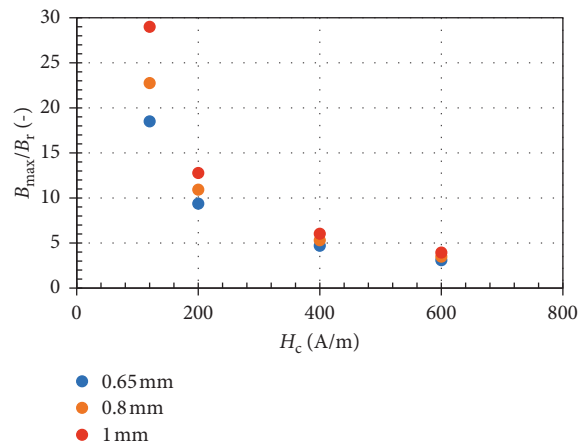


FIGURE 24: Maximum-to-remanent flux density ratio vs material coercivity.

The corresponding time histories of the damping force following the current (flux) rise/decay are revealed in Figure 28.

5.6.2. *Influence of Electric Conductivity.* It is well known that the ferromagnetic material's electric conductivity has a rather dramatic effect on the eddy currents induced in

solenoid structures. Here, we simulate the transient response of the damper subjected to 2 A current step inputs. The value of 5.8 MS/m is typical of low-carbon steel alloys, whereas 1 MS/m characterizes some soft magnetic composite materials. The resulting time history is revealed in Figure 29. As shown, as the conductivity decreases, the eddy currents are reduced, and the response of the damper becomes faster.

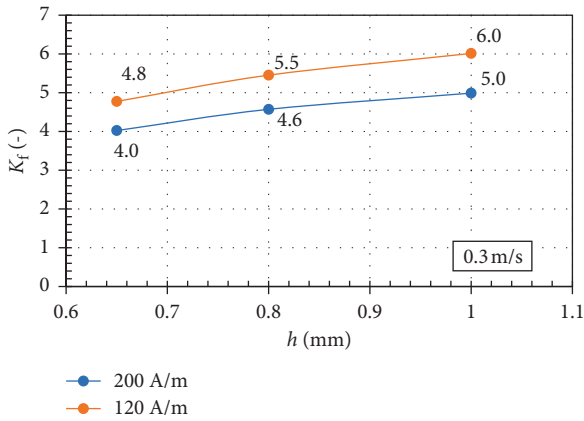


FIGURE 25: Turn-up ratio variation with gap height and coercivity, $V_r = 0.3$ m/s.

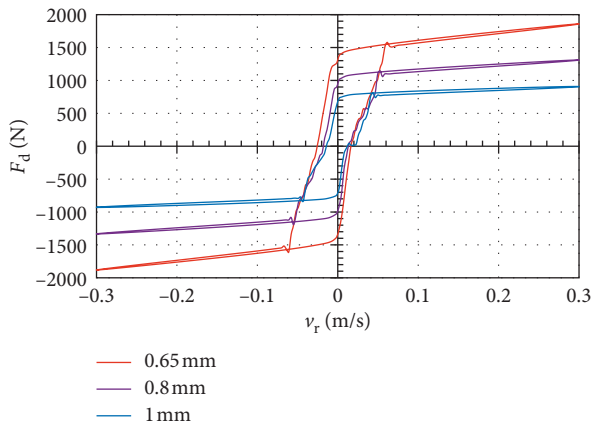


FIGURE 26: Gap height influence on damping force output, $I_{\max} = 2$ A $V_r = 0.3$ m/s.

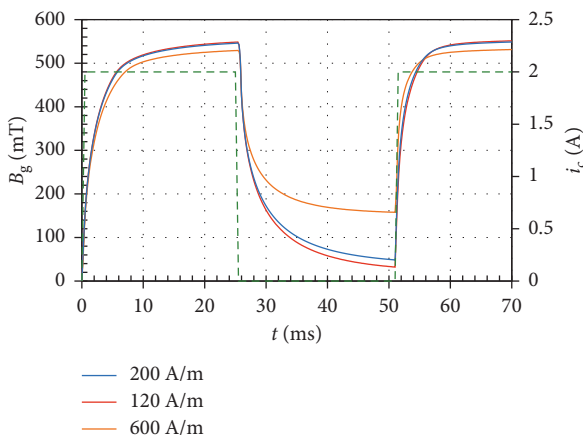


FIGURE 27: Coercivity H_c : (gap) averaged magnetic flux density time history.

5.6.3. Influence of Piston Velocity. Setting the electrical conductivity to 1 MS/m and the coercivity to 200 A/m, we then tested the influence of the piston velocity on the force. In the presented examples, the force output time histories were normalized for better comparison. The obtained results

imply that the slower the piston velocity for control current rise, the slower the magnitude of the force change rate generated. After exceeding the piston velocity of 0.2 m/s, the actuator response in the current rise stage is independent of the piston velocity (Figure 30). However, the exact velocity value will depend on the particular damper design. For comparison, the actuator response in the current drop stage is independent of the prescribed piston velocity.

Apart from the eddy currents, the main source of slower force rise is the compressibility of the MR fluid itself. Three different values of MR fluid bulk modulus were tested to illustrate this effect (Figure 31).

The primary response time of force (63.3% of final force) was calculated from the simulated data (Figure 30) (Figure 32). The primary response time for control current rise is influenced by the piston velocity. The lower the piston velocity, the lower the primary response time. However, the primary response time for control current drop is independent of piston velocity. It is noteworthy that similar trends were experimentally determined in other research studies [42, 43].

6. Conclusions and Summary

In this paper, we present the results of a modeling study involving a multiphysics model of a flow-mode MR damper. The model allows integrating an FE electromagnet model of the device with a hydraulic lumped parameter model of the device. The modeling approach relies only on the information which can be extracted from engineering drawings (geometry), material data sheets (material properties), and therefore, it can be used in studies on the performance of real actuators or virtual prototypes.

The electromagnet was verified experimentally. Based on the obtained data, we conclude that the model is capable of predicting the magnetic hysteretic behaviour of the MR valve. The results concerning the hydraulic model are simulated; however, it should be noted that the model is based on a well-established and experimentally verified theory [39]. To demonstrate the usefulness of the model, we applied it in a parametric study, in which the contribution of various geometric parameters and material properties to the output of the actuator was studied and analyzed. For instance, we can conclude the following.

- (i) Residual magnetic flux is directly related to the current history and the annular gap height
- (ii) Larger annular gaps induce lower remanent (residual) flux density and then less undesired force increase (Figures 22 and 23)
- (iii) Valves with larger annular gaps height reveal higher turn-up ratio (dynamic range), however, at the expense of maximum damping forces (Figures 25 and 26)
- (iv) Turn-up ratio (dynamic range) varies with the coercivity and gap height (Figure 25)
- (v) Demagnetizing current cycles are required to reduce/eliminate the residual flux (and the force increment due to the residual flux)

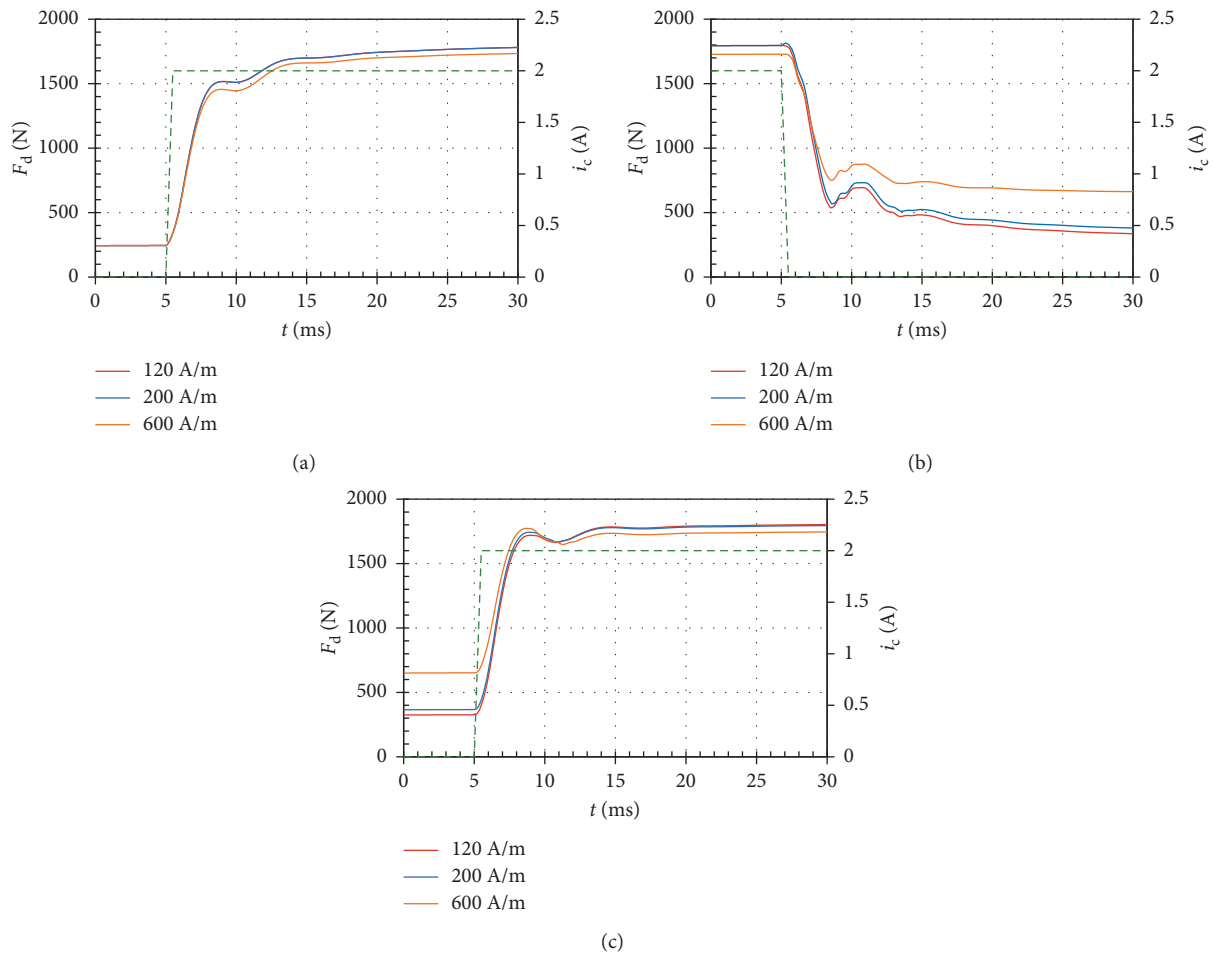


FIGURE 28: Impact of the coercivity H_c . Full line: damping force time history; green dashed line: current step input. (a) Force vs time: current rise (initial condition = demag.). (b) Force vs time: current drop. (c) Force vs time: current rise (no demag.).

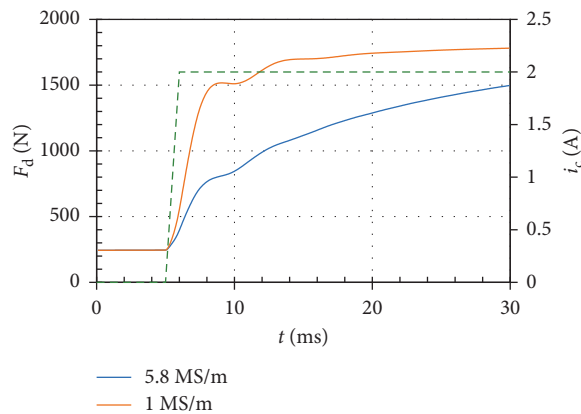


FIGURE 29: Core material's electric conductivity: Full line: damping force time history; green dashed line: current step input. $H_c = 200$ A/m, $V_r = 0.3$ m/s.

- (vi) The electrical conductivity has a major influence on the dynamic behaviour of the actuator (Figure 29)
- (vii) The piston velocity influences the actuator's response time. Low piston velocities degrade the response time in the current rise stage (Figures 30

and 32). It is likely due to the compressibility of the fluid (Figure 31).

The collected data enhance understanding the key mechanisms governing the flux/force output of MR

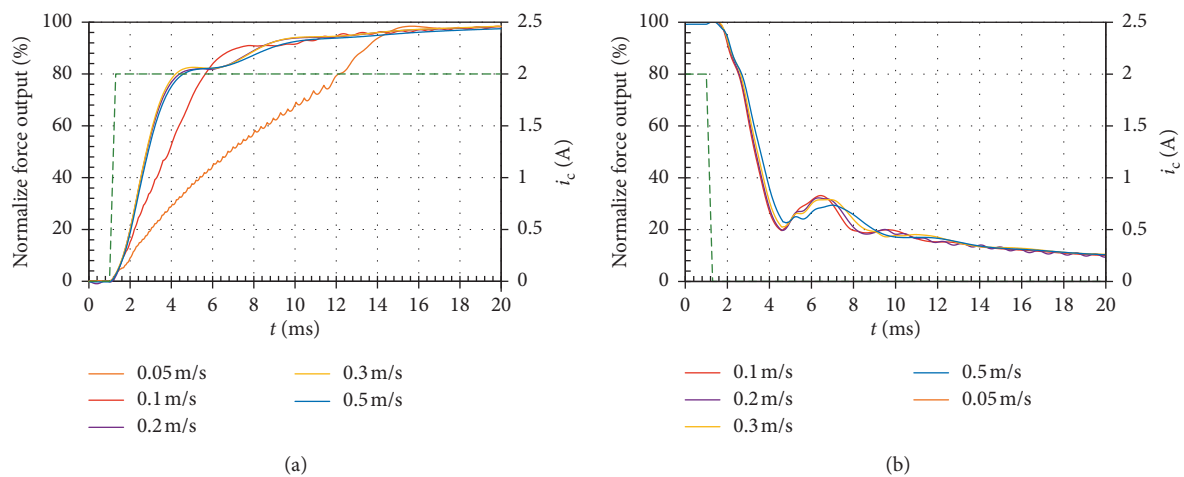


FIGURE 30: Influence of piston velocity for control current rise and drop (green dashed line) on the force output (full line). (a) Current rise. (b) Current drop.

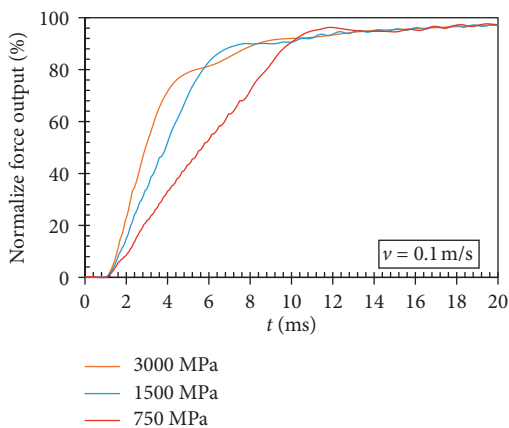


FIGURE 31: Influence of MR fluid bulk modulus on the force output at velocity 0.1 m/s.

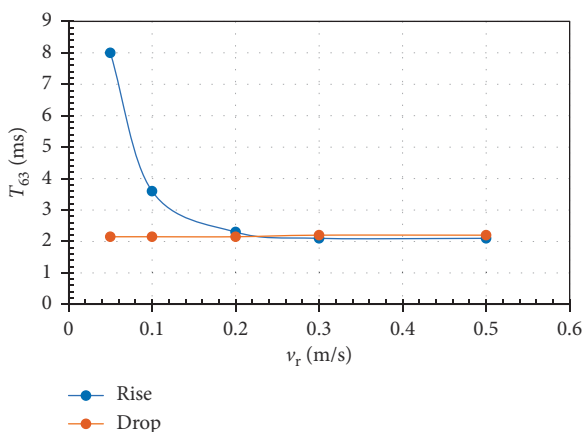


FIGURE 32: Influence of piston velocity on the primary response time for the rise and drop control current.

actuators. They allow for a clear separation of various contributors to the static and dynamic behaviour of such devices. In our opinion, the proposed model can be a useful

tool as it incorporates major key phenomena occurring in the actuator including magnetic hysteresis and remanence/coercivity, eddy currents, compressibility, and fluid inertia (hydraulic hysteresis), the MR effect. It allows separating the magnetic hysteresis from the hydromechanical one so that the two phenomena can be examined separately.

Data Availability

The data used to support the findings of this study are available from the corresponding author upon request.

Conflicts of Interest

The authors declare that they have no conflicts of interest.

Acknowledgments

The authors wish to acknowledge the support of the grant NAWA: E-Mobility and Sustainable Materials and Technologies (EMMAT) (number PPI/APM/2018/1/00027/U/001) sponsored by the Polish National Agency for Academic Exchange (NAWA).

References

- [1] J. Rabinow, "The magnetic fluid clutch," *Electrical Engineering*, vol. 67, no. 12, p. 1167, 1948.
- [2] J. Goldasz and B. Sapinski, *Insight into Magnetorheological Shock Absorbers*, Springer, Cham, Switzerland, 2015.
- [3] W. Kordonski and A. Shorey, "Magnetorheological (MR) jet finishing technology," *Journal of Intelligent Material Systems and Structures*, vol. 18, no. 12, pp. 1127–1130, 2007.
- [4] M. R. Jolly, J. W. Bender, J. D. Carlson, and L. Drive, "Properties and applications of commercial magnetorheological fluids," *Journal of Intelligent Material Systems and Structures*, vol. 10, no. 1, pp. 5–13, 1999.
- [5] A. Farjoud and E. A. Bagherpour, "Electromagnet design for magneto-rheological devices," *Journal of Intelligent Material Systems and Structures*, vol. 27, no. 1, pp. 51–70, 2016.

- [6] Z. Strecker, J. Roupec, I. Mazurek, O. Machacek, M. Kubik, and M. Klapka, "Design of magnetorheological damper with short time response," *Journal of Intelligent Material Systems and Structures*, vol. 26, no. 14, pp. 1951–1958, 2015.
- [7] Y.-M. Han, S.-B. Choi, and N. M. Wereley, "Hysteretic behavior of magnetorheological fluid and identification using Preisach model," *Journal of Intelligent Material Systems and Structures*, vol. 18, no. 9, pp. 973–981, 2007.
- [8] A. Sternberg, R. Zemp, and J. C. de la Llera, "Multiphysics behavior of a magneto-rheological damper and experimental validation," *Engineering Structures*, vol. 69, pp. 194–205, 2014.
- [9] C. P. Riley, "Effect of magnetic hysteresis in solenoid valve operation," *Sensor Letters*, vol. 11, no. 1, pp. 9–12, 2013.
- [10] Y. Chuang, S. Niu, S. L. Ho, W. Fu, and L. Li, "Hysteresis modeling in transient analysis of electric motors with AlNiCo magnets," *IEEE Transactions on Magnetics*, vol. 51, no. 3, pp. 1–4, 2015.
- [11] J. Goldasz, B. Sapinski, and Ł. Jastrzębski, "Assessment of the magnetic hysteretic behaviour of MR dampers through sensorless measurements," *Shock and Vibration*, vol. 2018, Article ID 3740208, 21 pages, 2018.
- [12] J. de Vicente, G. Bossis, S. Laci, and M. Guyot, "Permeability measurements in cobalt ferrite and carbonyl iron powders and suspensions," *Journal of Magnetism and Magnetic Materials*, vol. 251, no. 1, pp. 100–108, 2002.
- [13] K. C. Pitman, "The influence of stress on ferromagnetic hysteresis," *IEEE Transactions on Magnetics*, vol. 26, no. 5, pp. 1978–1980, 1990.
- [14] J. Zheng, Y. Li, Z. Li, and J. Wang, "Transient multi-physics analysis of a magnetorheological shock absorber with the inverse Jiles–Atherton hysteresis model," *Smart Materials and Structures*, vol. 24, no. 10, pp. 1–16, 2015.
- [15] B. F. Spencer Jr., S. J. Dyke, M. K. Sain, and J. D. Carlson, "Phenomenological model for magnetorheological dampers," *Journal of Engineering Mechanics*, vol. 123, no. 3, pp. 230–238, 1997.
- [16] I. D. Mayergoyz, "Dynamic Preisach models of hysteresis," *IEEE Transactions on Magnetics*, vol. 24, no. 6, pp. 2925–2927, 1988.
- [17] B. D. Coleman and M. L. Hodgdon, "A constitutive relation for rate-independent hysteresis in ferromagnetically soft materials," *International Journal of Engineering Science*, vol. 24, no. 6, pp. 897–919, 1986.
- [18] D. C. Jiles and D. L. Atherton, "Theory of ferromagnetic hysteresis," *Journal of Magnetism and Magnetic Materials*, vol. 61, no. 1–2, pp. 48–60, 1986.
- [19] D. C. Jiles, J. B. Thoenke, and M. K. Devine, "Numerical determination of hysteresis parameters for the modeling of magnetic properties using the theory of ferromagnetic hysteresis," *IEEE Transactions on Magnetics*, vol. 28, no. 1, pp. 27–35, 1992.
- [20] A. Raghunathan, Y. Melikhov, J. E. Snyder, and D. C. Jiles, "Modeling the temperature dependence of hysteresis based on Jiles–Atherton theory," *IEEE Transactions on Magnetics*, vol. 45, no. 10, pp. 3954–3957, 2009.
- [21] K. Chwastek, "Frequency behaviour of the modified Jiles–Atherton model," *Physica B: Condensed Matter*, vol. 403, no. 13–16, pp. 2484–2487, 2008.
- [22] J. Tellinen, "A simple scalar model for magnetic hysteresis," *IEEE Transactions on Magnetics*, vol. 34, no. 4, pp. 2200–2206, 1998.
- [23] Y. M. Han, S. C. Lim, H. G. Lee, S. B. Choi, and H. J. Choi, "Hysteresis identification of polymethylaniline-based ER fluid using Preisach model," *Materials & Design*, vol. 24, no. 1, pp. 53–61, 2003.
- [24] P. Yadmellat and M. R. Kermani, "Adaptive modeling of a magnetorheological clutch," *IEEE/ASME Transactions on Mechatronics*, vol. 19, no. 5, pp. 1716–1723, 2014.
- [25] J. An and D.-S. Kwon, "Modeling of a magnetorheological actuator including magnetic hysteresis," *Journal of Intelligent Material Systems and Structures*, vol. 14, no. 9, pp. 541–550, 2003.
- [26] C. Jędrzycka, P. Sujka, and W. Szeląg, "The influence of magnetic hysteresis on magnetorheological fluid clutch operation," *COMPEL—International Journal for Computation and Mathematics in Electrical and Electronic Engineering*, vol. 28, no. 3, pp. 711–721, 2009.
- [27] P. Guo, J. Xie, and X. Guan, "Dynamic model of MR dampers based on a hysteretic magnetic circuit," *Shock and Vibration*, vol. 2018, Article ID 2784950, 13 pages, 2018.
- [28] J. Goldasz, B. Sapinski, and L. Jastrzębski, "On the application of Bouc-Wen hysteresis approach for modeling of MR actuators," in *Proceedings of the Actuator 16th International Conference on New Actuators*, pp. 1–5, Breme, Germany, June 2018.
- [29] S. M. Chen, W. A. Bullough, and J. Hart, "CFD study of the flow in a radial electrorheological fluid clutch," *Journal of Physics: Conference Series*, vol. 21, no. 15, pp. 1569–1574, 2010.
- [30] D. Lin, P. Zhou, and A. Bergqvist, "Improved vector play model and parameter identification for magnetic hysteresis materials," *IEEE Transactions on Magnetics*, vol. 50, no. 2, pp. 18–21, 2014.
- [31] J. Goldasz and B. Sapinski, "Nondimensional characterization of flow-mode magnetorheological/electrorheological fluid dampers," *Journal of Intelligent Material Systems and Structures*, vol. 23, no. 14, pp. 1545–1562, 2012.
- [32] Lord Company, <http://www.lordmrstore.com/lord-mr-products/mrf-132dg-magneto-rheological-fluid>.
- [33] M. Rosu, P. Zhou, D. Lin et al., *Multiphysics Simulation by Design for Electrical Machines, Power Electronics, and Drives*, John Wiley & Sons, Hoboken, NJ, USA, 2018.
- [34] D. Lin, P. Zhou, C. Lu, N. Chen, and M. Rosu, "Construction of magnetic hysteresis loops and its applications in parameter identification for hysteresis models," in *Proceedings of the 2014 International Conference on Electrical Machines (ICEM)*, pp. 1050–1055, Berlin, Germany, September 2014.
- [35] M. Rosu, *Advanced Hysteresis Modeling*, Ansys, Canonsburg, PA, USA, 2017.
- [36] N. M. Wereley and L. Pang, "Nondimensional analysis of semi-active electrorheological and magnetorheological dampers using approximate parallel plate models," *Smart Materials and Structures*, vol. 7, no. 5, pp. 732–743, 1998.
- [37] W. Hu and N. M. Wereley, "Nondimensional damping analysis of flow-mode magnetorheological and electro-rheological dampers," in *Proceedings of the ASME 2003 International Mechanical Engineering Congress and Exposition*, pp. 265–272, American Society of Mechanical Engineers, Washington, DC, USA, November 2003.
- [38] R. W. Phillips, *Engineering Applications of Fluids with a Variable Yield Stress*, University of California, Berkeley, CA, USA, 1969.
- [39] J. Goldasz and B. Sapinski, "Verification of magneto-rheological shock absorber models with various piston configurations," *Journal of Intelligent Material Systems and Structures*, vol. 24, no. 15, pp. 1846–1864, 2013.
- [40] Mathworks Matlab, <https://www.mathworks.com>.

- [41] M. Kubík, O. Machacek, Z. Strecker, J. Roupec, P. Novak, and I. Mazurek, "Transient magnetic model of magnetorheological damper and its experimental verification," *MATEC Web of Conferences*, vol. 153, article 06002, 2018.
- [42] Z. Strecker, M. Kubík, P. Vitek, J. Roupec, D. Paloušek, and V. Šreibr, "Structured magnetic circuit for magnetorheological damper made by selective laser melting technology," *Smart Materials and Structures*, vol. 28, no. 5, article 055016, 2019.
- [43] M. Kubík, O. Macháček, Z. Strecker, J. Roupec, and I. Mazurek, "Design and testing of magnetorheological valve with fast force response time and great dynamic force range," *Smart Materials and Structures*, vol. 26, no. 4, article 047002, 2017.

CONCLUSIONS AND IMPLICATIONS FOR FURTHER RESEARCH

MR fluid development has been going on intensively for more than 35 years. Since then, MR fluid has undergone tremendous development. The MR fluid has been used in dampers, clutches, brakes, seals, or engine mounts. Currently, this technology is widely used in automotive. The most important application is in electronically controlled dampers. However, intensive fundamental research is still underway in the area of MR fluid itself and the development of new and progressive MR devices. The recent trend is the use of MR dampers with semi-active control, where the transient behaviour of the MR damper is very important (damper with short response time).

The habilitation thesis provides a short insight into MR fluid (chapter 2) and MR devices (chapter 3). Specifically, in chapter 2, the rheological, tribological, and transient response of MR fluid is discussed. The main goal of chapter 2 was to provide the current state of the art and highlight the main findings and some limitations of the previous studies. At the end of this chapter was presented the author's contribution to the field. The main findings of the author on the field of *MR fluid fundamental research* are:

- (i) The author of the thesis developed a unique rheometer design and a method for measuring the rheological response time of MR fluid in shear load mode [80]. It was determined the effect of shear strain rate, carrier fluid viscosity and magnetization on the rheological response time. The experimentally determined data were generalized in the form of Non-dimensional response time and Mason number. The master curve (Figure 13) was obtained from the measurement, which allows calculating the rheological response time of MR fluid for any MR device operating in shear mode during the design phase.
- (ii) The author determined the effect of the magnetic field, fluid viscosity and gap size on the hydrodynamic response time of MR fluid operating in valve mode and shear strain rates common in MR devices [79]. The measured data were generalized in the form of Non-dimensional response time on Bingham number, and one master curve was evaluated (Figure 11). The hydrodynamic response time for different MR damper configurations and different MR fluids can be determined from the master curve during the design phase.
- (iii) The author experimentally determined the MR fluid friction coefficient in a wide range of Hersey numbers (Stribeck curve) in a typical range of MR devices (Figure 15) [81].

Chapter 3 deals with magnetorheological devices and their transient behaviour. Specifically, the current state of the art in the MR damper, MR fluid seal and MR damper transient response were presented. The main factors affecting the MR damper transient response were also presented. At the end of this chapter, it is presented the author's contribution to the field. The main findings in the research field (*fundamental and applied research*) of MR devices and their transient response are:

- (iv) The design of an MR damper with a permanent magnet (fail-safe MR damper) was developed and tested [135]. The important result was that the permanent magnet significantly affected the MR damper transient response (Figure 27). This behaviour can be modelled by transient magnetic simulation quite precisely.
- (v) The unique approach for designing of MR damper with a short response time, great dynamic force range, good mechanical properties, and low weight was presented (Figure 28) [136].

This method is based on rods made of 3D metal printing manufacturing method. The author of the thesis also patented this method (EP 3373311 A1).

- (vi) The author creates the multiphysics model of the MR damper [137]. The effect of MR fluid compressibility is important, especially at low piston velocities. The response time course on piston velocity has an exponential character (Figure 31).
- (vii) The unique design of the MR fluid shaft seal, which allows high burst pressure and low friction torque, was presented (Figure 32) [138]. The main idea of the seal is based on MR fluid pinch model loading mode.

It can be stated that the presented papers extend the current state of the art in the field of the transient response of MR fluid and MR devices. Understanding the transient behavior of MR fluids is essential for the development of a new generation of MR fluids with the shortest possible response time. Even a small change in response time can be significant. The presented methods of MR damper design allow optimizing the response time or weight with regard to the requirements of the given technical application. Those methods ensure the lowest MR damper response time of around 1.3 ms. This fast damper significantly increases the performance of semi-actively controlled suspension systems. In automotive, this damper with semiactive control can improve comfort, improve driving handling or even shorten braking distances and thus passengers safety. In total, the *thesis is composed of 7 papers* (5x Q1, 1x Q2 and 1x Q3). All papers were published in peer-reviewed journals with a high impact factor.

It can be stated that the research and development in the field of MR fluids and MR devices are definitely not over. I assume that the large future research areas are (i) the durability of MR devices (especially seals), (ii) the durability of MR fluids under long-term loading, (iii) the transient response of MR fluids, (iv) high-velocity regime of MR fluid, or (v) rheology of new load mode of MR fluid (pinch mode). In my opinion, all these areas are interesting for high-quality research/ publication. In 2012, Murphy [141] stated that in 15 years (considered the year 2027), half of the automotive dampers are expected to rely on MR fluid. Unfortunately, the reality now is different. The main limit of this technology is the price of MR fluid itself, which is given by the high price of iron particles. So, in my opinion, the biggest challenge in the field of magnetorheology is the development of a method for producing high-quality CI powders quickly and cheaply. In the case of cheaper MR fluid, this technology will be used in most applications where any damping is required.

REFERENCES

- [1] FAKULTA DOPRAVNÍ ČVUT V PRAZE. *Technologické trendy v silniční dopravě*. 2018. Dostupné z: www.tpsd-ertrac.cz/file/smery-technologickeho-vyvoje-oblast-bezpecnost-silnicniho-provozu/
- [2] RABINOW, Jacob. The Magnetic Fluid Clutch. *Transactions of the American Institute of Electrical Engineers*. 1948, roč. 67, č. 2, s. 1308–1315. ISSN 0096-3860.
- [3] CARLSON, D. a A. ACHEN. *Magneto-Rheological Technology and Applications*. 2008.
- [4] KRAUZE, Piotr a Jerzy KASPRZYK. Driving Safety Improved with Control of Magnetorheological Dampers in Vehicle Suspension. *Applied Sciences*. 2020, roč. 10, č. 24, s. 8892. ISSN 2076-3417.
- [5] KUBÍK, Michal, Zbyněk STRECKER, Filip JENIŠ, Ondřej MACHÁČEK, Matěj PŘIKRYL a Petr ŠPALEK. Magnetorheological yaw damper with short response time for railway vehicle bogie. *GMM-Fachberichte*. 2021, roč. 2021-Febru, č. 98, s. 373–376. ISSN 14323419.
- [6] GOŁDASZ, J. a B. SAPIŃSKI. *Insight into magnetorheological shock absorbers*. 2015. ISBN 978-3-319-13232-7.
- [7] GORODKIN, S R, R O JAMES a W I KORDONSKI. Magnetic properties of carbonyl iron particles in magnetorheological fluids. *Journal of Physics: Conference Series*. 2009, roč. 149, s. 012051. ISSN 1742-6596.
- [8] CARLSON, J. David a Keith D. WEISS. Magnetorheological materials based on alloy particles. US5382373A. 1993. USA.
- [9] RWEI, Syang-Peng, Lee Yi WANG a Po-Wen YANG. Synthesis and Magnetorheology Study of Iron Oxide and Iron Cobalt Oxide Suspensions. *Journal of Nanomaterials*. 2013, roč. 2013, s. 1–7. ISSN 1687-4110.
- [10] FELT, D. W., M. HAGENBUCHLE, J. LIU a J. RICHARD. Rheology of a Magnetorheological Fluid. *Journal of Intelligent Material Systems and Structures*. 1996, roč. 7, č. 5, s. 589–593. ISSN 1045-389X.
- [11] DE VICENTE, Juan, Daniel J. KLINGENBERG a Roque HIDALGO-ALVAREZ. Magnetorheological fluids: A review. *Soft Matter*. 2011, roč. 7, č. 8, s. 3701–3710. ISSN 1744683X.
- [12] UPADHYAY, R V, Zarana LAHERISHETH a Kruti SHAH. Rheological properties of soft magnetic flake shaped iron particle based magnetorheological fluid in dynamic mode. *Smart Materials and Structures*. 2014, roč. 23, č. 1, s. 015002. ISSN 0964-1726.
- [13] SHAH, Kruti a Seung-Bok CHOI. The Field-Dependent Rheological Properties of Magnetorheological Fluids Featuring Plate-Like Iron Particles. *Frontiers in Materials*. 2014, roč. 1. ISSN 2296-8016.
- [14] KCIUK, Sławomir, Monika KCIUK, Tomasz MACHOCZEK a Wojciech KLEIN. Magnetorheological Suspension Based on Silicone Oil. In: . 2019, s. 201–219. Dostupné z: doi:
- [15] KUMBHAR, Bhau K., Satyajit R. PATIL a Suresh M. SAWANT. Synthesis and characterization of magneto-rheological (MR) fluids for MR brake application. *Engineering Science and Technology, an International Journal*. 2015, roč. 18, č. 3, s. 432–438. ISSN 22150986.
- [16] LÓPEZ-LÓPEZ, Modesto T., Pavel KUZHIR, Georges BOSSIS a Pavel MINGALYOV. Preparation of well-dispersed magnetorheological fluids and effect of dispersion on their magnetorheological properties. *Rheologica Acta*. 2008, roč. 47, č. 7, s. 787–796. ISSN 0035-4511.
- [17] THIAGARAJAN, Sandhiya a Amanda S. KOH. Performance and Stability of Magnetorheological Fluids—A Detailed Review of the State of the Art. *Advanced Engineering*

- Materials*. 2021, roč. 23, č. 6, s. 2001458. ISSN 1438-1656.
- [18] DOROSTI, A.H., M. GHATEE a M. NOROUZI. Preparation and characterization of water-based magnetorheological fluid using wormlike surfactant micelles. *Journal of Magnetism and Magnetic Materials*. 2020, roč. 498, s. 166193. ISSN 03048853.
- [19] BARBER, Daniel E. a J. David CARLSON. Performance Characteristics of Prototype MR Engine Mounts Containing Glycol MR Fluids. *Journal of Intelligent Material Systems and Structures*. 2010, roč. 21, č. 15, s. 1509–1516. ISSN 1045-389X.
- [20] YANG, Jianjian, Fernando VEREDA, Jose R MORILLAS a Juan DE VICENTE. Ternary solid-ferrofluid-liquid magnetorheological fluids. *Smart Materials and Structures*. 2018, roč. 27, č. 7, s. 075017. ISSN 0964-1726.
- [21] CORPORATION, Lord. *Lord technical data*. 2019.
- [22] GRUNWALD, A. a A.G. OLABI. Design of magneto-rheological (MR) valve. *Sensors and Actuators A: Physical*. 2008, roč. 148, č. 1, s. 211–223. ISSN 09244247.
- [23] MURAT, Ocalan. *Magnetorheological fluids for extreme environments : stronger, lighter, hotter*. B.m., 2011. Massachusetts Institute of Technology.
- [24] LLOYD, John R., Miquel O. HAYESMICHEL a Clark J. RADCLIFFE. Internal Organizational Measurement for Control of Magnetorheological Fluid Properties. *Journal of Fluids Engineering*. 2007, roč. 129, č. 4, s. 423–428. ISSN 0098-2202.
- [25] CLARACQ, Jerome, Jerome SARRAZIN a Jean-Pierre MONTFORT. Viscoelastic properties of magnetorheological fluids. *Rheologica Acta*. 2004, roč. 43, č. 1, s. 38–49. ISSN 0035-4511.
- [26] IDO, Y, T INAGAKI a T YAMAGUCHI. Numerical simulation of microstructure formation of suspended particles in magnetorheological fluids. *Journal of Physics: Condensed Matter*. 2010, roč. 22, č. 32, s. 324103. ISSN 0953-8984.
- [27] CLIMENT, Eric, Martin R. MAXEY a George Em KARNIADAKIS. Dynamics of Self-Assembled Chaining in Magnetorheological Fluids. *Langmuir*. 2004, roč. 20, č. 2, s. 507–513. ISSN 0743-7463.
- [28] GHAFFARI, Ali, Seyed Hassan HASHEMABADI a Mahshid ASHTIANI. A review on the simulation and modeling of magnetorheological fluids. *Journal of Intelligent Material Systems and Structures*. 2015, roč. 26, č. 8, s. 881–904. ISSN 1045-389X.
- [29] JÖNKKÄRI, Ilari, Matti ISAKOV a Seppo SYRJÄLÄ. Sedimentation stability and rheological properties of ionic liquid-based bidisperse magnetorheological fluids. *Journal of Intelligent Material Systems and Structures*. 2015, roč. 26, č. 16, s. 2256–2265. ISSN 1045-389X.
- [30] LI, Yuqing, Yiping LUO, Ying WANG, Jiao LUO a Yameng CHEN. Research on characterization method and influencing factors of sedimentation stability of magnetorheological fluid. *Korea-Australia Rheology Journal*. 2021, roč. 33, č. 4, s. 309–320. ISSN 1226-119X.
- [31] WIEHE, Ansgar a Jürgen MAAS. Large-scale test bench for the durability analysis of magnetorheological fluids. *Journal of Intelligent Material Systems and Structures*. 2013, roč. 24, č. 12, s. 1433–1444. ISSN 1045-389X.
- [32] TRENDLER, A.-M. a H. BÖSE. Influence of particle size on the rheological properties of magnetorheological suspensions. *International Journal of Modern Physics B*. 2005, roč. 19, č. 07n09, s. 1416–1422. ISSN 0217-9792.
- [33] SHAH, Kruti a Seung-Bok CHOI. The influence of particle size on the rheological properties of plate-like iron particle based magnetorheological fluids. *Smart Materials and Structures*. 2015, roč. 24, č. 1, s. 015004. ISSN 0964-1726.
- [34] LEE, Jae Yun, Seung Hyuk KWON a Hyoung Jin CHOI. Magnetorheological characteristics of carbonyl iron microparticles with different shapes. *Korea-Australia Rheology Journal*. 2019, roč. 31, č. 1, s. 41–47. ISSN 1226-119X.
- [35] DE VICENTE, Juan, Fernando VEREDA, Juan Pablo SEGOVIA-GUTIÉRREZ, María DEL PUERTO MORALES a Roque HIDALGO-ÁLVAREZ. Effect of particle shape in magnetorheology. *Journal of Rheology*. 2010, roč. 54, č. 6, s. 1337–1362. ISSN 0148-6055.
- [36] CHIRIAC, H a G STOIAN. Influence of particle size distributions on magnetorheological fluid performances. *Journal of Physics: Conference Series*. 2010, roč. 200, č. 7, s. 072095. ISSN 1742-6596.
- [37] ZSCHUNKE, F., R. RIVAS a P.O. BRUNN. Temperature Behavior of Magnetorheological Fluids. *Applied Rheology*. 2005, roč. 15, č. 2, s. 116–121. ISSN 1617-8106.

- [38] ZHANG, J Q, J ZHANG a Q JING. Effect of seven different additives on the properties of MR fluids. *Journal of Physics: Conference Series*. 2009, roč. 149, s. 012086. ISSN 1742-6596.
- [39] IERARDI, Rafael F a Antonio J F BOMBARD. Off-state viscosity and yield stress optimization of magneto-rheological fluids: A mixture design of experiments approach. *Journal of Physics: Conference Series*. 2009, roč. 149, s. 012037. ISSN 1742-6596.
- [40] MARDLES, E. W. J. Viscosity of Suspensions and the Einstein Equation. *Nature*. 1940, roč. 145, č. 3686, s. 970–970. ISSN 0028-0836.
- [41] MACOSKO, Christopher W. *Rheology: Principles, Measurements, and Applications*. B.m.: Wiley-VCH, 1996. ISBN 978-0-471-18575-8.
- [42] JEON, Jihoon a Sangkyun KOO. Viscosity and dispersion state of magnetic suspensions. *Journal of Magnetism and Magnetic Materials*. 2012, roč. 324, č. 4, s. 424–429. ISSN 03048853.
- [43] CARLSON, J.David a Mark R JOLLY. MR fluid, foam and elastomer devices. *Mechatronics*. 2000, roč. 10, č. 4–5, s. 555–569. ISSN 09574158.
- [44] MORILLAS, Jose R. a Juan DE VICENTE. Magnetorheology: a review. *Soft Matter*. 2020, roč. 16, č. 42, s. 9614–9642. ISSN 1744-683X.
- [45] SUSAN-RESIGA, Daniela. A Rheological Model for Magneto-rheological Fluids. *Journal of Intelligent Material Systems and Structures*. 2009, roč. 20, č. 8, s. 1001–1010. ISSN 1045-389X.
- [46] LI, W H, G CHEN a S H YEO. Viscoelastic properties of MR fluids. *Smart Materials and Structures*. 1999, roč. 8, č. 4, s. 460–468. ISSN 0964-1726.
- [47] MOHAMMADI, N., M. J. MAHJOOB, B. KAFFASHI a S. MALAKOOTI. An experimental evaluation of pre-yield and post-yield rheological models of magnetic field dependent smart materials. *Journal of Mechanical Science and Technology*. 2010, roč. 24, č. 9, s. 1829–1837. ISSN 1738494X.
- [48] PHILLIPS, Robert William. *Engineering applications of fluids with a variable yield stress*. B.m., 1969. niversity of California.
- [49] SEO, Youngwook P., Sangsok HAN, Junsok CHOI, Atsushi TAKAHARA, Hyoung Jin CHOI a Yongsok SEO. Searching for a Stable High-Performance Magnetorheological Suspension. *Advanced Materials*. 2018, roč. 30, č. 42, s. 1704769. ISSN 09359648.
- [50] PEI, Pei a Yongbo PENG. Constitutive modeling of magnetorheological fluids: A review. *Journal of Magnetism and Magnetic Materials*. 2022, roč. 550, s. 169076. ISSN 03048853.
- [51] WU, Xiangfan, Xingming XIAO, Zuzhi TIAN, Fei CHEN a Wang JIAN. Effect of Particle Characteristics and Temperature on Shear Yield Stress of Magnetorheological Fluid. *Journal of Magnetics*. 2016, roč. 21, č. 2, s. 244–248. ISSN 1226-1750.
- [52] BOSSIS, G., O. VOLKOVA, S. LACIS a A. MEUNIER. Magnetorheology: Fluids, Structures and Rheology. 2002, č. January, s. 202–230.
- [53] KUMAR, James Sathya, P. Sam PAUL, Girish RAGHUNATHAN a Divin George ALEX. A review of challenges and solutions in the preparation and use of magnetorheological fluids. *International Journal of Mechanical and Materials Engineering*. 2019, roč. 14, č. 1, s. 13. ISSN 1823-0334.
- [54] YANG, Yongbo, Lin LI a Guang CHEN. Static yield stress of ferrofluid-based magnetorheological fluids. *Rheologica Acta*. 2009, roč. 48, č. 4, s. 457–466. ISSN 00354511.
- [55] ZHANG, Xiangcheng, Xiaotong LIU, Xiaohui RUAN, Jun ZHAO a Xinglong GONG. The Influence of Additives on the Rheological and Sedimentary Properties of Magnetorheological Fluid. *Frontiers in Materials*. 2021, roč. 7. ISSN 2296-8016.
- [56] KUMAR, Manjesh, Hari Narayan SINGH YADAV, Abhinav KUMAR a Manas DAS. An overview of magnetorheological polishing fluid applied in nano-finishing of components. *Journal of Micromanufacturing*. 2021, s. 251659842110081. ISSN 2516-5984.
- [57] GAHR, K.-H.Zum. Wear by hard particles. *Tribology International*. 1998, roč. 31, č. 10, s. 587–596. ISSN 0301679X.
- [58] WANG, Na, Shuo PANG, Cuili YE, Tingting FAN a Seung-Bok CHOI. The friction and wear mechanism of O-rings in magnetorheological damper: Numerical and experimental study. *Tribology International*. 2021, roč. 157, s. 106898. ISSN 0301679X.
- [59] LI, Yuqing, Zhibin SU, Yiping LUO, Ying WANG, Jiao LUO a Dongsheng JI. Study on the Friction and Wear Properties of Magnetorheological Fluids Based on Different Lubricant Formulas. *Journal of Superconductivity and Novel Magnetism*. 2021, roč. 34, č. 3, s. 943–950.

ISSN 15571947.

- [60] HU, Z.D., H. YAN, H.Z. QIU, P. ZHANG a Q. LIU. Friction and wear of magnetorheological fluid under magnetic field. *Wear*. 2012, roč. 278–279, s. 48–52. ISSN 00431648.
- [61] IYENGAR, VARDARAJAN R., FOISTER, Robert T. Durable magnetorheological fluid compositions. US6599439B2. 2000. USA.
- [62] ZHANG, Peng, Kwang Hee LEE a Chul Hee LEE. Friction behavior of magnetorheological fluids with different material types and magnetic field strength. *Chinese Journal of Mechanical Engineering (English Edition)*. 2016, roč. 29, č. 1, s. 84–90. ISSN 10009345.
- [63] WONG, P.L, W.A BULLOUGH, C. FENG a S. LINGARD. Tribological performance of a magneto-rheological suspension. *Wear*. 2001, roč. 247, č. 1, s. 33–40. ISSN 00431648.
- [64] WALKER, C.I. a M. HAMBE. Influence of particle shape on slurry wear of white iron. *Wear*. 2015, roč. 332–333, s. 1021–1027. ISSN 00431648.
- [65] SHAHRIVAR, K., A.L. ORTIZ a J. DE VICENTE. A comparative study of the tribological performance of ferrofluids and magnetorheological fluids within steel–steel point contacts. *Tribology International*. 2014, roč. 78, s. 125–133. ISSN 0301679X.
- [66] ZHANG, Peng, Kwang-Hee LEE a Chul-Hee LEE. Friction behavior of magnetorheological fluids with different material types and magnetic field strength. *Chinese Journal of Mechanical Engineering*. 2016, roč. 29, č. 1, s. 84–90. ISSN 1000-9345.
- [67] JOLLY, M. R., J. W. BENDER a J. D. CARLSON. Properties and Applications of Commercial Magnetorheological Fluids. *Journal of Intelligent Material Systems and Structures*. 1999, roč. 10, č. 1, s. 5–13. ISSN 1045-389X.
- [68] MAAS, Jurgen a Dirk GUTH. Experimental Investigation of the Transient Behavior of MR Fluids. In: *ASME 2011 Conference on Smart Materials, Adaptive Structures and Intelligent Systems, Volume 1*. B.m.: ASMEDC, 2011, s. 229–238. ISBN 978-0-7918-5471-6.
- [69] WU, Guangbin, Zhimin FENG, GANG ZHANG a Zhenning HOU. Experimental study on response time of magnetorheological damper. In: *2011 2nd International Conference on Artificial Intelligence, Management Science and Electronic Commerce (AIMSEC)*. B.m.: IEEE, 2011, s. 3968–3972. ISBN 978-1-4577-0535-9.
- [70] SHERMAN, Stephen G. *Magnetorheological fluid dynamics for high speed energy absorbers*. B.m., 2017. University of Maryland (College Park, Md.). Dostupné z: doi:
- [71] LAUN, Hans Martin a Claus GABRIEL. Measurement modes of the response time of a magneto-rheological fluid (MRF) for changing magnetic flux density. *Rheologica Acta*. 2007, roč. 46, č. 5, s. 665–676. ISSN 0035-4511.
- [72] GONCALVES, Fernando D. *Characterizing the Behavior of Magnetorheological Fluids at High Velocities and High Shear Rates*. B.m., 2005. Virginia Polytechnic Institute and State University. Dostupné z: <http://hdl.handle.net/10919/26142>
- [73] JOLLY, M. R., J. W. BENDER a Robert Timothy MATHERS. Indirect measurements of microstructure development in magnetorheological fluids. *International Journal of Modern Physics B*. 1999, roč. 13, č. 14–16, s. 2036–2043. ISSN 02179792.
- [74] HORVÁTH, Barnabás, Péter DECSI a István SZALAI. Measurement of the response time of magnetorheological fluids and ferrofluids based on the magnetic susceptibility response. *Journal of Intelligent Material Systems and Structures*. 2021, s. 1045389X2110386. ISSN 1045-389X.
- [75] KOYANAGI, Ken'Ichi a Tomohiro TERADA. Time Response Model of ER Fluids for Precision Control of Motors. *Journal of Intelligent Material Systems and Structures*. 2010, roč. 21, č. 15, s. 1517–1522. ISSN 1045-389X.
- [76] CHOOI, Weng W. a S. O. OYADIJI. The relative transient response of MR fluids subjected to magnetic fields under constant shear conditions. In: Kon-Well WANG, ed. *SPIE Smart Structures and Materials + Nondestructive Evaluation and Health Monitoring*. 2005, s. 456–465.
- [77] SAHIN, Huseyin, Faramarz GORDANINEJAD, Xiaojie WANG a Yanming LIU. Response time of magnetorheological fluids and magnetorheological valves under various flow conditions. *Journal of Intelligent Material Systems and Structures*. 2012, roč. 23, č. 9, s. 949–957. ISSN 1045-389X.
- [78] GAVIN, H. P., R. D. HANSON a F. E. FILSKO. Electrorheological Dampers, Part I: Analysis and Design. *Journal of Applied Mechanics*. 1996, roč. 63, č. 3, s. 669–675. ISSN 0021-8936.

- [79] KUBÍK, M, K ŠEBESTA, Z STRECKER, F JENIŠ, J GOLDASZ a I MAZŮREK. Hydrodynamic response time of magnetorheological fluid in valve mode: model and experimental verification. *Smart Materials and Structures*. 2021, roč. 30, č. 12, s. 125020. ISSN 0964-1726.
- [80] KUBÍK, Michal, Josef VÁLEK, Jiří ŽÁČEK, Filip JENIŠ, Dmitry BORIN, Zbyněk STRECKER a Ivan MAZŮREK. Transient response of magnetorheological fluid on rapid change of magnetic field in shear mode. *Scientific Reports*. 2022, roč. 12, č. 1, s. 10612. ISSN 2045-2322.
- [81] ROUPEC, Jakub, Filip JENIŠ, Zbyněk STRECKER, Michal KUBÍK a Ondřej MACHÁČEK. Stribeck Curve of Magnetorheological Fluid within Pin-on-Disc Configuration: An Experimental Investigation. *Materials*. 2020, roč. 13, č. 20, s. 4670. ISSN 1996-1944.
- [82] SCHWARTZ, Mel, ed. *Encyclopedia of Smart Materials*. Hoboken, NJ, USA: John Wiley & Sons, Inc., 2002. ISBN 0471216275.
- [83] AKHRAS, G. SMART MATERIALS AND SMART SYSTEMS FOR THE FUTURE. *Candien military journal*. 2000, s. 7.
- [84] GONCALVES, F D a J D CARLSON. An alternate operation mode for MR fluids—magnetic gradient pinch. *Journal of Physics: Conference Series*. 2009, roč. 149, s. 012050. ISSN 1742-6596.
- [85] LEE, Tae-Hoon, Byung-Hyuk KANG a Seung-Bok CHOI. A quasi-static model for the pinch mode analysis of a magnetorheological fluid flow with an experimental validation. *Mechanical Systems and Signal Processing*. 2019, roč. 134, s. 106308. ISSN 08883270.
- [86] GOŁDASZ, Janusz a Bogdan SAPIŃSKI. Magnetostatic Analysis of a Pinch Mode Magnetorheological Valve. *Acta Mechanica et Automatica*. 2017, roč. 11, č. 3, s. 229–232. ISSN 2300-5319.
- [87] GONG, Xinglong, Xiaohui RUAN, Shouhu XUAN, Qifan YAN a Huaxia DENG. Magnetorheological Damper Working in Squeeze Mode. *Advances in Mechanical Engineering*. 2014, roč. 6, s. 410158. ISSN 1687-8140.
- [88] PATEL, Jitenkumar D. a Dipal PATEL. Design Optimization of Squeeze Mode Magnetorheological Damper. *Applied Mechanics and Materials*. 2018, roč. 877, s. 391–396. ISSN 1662-7482.
- [89] YAZID, Izyan Iryani Mohd, Saiful Amri MAZLAN, Takehito KIKUCHI, Hairi ZAMZURI a Fitriani IMADUDDIN. Design of magnetorheological damper with a combination of shear and squeeze modes. *Materials & Design (1980-2015)*. 2014, roč. 54, s. 87–95. ISSN 02613069.
- [90] SUN, S S, D H NING, J YANG, H DU, S W ZHANG a W H LI. A seat suspension with a rotary magnetorheological damper for heavy duty vehicles. *Smart Materials and Structures*. 2016, roč. 25, č. 10, s. 105032. ISSN 0964-1726.
- [91] LEE, Jae-Hoon, Changwan HAN, Dongsu AHN, Jin Kyoo LEE, Sang-Hu PARK a Seonghun PARK. Design and Performance Evaluation of a Rotary Magnetorheological Damper for Unmanned Vehicle Suspension Systems. *The Scientific World Journal*. 2013, roč. 2013, s. 1–10. ISSN 1537-744X.
- [92] SHAMIED, H. *Modelling, design optimization and control of magnetorheological brakes automotive applications*. B.m., 2017. Concordia University.
- [93] POYNOR, J. *Innovative Designs for Magneto-Rheological Dampers*. B.m., 2001. Virginia Polytechnic Institute and State University.
- [94] GUO, Chaoyang, Xinglong GONG, Luhang ZONG, Chao PENG a Shouhu XUAN. Twin-tube-and bypass-containing magneto-rheological damper for use in railway vehicles. *Proceedings of the Institution of Mechanical Engineers, Part F: Journal of Rail and Rapid Transit*. 2015, roč. 229, č. 1, s. 48–57. ISSN 0954-4097.
- [95] JENSEN, E., M OLIVER a M KRUCKEMEYER. Twin-tube magnetorheological damper. US20020139624A1. 202n. 1. USA.
- [96] GOŁDASZ, Janusz. Theoretical study of a twin-tube magnetorheological damper concept. *Journal of Theoretical and Applied Mechanics*. 2015, s. 885. ISSN 1429-2955.
- [97] YUAN, Xianju, Tianyu TIAN, Hongtao LING, Tianyu QIU a Huanli HE. A Review on Structural Development of Magnetorheological Fluid Damper. *Shock and Vibration*. 2019, roč. 2019, s. 1–33. ISSN 1070-9622.
- [98] STRECKER, Z., J. ROUPEC, I. MAZUREK, O. MACHACEK, M. KUBIK a M. KLAPKA.

- Design of magnetorheological damper with short time response. *Journal of Intelligent Material Systems and Structures*. 2015, roč. 26, č. 14, s. 1951–1958. ISSN 1045-389X.
- [99] HU, Guoliang, Fengshuo LIU, Zheng XIE a Ming XU. Design, Analysis, and Experimental Evaluation of a Double Coil Magnetorheological Fluid Damper. *Shock and Vibration*. 2016, roč. 2016, s. 1–12. ISSN 1070-9622.
- [100] YANG, G., B.F. SPENCER, J.D. CARLSON a M.K. SAIN. Large-scale MR fluid dampers: modeling and dynamic performance considerations. *Engineering Structures*. 2002, roč. 24, č. 3, s. 309–323. ISSN 01410296.
- [101] GOLDASZ, Janusz. Study of a magnetorheological fluid damper with multiple annular flow gaps. *International Journal of Vehicle Design*. 2013, roč. 62, č. 1, s. 21. ISSN 0143-3369.
- [102] POTNURU, Mutyala Rao, Xiaojie WANG, Sreeram MANTRIPRAGADA a Faramarz GORDANINEJAD. A compressible magneto-rheological fluid damper-liquid spring system. *International Journal of Vehicle Design*. 2013, roč. 63, č. 2/3, s. 256. ISSN 0143-3369.
- [103] IMADUDDIN, Fitriani, Saiful Amri MAZLAN, UBAIDILLAH, Muhammad Hafiz IDRIS a Irfan BAHUDDIN. Characterization and modeling of a new magnetorheological damper with meandering type valve using neuro-fuzzy. *Journal of King Saud University - Science*. 2017, roč. 29, č. 4, s. 468–477. ISSN 10183647.
- [104] LEE, Tae-Hoon a Seung-Bok CHOI. On the response time of a new permanent magnet based magnetorheological damper: experimental investigation. *Smart Materials and Structures*. 2019, roč. 28, č. 1, s. 014001. ISSN 0964-1726.
- [105] BÖSE, Holger a Johannes EHRLICH. Magnetorheological dampers with various designs of hybrid magnetic circuits. *Journal of Intelligent Material Systems and Structures*. 2012, roč. 23, č. 9, s. 979–987. ISSN 1045-389X.
- [106] BAI, Xian-Xu a Norman M. WERELEY. A fail-safe magnetorheological energy absorber for shock and vibration isolation. *Journal of Applied Physics*. 2014, roč. 115, č. 17, s. 17B535. ISSN 0021-8979.
- [107] SREEDHAR, B.K., R. Nirmal KUMAR, Prashant SHARMA, Shivprakash RUHELA, John PHILIP, S.I. SUNDARRAJ, N. CHAKRABORTY, M. MOHANA, Vijay SHARMA, G. PADMAKUMAR, B.K. NASHINE a K.K. RAJAN. Development of active magnetic bearings and ferrofluid seals toward oil free sodium pumps. *Nuclear Engineering and Design*. 2013, roč. 265, s. 1166–1174. ISSN 00295493.
- [108] ZHANG, Yanjuan, Decai LI, Yibiao CHEN a Zhenkun LI. A Comparative Study of Ferrofluid Seal and Magnetorheological Fluid Seal. *IEEE Transactions on Magnetics*. 2018, roč. 54, č. 12, s. 1–7. ISSN 0018-9464.
- [109] URRETA, Harkaitz, Gorka AGUIRRE, Pavel KUZHIR a Luis Norberto LOPEZ DE LACALLE. Seals Based on Magnetic Fluids for High Precision Spindles of Machine Tools. *International Journal of Precision Engineering and Manufacturing*. 2018, roč. 19, č. 4, s. 495–503. ISSN 2234-7593.
- [110] KORDONSKI, W. I. a S. R. GORODKIN. Magnetorheological Fluid-Based Seal. *Journal of Intelligent Material Systems and Structures*. 1996, roč. 7, č. 5, s. 569–572. ISSN 1045-389X.
- [111] HEGGER, Christian a Jürgen MAAS. Smart sealing for magnetorheological fluid actuators. *Journal of Intelligent Material Systems and Structures*. 2019, roč. 30, č. 5, s. 689–700. ISSN 1045-389X.
- [112] YOON, Dal-Seong, Gi-Woo KIM a Seung-Bok CHOI. Response time of magnetorheological dampers to current inputs in a semi-active suspension system: Modeling, control and sensitivity analysis. *Mechanical Systems and Signal Processing*. 2021, roč. 146, s. 106999. ISSN 08883270.
- [113] OH, Jong-Seok, Kyungho JEON, Gi-Woo KIM a Seung-Bok CHOI. Dynamic analysis of semi-active MR suspension system considering response time and damping force curve. *Journal of Intelligent Material Systems and Structures*. 2021, roč. 32, č. 13, s. 1462–1472. ISSN 1045-389X.
- [114] STRECKER, Zbyněk, Ivan MAZŮREK, Jakub ROUPEC a Milan KLAPKA. Influence of MR damper response time on semiactive suspension control efficiency. *Meccanica*. 2015, roč. 50, č. 8, s. 1949–1959. ISSN 0025-6455.
- [115] MACHACEK, Ondrej, Michal KUBIK a Petr NOVÁK. A new method of magnetorheological damper quality evaluation. *Engineering Mechanics 2017*. 2017, č. May, s. 594–597.

- [116] MAAS, Jürgen a Dirk GÜTH. Experimental Investigation of the Transient Behavior of MR Fluids. In: *Conference on Smart Materials, Adaptive Structures and Intelligent Systems*. B.m.: ASME, 2011, s. 1–9. ISBN 978-0-7918-5471-6.
- [117] KOO, Jeong-Hoi, Fernando D GONCALVES a Mehdi AHMADIAN. A comprehensive analysis of the response time of MR dampers. *Smart Materials and Structures*. 2006, roč. 15, č. 2, s. 351–358. ISSN 0964-1726.
- [118] KOO, Jeong-Hoi, Fernando D GONCALVES a Mehdi AHMADIAN. A comprehensive analysis of the response time of MR dampers. *Smart Materials and Structures*. 2006, roč. 15, č. 2, s. 351–358. ISSN 0964-1726.
- [119] GUAN, Xinchun, Pengfei GUO a Jinping OU. Study of the response time of MR dampers. In: Jinsong LENG, Anand K. ASUNDI a Wolfgang ECKE, ed. . 2009, s. 74930U.
- [120] ZHANG, Hong Hui, Hai Peng XU, Chang Rong LIAO a Zhao Xiang DENG. Dynamic Response of Magnetorheological Fluid Damper for Automotive Suspension and the Influence by Long-Time Standing-Still. *Applied Mechanics and Materials*. 2011, roč. 105–107, s. 1689–1692. ISSN 1662-7482.
- [121] TAKESUE, Naoyuki, Junji FURUSHO a Yuuki KIYOTA. Fast Response MR-Fluid Actuator. *JSME International Journal Series C*. 2004, roč. 47, č. 3, s. 783–791. ISSN 1344-7653.
- [122] TAKESUE, N., J. FURUSHO a Y. KIYOTA. Analytic and experimental study on fast response MR-fluid actuator. In: *2003 IEEE International Conference on Robotics and Automation (Cat. No.03CH37422)*. B.m.: IEEE, nedatováno, s. 202–207. ISBN 0-7803-7736-2.
- [123] GIORGETTI, A, N BALDANZINI, M BIASIOTTO a P CITTI. Design and testing of a MRF rotational damper for vehicle applications. *Smart Materials and Structures*. 2010, roč. 19, č. 6, s. 065006. ISSN 0964-1726.
- [124] OCCHIUZZI, A, M SPIZZUOCO a G SERINO. Experimental analysis of magnetorheological dampers for structural control. *Smart Materials and Structures*. 2003, roč. 12, č. 5, s. 703–711. ISSN 0964-1726.
- [125] GONCALVES, Fernando D., Jeong-Hoi KOO a Mehdi AHMADIAN. Experimental Approach for Finding the Response Time of MR Dampers for Vehicle Applications. In: *Volume 5: 19th Biennial Conference on Mechanical Vibration and Noise, Parts A, B, and C*. B.m.: ASMEDC, 2003, s. 425–430. ISBN 0-7918-3703-3.
- [126] VIVAS-LOPEZ, Carlos A., Juan C. TUDON-MARTINEZ, Alfonso ESTRADA-VELA, Jorge DE JESUS LOZOYA-SANTOS a Ruben MORALES-MENENDEZ. Damping Variation Effects in Vehicle Semi-active MR Suspensions: A Stress Concentration Analysis. *Frontiers in Materials*. 2021, roč. 8. ISSN 2296-8016.
- [127] HUANG, Xi, Miao YU, Ai-jun CHEN, Chang-rong LIAO a Wei-min CHEN. Analysis of dynamic response time of MR damper and its influential factors. *Journal of Chongqing University: Natural Science Edition*. 2006, s. 808-810+813.
- [128] ZHANG, Hong-hui, Jing TONG a Hai-peng XU. Analysis on dynamic response and influential factors of Magneto-rheological damper for automotive suspension. *Journal of Chongqing University: Natural Science Edition*. 2010, roč. 33, č. 12, s. 88–94.
- [129] YANG, Guangqiang, Billie F. SPENCER, Hyung-Jo JUNG a J. David CARLSON. Dynamic Modeling of Large-Scale Magnetorheological Damper Systems for Civil Engineering Applications. *Journal of Engineering Mechanics*. 2004, roč. 130, č. 9, s. 1107–1114. ISSN 0733-9399.
- [130] STRECKER, Zbynek, Jakub ROUPEC, Ivan MAZUREK, Ondrej MACHACEK, Michal KUBIK a Milan KLAPKA. Design of magnetorheological damper with short time response. *Journal of Intelligent Material Systems and Structures*. 2015, roč. 26, č. 14, s. 1951–1958. ISSN 1045-389X.
- [131] FRIEDMAN, A J, S J DYKE a B M PHILLIPS. Over-driven control for large-scale MR dampers. *Smart Materials and Structures*. 2013, roč. 22, č. 4, s. 045001. ISSN 0964-1726.
- [132] ZHENG, Jiajia, Zhaochun LI, Jeong-Hoi KOO a Jiong WANG. Analysis and compensation methods for time delays in an impact buffer system based on magnetorheological dampers. *Journal of Intelligent Material Systems and Structures*. 2015, roč. 26, č. 6, s. 690–700. ISSN 1045-389X.
- [133] MAAS, Jürgen a Dirk GÜTH. Experimental Investigation of the Transient Behavior of MR

- Fluids. In: *ASME 2011 Conference on Smart Materials, Adaptive Structures and Intelligent Systems, Volume 1*. B.m.: ASMEDC, 2011, s. 229–238. ISBN 978-0-7918-5471-6.
- [134] FARJOD, Alireza a Esmael A BAGHERPOUR. Electromagnet design for magnetorheological devices. *Journal of Intelligent Material Systems and Structures*. 2016, roč. 27, č. 1, s. 51–70. ISSN 1045-389X.
- [135] JENIŠ, F, M KUBÍK, O MACHÁČEK, K ŠEBESTA a Z STRECKER. Insight into the response time of fail-safe magnetorheological damper. *Smart Materials and Structures*. 2021, roč. 30, č. 1, s. 017004. ISSN 0964-1726.
- [136] STRECKER, Zbyněk, Michal KUBÍK, Petr VÍTEK, Jakub ROUPEC, David PALOUŠEK a Vít ŠREIBR. Structured magnetic circuit for magnetorheological damper made by selective laser melting technology. *Smart Materials and Structures*. 2019, roč. 28, č. 5, s. 055016. ISSN 0964-1726.
- [137] KUBÍK, M. a J. GOLDASZ. Multiphysics Model of an MR Damper including Magnetic Hysteresis. *Shock and Vibration*. 2019, roč. 2019, s. 1–20. ISSN 1070-9622.
- [138] KUBÍK, M, D PAVLÍČEK, O MACHÁČEK, Z STRECKER a J ROUPEC. A magnetorheological fluid shaft seal with low friction torque. *Smart Materials and Structures*. 2019, roč. 28, č. 4, s. 047002. ISSN 0964-1726.
- [139] KUBÍK, M., Z. STRECKER, J. ROUPEC, I. MAZŮREK, O. MACHÁČEK, D. PALOUŠEK a D. KOUTNÝ. Skelet jádra tvořeného pruty z feromagnetického materiálu. 307249. 2018. Czech Republic.
- [140] KUBÍK, M., Z. STRECKER, I. MAZŮREK, P. DANIEL a M. PŘIKRYL. Semiaktivní magnetoreologický tlumič. 159036. Czech republic.
- [141] MURPHY, T. *MR dampers bound for high volume*. 2012. Dostupné z: www.wardsauto.com

LIST OF FIGURES

Figure 1 Mounted MR damper on railway vehicle during testing on real track [5]	11
Figure 2 Magnetorheological effect; left: without the magnetic field, right: with the application of magnetic field (blue arrow)[22]	13
Figure 3 The particle chains behaviour of MR fluid during flow in the case: (a) without magnetic field, (b) with the magnetic field, (c) after turning off the magnetic field, and (d) after applying demagnetization magnetic field [23]	14
Figure 4 Typical yield stresses [50]	15
Figure 5 Effect of magnetic field on friction coefficient Hu et al. experiments (left) [60], Zhang experiments(right) [62]	16
Figure 6 The effect of particle size on friction coefficient and wear for O-ring seal flooded in MR fluid [58]	17
Figure 7 First-order system	18
Figure 8 The time dependency of shear stress on step change of control signal from Sherman model (left) [70] and Koyanagi experiments (right)[75]	19
Figure 9 Velocity profile development of MR fluid under magnetic field [72]	19
Figure 10 Layouts of the test rig [79]	21
Figure 11 The results of the experiments [79]	22
Figure 12 Experimental test rig [80]	22
Figure 13 Generalization of measured data [80]	23
Figure 14 Layouts of the test rig [81]	23
Figure 15 The results of the experiments [81]	24
Figure 16 Feedback mechanism of the smart material system [83]	59
Figure 17 Operating mode of MR fluid [92]	60
Figure 18 Mono-tube magnetorheological damper [43]	60
Figure 19 Single-coil structure (left); three-coil structure (right): 1, magnetic circuit; 2, electromagnetic coil; 3, annular gap; 4, magnetic flux lines; 5, non-magnetic section [97]	61
Figure 20 Dual-gap piston structure (left)[6]: 1, core coil; 2, electromagnetic coil; 3, gap 1; 4, gap 2;5, non-magnetic spacer; 6, sleeve; meandering valve (right) [97]:1, magnetic circuit; 2, electromagnetic coil; 3, meandering path	61
Figure 21 Conventional design of seal with magnetic fluid [107]	62
Figure 22 Response time definition	63
Figure 23 MR control valve with laminated magnetic circuit:1, rod; 2, sleeve; 3, annulus gap; 4, lids; 5, magnetic poles; 6,coil core; 7, electromagnetic coil; 8, casing [6]	64
Figure 24 The effect of piston velocity on MR damper response time [118]	65
Figure 25 Developed MR damper with short response time mounted on locomotive Škoda Transportation during testing (left), the main idea of structured magnetic circuit patent (right)	67
Figure 26 MR piston with permanent magnet;1, 2, 3 magnetic circuits; 4, lids; 5, piston rod; 6, permanent magnets; 7, an electromagnetic coil [135]	68
Figure 27 The course of primary response time (63 %) on orientation and magnitude of electric current for configuration with electric current step rise (left) and drop (right)	68
Figure 28 The structured core optimized for weight and homogenous magnetic flux density in the gap (left), manufactured structure by 3D metal printing method (right)	69
Figure 29 Performance comparisons of MR pistons	69
Figure 30 High-level Simscape model layout [137]	69
Figure 31 Effect of electric conductivity on the course of damping force (left); The effect of piston velocity of primary response time (right)[137]	70

Figure 32 Function principle of a pinch magnetorheological fluid seal (left) and test rig (right) . . . 70
Figure 33 The effect of rotation on friction torque (left) and pinch seal burst pressure (right) 71